The effects of magma plumbing system processes on the crystal cargo: a geochemical, textural and numerical modelling approach

Submitted by

Camilla Imarisio

For the degree of Doctor of Philosophy

Department of Earth Sciences

Royal Holloway, University of London

Supervisor: Dr. Christina Manning

September 2018

Declaration of Authorship

I Camilla Lara Imarisio hereby declare that this thesis and the work presented in it is entirely my own. Where the work of others has been consulted, this is always clearly stated.

Signed:

Date:

Acknowledgements

To my supervisor, Christina Manning, for guidance, (criticism) and advice throughout. For always believing, supporting me and guiding me to pursue new ideas, this PhD would have not been possible without you. I guess motivational Lego mini-figures and food also helped. To Pete Burgess, for stepping into this project and for the extremely valuable help and support. To Matthew Thirlwall, Dave McGarvie and Federico Lucchi, for their collaboration and critical discussion. Further thanks to the technical staff, Kevin and Neil, for their work and sample prep even though "I promise this is the last one" definitely was not the last one. I also thank Richard Hinton, the Edinburgh Ion Microprobe Facility staff and NERC for providing the funding and advice for the collection of SIMS data. Funding from the Research Committee, University of London, VMSG and the Mineralogical Society must be acknowledged for the support towards analytical costs and conferences attendance.

It would be impossible to name everyone who has supported me throughout this PhD. To all the postgrads and friends in Egham past and present, and to the members of the Volleyball Club, for providing fun times and enjoyable distractions. In particular thanks to Silvia, my co-conspirator, for the endless laughs and detailed drawings. To Arnaud, for supplying appropriate South Park quotes. To Albi, for excellent Camillabug repelling skills, and being ok fun. To Nathaniel, for being a perfect victim of pranks, for supplying yearly haggis/welsh cakes, for teaching me to play the bagpipes and being quite entertaining (except for the loud welsh singing). To my volcano buddy Sandy, desk neighbour Amy and Christofino for office chat and entertainment. To Zøé, for timely drawing skills, occasional Volcanoes Top Trumps, cake and Lava Tour. To little sister Gaietta, for sharing my passion for volleyball and food. To my friends back home: Ste, Clara, Illy, Linda, Coco, Marta and Fra for shortening the distance between us day after day, as if no time had gone past.

To James, for being endlessly caring and supportive, even through the toughest times. For feeling like home away from home. Long may our exploring continue.

The biggest thanks goes to my family. To mamma, papi, Filippo and Pietro for infinite support and encouragement in every step of this PhD and my life. For always being there for me, no matter the distance. To nonna Bianca, for still asking me how archaeology school is going, for the "carnina buona" and courgette flowers; to nonno M., Marco, Anna, Zia dei gatti, Martina, Sarah, Carla, Paola, and nonni Tina e Giancarlo for your unconditional love.

Abstract

The products of volcanic eruptions are the final result of a variety of processes such as fractional crystallisation, magma mixing and crustal assimilation. It is one of the challenges of modern volcanology to unravel the history of these products to better understand magma plumbing systems underlying volcanic centres and provide a strong basis for volcanic hazard assessment. Magmatic crystals, and plagioclase in particular, record information on the environment in which they grew in and hence zoned crystals store a detailed history of the conditions they have been stored in and the processes that have occurred, unfortunately due to complex mineral-melt relationships and complex crystallisation dynamics, these processes are difficult to quantify. For this thesis, a range of geochemical analyses has been used to investigate the chemical composition of volcanic rocks and crystals. Coupled with extensive macro and micro-textural petrological observations, these have been used to study the plumbing system of two volcanic centres in a plume centred rift zone and a subduction zone setting. The two centres differ from one another in terms of geodynamic setting, dominating magmatic open system processes, eruptive style, and erupted product composition and petrological characteristics. As well as providing the basis for investigating the full extent and differences of the effects of magmatic processes on the crystal cargo in rift versus volcanic arc settings, this also provided the opportunity to investigate the extent and dynamics of magmatic open system processes at these volcanic centres, where whole rock studies had so far been dominant.

Torfajökull is the largest silicic centre in Iceland and its last two historic eruptions, 871AD and 1477, have erupted simultaneously with the Veiðivötn fissure. The products of these eruptions provide a petrological and geochemical insight into magma mixing between basaltic and rhyolitic melts as well as mush entrainment processes. Volcanic chronometers, such as diffusion modification, have been used to model the timescales of these processes and have shown very quick mixing/entrainment to eruption times, on the scale of days, suggesting a strong link between melt interaction and eruption triggering. Magmatic processes and their extent can vary drastically between volcanic centres. To provide a comparison, lavas from Salina, Aeolian Islands, were sampled, where whole rock studies of intermediate lavas have been interpreted as the products of fractional crystallisation and crustal assimilation processes, common in volcanic arcs. The crystal cargoes hosted in these products provide an insight into the effects of magmatic recharge, crustal assimilation,

prolonged crustal storage and high water contents on crystal cargo chemistry, as well differences in plumbing system structure and evolution.

The data acquired from both volcanic systems is used to develop and test CrystalMath, a new numerical model developed which aims to forward model the evolution of a magma and its olivine - clinopyroxene - plagioclase crystalline assemblage. The model outputs the geochemical evolution of the melt and that of each crystal, and a 3D thin section like image providing a visual representation of the zoned crystals and the overall texture of the "rock". This forward model can be used to test and better quantify a range of crystallisation parameters and magmatic processes and their effects on the crystal cargo, using natural samples as a tie point.

“Look up at the stars and not down at your feet. Try to make sense of what you see, and wonder about what makes the Universe exist. Be curious."

Stephen Hawking

“He looked into the hole, and like any hole it said, Jump.”

Susan Sontag, The Volcano Lover: A Romance, 1992.

Table of Contents

List of Figures

List of Tables

Chapter 1

Aims

The overarching aim of this thesis is to contribute to the better understanding of the information preserved in crystal cargoes to reconstruct magmatic histories and plumbing system dynamics. In order to do this, this thesis has three sub-objectives aiming to investigate the effects of a variety of magma open system processes on the crystal cargo in order to better isolate, identify and quantify their effects on final magma composition and properties. A particular focus is given comparing the ability to assess sub surface processes in different tectonic environments including a rift-plume-interaction setting and a volcanic arc. The resulting data was then used to test a newly developed numerical model aimed at reproducing magmatic evolution with a focus on crystal cargo chemistry and textures. The three sub-projects had the following aims:

- To provide a comprehensive database of crystal cargo textures and chemistry for the mingled and hybrid products of the latest twinned eruptions of Torfajökull and Veiðivötn, Iceland, in order to provide information on extent, location and timescales of interactions between the two systems.
- As a comparison, a selection of intermediate and mingled products from the island of Salina, Aeolian Arc, was used in order to provide an understanding of the effects of arc volcanism open magma plumbing system processes, such as mixing, assimilation and crustal storage on the crystal cargo of intermediate products focussing on plagioclase microtextures and chemistry.
- To initiate the development of CrystalMath, a user-friendly numerical model able to forward model variations in texture and geochemistry across crystal populations and single crystals throughout magmatic evolution. Using user defined input parameters and conditions, the model utilises a set of published equations to reproduce geochemical and textural variation in crystals which can be directly compared to that of the natural samples, also providing a tool to investigate the relationship between crystallisation and nucleation rates. The data acquired in the Iceland and Salina studies is used as a test dataset for the model.

An overview and introduction on crystal cargoes studies, Icelandic and Aeolian Arc volcanism and numerical modelling of igneous systems is given in the following sections.

Thesis Outline

1. In this chapter a generic introduction to volcanic systems is given, with a particular emphasis on the study of crystal cargoes to reconstruct magmatic plumbing systems. A short introduction on Icelandic volcanism and the Aeolian Islands volcanoes is given, with a focus on the Torfajökull volcanic system and the island of Salina. Finally a brief review of numerical modelling of magmatic processes is presented alongside thesis aims and rationale.
2. In this chapter the sampling and geochemical analytical methods used to acquire the data in this thesis are presented.
3. In this chapter, presented in paper manuscript format, the data acquired for the Torfajökull volcanic system and a final plumbing system model is presented from textural and crystal cargo geochemistry interpretation, with a focus on magma mixing, mingling and entrainment processes.
4. In this chapter, presented in paper manuscript format, the data acquired for the island of Salina is presented, utilising crystal cargo geochemistry and textures for interpretation, with a focus on magma mixing, crustal assimilation and crustal storage conditions and processes.
5. In this chapter, presented in paper manuscript format, crystalMath is presented as a new forward model for the modelling of geochemistry and textural variations in crystal cargoes assemblages throughout magmatic evolution.
6. In this chapter a final critical evaluation, thesis conclusions and future research directions are presented.

1. Introduction

Approximately 800 million people live close to and are affected by active volcanoes (Brown et al. 2012). The goal of volcanological research is to improve the assessment of hazards imposed by volcanic eruptions by improving our understanding of underlying processes. But in order to be accurate, long term volcanic forecasting requires detailed knowledge of past volcanic activity.

Volcanoes vary greatly in eruptive style and behaviour due to their different tectonic setting, magma composition and eruptive conditions (Cashman et al. 2013 and references therein). There are several factors which affect volcanic eruption styles. These include rate of magma supply and eruption intensity, crystal content, magmatic water and gas contents, temperature, magma viscosity and the presence of external water (e.g. Cashman et al. 2013; Caricchi et al. 2014; Caricchi and Blundy 2015; Cassidy et al. 2018). These factors are greatly dependent on magmatic evolution (i.e. the extent of undergone fractional crystallisation) which in turn is affected by magma storage and processes occurring in plumbing systems and, ultimately, by their tectonic setting (e.g. Annen et al. 2006; Blundy and Cashman 2008; Caricchi and Blundy 2015; Sparks and Cashman 2017; Cassidy et al. 2018). Similarly, it is essential to understand which processes could be acting as eruption triggers, and how to recognise them in the erupted products. These processes commonly include recharge - the introduction of new melt into the system – which may disrupt the network and remobilise the crystals in the mush zone due to the introduction of new gases, increased heat causing conductive self-mixing or by fracturing the network (Murphy et al. 2000; Ruprecht et al. 2012; Cashman et al. 2013; Burgisser & Bergantz 2011; Bachmann & Huber 2016; Costa et al. 2010). Commonly the term "recharge" refers to the introduction of a mafic primitive melt into a more evolved system, however injection of silicic/dacitic magma has also been documented to be able to trigger eruptions (Smith et al. 2009). Whilst recharge is effectively a form of magma mixing event taking place within the same volcanic system, magma mixing however can also refer to any type of interaction between melts, even melts belonging to different systems (Walter et al. 2014). Other eruption triggering mechanisms include pressure build up in the chamber which can be caused by crystallisation of a water supersaturated magma (Tait et al. 1989), and changes in mechanical and stress conditions in the chamber, referred to as tectonic triggering (Gravley et al. 2007).

Therefore, understanding processes occurring during magma shallow storage in the crust is a critical aspect for characterising the composition and the eruptive behaviour of a volcano. Over the past decade these studies have been focussing on the crystal cargoes hosted in erupted products as a tool to reconstruct magmatic histories (e.g. Vance 1965, Ginibre et al. 2002, Jerram & Martin 2008; Streck 2008; Viccaro et al. 2010; Neave et al. 2014, Cooper 2017).

1.1 Crystal Cargoes Studies

Igneous rocks are the main product of volcanic processes and can give us insights into volcanic behaviour and eruption style. Whole rock analysis of igneous rocks can give us information of the magma composition, fractional crystallisation processes and to some extent magma origin and melting processes (e.g. Mørk 1984; McGarvie 1984; Ellam et al. 1989; Ellam and Harmon 1990; McGarvie et al. 1990; Calanchi et al. 1993; Gertisser and Keller 2000; Peccerillo et al. 2004; Zellmer et al. 2008; Lucchi et al. 2013). However, for processes such as magma mixing, whole rock analyses are insufficient as they are the result of a series of superimposed differentiation and evolution processes making it difficult to track and quantify magma evolution. On its journey to the Earth's surface magma evolves as various processes take place; shallow level processes in particular can change the signature of a melt, its behaviour and crystal content (Browne & Gardner 2006; Humphreys et al. 2008; Costa et al. 2010; Viccaro et al. 2010; Druitt et al. 2012; Renjith 2014; Cassidy et al. 2018; Pankhurst et al. 2018;).

Understanding sub-volcanic systems relies on studying the erupted products; these are in fact rarely composed of a single crystal population originating from the same batch of magma. Over the past decade, studies of crystal populations have revealed that crystal cargoes comprise of up to four main components forming what we refer to as the crystal cargo: phenocrysts, xenocrysts, antecrysts and microlites as illustrated in Figure 1.1 (i.e. Jerram & Martin 2008).

Mineral-Melt Equilibrium and Disequilibrium

Minerals are a product of specific time and crystallisation conditions in the evolution of the melt, and therefore the whole rock is a combination of different components representing different stages of magmatic evolution. Records of disequilibrium are present in erupted lavas, for example the juxtaposition of two or more phase that are out of equilibrium with each other and resorbed crystals. Models of magma evolution must

therefore include the effects and causes of disequilibrium and their role in unravelling magmatic histories.

Cargoes found in erupted lavas may not have crystallised from the same melt in which they are hosted in. Phenocrysts, for example, were originally defined to be crystals visibly larger than the groundmass (Iddings 1899). This soon developed into the idea that phenocrysts were instead grains that appeared to be in equilibrium with its host rock (Cox et al. 1979), until recent studies that suggested that these are grains that appear to have crystallised in equilibrium with the host melt at some point during its magmatic evolution (Jerram & Martin 2008). In contrast to this, xenocrysts were suggested to be crystals which showed no relationship with the host melt, and were thought to be assimilated from previous magma batches into their carrier melt (Harker 1986). Later studies focussing on major element and isotopic disequilibrium between crystals and their host melt (e.g. Davidson et al. 2007; Halldórsson et al. 2008) highlighted the fact that this original classification was inadequate and not representative of the whole range of cargoes observed in erupted lavas. This lead to the suggestion of the term antecryst, representing grains which are thought to have crystallised from a melt similar to the host melt, but not in the same melt as in which they are erupted. The melt could have had a similar source but followed a different evolutionary path through the plumbing system (e.g. Davidson et al. 2007, Jerram & Martin 2008). A fourth type of cargo is also present – microlites, which differ from all the previous types of cargoes in both size and origin. These small crystals are the result of rapid nucleation and growth caused by degassing upon eruption (Jerram & Martin 2008). Due to their late crystallisation, they are in chemical equilibrium with the melt and could be therefore used to constrain glass composition.

Due their complex origins, crystals in volcanic rocks are rarely homogeneous in composition. As the melt in which they are hosted evolves and differentiates, both the major and trace element chemistry of the crystals also changes. Zoning patterns in crystals can therefore be used to track changes in the environment in which they were crystallising in (e.g. Vance 1965; Kirkpatrick 1975; Ginibre et al., 2002). Although phase equilibria studies have provided insights into the nature of magmatic processes (e.g. Roeder and Emslie 1970; Drake and Weill 1975; Ford et al. 1983; Beattie et al. 1991; Blundy and Wood 1991, 2003; Bindeman et al. 1998; Li and Ripley 2010), the validity of using equilibrium experiments to understand disequilibrium features in natural samples remains a caveat in igneous systems modelling. As a results of this, throughout this study it is

important to note the comparison of mineral chemistry to that of the whole rock can result in discrepancies. Throughout this thesis, for crystal populations used to infer magmatic processes, crystal-melt relationships will be considered on a zone to zone basis. This will be particularly relevant when using crystals for thermobarometric calculations (presented in Chapter 3 and 4), where crystal chemistry and back calculated melt compositions should be considered separately from the whole rock.

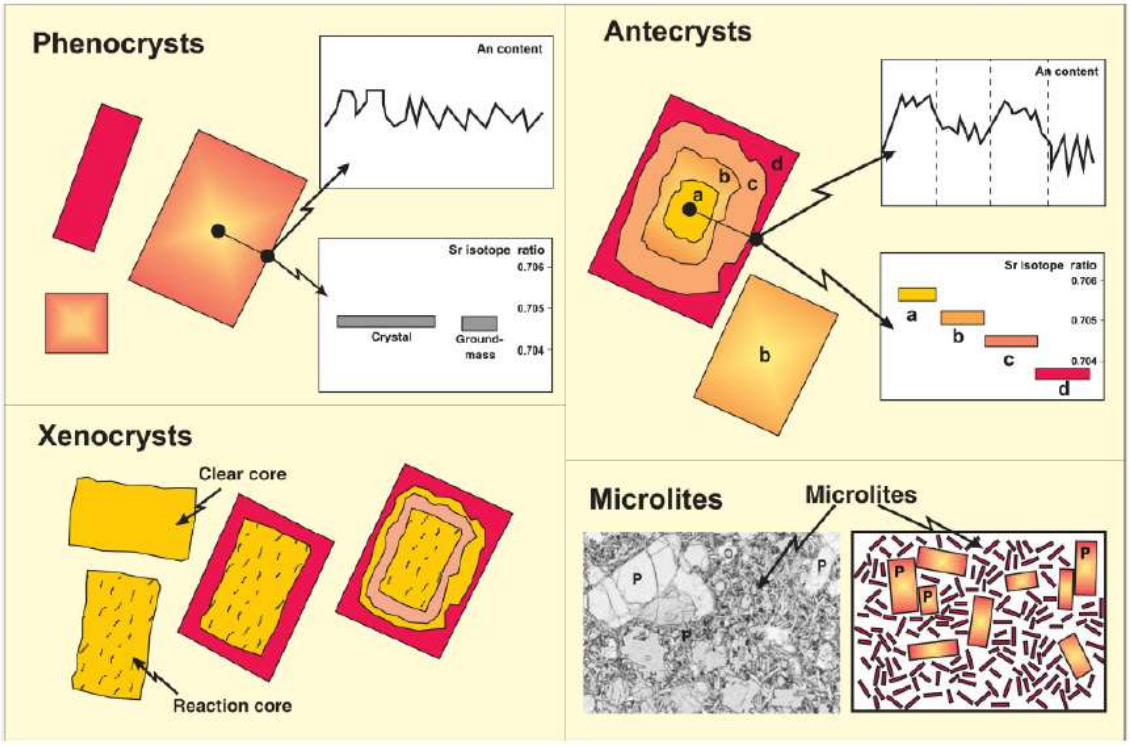

Figure 1. 1: schematic description of the different crystal populations that can be identified in a single sample as part of the crystal cargo: phenocrysts, xenocrysts, antecrysts and microlites (from Jerram et al (2018), modified from Jerram and Martin (2008)). It is important to note that these descriptions are not always relatable to natural samples, and this has been explained in the text (e.g. disequilibrium features in phenocrysts).

Controls on Crystallisation and Textures

As previously mentioned, the textures and composition of minerals record the physical and chemical conditions in which they crystallised in, and this in turns represents the processes occurring in the magmatic system. Plagioclase is particularly useful in this regard as it is found in abundance across a wide range of compositions and tectonic settings such as mid-ocean ridges (e.g. Nielsen et al. 1994; Lange et al. 2013), ocean islands (e.g. Cullen et al. 1989), and continental arcs (e.g. Ginibre et al. 2002; Cashman and Blundy 2013).

Nevertheless, the strong dependency of plagioclase anorthite on melt water content and pressure (Panjasawatwong et al.1995; Putirka, 2005), as well as temperature and melt composition, complicates the relationship between plagioclase and melt. The resulting growth, dissolution and nucleation kinetics affect plagioclase composition and morphologies. Experimentally, these have been shown to be a function of undercooling (Lofgren 1972, Lofgren 1974) where the increase in the degree of undercooling under equilibrium conditions results in the change from tabular to skeletal crystal morphologies, accompanied by crystallisation of more evolved compositions. The rate of undercooling also plays a major role in the macro-textural characteristics of erupted products. Nucleation and growth rates are in fact a function of crystallisation temperature and magma temperature (Kirkpatrick 1975; Kirkpatrick 1978) and control phenocrysts content and size, new growth, and microlite nucleation, as shown in Figure 1.2.

Microtexturally, rapid crystal growth due to undercooling can cause dissolution in the crystal cores as well as geochemical disequilibrium of minor trace elements which become highly concentrated in the outer newly crystallised rim (Bottinga et al. 1996). Under these conditions, plagioclase crystals can also display minor reverse zoning, creating areas of high and low amplitude oscillatory zoning as the result of the crystal attempting to attain its equilibrium growth conditions (Smith and Lofgren 1979). Large degrees of undercooling can also be observed in the case of magma mixing, where these changes are accompanied by distinct changes in composition.

As previously stated, decreasing temperature (or undercooling) is the main driver of crystallisation (Kirkpatrick 1975; Kirkpatrick 1978). Assuming a constant pressure and water content, this results in magmatic differentiation and an increasingly more albitic plagioclase composition. In the opposite case, in case of temperature increase at a constant melt composition, plagioclase could superheat under disequilibrium conditions and become resorbed. Resorption is a common kinetic texture of plagioclase, and can also occur in dry systems under water-undersaturated decompression (Nelson and Montana 1992). Similarly, decompression from high to low pressures causes a decrease in plagioclase anorthite (Nelson and Montana 1992; Panjasawatwong et al. 1995; Blundy and Cashman 2005) as well as resorption in the core of the crystal (i.e. coarse sieves (Renjith, 2014). These range of textures can therefore be used to reconstruct the crystallisation environment in which the crystals grew in, and their overall crystallisation histories.

Crystal Cargoes Textures and Zoning & Associated Processes

Mineralogists and petrologists started recognising fine scale heterogeneities in crystals thanks to the advent of polarised microscopy in the 19th century and since then the interpretation of crystals and mineral zoning patterns has developed. Enhanced micro textural studies have allowed to recognise different types of features developing during the growth and dissolution of crystals which can help us develop qualitative relationships between textures and magmatic processes (e.g. Zieg & Lofgren 2006; Costa et al. 2008; Humphreys et al. 2008; Jerram & Martin 2008; Viccaro et al. 2010; Renjith 2014).

According to the classification by Jerram & Martin (2008) (Figure 1.1), phenocrysts are considered to be co-genetic to the melt in which they are hosted in. In equilibrium, these are often euhedral with normal zoning patterns indicating growth and crystallisation driven by undercooling in a stable environment, with gradual changes in chemistry towards more evolved compositions, as expected as a result of fractional crystallisation. Nevertheless, we now know that processes such as rapid crystal growth, decompression and convection within the chambers could result in phenocrysts developing more complex zoning patterns (e.g. oscillatory zoning) (Ginibre et al. 2002; Streck , 2008; Renjith 2014) and sieving textures (Nelson and Montana 2002; Renjith 2014) (Figure 1. 2). In the case of magmatic recharge, undercooling would cause phenocrysts to develop disequilibrium reaction rims (Bottinga et al. 1996) and compositionally reverse zoned rims (e.g. Tepley et al. 1999; Ginibre et al. 2002; Humphreys et al. 2006; Ginibre et al. 2007; Streck, 2008; Viccaro et al. 2010; Neave et al. 2014; Renjith 2014; Viccaro et al. 2016). Xenocrysts and antecrysts, considered to be crystals inherited from a batch of magma different to that in which they are hosted in upon eruption (Jerram & Martin 2008), often show disequilibrium textures, such as irregular crystal edges, compositional zoning often showcasing reverse and/or abrupt zoning patterns and disequilibrium inner areas of the crystal, such as resorbed surfaced (Figure 1. 2). Recycling of these crystals can result in different zones and overgrowths, and their residence times do not relate to that of the magma system. They may however provide constraints on timescales of assimilation and mixing processes (e.g. Davidson et al. 2001; Costa et al. 2003; Morgan et al. 2004; Costa et al. 2008; Costa et al 2010, Druitt et al 2012; Cooper and Kent 2014; Petrone et al. 2016; Viccaro et al. 2016, Ubide & Kamber 2018). Antecrysts - genetically related to the magmatic system in which they are hosted in - do not originate from the

same magma batch as the phenocryst cargo. Texturally they can display characteristics typical of both phenocrysts and xenocrysts (Jerram & Martin 2008).

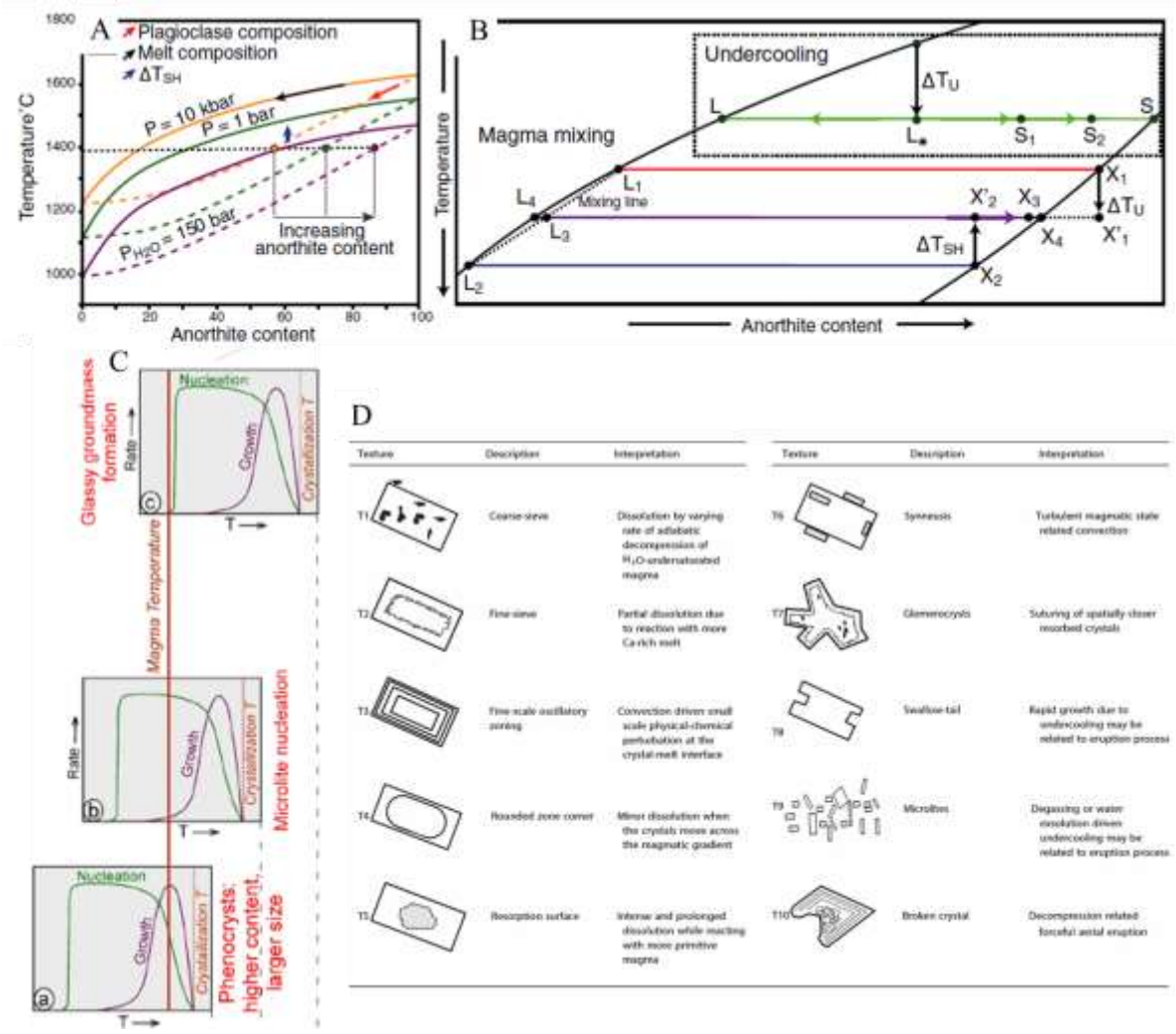

Figure 1. 2: A & B: phase diagrams illustrating the kinetic controls on plagioclase composition and crystallisation. A – albite-anorthite phase diagram illustrating the effects of temperature, pressure and water content on plagioclase composition, B – albite-anorthite phase diagram showing the effects of undercooling and mixing on plagioclase composition (from Bennett et al. 2019); C: schematic representation of the effects of increasing temperature on the kinetics of crystallisation, and the resultant petrographic characteristics (from Francalanci et al. 2014); D: schematic table describing the range of microtextures observed in plagioclase crystals and interpretation of the magmatic processes responsible for each microtexture type (modified from Renjith (2014)).

Crystal textures are most commonly divided into zoning, a result of compositional variations within the crystal, and intra-grain textures such as sieving and other structural characteristics (Figure 1. 2) (e.g. Jerram & Martin 2008; Streck 2008; Viccaro et al. 2010; Renjith 2014). Both normal and reverse zoning can be continuous or have an abrupt (or discontinuous) nature, where a sudden change in composition is observed between, for

example, core and rim. These abrupt changes are associated with arrested crystal growth due, for example, to disequilibrium conditions such as magma mixing (Tepley et al. 1999; Davidson et al. 2001; Ginibre et al. 2002 and references therein, Humphreys et al. 2006; Davidson et al. 2007; Ginibre et al. 2007; Streck 2008; Viccaro et al. 2010; Browne & Gardner 2006; Humphreys et al. 2008; Costa et al. 2010; Druitt et al. 2012; Churikova et al. 2013; Shea & Hammer 2013; Renjith 2014; Shea et al. 2015: Petrone et al. 2016; Viccaro et al. 2016). Prolonged disequilibrium conditions can cause the resorption of some areas of the crystal, followed by re-equilibration and growth, resulting in crystal zoning irregular in shape and width, also referred to as "convolute" zoning. Finally, crystals are often subject to transport within the chamber, where convection causes changes in pressure and temperature conditions of crystallisation and growth resulting in oscillatory zoning (e.g. Jerram & Martin 2008; Streck 2008; Viccaro et al. 2010; Renjith 2014;). These zones oscillate regularly across the crystal and are usually smaller in width than abrupt zoning caused for example by magmatic recharge or mixing (abrupt zoning).

Similarly to zoning, structural and physical microtextures can also be associated to a series of magmatic processes (e.g. Jerram & Martin 2008; Streck 2008; Viccaro et al. 2010; Renjith 2014 and references within). Coarse sieving textures, identified as large subrounded areas of dissolution in the crystal, often found in the core, are thought to be a result of decompression (Humphreys et al. 2006; Jerram & Martin 2008; Streck 2008; Viccaro et al. 2010; Renjith 2014 and references therein). As described above, in some cases this is also associated to rapid skeletal growth as a result of undercooling (Kuo and Kirkpatrick, 1982) which, if in relation to eruption processes, may also cause a swallow tail feature in the crystal outer zone (Renjith 2014). Fine sieving patterns are also a result of crystal dissolution, nevertheless these are smaller in size, and usually concentrated around a particular zone. Fine sieving patterns are indicative of disequilibrium upon interaction with a new melt of different composition (Renjith 2014 and references therein). Intense and prolonged disequilibrium and dissolution would eventually result in resorption surfaces, often found in the inner zones (and cores) of the crystals. Upon dissolution and re-crystallisation, spatially close crystals can suture and merge together to form glomerocrysts (Hansen & Grönvold, 2000; Gurenko & Sobolev, 2006; Ridley et al., 2006; Holness et al., 2007; Costa et al., 2010; Neave et al 2014, Ubide et al. 2014). Turbulent magmatic convection can also cause clots of crystals, nevertheless these usually showcase similar orientation, and are not a result of dissolution events (Renjith

2014). This process is also referred to as “synneusis”. These processes and associated textures are discussed further and in more detail alongside the data in Chapter 3 and Chapter 4.

Combining Zoning, Textures and Geochemical Modelling

Figure 1.3 schematically illustrates the advantages of acquiring subgrain geochemical data compared to single grain and whole rock (WR) analysis. The upper part of the image shows four different crystals from the same sample. They all present different zoning patterns, illustrated by different and distinct colour coded zones. The graphs at the bottom, showing the trace element concentrations, show that only with subgrain analysis it becomes clear that the colour coded zones of the crystals have a different compositions representing discrete events which are shared to different extents by the four crystals (Davidson et al. 2007), rather than the homogeneised signature represented by the whole rock (WR). Recent technological improvements have given the possibility to analyse crystal cargoes and acquire higher precision data allowing us to measure isotopic and geochemical signatures on the scale of individual crystals and thus integrate geochemical data to petrographical information, such as textures and zoning patterns to understand a large range of magmatic processes such as fractionation, degassing, magma mixing and storage and ascent in the crust (Tepley et al. 1999; Davidson et al. 2001; Browne & Gardner 2006; Humphreys et al. 2006; Davidson et al. 2007; Ginibre et al. 2007; Humphreys et al. 2008; Streck 2008; Viccaro et al. 2010; Costa et al. 2010; Druitt et al. 2012; Shea & Hammer 2013; Renjith 2014; Shea et al. 2015; Petrone et al. 2016; Viccaro et al. 2016). Geochemical modelling of crystal cargoes can allow us to extract valuable information to quantify the rates and location of magmatic processes.

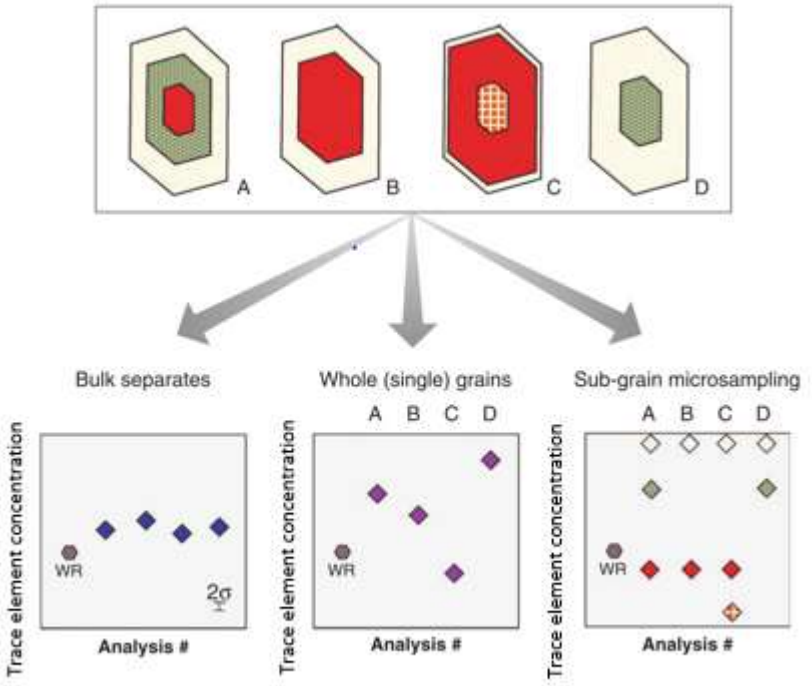

Figure 1. 3: schematic comparison of information provided from crystal analysis on different scales, highlighting the amount of information that can be acquired from subgrain analysis (right) compared to whole rock (WR data point) or single grain (middle) modified from Davidson et al. (2007b) to focus on trace element zoning in crystals.

Alongside geochemical and textural studies, thermobarometry models (Ford et al. 1983; Putirka et al. 2003; Putirka 2005; Putirka 2008; Ridolfi & Renzulli 2012; Neave & Putirka 2017), crystallisation kinetic models (Cashman & Marsh 1988; Marsh 1988; Armienti et al. 1994; Couch et al. 2003; Hersum & Marsh 2007; Tsune & Toramaru 2008; Pupier et al. 2008; Shea & Hammer 2013; Mollo & Hammer 2017), diffusion models (e.g. Davidson et al. 2001; Costa et al. 2003; Morgan et al. 2004; Costa et al. 2008; Costa et al 2010, Druitt et al 2012; Cooper and Kent 2014; Petrone et al. 2016; Viccaro et al. 2016, Ubide & Kamber 2018) and mineral-melt partitioning models (e.g. Blundy and Wood 1991; Beattie 1994; LaTourrette et al. 1995; Wood and Blundy 1997; Bindeman et al. 1998; Green et al. 2000; Ren et al. 2003; Matzen et al. 2013), have been used to further constrain and quantify processes by providing information on composition, pressure (and depth), temperature and timings of crystallisation.

1.2 Reconstructing Volcanic Plumbing Systems

Understanding the meaning of variations in crystals implies leaving behind the concept of crystals just floating in a magma chamber, and embrace the idea of complicated

plumbing systems and magma evolution pathways (Viccaro et al. 2010; Turner et al. 2013; Nicotra et al. 2014; Caricchi & Blundy 2015; Burchardt & Galland 2016). Whilst single crystal studies can give us an insight into magmatic history and processes, it is the study of compositionally and spatially different crystal populations, or phase assemblages, which allow us to cross-correlate them giving us a wider overview of the variety of magmatic processes occurring prior to eruption as shown in Figure 1. 4 and their links to the plumbing system structure (Tepley et al. 1999; Davidson et al. 2001; Browne & Gardner 2006; Humphreys et al. 2008; Viccaro et al. 2010; Churikova et al. 2013; Shea & Hammer 2013; Renjith 2014; Shea et al. 2015; Petrone et al. 2016; Viccaro et al. 2016).

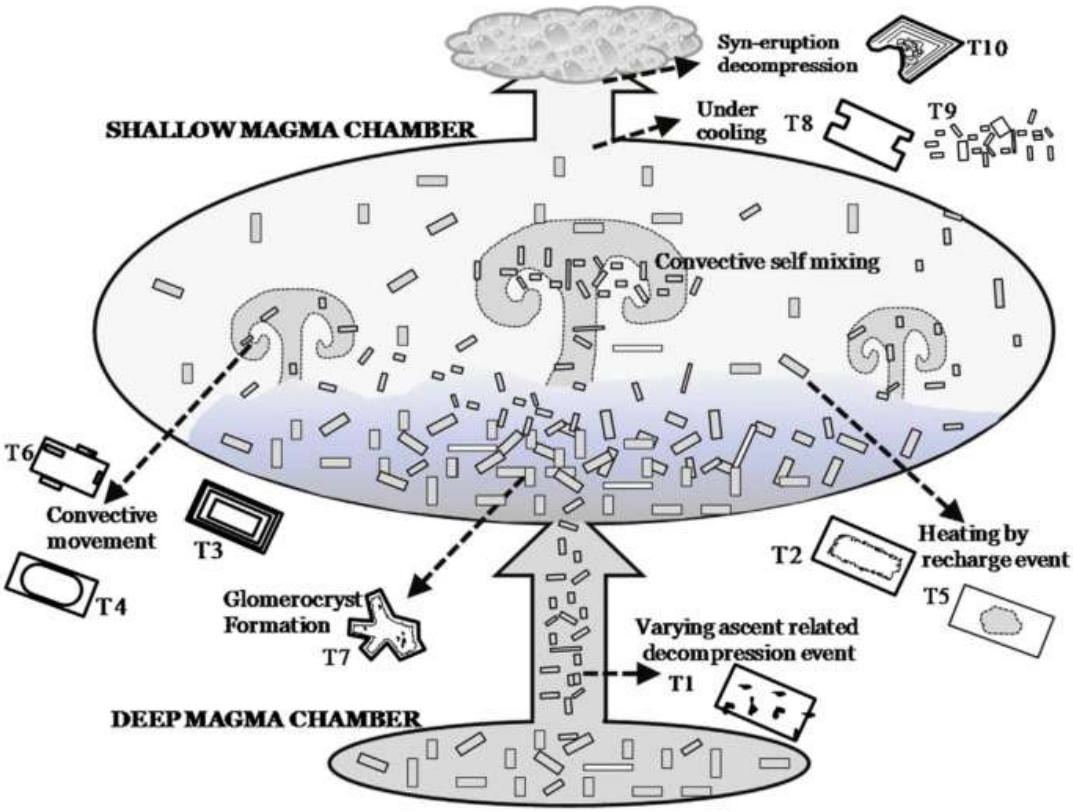

Figure 1. 4: magmatic processes reconstruction by combining micro textural information to geochemical compositional profiles of plagioclase phenocrysts (from Renjith (2014)). More recent studies have now shown that plumbing system structures are more complex than the traditional image of a single large magmatic chamber.

Over the past ten years or so, studies of magma storage regions have changed the traditional view of magma chambers as large, molten bodies of melt (as illustrated in Figure 1. 4). The integration of geochemical and geophysical data with numerical models has provided new views into the evolution of magma storage regions where plumbing

systems have been recognised to be composed of a deep system of interconnected mush zones and conduits (Figure 1. 5), and, sometimes multiple, magmatic chambers containing melt (Hildreth 2004; Annen et al. 2006; Caricchi & Blundy 2015; Cashman et al. 2013; Sparks & Cashman 2017). Plumbing system systems vary across tectonic settings, forming as a response to different crustal processes (Edmonds et al 2019), and mush zones are found both as trans-crustal systems (spanning the length of the reservoir in the crust and beyond) and as sub-solidus areas separating stacked storage zones (Figure 1. 5) (Edmonds et al 2019). Mush zones underneath volcanic centres contain both crystals and differing proportions of interstitial melt and are thought to be non-eruptible, acting as a rheological barrier (Bachmann & Huber 2016; Bégué et al. 2014; Gelman et al. 2013; Caricchi & Blundy 2015; Burgisser & Bergantz 2011; Bergantz et al. 2015). Cumulate and mush disaggregation is now a widely recognised process which can be identified from the compositional variability of the erupted products (e.g. Salaün et al. 2010; Passmore et al. 2012) and from the textural and compositional variation of their hosted cargoes (Hansen & Grönvold, 2000; Gurenko & Sobolev, 2006; Ridley et al., 2006; Holness et al., 2007; Costa et al., 2010; Neave et al 2014, Ubide et al. 2014). A better understanding of mush entrainment and disaggregation processes is important as it sheds light on the timing and location of this processes, which in turn can be linked to eruption triggers (e.g. Costa et al. 2010, Ubide & Kamber 2018).

Whilst combining high resolution geochemical and textural studies with geophysical observations has revolutionised our understanding of magmatic plumbing systems and processes, the timescales, extent and location of this processes remain to be fully understood. In particular, these can vary drastically between tectonic settings and different volcanic systems, where further integration of these studies could provide a more holistic and multidisciplinary view and understanding of subvolcanic plumbing systems.

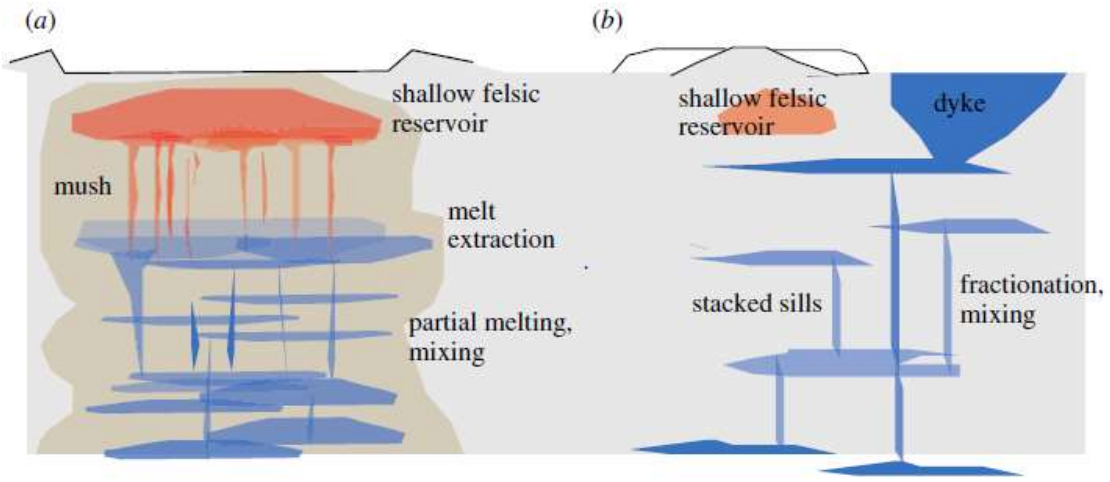

Figure 1. 5: schematic representation of two different end-member types that may exist in a) volcanic arc settings and b) in Icelandic rift-plume dominated settings (from Edmonds et al. (2019)). Type "a" systems may sometimes be referred to as trans-crustal mush systems, where the reservoir may span the whole length of the crust or beyond. Type "b" settings are instead characterised by the presence of subsolidus material separating multiple "stacked" magma storage zones (e.g. sills). These structural differences also result and are a result of different crustal processes.

1.2.1 Overview of Current Numerical Models for Igneous Systems

Even though qualitative data and observations of the crystal cargoes can give us an insight into magma plumbing system processes, quantitative data can constrain more detailed physical models of these processes. The literature provides plenty of data and information on modelling crystal growth, interpreting igneous textures through modelling of crystal size distribution (CSD) and experimental techniques (Cashman & Marsh 1988; Marsh 1988; Higgins 2000; Higgins 2002; Armienti et al. 1994; Pupier et al. 2008; Schiavi et al. 2010; Ni et al. 2014; Špillar & Dolejš 2015; Mollo & Hammer 2017). The idea behind CSD is to find a set of governing equations during nucleation and growth which would conserve the number of crystals, balancing the nucleation of new crystals and the loss of some due to a series of magmatic processes. This can enable us to obtain the number, size and shape of the crystals in an igneous rock reflecting the physical conditions under which the crystals nucleated, grew and the equilibrium-disequilibrium events during the cooling history of a melt (e.g. Cashman and Marsh 1988; Marsh 1988; Armienti et al. 1994; Higgins 2000, 2002; Pupier et al. 2008; Schiavi et al. 2010; Ni et al. 2014; Špillar and Dolejš 2015; Mollo and Hammer 2017). Models such as CrystalMoM (Colucci et al. 2017) have been developed to study the kinetic crystallisation in magmatic systems, and to obtain nucleation and growth rates of volcanic crystals from magmatic textures (Špillar & Dolejš 2014). Nevertheless these rates are often difficult to constrain and to apply to

scaled down models. Softwares (e.g. MELTS) exist which are designed to facilitate thermodynamic modelling and equilibrium in magmatic systems over a determined pressure and temperature range in order to help the determination of which mineral assemblage would crystallise under specific conditions (Ariskin et al. 1993; Ghiorso & Sack 1995; Smith & Asimow 2005). More recently, the development of Petrolog3 (Danyushevsky & Plechov 2011) has allowed the modelling of equilibrium crystalline assemblages during fractional crystallisation. Textural models (e.g. Viccaro et al. 2010; Renjith 2014) have shown to be able to qualitatively describe open system processes, however they do not provide a tool for quantification.

Existing models are not focussed on crystal cargoes evolution, and instead focus on whole rock. Moreover these models do not provide data and graphical outputs which can be easily and directly compared to natural samples and data. With existing models focussed on whole rock, it is not possible to see the variation within single crystals and across populations and how these are affected by crystal growth and nucleation processes as well as superimposed shallow plumbing system processes such as magma mixing and assimilation.

In this general context, two different volcanic systems have been selected: the Torfajökull volcanic system, Iceland (Chapter 3), and the island of Salina in the Aeolian Islands (Chapter 4). For both systems extensive whole rock studies were previously carried out, nevertheless crystal cargoes remain largely unexplored, and quantification and characterisation of plumbing systems and processes partially unconstrained. The Torfajökull system (rift plume setting) will be used to focus on interactions between magmatic systems, and the resulting mixed and mingled products. In contrast, the island of Salina (volcanic arc setting) will be used to investigate these process at volcanic arcs, with a particular focus on intermediate compositions and the products of assimilation and entrainment processes. Both datasets will be used to test a new numerical model (Chapter 5), focussed on the crystal cargo, which can be used to quantitatively constrain initial crystallisation conditions, and extent of magmatic processes resulting in the large geochemical variation observed across populations and within single crystals. Thin section-like outputs resulting from this model can also be compared to natural samples, therefore providing a further tool for crystal cargoes studies to petrologists and non-experts alike.

1.3 Rifts and Hot spots: Icelandic volcanism

Iceland is located at the junction between the Reykjanes Ridge in the south and the Kolbeinsey Ridge in the north where the NE Atlantic plate boundary interacts with a deep-seated mantle plume (Gudmundsson 2000; Thordarson & Larsen 2007; Shorttle et al. 2013; Jacoby & Gudmundsson 2007; M F Thirlwall et al. 1994). The interaction between a mid ocean ridge and a mantle plume results in high-rate melt production, due to adiabatic melting and high temperatures, and thus abundant and frequent volcanic activity at the surface (Thordarson & Larsen 2007). The mantle plume that now sits beneath the Vatnajökull glacier at a depth of ~400km (Gudmundsson 2000), has been active for the past 65 Ma and can be tracked back to the formation of the North Atlantic Igneous Province as shown in figure 1.5. Iceland's construction begun 24 Ma but the exposed rocks only date back to 14-16 Ma and is the only part of that is still volcanically active (Thordarson & Larsen 2007).

Due to the high melt production, the most obvious surface expression of the interaction between the mantle beneath Iceland and the plume is the very intensive volcanism along the spreading ridges; this is confined to one major zone referred to as the Neovolcanic Zone which itself has three geographically distinct subzones: the Western, Eastern and Northern Volcanic Zones (Jacoby & Gudmundsson 2007), shown in Figure 1. 6.

In SW Iceland the spreading is expressed on land by the Western Volcanic Zone that, extending to the north, leads to the Northern Volcanic Zone. The Mid Iceland Volcanic zone represents a region along which the ridge is offset; from here the Eastern Volcanic Zone propagates to the SE of Iceland and rift relocation, due to the movement of the lithospheric plate with respect to the plume, will eventually cause the transfer of the focus of extension from the Western to the Eastern Volcanic zone (Hardarson et al. 1997). This rift relocation, "rift-jump", phenomenon has previously taken place at 24Ma, 15Ma, 7Ma and 3Ma forming segments of 300-400km and leaving behind paleorifts. These repeated jumps are thought to happen in order to maintain the rift position near the plume as shown by their movement in a south-eastward propagating motion, towards the current plume location (Hardarson et al. 1997; Jacoby & Gudmundsson 2007; Thordarson & Larsen 2007)

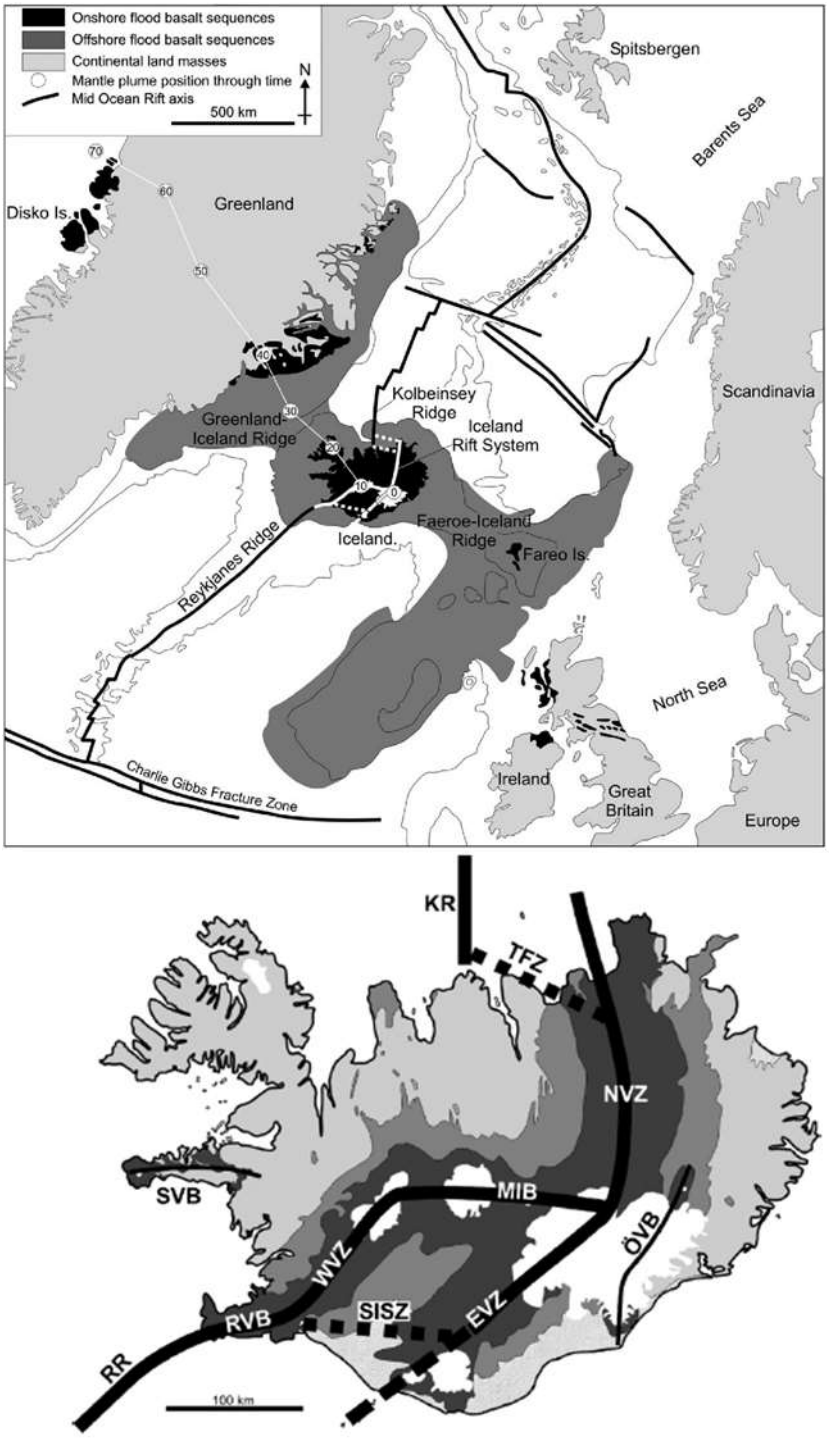

Figure 1. 6: Top: sketch tectonic map of the Iceland Plume track from 70 Ma until its present day location underneath Iceland. White lines over Iceland represent the subaerial spreading ridges and Icelandic rift zones (from Thordarson and Larsen (2007)); Bottom: enlarged map of Iceland showing the different volcanic zones and belts: RR, Reykjanes Ridge; RVB, Reykjanes Volcanic Belt; SISZ, South Iceland Seismic Zone; WVZ, West Volcanic Zone; MIB, Mid-Iceland Belt; EVZ, East Volcanic Zone; NVZ, North Volcanic Zone; TFZ, Tjörnes Fracture Zone; KR, Kolbeinsey Ridge; O¨ VB, Öræfi Volcanic Belt; SVB, Snæfellsnes Volcanic Belt (from Thordarson and Larsen (2007).

Volcanism in Iceland is characterised by the presence of volcanic systems, featuring a central volcano which represents the focal point of volcanic activity and a dyke or fissure swarm which is aligned sub-parallel to the axis of the volcanic zone (Thordarson & Larsen 2007). Several studies proposed contrasting mechanisms to explain the behaviour of Icelandic volcanic systems (Sigurdsson & Sparks 1978; Gudmundsson 1995; Gudmundsson 2000) and have been summarised by Thordarson and Larsen (2007):

a) Rifting in the volcanic system driven by magma replenishment of a shallow crustal reservoir followed by lateral injection of a dyke into the fissure swarm (Figure 1. 7).
b) Rifting episode driven by magma pressurisation of a deep reservoir followed by sub-vertical injection of dykes into the upper crust (Figure 1. 7).

Iceland provides an ideal setting to study magmatic processes as it features almost all eruptive styles and products on Earth, including explosive stratovolcanoes such as Hekla (Thordarson & Larsen 2007). Whilst rift zone products are often basaltic and tholeiitic in composition, central volcanoes and flank zone volcanic centres show higher proportions of evolved magmas and alkaline basalts (Macdonald et al. 1990b; Thordarson & Larsen 2007; Shorttle & Maclennan 2011).

The activity in Icelandic systems is linked to distinct tectonic rifting episodes and the activation of a system often results in volcano-tectonic episodes characterised by the occurrence of earthquake swarms and volcanic eruptions (Björnsson et al. 1977; Sigurdsson & Sparks 1978; Hartley & Thordarson 2013;).

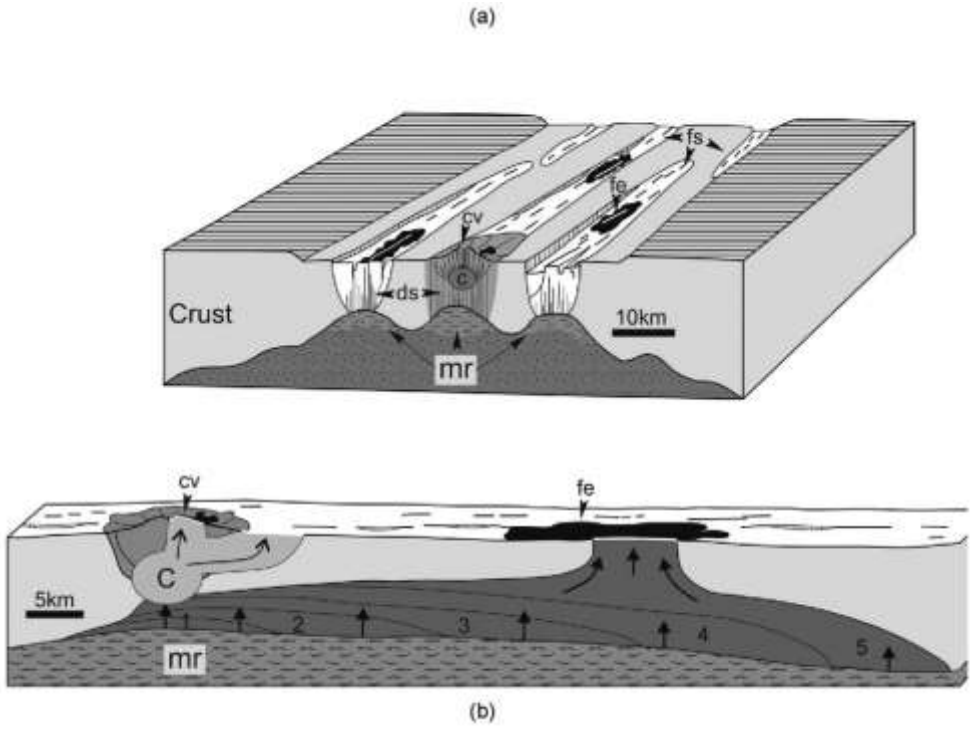

Figure 1. 7: cartoon illustrating the two proposed models for Icelandic volcanic system structure and behaviour as described in the text. mr: magma reservoir; c: crustal magma chamber; ds: dyke swarm; cv: central volcano; fs: fissure swarm; fe: fissure eruption (from Thordarson and Larsen (2007)

Recent seismic and eruptive events at Barðabunga volcano in Iceland have again highlighted the potential hazards associated to closely related volcanic systems. After the onset of the eruption, a 45km long dyke was quickly emplaced and gradually extended towards the North-East, threatening to intersect the plumbing system of Askja, one of Iceland's major stratovolcanoes. Gudmundsson et al. (2014) discussed the possibility of earthquakes, generated by the propagating dyke, triggering eruptions at close volcanic centres; observations were based on mechanical interactions and no exchange of material has been observed. In contrast, the Torfajökull – Veiðivötn volcanic systems have shown simultaneous rift and central volcano eruptions with evidence for interaction between the magmas feeding the two systems.

1.3.1 The Torfajökull – Veiðivötn volcanic systems

Torfajökull is a flank zone central volcano, meaning that the area experienced little rifting, and has been active for at least 400 ka. It is the largest collapse caldera structure in the Neovolcanic Zone (Andrew & Gudmundsson 2008) and the largest rhyolitic centre in Iceland, having erupted around 250 km^3 of subglacial and subaerial rhyolite (McGarvie 1984; McGarvie et al. 1990; McGarvie et al. 2006; Larsen et al. 2015). Torfajökull

intersects the South-West tip of the Veiðivötn fissure swarm (Figure 1. 8, Figure 1. 9) and there has been evidence for simultaneous activity between the two systems. A mechanism of lateral dyke propagation from one system to another (McGarvie 1984; McGarvie et al. 1990) has been proposed, and it is the interaction of the mafic melt from the Veiðivötn fissure with the Torfajökull rhyolites that triggers eruptions. The last well documented event happened during the last eruption of Torfajökull in 1477-1480 (Figure 1. 10), however simultaneous eruption are also documented in the 871AD Hrafntimuhraun eruption and the Háölduhraun ~6500 years ago (Mørk 1984; McGarvie 1984; McGarvie et al. 1990; Zellmer et al. 2008).

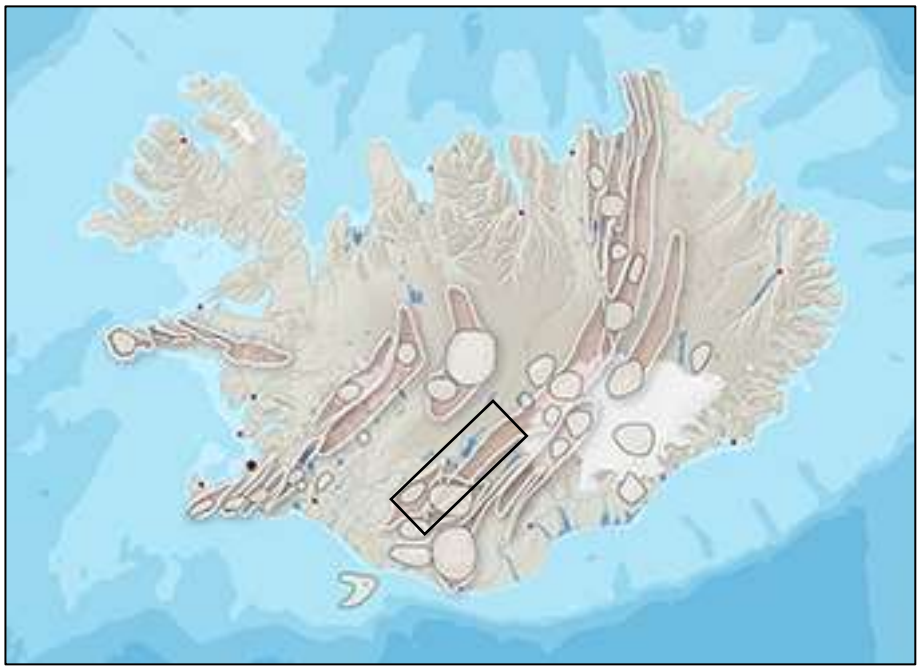

Figure 1. 8: simplified map of Iceland highlighting the location of central volcanoes (grey circular areas) and fissure swarm (elongated brown areas). The rectangle shows the location of the Torfajökull central volcano and the Veiðivötn fissure swarm (from http://icelandicvolcanoes.is/).

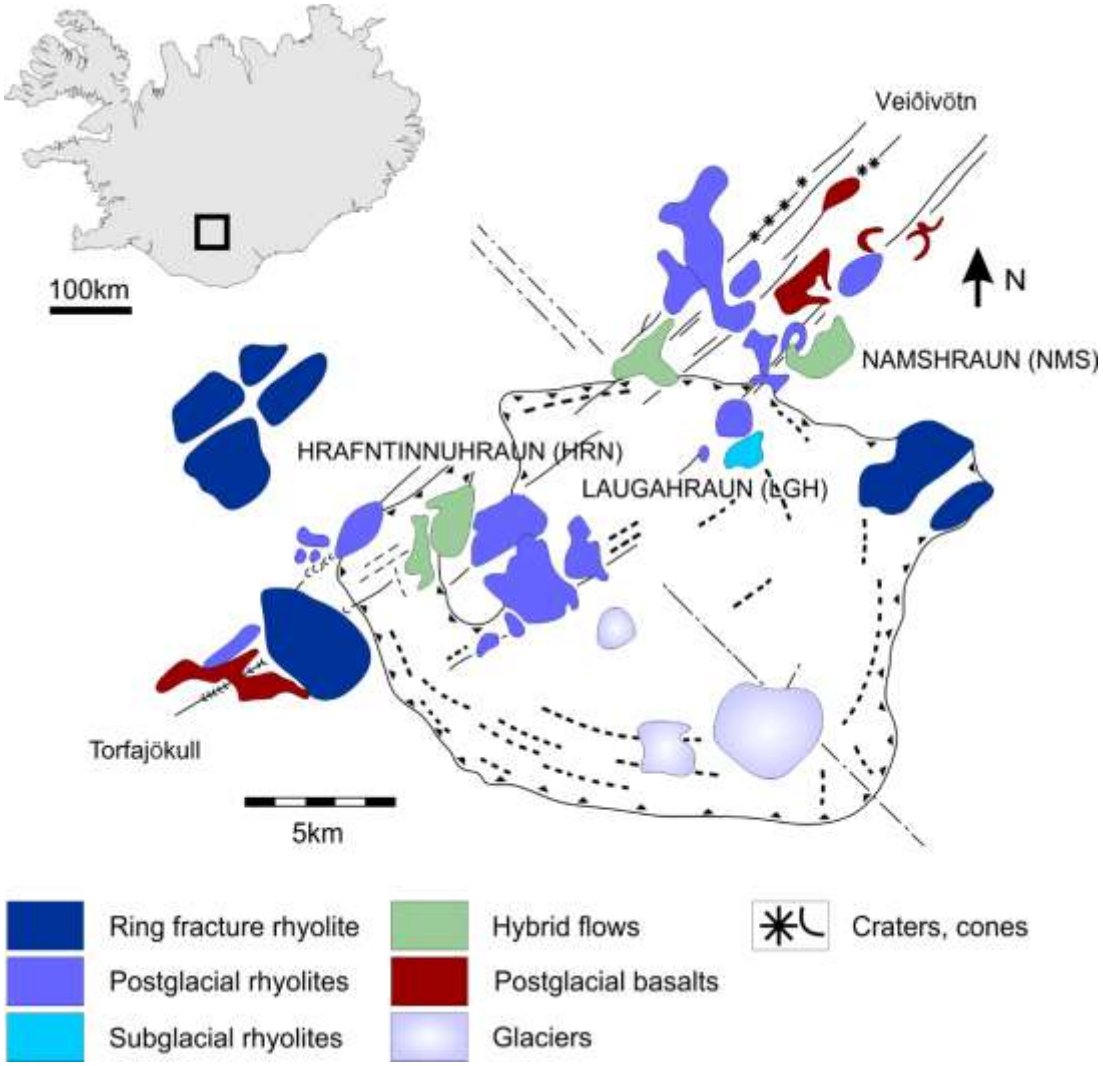

Figure 1. 9: simplified map of the Torfajökull (SW) central volcano showing the intersection with the Veiðivötn fissure (NE) and the distribution of basaltic, rhyolitic and hybrid flows (modified after McGarvie (1984)).

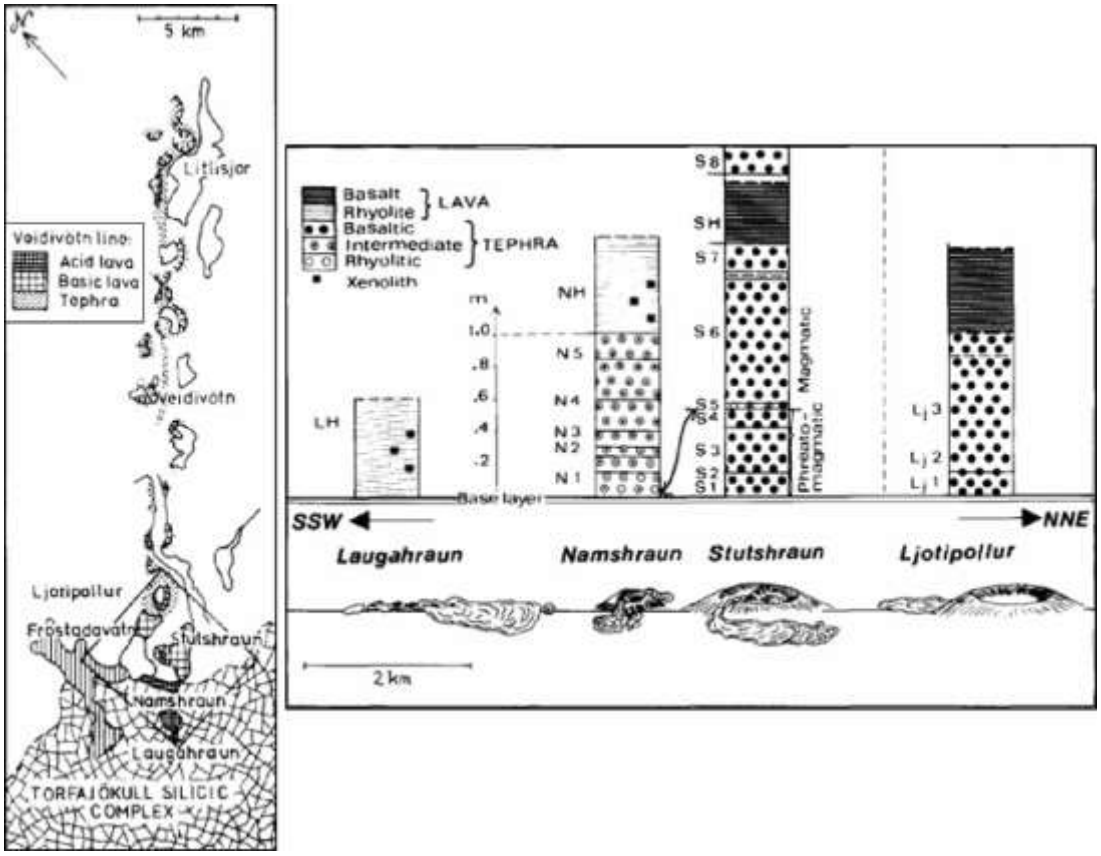

Figure 1. 10: left: simplified map of the 1744 coupled eruption of Torfajökull and Veiðivötn; right: stratigraphy of the erupted products and sketch of the 1477 eruption sites (from Mørk (1984)).

Whilst the tholeiite magma erupting from the Veiðivötn fissure swarm is known to have come and originated from the Bardarbunga central volcano (McGarvie 1984; Macdonald et al. 1990b; McGarvie et al. 1990; Zellmer et al. 2008), there is a degree of uncertainty on the origins of the Torfajökull magma. There is abundant geophysical and geochemical data suggesting the presence of shallow magma chambers underneath many active volcanoes in Iceland (Thordarson & Larsen 2007). Torfajökull, having a large caldera and having been recently active, leads to suggestions that it may be fed by a large sized magma reservoir. Seismic studies (Soosalu & Einarsson 2004; Soosalu et al. 2006) found a large aseismic volume in the western part of the caldera which has been interpreted by the authors to be a cooling magma chamber. Shallow seismicity has also been detected in the central area suggesting that some sort of intrusion may still be on going (Soosalu & Einarsson 2004, Soosalu et al. 2006). However the authors found no evidence for the presence of large amount of molten material beneath Torfajökull.

The abundant rhyolitic eruptions, which make Torfajökull the largest silicic centre in Iceland, have also lead petrologists to investigate and question the origins and formation

of these highly silicic melts. One line of thought supports the idea that the Torfajökull central volcano is fed by a silicic chamber overlying a network of olivine-alkali-basaltic dikes, pods and lenses (McGarvie 1984). Authors have also suggested extensive ~90% fractional crystallisation of basaltic magmas to obtain rhyolites, followed by assimilation or contamination from the crust (Macdonald et al. 1990b). Large variations in magmatic ^{18}O in most evolved Icelandic lavas suggest the involvement of meteorically altered crust in the petrogenesis of such lavas (Jónasson 2007; Martin & Sigmarsson 2010; Bindeman et al. 2012). It has therefore been suggested that rhyolites at Torfajökull are generated by small degree of partial melting of either fresh or hydrothermally altered old basaltic crust (Gunnarsson et al. 1998; Zellmer et al. 2008).

The Torfajökull volcanic system provides an ideal setting to investigate the effects of magma mixing and mingling on the evolution of the melt, and how this affects crystal cargoes textures and chemistry. As well as displaying relatively simple mineralogy compared, for example, to arc magmas, Icelandic lavas are also less prone to crustal assimilation making fractional crystallisation and mixing processes easier to distinguish and evaluate. Moreover, Torfajökull also provides evidence for magma mixing within the same plumbing system, as well as fissure-central volcano interactions between different volcanic systems.

1.4 Subduction zones: Volcanic arcs volcanism

Volcanic arcs are the surface expression of the interaction between a lithospheric plate subducting underneath another. Subduction zone processes have long been recognised to contribute to the accretion of the continental crust, to act as a recycling mechanism to create heterogeneities in the upper mantle and to encourage convection in the mantle (Grove & Kinzler 1986; Tatsumi et al. 1989; Hawkesworth et al. 1993; Thirlwall et al. 1994; Macdonald et al. 2000; Annen et al. 2006; Davidson et al. 2007). Several models have been proposed for arc magmagenesis (Arculus and Wills 1980; Davidson 1987; Tatsumi et al. 1989; Hawkesworth et al. 1993; Pearce and Peate 1995; Plank and Langmuir 1998; Macdonald et al. 2000) and have been summarised by Macdonald et al. (2000) in 5 main stages:

1. At 50-60 km depth, the amphibolite in the upper layer of the subducting slab begins to dehydrate, releasing fluids into the overlying mantle wedge. At this stage subducted sediments could also start melting.
2. Amphibole forms as response to the hydration of the wedge. Convection caused by viscous coupling to the subducting plate drags down the amphibole peridotite until a depth of ~110 km where amphibole is not stable anymore and breaks down to release aqueous fluids promoting partial melting.
3. Once critical melt density is reached, diapirs of partial melt zones migrate upwards.
4. Further melting within the diapirs is enhanced by decompression and migration into hotter rocks.
5. A convective counter flow forms as a response to downward drag of the boundary layer near the slab. This mechanism focuses the melt diapirs in the wedge into a shallow corner above which arc volcanoes form.

This mechanism of magmagenesis implies the possible involvement of up to five components, these being the mantle wedge, aqueous fluids, subducted sediments, slab melting and shallow crustal sediments. The resulting geochemistry and erupted products are characterised by three distinctive features of arc magmas: high water contents and explosive eruptive behaviour, high oxidation states and LILE enrichment compared to LREE, HFSE and Th contents (Arculus & Wills 1980; Grove & Kinzler 1986; Davidson 1987; Tatsumi et al. 1989; Hawkesworth et al. 1993; Thirlwall et al. 1994; Pearce & Peate

1995; Plank & Langmuir 1998; Macdonald et al. 2000; Annen et al. 2006; Davidson et al. 2007) which in turn affect the crystal cargo geochemistry.

1.4.1 The Aeolian Islands volcanic arc

Comprised of 7 volcanic islands (Alicudi, Filicudi, Salina, Lipari, Vulcano, Panarea and Stromboli) and several seamounts (Marsili, Eolo, Enarete, Sisifo, Lametini, Alcione and Palinuro), the Aeolian Islands volcanic arc (Figure 1. 11) is related to the subduction of the African plate underneath the Eurasian plate. The half-ring shaped volcanic islands are located between the South Tyrrhenian back arc and the Calabrian orogenic belt and formed due to the SE rollback of the Ionian slab beneath the Calabrian arc (Ventura 2013). Located between the Marsili basin, a subsiding ocean-type crust, and the Calabrian arc, characterised by continental-type crust, the Aeolian Islands overlie a crust comprised of different layers: unconsolidated sediments and volcaniclastics (<2 km), silicic metapelites of the Calabrian arc (2.3-5 km) and two deep layers of felsic and mafic granulites (5-15 km and 5-50 km respectively) (De Astis et al. 2003; Ventura 2013). The average Moho depth is of ~15 km in the eastern sector and 25 km in the western sector (De Astis et al. 2003; Ventura 2013) with a sudden decrease in Moho depth observed at the Salina-Lipari-Vulcano alignment.

Figure 1. 11: map showing the location of the island of Salina, in the central sector of the Aeolian Islands arc, and its position relative to the Italian mainland. All the volcanic

islands, volcanic edifices and seamounts of the Aeolian arc are also illustrated (from Lucchi et al. (2013)).

The Aeolian volcanoes have been active since 1.3 Ma (Lucchi et al. 2013). Early volcanic activity in the western sector of the archipelago (Alicudi and Filicudi) was associated with the Sisifo-Alicudi Fault system, a WNW-ESE striking tear related to the rollback of the slab, during the Pliocene to Early Pleistocene. The Fault System has since moved in response to transpressive tectonics and is now subject to NNW-SSE compressive strain which may inhibit volcanism. The active boundary of the subducting slab is now represented by the Middle-Late Pleistocene Tindari-Letojanni Fault System, which runs NNW-SSE along the Salina-Lipari-Vulcano alignment in the central sector of the arc (De Astis et al. 2003; Ventura 2013). The eastern sector of the archipelago (Panarea and Stromboli) is instead affected by NE-SW trending faults, thought to represent the horsetail of the Tindari-Letojanni fault system (Ventura 2013). In contrast with the western sector, the current extensional and strike-slip stress regimes present in the central and eastern sectors of the arc allow the presence of sub-vertical plumbing systems in which magma can be stored and raise to the surface (De Astis et al. 2003). Currently volcanism is active in the central sector on the islands of Lipari and Vulcano, last erupted in AD 1230 and 1888-1890 respectively. In the Eastern sector, Panarea presents hydrothermal activity and Stromboli is persistently active (Peccerillo et al. 2013).

Overall, Aeolian volcanism is associated with the interplay between arc collision zone processes and extensional processes developed due to strain related to mantle upwelling processes. This can be recognised in the strong variations in structural, volcanological and petrological characteristics present in the three main sectors of the archipelago.

1.3.2 Petrogenesis and geodynamics

The seven islands are composite structures built by superimposed volcanic centres characterised by volcanic activity as well as tectonic events (Peccerillo et al. 2013). Overall, the magma composition ranges from calc-alkaline basaltic andesites to more rhyolitic and shoshonitic volcanism from west to east, from older to younger activity (Ellam & Harmon 1990; Francalanci et al. 1993; Peccerillo et al. 2004; Peccerillo et al. 2013; Zamboni et al. 2016).

Peccerillo et al. (2013) reviewed the currently available petrological and geochemical data to summarise magma genesis and evolution interpretations along the Aeolian arc. The main characteristics are highlighted below:

- Fractional Crystallisation: magmas erupted in the Aeolian arc have undergone extensive fractional crystallisation processes which resulted in basalts evolving to more intermediate and acidic compositions. The main crystallising phases are olivine, pyroxene and plagioclase as suggested by curved trends for major and trace elements (MgO, Ni, Cr, Sr vs SiO_2) (Peccerillo et al. 2013). Magma evolution increases from the external to the more central islands and rhyolites are present at Panarea, Salina, Lipari and Vulcano. The latter three centres lie on the Tindari-Letojanni fault and it is thought that the resulting transtensional tectonics allowed for the formation of large crustal reservoirs where magma could pond and evolve over time. Geobarometry studies suggest an overall upwards migration of magma chambers where deeper (21-18 km) magmatic reservoirs fed basaltic magmas, whilst shallower chambers (15-12 km) contained more evolved melts (Peccerillo et al. 2013).
- Magma Mixing and Mingling: physical interactions between magmas are widely recognised in the Aeolian Islands volcanoes and are mostly represented by the presence of mafic enclaves hosted in evolved lavas from Lipari, Vulcano, Panarea and Salina (Calanchi et al. 1993; De Rosa et al. 2002; Perugini et al. 2004; Lucchi et al. 2013). Evidence for complete mixing is less evident and this could be due to a lack of compositional contrasts between mafic and silicic end-members or due to re-equilibration of hybrid magmas (Peccerillo et al. 2013).
- Crustal Assimilation: positive correlations between $^{87}Sr/^{86}Sr$ and $\delta^{18}O$ with SiO_2 are common for the Aeolian Islands (Ellam & Harmon 1990) suggesting that assimilation – fractional crystallisation (AFC) processes played an important role in magmatic evolution (Peccerillo et al. 2013). Mafic compositions have also displayed variable trace element and isotopic signatures, and this is thought to be caused by complex RFTA processes (refilling, fractionation, tapping and assimilation) as described by O'Hara (1977).
- Mantle Sources and Melting: Sr-, Nd- and Pb- isotopic signatures, as well as incompatible trace element ratios, are different across the arc. This could be caused by the differing composition of the crust (and fluids) underlying the island, where upper crustal material is likely to be affecting Stromboli whilst and more basaltic oceanic type crust is affecting the western and eastern sector. It is also suggested that different original mantle wedges are involved in the subduction

zone with an OIB-type mantle feeding the external islands (Stromboli and Alicudi) and a depleted MORB-type mantle feeds the central arc. An heterogeneous mantle source associated with decreasing degrees of partial melting is also associated with a switch from calc-alkaline to shoshonitic magmatism at Vulcano whilst polybaric melting of a sediment contaminated heterogeneous mantle is thought to be responsible for the calc-alkaline and shoshonitic magmatism at Stromboli.

1.4.3 The island of Salina

Located in the northernmost part of the central sector (Figure 1. 11), at the intersection between the E-W trending structures of the western arc and the NNW-SSE trending Tindari-Letojanni Fault System, Salina is a Middle to Late Pleistocene volcanic complex formed over six eruptive epochs between ~244 and 15.6 ka (Lucchi et al. 2013).

The Salina volcanic suite spans a range of compositions from sub-alkaline basalts to rhyolite mostly following a calc-alkaline differentiation trend. Whilst basalt is the most common composition on Salina, andesites and dacites are also present and rhyolitic rocks characterise the final eruptive stages of the island.

Combining a database of previous studies and new data, Lucchi et al. (2013) subdivided the eruptive history of Salina in six Epochs (Figure 1. 12), each one associated with a switch in eruptive edifice and composition of erupted products as well as periods of quiescence and volcano-tectonic collapses. It is important to note that unlike every other eruptive epoch and centre, the Pizzo Corvo volcano (in the West of the island, Figure 1. 12) has not been included in the eruptive history due to its uncertain age and stratigraphic position. The eruptive history of Salina (Lucchi et al. 2013) is summarised below:

1. Epoch 1 (224-226 ka) – Pizzo Capo volcano evolved as a NE-SW trending fissure, mostly composed of scoriaceous deposits and basaltic massive blocky lava flows resulting from alternating strombolian and effusive activity.
2. Epoch 2 (240 ka) – Pizzo Capo volcano's activity is renewed following a sector collapse and thick successions of interlayered basaltic scoria and lavas was deposited mostly from the NE-SW fissure.
3. Epoch 3 (160-131 ka) – Monte Rivi and Monte Fossa delle Felci volcanoes represent renewal of volcanism on Salina following a long quiescence period. The stratocones are aligned in NNW-SSE direction are a result of strombolian activity

which characterised the early stages of both edifices. Persistent strombolian activity at Monte Fossa delle Felci is recorded by coarse grained tuff-breccia containing volcanic, metamorphic and sedimentary lithic components. Significant effusive phases alternated with strombolian activity generating thick lava flows of basaltic-basaltic andesite composition.

4. Epoch 4 (147-121 ka) – Following a period of quiescence, Monte Fossa delle Felci latest activity began with a sub-plinian character and is characterised by a change in composition to dacitic and later andesitic lavas and scoriaceous products.
5. Epoch 5 (70-57 ka) – The Monte dei Porri stratocones was constructed on the western side of Salina, characterised by massive lava flows in its early activity, it then produced a predominantly basaltic and andesitic thick and widespread pyroclastic succession (The Grey Porri Tuffs). The later stages of activity alternated explosive to effusive periods producing alternate scoriaceous deposits and thick lava flows.
6. Epoch 6 (30-15.6 ka) – renewal of volcanism on Salina from the Pollara depression formed a thick andesitic flow which followed strombolian basaltic scoria, implying a reawakening of the magmatic system. This was followed by strombolian to sub-plinian fallout units containing basaltic andesitic scoria, grey banded pumices and white rhyolitic pumices lithic fragments indicating a compositionally inversely zoned event. The activity of Pollara, and Salina, terminated with a massively stratified pyroclastic succession of banded pumices and vulcanian type pyroclastic density currents.

The eruptive history of Salina shows a tectonically controlled progressive variation in volcanism and vent location (within the same volcanic centre) from NE to SW (Figure 1. 12). This was then followed by a jump in volcanism to the West on the island (Pollara, Figure 1. 12) following a sector collapse event (Monte dei Porri) which ended volcanism and was followed by a long period of quiescence. The progressive east to west chemical variation and evolution, from calc-alkaline basalts to andesites and high-K dacites to rhyolites (Figure 1. 12), are seen to be the result of varying degrees of contamination of primary magmas as well as fractional crystallisation and magma mixing processes. The correlation between major and trace element and isotopic signatures suggest that crustal assimilation play an important role in the evolution of Salina's magmas (Ellam & Harmon

1990; Calanchi et al. 1993; Francalanci et al. 1993; Gertisser & Keller 2000; Perugini et al. 2004; Lucchi et al. 2013; Nicotra et al. 2014).

The Salina volcanic suite provides the opportunity to observe the effect of arc volcanoes plumbing system processes, such as magma mixing and crustal assimilation, on the crystal cargo chemistry. Amongst the Aeolian Islands volcanoes, Salina in particular shows large variations in geochemistry during its eruptive history from basalts to rhyolites as well as the presence of intermediate dacites which have been previously suggested to be representative of extensive crustal assimilation processes. Moreover Salina also presents amphibole crystals amongst its erupted cargo, which are not found in all other Aeolian Islands volcanoes (Lucchi et al. 2013). The detailed eruptive history (Lucchi et al. 2013) also means that our samples can be placed within a stratigraphic unit with confidence.

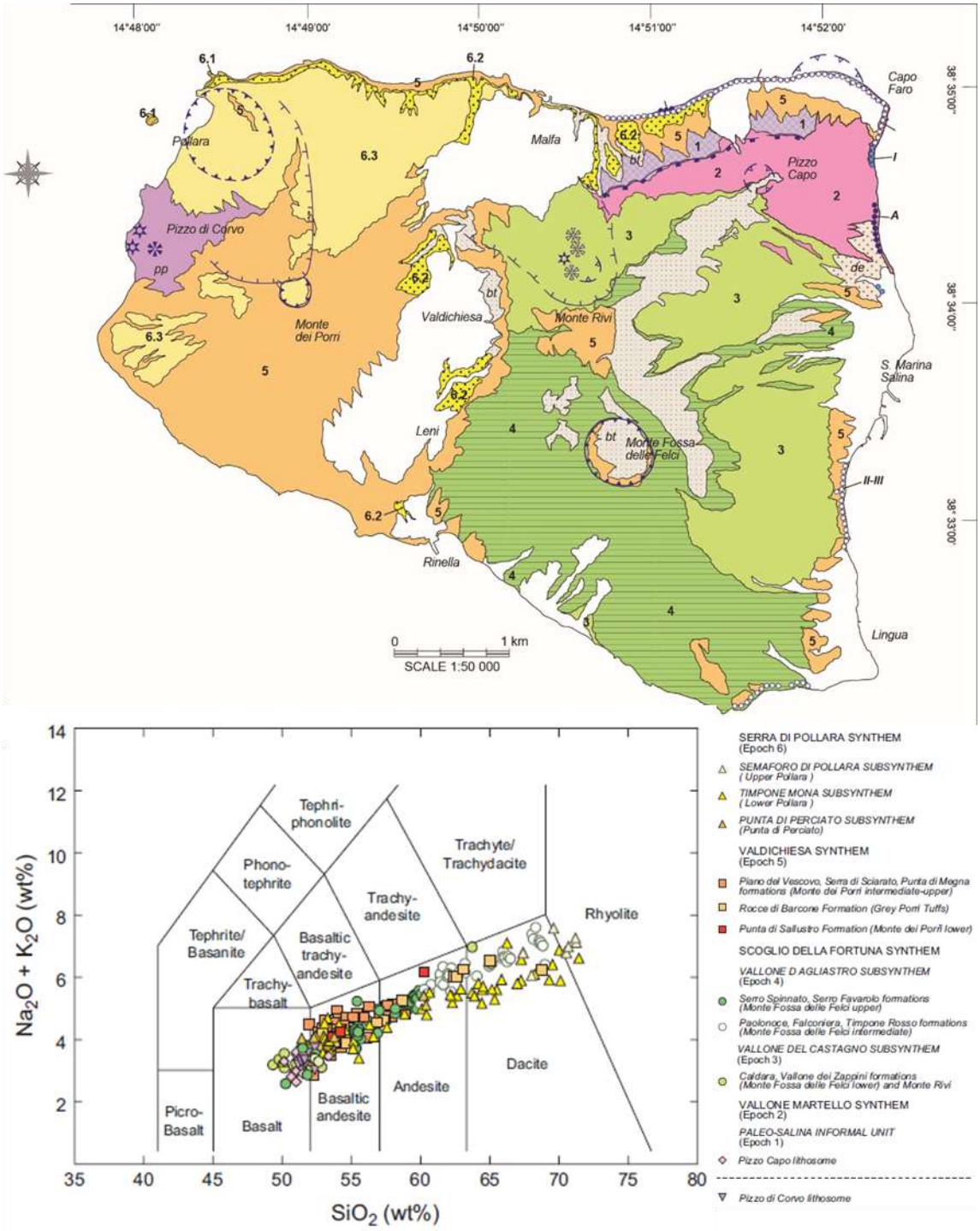

Figure 1. 12: top: simplified geological map of Salina showing the exposure and location of the 6 eruptive epochs, numbered 1-6 (from Lucchi et al. (2013)); bottom: geochemical variations between different eruptive epochs on the island of Salina, with a progressive evolution to more evolved and higher alkali content from Epoch 1 to Epoch 6.

Chapter 2

2. Methodology

2.1 Sample Collection

A selection of Icelandic samples for Torfajökull were donated by Dave McGarvie (The Open University) for the 871AD and 1477 eruptions. The samples include the following flows: Hrafntinnuhraun for the 871AD eruption; Stutshraun, Frostadavatn, Námshraun and Laugahraun for the 1477 eruption (further information is in Supplementary Data File 1 and Chapter 3). Whole rock analyses for these samples were carried out by Dave McGarvie and co-workers (Macdonald et al. 1990a; McGarvie et al. 1990; McGarvie 1984) with the exception of sample HRN-1 which was analysed at Royal Holloway University. Further information on the location of these flows and their characteristic is given in Chapter 3.

The 17 samples from the island of Salina, in the Aeolian Islands, were collected by the author during a field campaign in September 2016. Where possible, two or more lava and pumice samples were collected from both proximal and distal region of the flows taking care in avoiding possible areas of crystal accumulation and sorting, alteration surfaces and other features which may affect geochemical results. Nevertheless the collection of most proximal samples was inhibited by dense vegetation, restriction to paths and inaccessibility of exposure (e.g. steep cliffs). Samples SAL-64, SAL-62, LP-7 and LP-12 were donated by Federico Lucchi (University of Bologna). The collection location of each sample was measured by GPS and is shown in the map in

Figure 2. 1.

Due to their abundance, a particular focus was given to basaltic samples in both settings. Less abundant rhyolitic samples were collected and analysed when possible in order to provide reference end-members for hybrid samples and more intermediate compositions.

Sample	Epoch	Edifice	Formation	Age (ka)
MFF-2	3	Monte Fossa delle Felci	Vallone dei Zappini	~160-131
MFF-3	3	Monte Fossa delle Felci	Vallone dei Zappini	~160-131
MFF-1	3	Monte Fossa delle Felci	Caldara	~160-131
SAL-92	4	Monte Fossa delle Felci	Falconiera	~147-121
SAL-64	4	Monte Fossa delle Felci	Paolonoce	~147-121
MFF-8	4	Monte Fossa delle Felci	Serro Favarolo	~147-121
MP-1	5	Monte dei Porri	Punta di Megna	~70-57
RI-3	5	Monte dei Porri	Punta di Megna	~70-57
RI-4	5	Monte dei Porri	Punta di Megna	~70-57
RI-5	5	Monte dei Porri	Punta di Megna	~70-57
RI-7	5	Monte dei Porri	Punta di Megna	~70-57
RI-8	5	Monte dei Porri	Punta di Megna	~70-57
MFF-7	5	Monte dei Porri	Serra di Sciarato	~70-57
PO-1	5	Monte dei Porri	Serra di Sciarato	~70-57
MA-1	5	Monte dei Porri	Piano del Vescovo	~70-57
LP-7	6	Pollara	Punta Fontanelle	~30-15.6
LP-12	6	Pollara	Punta Fontanelle	~30-15.6

Figure 2. 1: (top): sampling locations on the island of Salina (Aeolian Islands). Locations were measured by GPS with the exception of samples SAL-64, SAL-92, LP-7 and LP-12 which were located using a geological map. (bottom): samples name, eruptive epoch, formation and age (Lucchi et al. 2013).

2.3 Analytical Techniques

2.3.1 Microscopy and point counting

Prior to geochemical analyses each sample was cut into two or more thin sections taking particular care in targeting different areas of the whole sample, especially where large macroscopic variability was visible. These sections were assessed to be representative of the whole sample, and examined using a petrographic microscope. Point counting was carried out in order to determine crystal phase proportions and vesicularity for each sample. Thin sections were mounted on a mechanical slide holder fixed to a petrographic microscope at a magnification of 4x and, when necessary, 10x and moved in steps of 0.3~0.5 mm in the x and y direction. 1000 points were counted for more aphyric samples whilst 1500 were counted for crystal rich samples. Size threshold was set at 150 μm, therefore crystals with long axes below this number were counted as groundmass. Different crystal textures were not taken into account during point counting, with crystals only being discriminated in terms of mineral phases. In order to assess the reproducibility of point counting measurements, repeat counts of the samples by three different people and occasionally on more than one thin section for the same sample. The author also point-counted the same sample three times to assess precision. The average standard error for each mineral phase, groundmass and vesicularity are reported in Table 2. 1.

There is a good reproducibility with only clinopyroxene and vesicles showing 1 count standard error. Whilst precision is poorer than reproducibility, with a total of 1000-1500 counts per thin section the error is negligible.

	Standard Error on point counts							
	Ol	Cpx	Plg	Hbl	Bi	Oxides	Gmass	Ves
Precision	4	3	1	3	0	0	4	9
% Precision	0.4	0.3	0.1	0.3	0.0	0.0	0.4	0.9
Reproducibility	0	1	0	0	0	0	0	1

Table 2. 1: standard error on point counting results. Ol is olivine, Cpx is clinopyroxene, Plg is plagioclase, Hbl is hornblende, Bi is biotite, Gmass is biotite and Ves is vesicles.

2.3.2 Crystal size distribution calculations

Crystal size is one of the most commonly quantified parameter in crystal studies. The possibility of analysing crystal size distributions (CSDs) from a thin section can give information on different petrological aspects; of particular interest is the possibility of using CSDs to identify populations of crystals, different in size and or age, from a single section (Higgins 2002; Armienti et al. 1994; Higgins 2000; Marsh 1988; Cashman & Marsh 1988). On plots of crystal length against the natural logarithm of population density, it has been shown that population of older and hence larger crystals show shallower negative gradients compared to smaller and younger crystals (Higgins 1996; Neave et al. 2017; Marsh 1988; Armienti et al. 1994), whereas crystals with the same magmatic and thermal history are expected to lie within a single gradient line on a CSD plot (e.g. see Higgins 1996; Neave et al. 2017; Marsh 1988; Armienti et al. 1994).

Samples for crystal size distributions (8 for Torfajökull and 4 for Salina) were selected following microscope observations and point counting, focussing on samples with different chemistry (basaltic, trachytic and rhyolitic) and petrological characteristics (zoned phenocrysts, glomerocrysts). CSDs were calculated using thin section maps created from thin section photographs taken with a camera and filter at a 10x magnification (Figure 2. 2), and by manually tracing each crystal and turning the image into black and white binary images (Figure 2. 3). The image was then loaded into ImageJ (Schindelin et al. 2012) and threshold (B&W) and scale bar were applied. Following this, the image was analysed for size information using the "Analyse Particle" tool, selecting as "Set Measurements" "Area", "Centroid" and "Fit ellipse". The minimum size was set as 10 pixels (10-Infinity), with a circularity of 0.00-1.00 and selecting "Exclude on edges" in order to avoid calculating the size of crystals on the side of the section who were cut or broken during thin-section making. The program then outputs a table of results which can be uploaded in CSDCorrections (Higgins 2000). This latter program performs stereological corrections and produces ln population density vs. crystal long axis length (mm) calculations and plots. For CSD calculations, the thin section area has to be adjusted, the vesicularity input (from point counting) and the fabric selected (Massive). Following this, the "Measurement" was set to "Ellipse Major Axis", and the crystal roundness and crystal axial proportions selected.

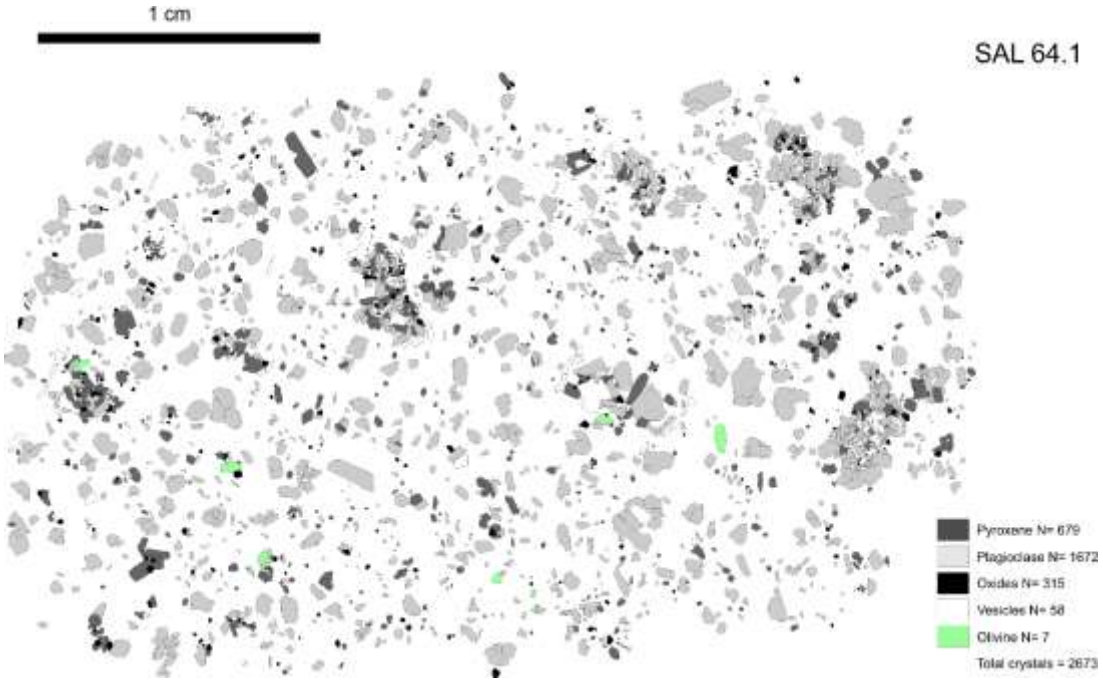

Figure 2. 2: manually traced thin section map for sample SAL-64.1 showing the number of pyroxene, plagioclase, olivine, oxides and vesicles in the thin section, with a total crystal number of 2673.

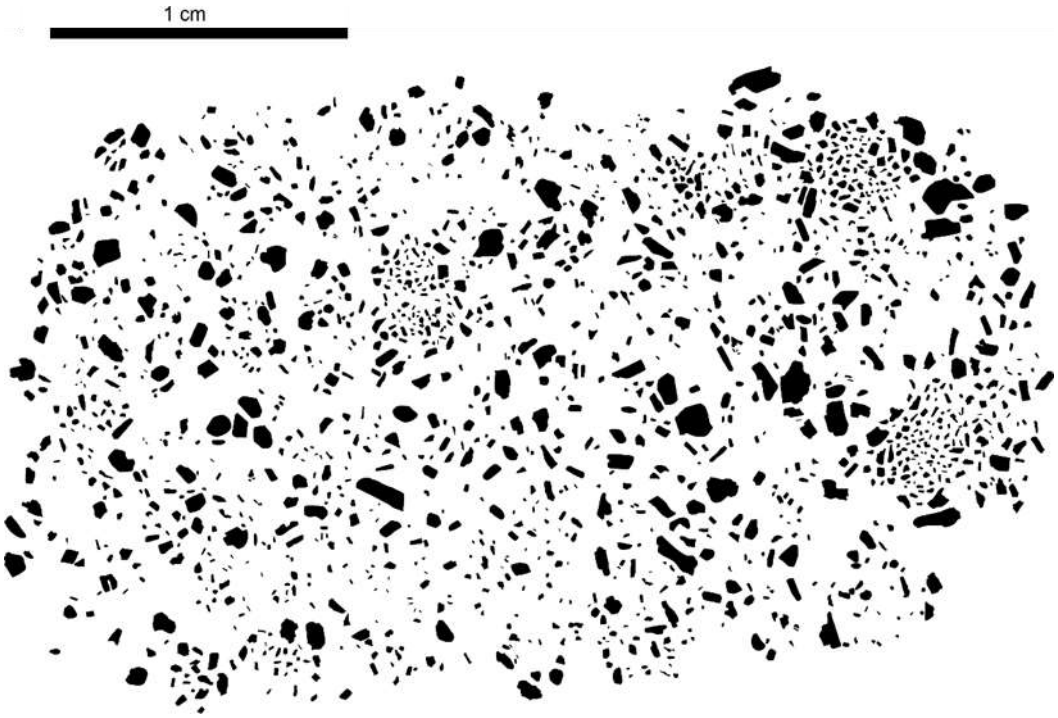

Figure 2. 3: binary image for plagioclase crystals from sample SAL-64.1 (Figure 2. 3). For crystal size distribution analyses, touching plagioclase crystals (e.g. in glomerophyric clusters) had to be manually separated, but this has no effect on the final result as only crystal number and size is relevant for CSD analyses, and not their spatial distribution. Scale is 1 cm.

2.3.3 Sample Preparation and X-Ray Fluorescence (XRF)

X-ray Fluorescence works on wavelength-dispersive spectroscopic principles, where the sample material being analysed is excited with high energy, short wavelength radiation (X-rays) and ionised. When a sample is illuminated by a primary incident X-ray beam, produced from a Rh target, it becomes excited. The atoms in the sample absorb X-ray energy by ionising and releasing energy. These emitted X-rays are characteristic of the type of atoms present in the sample. In order to be able to measure the intensity of each wavelength characteristic of each element, the different wavelengths are separated into a spectrum by diffraction, using a crystal of known atomic spacing. Two types of detectors, gas flow proportional counter and scintillation detector, are then used to analyse intensities of low energy and high energy X-rays respectively.

Major and trace elements for whole rock analysis were analysed by X-Ray Fluorescence (XRF) at Royal Holloway University using the 2010 PANalytical Axios sequential spectrometer with a 4kW Rh-anode X-ray tube and wide range diffraction crystals following the method by Thirlwall et al. (2000). Samples were prepared by removing altered surfaces using an hydraulic splitter. Following this, a jaw crusher was used to break the samples into chips approximately ~1-2 cm long, which were then crushed into a fine powder using a tungsten carbide vibratory disc mill at 1500 rpm for 45-60 seconds.

Major elements were determined analysing glass fusion discs obtained from 0.7g of rock powder heated at 1100 °C in a furnace with a 1:6 sample to flux ratio of lithium tetraborate flux containing La_2O_3 as a heavy absorber following the method by Thirlwall et al. (2000). After fusion, the Pt crucible containing the sample was re-fused and swirled over a meker burner to ensure homogenisation, and then cast and flattened on a hotplate using an aluminium plunger. Quality control was ensured by cleaning the Pt crucibles in HCl solution and thoroughly rinsed with water. Trace elements were analysed using pressed pellets made by mixing 10g of sample powder and 1 ml of polyvinyl alcohol binder solution. Once mixed, the powder was poured into an aluminium cup and pressed using a tungsten carbide hydraulic press and left in the oven (110 °C) to dry. The press was cleaned inbetween each sample using acetone in order to avoid cross contamination. Trace elements were determined using matrix corrections calculated from major elements composition (Thirlwall et al. 2000). In the following chapters, these XRF analyses are incorporated and used alongside already published data in the literature for both Iceland (Chapter 3) and Salina (Chapter 4). It is important to note that only sample HRN-1 for

Iceland was analysed for this thesis, as the XRF data for the rest of the samples was provided by Dave McGarvie.

In comparison to solution ICP-MS, for XRF analyses more sample is required. Across different elements, the limit of detection for XRF is at the ppm scale. Whilst other techniques allow for lower detection limits, most common elements analysed in geological samples have higher concentrations and are therefore not affected.

The precision and accuracy of major and trace elements analyses were estimated by running three international standards (BCR-2, BHVO-1, BIR-1 (Govindaraju et al., 1994)). 2sd error for major and trace elements is reported in Table 2. 2 and Table 2. 3. Errors across the major elements (SiO_2, Al_2O_3, FeOt, MgO, CaO and Na_2O) are <0.2 wt.%. Trace elements (Ni, V, Sc, Pb, Sr, Rb, Zr, Nb, Th, U, and Y) errors are < 3 ppm, except for Ba (<5.6 ppm) and Cr (<13.6 ppm) showing good accuracy.

XRF run parameters are reported in Table 2. 4 and count times in Table 2. 5.

Repeat analyses of an Icelandic sample (I112) shows good reproducibility and analytical precision (BCR-2, BHVO-1 (Govindaraju et al., 1994)) for all major elements, with the highest error of 0.15 wt.% being for SiO_2. Similarly, trace element reproducibility data for a different Icelandic sample (I330) is good, with elements such as F having larger errors. Nevertheless these elements are not used for interpretation and discussion in the following chapters (Chapter 3 and 4), and are therefore negligible (Table 2. 6).

Major elements (wt.%)									
SiO_2	Al_2O_3	Fe_2O_3	MgO	CaO	Na_2O	K_2O	TiO_2	MnO	P_2O_5	Cr_2O_3
0.19	0.12	0.15	0.06	0.03	0.03	0.01	0.01	0.00	0.00	0.01

Table 2. 2: example major elements reproducibility, error is 2sd. Maximum error is 0.19 wt.%.

Trace elements (ppm)												
Ni	Cr	V	Sc	Pb	Sr	Rb	Ba	Zr	Nb	Th	U	Y
2.9	13.6	2.4	0.9	0.2	1.7	0.2	5.6	0.7	0.3	0.3	0.4	0.3

Trace elements (ppm)				
La	Ce	Nd	Sm	Yb
1.7	2.1	2.0	2.0	0.4

Table 2. 3: example trace elements reproducibility, error is 2sd. Maximum error is 13.6 ppm and is reported for Cr.

	Kv	Ma	Collimator	X-crystal	+offs	-offs	Detector	LL	UL
SiO_2	60	45	C	6			FL	25	76
Al_2O_3	60	45	C	4		5	FL	27	78
Fe_2O_3	60	45	F	2		1.6	FL	14	69
MgO	60	45	C	5	3		FL	24	70
CaO	60	45	F	2		4.5	FL	26	72
Na_2O	60	45	C	5	3.3		FL	26	72
K_2O	60	45	F	2	3.5		FL	25	75
TiO_2	60	45	F	2	0		FL	28	75
TiO_2 Rh	95	30	F	2	3.74		FL	27	75
MnO	60	45	F	2		0.9	FL	14	70
P_2O_5	60	45	C	3	3.2		FL	35	70
Ni	60	45	F	2		0	FL	14	71
Cr	60	45	F	1		1.5	FL	13	76
V	60	45	F	1		2.5	FL	32	70
Sc	60	45	F	2		0	FL	28	63
Pb	90	30	F	2	0.78		FS	25	73
Sr	90	30	F	2	0.7		FS	25	73
Rb	90	30	F	2			FS	25	73
Ba	90	30	F	7	1.8	3	FL	28	63
Zr	90	30	F	2			FS	25	73
Nb	90	30	F	2		0.4	FS	25	73
Th	90	30	F	2			FS	25	73
Y	90	30	F	2	0.56		FS	25	73
La	60	45	F	1		2	FL	27	58
Ce	60	45	F	1		1.68	FL	13	76
Nd	60	45	F	1	4.3		FL	13	76

Table 2. 4: XRF run instrument parameters and settings.

Rh traces		W traces		W majors	
Element	**Count time (s)**	**Element**	**Count time (s)**	**Element**	**Count time (s)**
Pb	50	**Ca**	4	**Fe**	4
Pb+	50	**Sc**	50	**Fe-**	2
Th	50	**Sc-**	50	**Mn**	4
TRb	30	**Ti**	16	**Mn-**	4
Sr	20	**Ti+**	16	**Ti**	16
Sr+	50	**La**	50	**Ti+**	16
Y	40	**La+**	50	**Ca**	4
Y+	50	**Ba**	50	**Ca-**	2
Nb	100	**Ba-**	50	**K**	10
Nb-	100	**V**	16	**K+**	8
Ti1	10	**V-**	16	**P**	30
Ti1+	4	**Ba1+**	16	**P+**	30
		Nd	50	**Si**	20
		Nd+	50	**S1**	6
		Ce	50	**Mg**	40
		Ce-	50	**Mg+**	40
		Cr	10	**Na**	40
		Cr-	10	**Na+**	40
		Ni	10	**Al**	80
		NI+	10	**Al-**	40

Table 2. 5: XRF count times.

Sample	BCR2	BCR2 mean	Results for six replicate XRF preparations of basalt I112							
	recommended	(N=3)	I112	I112	I112	I112	I112	I112	Mean	2sd
SiO_2	54.10	54.07	45.51	45.43	45.59	45.60	45.62	45.62	45.56	0.15
Al_2O_3	13.50	13.47	13.87	13.82	13.86	13.90	13.86	13.98	13.88	0.11
Fe_2O_3T	13.80	13.79	12.74	12.69	12.73	12.71	12.68	12.57	12.68	0.12
MgO	3.59	3.56	10.08	9.96	9.98	10.05	10.01	10.09	10.03	0.11
CaO	7.12	7.12	11.17	11.17	11.17	11.20	11.19	11.14	11.17	0.04
Na_2O	3.16	3.10	2.25	2.28	2.28	2.29	2.32	2.29	2.29	0.04
K_2O	1.790	1.80	0.78	0.79	0.78	0.78	0.78	0.78	0.78	0.01
TiO_2	2.260	2.26	2.64	2.63	2.65	2.65	2.65	2.63	2.64	0.02
MnO	0.196	2.20	0.20	0.20	0.20	0.20	0.19	0.19	0.20	0.01
P_2O_5	0.350	0.35	0.44	0.46	0.45	0.46	0.46	0.45	0.45	0.01
Total	99.87	99.73	99.69	99.44	99.70	99.83	99.75	99.75	99.69	0.27

Table 2. 6: XRF repeat analyses for major elements in Icelandic sample I112, and trace elements in sample I330, show good reproducibility for all major elements, with the largest errors being associated to elements with higher concentrations. Trace elements also show good reproducibility, with higher errors associated to light elements, such as F, which release a lower amount of X-Rays and are therefore better constrained if found in higher concentrations.

Sample..	BHVO1	BHVO1	Results for six replicate XRF preparations of basalt I330							
..Continued..	recommended	means	I330	I330	I330	I330	I330	I330	Mean	2sd
Ni	118	118	49	48	48	48	49	49	49	0.8
Co	45	44	49	48	49	50	49	48	49	2
Cr	287	291	132	135	135	131	134	135	133	3
V	317	312	341	348	345	345	344	346	345	5
Sc	31.8	31.3	39.7	40.6	41.1	40.9	40.6	40.4	40.6	0.9
Cu	137	138	120	121	121	120	120	122	121	1.1
Zn	106	102	107	107	108	109	108	108	108	1.2
S	93	93	122	126	193	126	126	131	131	17
F	385	320	253	234	275	243	250	263	252	26
Cl	93	99	79	83	83	83	81	81	82	5
Ga	21	21.1	19.0	19.7	19.4	19.6	19.6	19.7	19.5	0.5
Pb	2.4	2.0	0.9	0.5	1.0	1.0	0.6	0.8	0.8	0.4
Sr	396	390.3	174.4	174.9	174.8	174.1	173.8	174.4	174.4	0.8
Rb	9.2	8.9	6.1	6.1	6.1	6.1	6.1	6.1	6.1	0.1
Ba	133	137	68	68	68	367	70	70	68	3
Zr	174	172.6	147.2	147.5	147.7	147.1	146.8	147.5	147.3	0.6
Nb	18.6	19.1	13.9	13.7	14.1	13.9	13.9	14.0	13.9	0.2
Ta	1.21	1.7	-0.3	0.4	0.7	0.1	0.7	0.1	0.4	0.9
Mo	1	1.0	0.8	0.8	0.6	0.6	0.5	0.8	0.7	0.3
Th	1.2	1.2	1.1	0.8	1.1	0.9	1.0	1.1	1.0	0.3
U	0.4	0.5	0.5	0.4	0.6	0.6	0.4	0.3	0.5	0.3
Y	26	26.4	34.4	34.2	34.3	34.4	34.3	34.5	34.3	0.2
La	15.5	17.5	11.5	12.0	12.5	11.8	11.3	12.6	11.9	1.0
Ce	38.1	40.8	30.0	28.6	28.3	28.1	27.4	27.4	28.4	1.9
Nd	24.7	25.6	18.3	17.9	18.3	18.6	18.2	17.2	18.4	2.2

2.3.4 Secondary Ion Mass Spectrometry (SIMS)

Ion microprobes (SIMS) use a primary ion beam focussed on a sample surface to generate secondary ions. The collision cascade results in the ejection and ionisation of atoms and molecules from the sample. These are then accelerated into a mass spectrometer where prior to detection they are separated according to their energy and mass/charge ratio. For this thesis, a point analysis mode was operated, where the beam is stationary and is used to determine the composition at one specific point. SIMS is able to measure trace element concentrations with a smaller amount of material and at higher spatial resolutions compared to LA-ICP-MS.

All SIMS data discussed in this thesis was collected at the NERC Ion Microprobe Facility at the University of Edinburgh in August 2017. Thin sections were thoroughly polished at Royal Holloway University and then cut into rounds and gold-coated at the University of Edinburgh. SIMS analyses were carried out to acquire high resolution core-rim, and outer rim compositional profiles of plagioclase crystals which displayed abrupt zoning patterns and fine scale oscillatory zoning. A limited number of elements was analysed, with major elements being used for calculating anorthite profiles, and Mg and Sr for the modelling of diffusion modification and chronometry. Other elements such as Fe and Ba were excluded to reduce the analytical run time.

Major and trace elements analyses on plagioclase crystals were made using a 10kV primary O^- ion beam with a beam current of 5nA and a secondary accelerating voltage of 4500V minus a 75V offset on a Cameca IMS-4f ion microprobe. Peak position was adjusted before each analysis with isotopes being measured for 10 cycles. Masses 38.3 and 130.5 were also measured for background corrections. Counting times for each isotopic mass are reported in Table 2. 7.

Isotope	Counting time (s)
^{23}Na	2
^{24}Mg	5
^{27}Al	2
^{30}Si	2
38.3	1
^{39}K	2
^{40}Ca	2
^{88}Sr	3
130.5	5

Table 2. 7: SIMS analytical counting times for the selected elements. Fe and Ba were not analysed as SIMS analyses were carried out to provide data for diffusion modelling, as well as to reduce run time and maximise the allocated SIMS time.

Elemental concentrations were calculated by normalising Si to the Ca/Si ratio using NIST610 (Jochum et al. 2005) as the calibration standard. Each element was individually corrected based on comparison of known ion yields relative to ^{30}Si for the plagioclase standards with those of glass standards (Hinton 1990). Repeat analyses of plagioclase standards SPH-1 (Irving & Frey 1984) and Lake County (Meyer et al. 1974) were carried out in order to estimate precision and indicated a determination of trace elements with a relative precision of ±5%. SIMS data is further discussed in Chapter 3 and Chapter 6.

2.3.5 Laser Ablation Inductively Coupled Plasma Mass Spectrometry (LA-ICP-MS)

Major and trace elements were analysed *insitu* from thin sections in olivines, clinopyroxenes and plagioclases using the LA-ICP-MS system at Royal Holloway University. The rationale for using this analytical technique, as well as a critical discussion of its advantages and limitations, is provided in Chapter 6, following the presentation and discussion of the acquired crystal data in Chapters 3 and 4.

The laser is a Resonetics 193nm ArF excimer laser coupled to an Agilent 8900 ICP-QQQ ICPMS. The ablated material is entrained in He_2 and is combined with Ar as it leaves the ablation cell to reach the quadrupole. The presence of a "squid" minimises the potential for spectral anomalies and smoothes the signal before it is introduced into the mass spectrometer. The LA-ICP-MS is tuned prior to analysis by ablating a glass standard NIST612 before analyses in order to reduce background noise, a $^{232}ThO/^{232}Th$ ratio of <0.2% and a $^{232}Th/^{238}U$ ratio >0.9 was aimed to be maintained whilst achieving the highest possible signal. The analysed minerals require different ablation and acquisition parameters. External standards for anorthite and labradorite (NMNH 137041, NMNH 115900), and chromium augite (NMNH 164905) were used to normalise major element data, which was corrected using correlations generated from electron microprobe data and stoichiometric relationships resulting in a 100% total. NIST glass 612 (Jarosewich 2002) was run alongside the samples to normalise trace element concentrations which are not as abundant in mineral standards (Thirlwall and Manning, in prep).

For glass analyses, ATHO-G rhyolite and St Helen's dacite standard glasses were analysed alongside the NIST glasses.

The laser and ICP parameters and settings used for each mineral phase is summarised in Table 2. 8 and Table 2. 9.

ICPMS- Agilent 8900 ICP-QQQ	
RF power	1280-1320 (optimised during tuning)
Carrier gas flow	~0.5 ml/min (optimised during tuning)
Coolant gas flow	15 l/min
Aux gas flow	1 l/min
Sampler/skimmer cones	Ni
Extraction lenses	ce
Laser ablation system	
Energy density (fluence) on target	27mj/cm^2
ThO+/Th+	~0.2%
He gas flow	850 ml/min
N2 gas flow	6 ml/min
Laser repetition rate	5Hz (cpx) 8Hz (plag)
Spot size	57 µm (plag, cpx)

Table 2. 8: Laser and ICP-MS run parameters (Thirlwall and Manning, in prep.).

Mineral	Spot Size	Repetition Rate	Fluence	Delay 3	Delay 4	Ablation Time
Olivine	74 µm	8 Hz	58 mJ	20 s	20 s	24 s
Plagioclase	57 µm	8 Hz	58 mJ	18 s	18 s	24 s
Clinopyroxene	57 µm	5 Hz	58 mJ	15 s	15 s	20 s
Groundmass	57 µm	5 Hz	58 mJ	15 s	15 s	20 s

Table 2. 9: LA-ICP-MS settings for ablation and acquisition parameters for minerals and groundmass.

Integration (dwell) times used for each measurement in the ICP-MS varied depending on the mineral being analysed, these are summarised in Table 2. 10.

2.3.5.1 Instrument precision and accuracy

Figure 2. 4, Figure 2. 5 and Figure 2. 6 and Table 2. 11, Table 2. 12 and Table 2. 13 below show the average standard deviation (2sd) from the minerals reference material analyses (accuracy) and standard deviation (2sd) across the same run and across different days of analyses (precision). The graphs illustrate measured standard values whilst the lines and shaded areas represent the accepted standard values obtained from the GEOREM and Smithsonian Microbeam Standards Data Sheets, all major elements are in wt.% and trace elements in ppm.

Table 2. 11, Table 2. 12 and Table 2. 13 show that the 2sd errors on mineral standards is low. For olivine major elements is <0.02 wt.% and for trace elements <19.80 ppm. For clinopyroxene major elements the error is <0.36 wt.% and for Cr <127 ppm. For plagioclase the error on major element is of <0.55 wt.% and on Sr <18.2 ppm. Comparing standard runs across the same run and across different days of analyses has shown little

variation in elemental concentration suggesting that long run times do not affect instrumental precision. Errors for groundmasses runs are larger, especially for Al_2O_3 and FeO for the standards ATHO-G and St-Hs, but remain relatively low for major and trace elements for NIST 610 which was processes as an unknown. The graphs in Figure 2. 4, Figure 2. 5 and Figure 2. 6 show the range of trace element concentrations analysed for NIST 610 and their relationship to NIST 610 runs during mineral analyses. Only trace elements of particular relevance to this study have been illustrated for olivine, clinopyroxene and plagioclase and all show good agreement with the published range of values.

The rationale and critical evaluation for using LA-ICP-MS and SIMS, as opposed to other analytical techniques, e.g. EPMA), is discussed in chapter 6 following the presentation and discussion of the acquired crystal data (e.g. Chapter 3). Nevertheless the Figure 2.6 briefly shows that the results of SIMS and LA-ICP-MS analyses on the same Icelandic sample are comparable in terms of elemental concentrations.

	Integration times (s)			
Isotope	**Olivine**	**Plagioclase**	**Clinopyroxene**	**Groundmass**
^{7}Li	0.02		0.02	0.02
^{23}Na		0.01	0.01	0.01
^{25}Mg	0.01	0.02	0.01	0.01
^{27}Al	0.02		0.01	0.01
^{29}Si	0.01	0.01	0.01	0.01
^{39}K		0.02	0.02	0.02
^{44}Ca	0.02	0.02	0.01	0.01
^{45}Sc	0.1		0.01	0.01
^{49}Ti	0.06	0.02	0.01	0.01
^{51}V	0.01		0.01	0.01
^{53}Cr	0.01		0.01	0.01
^{55}Mn	0.01		0.01	0.01
^{57}Fe	0.01	0.02	0.01	0.01
^{60}Ni	0.01		0.01	0.01
^{85}Rb		0.03	0.02	0.02
^{88}Sr	0.15	0.03	0.02	0.02
^{89}Y	0.06	0.05	0.02	0.02
^{90}Zr	0.151		0.02	0.02
^{93}Nb	0.02	0.03	0.05	0.05
^{137}Ba		0.05	0.03	0.03
^{138}Ba	0.02			
^{139}La		0.05	0.03	0.03
^{140}Ce			0.02	0.02
^{146}Nd			0.02	0.02
^{149}Sm		0.05	0.02	0.02
^{153}Eu		0.05	0.02	0.02
^{157}Gd		0.05	0.02	0.02
^{163}Dy			0.02	0.02
^{166}Er			0.02	0.02
^{172}Yb	0.1		0.02	0.02
^{178}Hf			0.05	0.05
^{208}Pb		0.05	0.02	0.02
^{232}Th			0.02	0.02
^{238}U			0.02	0.02

Table 2. 10: isotopes integration and dwell times for minerals and groundmass during LA-ICP-MS runs.

	Olivine			Clinopyroxene		
Element	**2sd**	**Days 2sd**	**Run 2sd**	**2sd**	**Days 2sd**	**Run 2sd**
Li	0.53	0.35	0.13	-	-	-
Na_2O	-	-	-	0.01	0.03	0.07
MgO	0.01	0.00	0.03	0.20	0.02	0.03
Al_2O_3	0.01	0.01	0.00	0.36	0.24	0.03
SiO_2	0.00	0.00	0.01	0.21	0.00	0.00
K_2O	-	-	-	0.00	0.00	0.00
CaO	0.01	0.01	0.01	0.11	0.30	0.05
Sc	0.32	0.10	0.00	-	10.70	3.83
TiO_2	0.00	0.00	0.00	0.01	0.00	0.02
V	0.25	0.15	0.01	-	57.16	39.63
Cr	19.88	1.37	0.20	127.20	205.79	39.63
MnO	0.00	0.00	0.00	-	0.00	0.00
FeO	0.00	0.000	0.04	-	0.09	0.02
Ni	12.25	30.07	6.67	-	3.29	2.46
Rb	-	-	-	-	0.01	0.01
Sr	-	0.00	0.00	-	10.043	0.15
Y	0.01	0.00	0.00	-	1.75	0.03
Zr	0.00	0.00	0.00	-	2.51	0.07
Nb	-	0.00	0.00	-	0.04	0.00
Ba	-	0.00	0.00	-	0.03	0.02
La	-	-	-	-	0.28	0.01
Ce	-	-	-	-	0.85	0.03
Nd	-	-	-	-	0.90	0.04
Sm	-	-	-	-	0.32	0.02
Eu	-	-	-	-	0.11	0.04
Gd	-	-	-	-	0.37	0.01
Dy	-	-	-	-	0.35	0.03
Er	-	-	-	-	0.20	0.01
Yb	0.01	0.01	0.00	-	0.15	0.01
Hf	-	-	-	-	0.13	0.01
Pb	-	-	-	-	0.17	0.13
Th	-	-	-	-	0.01	0.00
U	-	-	-	-	0.00	0.00

Table 2. 11: accuracy and precision for analysed major and trace elements in olivine and clinopyroxene standards (San Carlos olivine and NMNH 164905) LA-ICP-MS analyses.

	Anorthite (An_{95})			Labradorite (An_{65})		
Element	**2sd**	**Days 2sd**	**Run 2sd**	**2sd**	**Days 2sd**	**Run 2sd**
Li	-	-	-	-	-	-
Na_2O	0.00	0.03	0.01	0.13	0.04	0.03
MgO	0.01	0.01	0.00	0.00	0.01	0.00
Al_2O_3	0.55	0.03	0.01	0.16	0.06	0.05
SiO_2	0.08	0.05	0.02	0.20	0.09	0.07
K_2O	0.01	0.00	0.00	0.03	0.00	0.00
CaO	0.02	0.26	0.24	0.32	0.33	0.11
Sc	-	-	-	-	-	-
TiO_2	0.01	0.00	0.00	0.00	0.00	0.00
V	-	-	-	-	-	-
Cr	-	-	-	-	-	-
MnO	-	-	-	-	-	-
FeO	-	-	-	-	-	-
Fe_2O_3	0.10	0.01	0.00	0.14	0.06	0.00
Ni	-	-	-	-	-	-
Rb	-	0.02	0.01	-	0.02	0.01
Sr	18.19	2.85	1.80	-	17.13	2.57
Y	-	0.00	0.00	-	0.09	0.04
Zr	-	-	-	-	-	-
Nb	-	0.00	0.00	-	0.01	0.00
Ba	-	0.24	0.23	-	2.89	0.40
La	-	0.04	0.00	-	0.04	0.01
Ce	-	-	-	-	-	-
Nd	-	-	-	-	-	-
Sm	-	0.05	0.00	-	0.04	0.01
Eu	-	0.12	0.00	-	0.09	0.00
Gd	-	0.21	0.00	-	0.13	0.00
Dy	-	-	-	-	-	-
Er	-	-	-	-	-	-
Yb	-	-	-	-	-	-
Hf	-	-	-	-	-	-
Pb	-	0.29	0.03	-	0.49	0.30
Th	-	-	-	-	-	-
U	-	-	-	-	-	-

Table 2. 12: major and trace element accuracy and precision for anorthite (NMNH137041) and labradorite (NMNH115900) LA-ICP-MS analyses.

	NIST 612	NIST 610	ATHO-G	St-Hs
Element	**2sd**	**2sd**	**2sd**	**2sd**
Li	1.75	0.00	2.02	4.21
Na_2O	0.83	2.95	0.92	0.18
MgO	0.01	0.00	0.04	0.06
Al_2O_3	0.00	0.05	3.72	8.18
SiO_2	0.00	1.90	0.00	0.58
K_2O	0.24	0.00	0.13	0.09
CaO	0.91	0.26	0.01	0.32
Sc	0.17	22.26	0.32	1.51
TiO_2	0.16	0.01	0.06	0.00
V	1.49	12.54	0.01	65.38
Cr	3.09	6.61	0.42	10.72
MnO	0.01	0.00	0.02	0.01
FeO	0.79	0.05	3.53	5.30
Fe_2O_3	-	-	-	-
Ni	2.69	172.30	34.87	3.73
Rb	2.16	4.44	45.89	0.83
Sr	44.80	11.28	19.72	1.45
Y	47.00	10.92	17.87	0.56
Zr	266.93	1.85	38.01	12.70
Nb	27.97	95.68	15.05	0.06
Ba	298.77	162.04	107.24	2.36
La	27.24	107.20	13.23	0.13
Ce	63.31	36.00	32.21	0.49
Nd	30.02	3.96	10.31	0.41
Sm	4.61	2.08	3.31	0.02
Eu	1.73	2.04	6.04	0.02
Gd	4.56	15.59	3.40	0.08
Dy	5.81	14.92	2.90	0.10
Er	2.19	11.87	4.10	0.02
Yb	2.18	0.29	2.94	0.03
Hf	4.39	33.93	2.98	0.36
Pb	0.95	164.79	2.29	0.99
Th	0.70	2.68	2.33	0.44
U	2.11	71.61	2.91	0.03

Table 2. 13: major and trace element accuracy and precision for standard glasses LA-ICP-MS analyses.

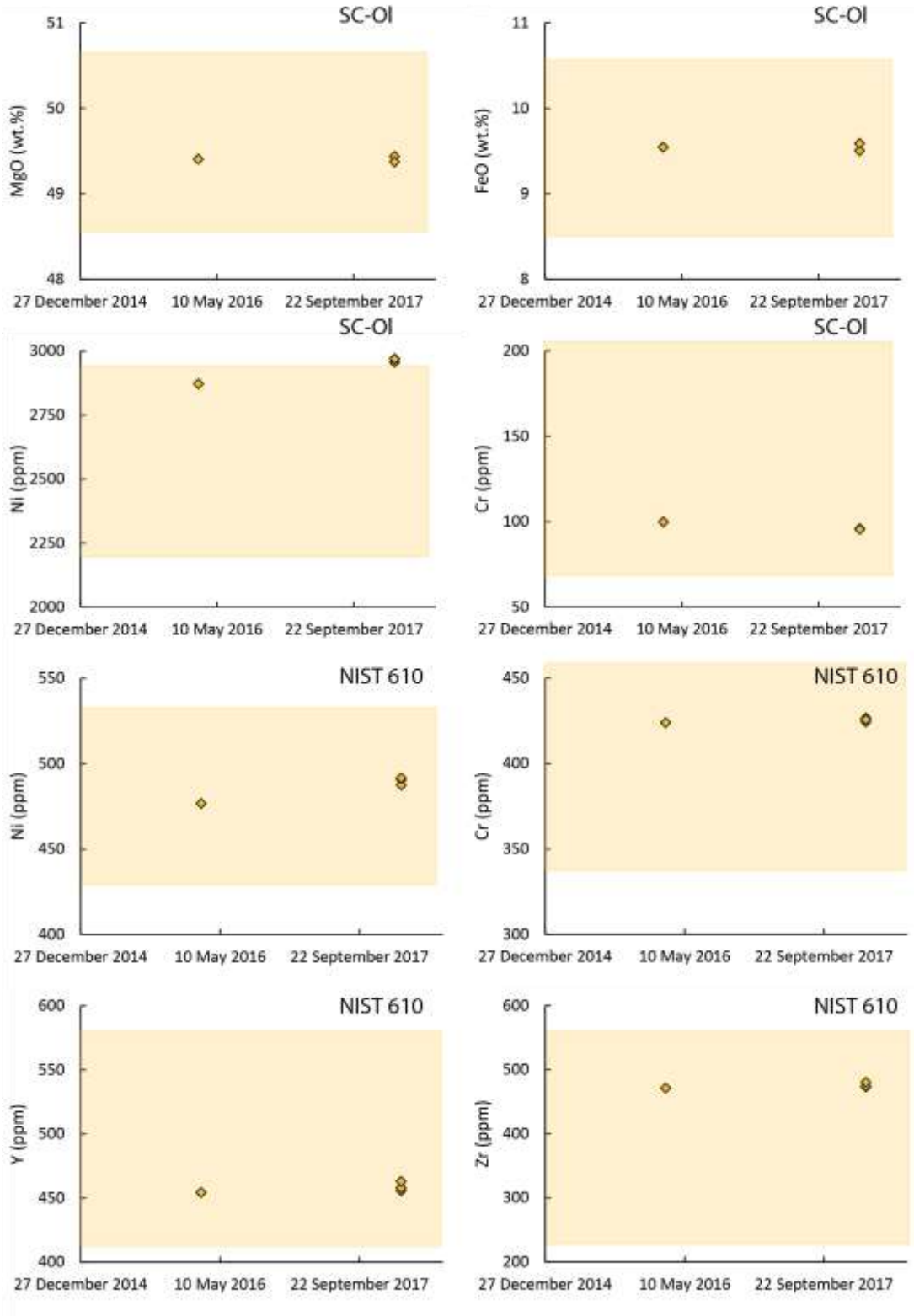

Figure 2. 4: olivine major and trace element LA-ICP-MS analyses for mineral and glass standards compared to published standards values (represented by the yellow field). All shown elements show good accuracy, with only Ni showing particularly high recoveries.

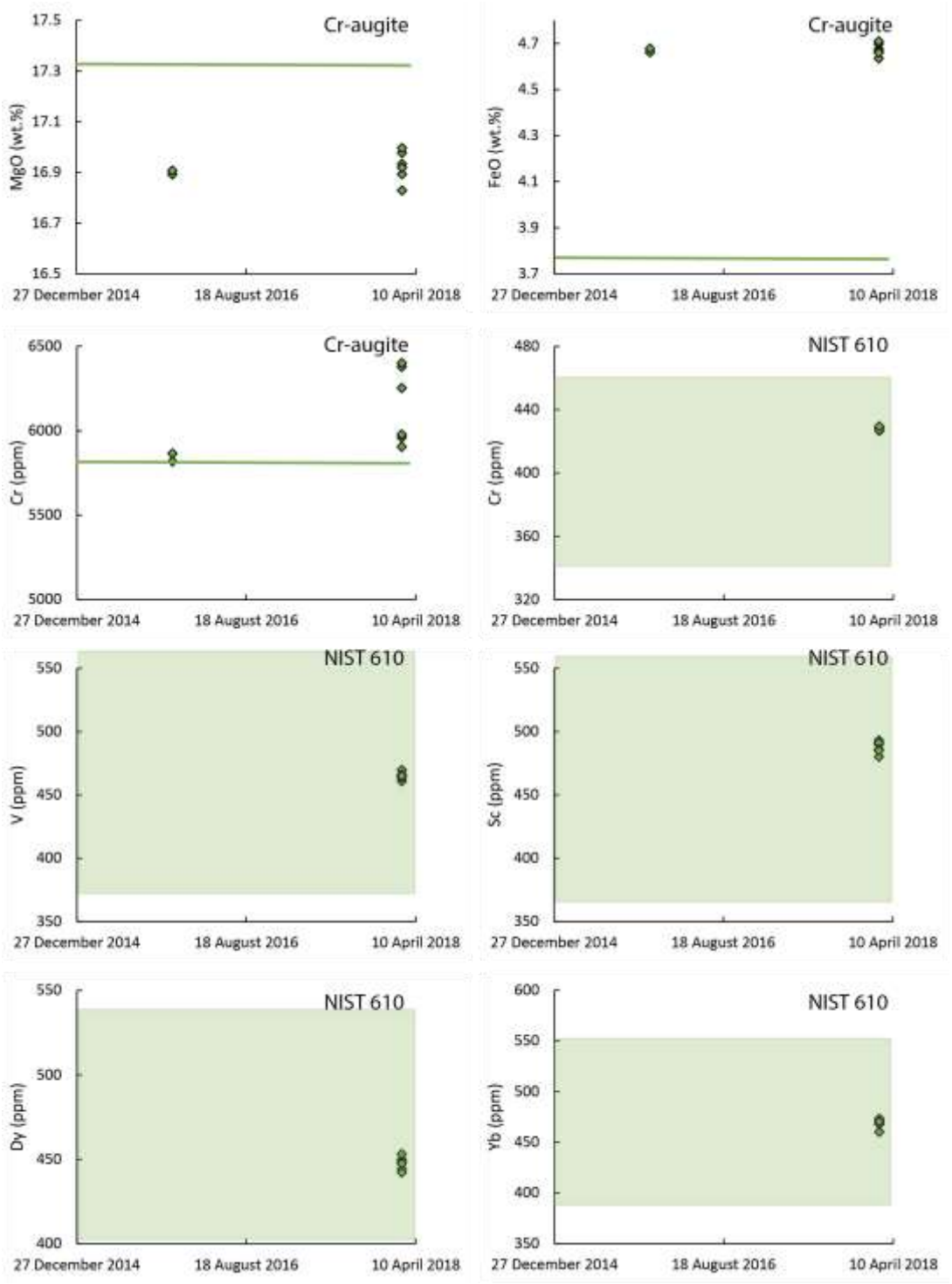

Figure 2. 5: clinopyroxene major and trace element LA-ICP-MS analyses for mineral (NMNH164905) and glass standards compared to published standards values (represented by the green field and solid lines). Errors for MgO, FeO and Cr are just outside of error. Cr in particular shows a large spread of data on the same run day, suggesting changes in instrument stability throughout.

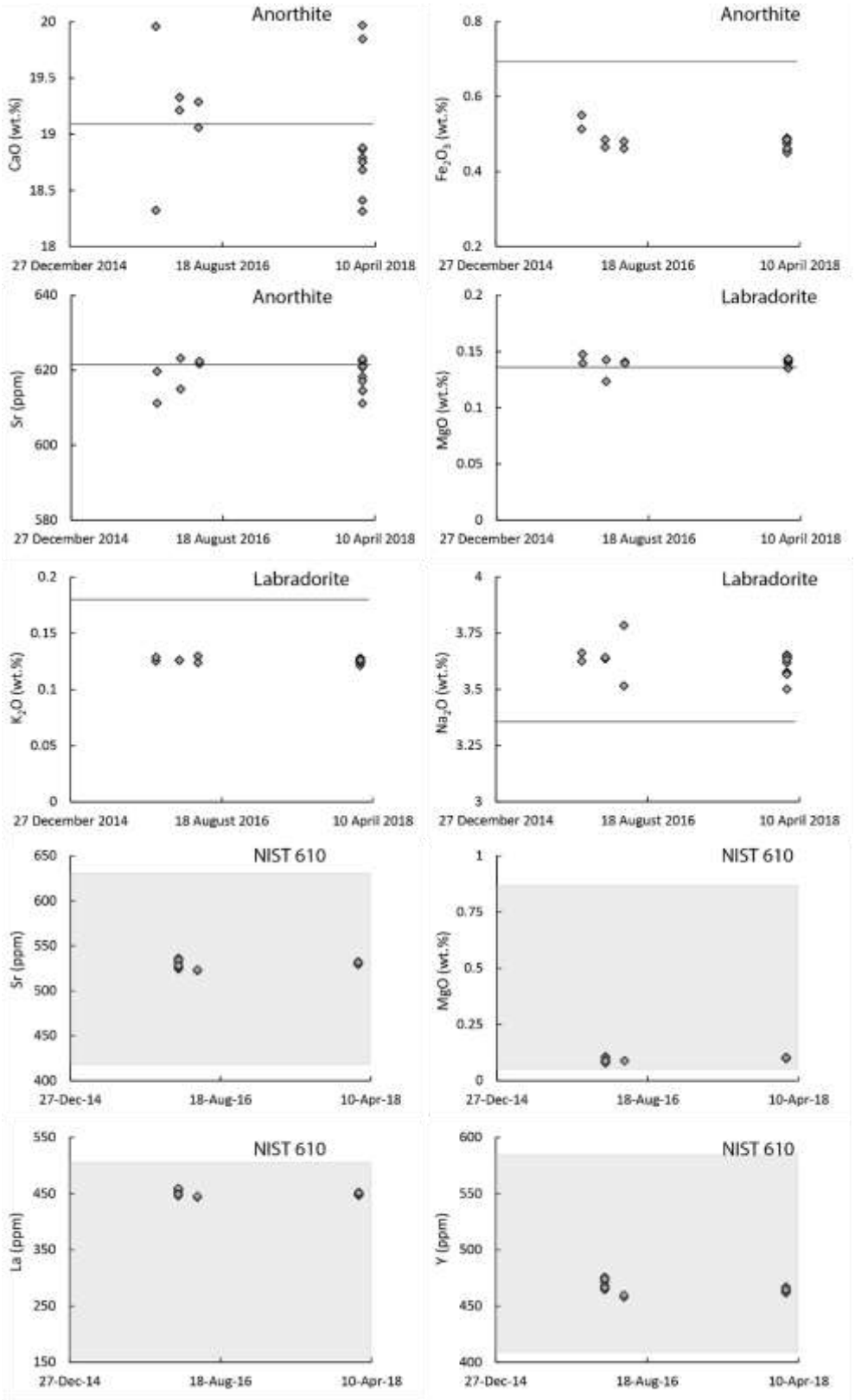

Figure 2. 6: plagioclase major and trace element LA-ICP-MS analyses for anorthite and labradorite mineral (NMNH137041 and NMNH115900) and glass standards compared to published standard values (represented by the grey fields and solid lines). Similarly to clinopyroxene, plagioclase deviations from standard values are outside of error and show large variation throughout the day, possibly due to changes in instrument stability throughout the day.

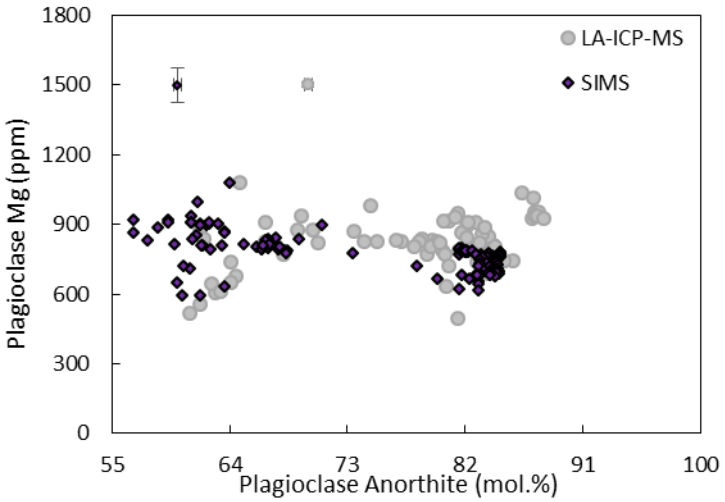

Figure 2.7: example comparison of LA-ICP-MS and SIMS data for plagioclase in a transitional basalt (further discussed in Chapter 3). The graph shows that despite the significant differences in spatial resolution (2µm for SIMS vs 57µm for LA-ICP-MS), the analytical results are comparable and within error.

2.3.6 Electron Probe Microanalysis (EPMA)

Plagioclase major elements mineral analyses were performed by the laboratory at the University of Edinburgh using a Cameca SX100, with an operating potential of 15 KV and a beam current of 10nA and a spot size of 5µm. Counting times for major elements (Al, Si, Ca, Mg, K, Fe and Mn) was of 20 s with the exception of Ti (60 s) and Na (10 s). Trace element Sr counting times were of 30s. The average std on wt.% for Na, Al, Si, Ca, Mg, K, Ti, Fe, Mn and Sr were as follow: 0.12, 0.33, 0.40, 0.28, 0.00, 0.01, 0.02, 0.01, 0.01 and 122. A jadeite and clinopyroxene standard was used for calibration (results in Supplementary Data File 3.5).

EMPA data is not discussed in detail in the following Chapters (3 and 4) and analyses were carried out on a few selected Icelandic samples' grains in order to assess the best areas to target for following SIMS analyses. The data is also discussed in Chapter 6 to illustrate the comparability of results with the LA-ICP-MS analyses on which most of this thesis is based on.

Chapter 3

3. Mixing, Mingling and Mushes: timing and dynamics of Torfajökull's twinned eruptions.

This chapter is presented in paper format and will be submitted to Contributions to Mineralogy and Petrology.

C.L. Imarisio wrote the manuscript, plotted and interpreted the data. C.J. Manning contributed to the writing of the manuscript. C.L Imarisio and C.J. Manning analysed the samples at RHUL. The EIMF group at the University of Edinburgh contributed to the methodology and collection of SIMS data. D. McGarvie contributed to the manuscript providing samples, field and volcanological background. M.F. Thirlwall and all the authors made suggestions and comments on the manuscript.

Supplementary Files are attached to the thesis.

Mixing, Mingling and Mushes: timing and dynamics of Torfajökull's twinned eruptions.

Camilla L. Imarisio[1*]; Christina J. Manning[1]; Dave McGarvie[2]; Matthew F. Thirlwall[1]

[1]Department of Earth Sciences, Royal Holloway University of London, Egham Hill, TW20 0EX, UK

[2]Department of Environment, Earth and Ecosystem Science, The Open University, MK7 6AA, UK

*corresponding author: camilla.imarisio.2010@live.rhul.ac.uk; 07776 420870

Abstract

Magma mixing has long been recognised as an eruption trigger. This results in varied textural and chemical compositions erupted at the surface which can be used to disentangle magmatic histories. The Torfajökull volcanic system, Iceland, provides evidence for interaction between mafic and silicic magmas in the form of hybrid lavas and mingled products, highlighting the interactions between the central volcano and the Veiðivötn fissure. This is a common process in Iceland where volcano-tectonic episodes are frequent, the last of which was the 2014 Holuhraun eruptive episode. We carried out a detailed petrological study, focussing on crystal microtextures and chemistry, to better quantify the nature, location and timescales of these interactions. We show that the geochemical variability of the basalts erupted at Torfajökull is partly caused by entrainment of mush crystals, which are then stored in the shallow crust for ~10 days. Mush rich melts, originating from Torfajökull, and fissure tholeiites, originating from Veiðivötn, interact with shallow crustal rhyolite pockets formed by crustal melting. These interactions result in the eruption of rhyolites and hybrid trachytes which display evidence for magma mingling and failed hybridisation, such as mafic enclaves. Fast timescales of mixing to eruption affect the Torfajökull system, where injection of fissure tholeiites and recharge act as eruption triggers.

Keywords

magma mixing; eruption trigger; crystal cargo; plagioclase; petrology

INTRODUCTION

Understanding eruption triggering mechanisms is at the base of volcanic hazard assessment. These processes include pressure build up in the chamber, caused by crystallisation of a water supersaturated magma (Tait et al. 1989) and tectonic triggers, which result in changes in the mechanical and stress conditions in the chamber (Gravley et al. 2007). Nevertheless magma recharge and mixing has long been recognised as one of the main volcanic eruption triggers as introducing heat and gases into the system disrupts the crystal network, inducing fracturing and conductive self-mixing (Sparks et al. 1977; Murphy et al. 2000; Ruprecht et al. 2012; Cashman et al. 2013).

Whilst recharge is commonly used to describe the injection of a basaltic magma into a more evolved reservoir belonging to the same system, Smith et al. (2009) and Druitt et al. (2012) also documented eruption triggering by injection of dacitic magma. The term magma mixing, instead, can refer to any type of melt interaction even between different systems. The introduction of any new magma into a pre-existing reservoir causes perturbations in the chemical composition of the magma, its temperature and volatile content. Nevertheless mixing processes may be inhibited by chemical and thermodynamic differences between the two melts (Sparks and Marshall 1986) and the degree of interaction can result in a wide range of mingled products which are frozen upon eruption. One of the challenges in modern volcanology is to unravel the magmatic histories of these products in terms of pre-eruptive storage conditions, extent and timing of interactions.

At volcanic centres where the plumbing system is formed by deep networks of interconnected conduits and shallower chambers, allowing magmatic evolution and the formation of more evolved melts (Hildreth 2004; Annen et al. 2006), magma mixing is a common process. Iceland has long been characterised by bimodal volcanism, fissure-central volcanoes interactions and relatively simple petrology. Coupled with the fact that it features almost all volcanic eruptions styles and products on Earth (Thordarson and Larsen 2007), Iceland makes an ideal setting to study interactions between basaltic and rhyolitic melts. Volcanic systems in the Icelandic rift zones are commonly characterised by a fissure swarm, a central volcano or both. Numerous volcanic tectonic episodes have occurred in Iceland (Björnsson et al. 1977; Sigurdsson and Sparks 1978; Hartley and Thordarson 2013), where melt was transported and erupted along a fissure system, the latest of which is the 2014 Holuhraun episode which yet again shed light into the possibility of dyke propagation along fissures to intersect the plumbing system of a central volcano (Gudmundsson et al. 2014).

Iceland is located in the North Atlantic, situated on the Mid Atlantic Ridge at the junction between the Reykjanes Ridge in the south and the Kolbeinsey Ridge in the north. The formation of Iceland as a subaerial volcanic island is the result of melt over production thought to be due to i) the interaction between a spreading ridge and a mantle plume (Thirlwall et al. 1994; Gudmundsson 2000; Trønnes 2002; Thordarson and Larsen 2007; Shorttle et al. 2013); or ii) the presence of anomalously

fertile mantle focussed on the spreading centre (Foulger et al. 2000; Foulger 2002; Anderson 2005; Foulger and Anderson 2005; Lundin and Dore 2005). Currently, this melt over production manifests as extensive volcanism focussed along actively spreading rift zones within the Neovolcanic Zone. This itself has three geographically distinct subzones: the Western, Eastern and Northern Volcanic Zones (Gudmundsson and Andrew 2007; Thordarson and Larsen 2007). Volcanic fissure swarms are a common feature of Icelandic volcanic zones and tend to be aligned in the direction of spreading of the volcanic zone in which they are located. When present, the central volcano is the largest edifice within the system and is the focus of most volcanic activity (Thordarson and Larsen 2007). Whilst rift zones basalts are more tholeiitic in composition, in the flank zones, where little spreading activity takes place, the volcanic systems are characterised by larger central volcanoes associated with a higher proportion of evolved magmas and more alkaline basalts. The Torfajökull volcanic centre provides evidence for interactions between fissure and central volcano volcanism.

The Torfajökull volcanic system

The Torfajökull volcanic system contains the largest silicic centre in Iceland (Walker 1974), having erupted around 250 km^3 of subglacial and subaerial rhyolite in the last ~1Ma of volcanic activity (McGarvie 1984; Tuffen et al. 2008). Located at the junction between the Eastern Rift Zone (ERZ) and the Southern Flank Zone (SFZ), Torfajökull intersects the south-west tip of the Veiðivötn fissure swarm and there has been evidence for simultaneous activity between the two systems (fig. 1) (McGarvie 1984; Mørk 1984a; Zellmer et al. 2008). Previous work (Blake 1984; Larsen 1984; McGarvie 1984; McGarvie et al. 1990) has highlighted the variability observed in lavas from Torfajökull. These range from basalts to trachy-andesites and dacites to rhyolites and this is thought to be due to the interaction between three compositionally distinct end members: Torfajökull rhyolites, Torfajökull transitional basalts and Veiðivötn tholeiitic basalts.

It has been proposed that the source of tholeiitic magmas erupting at Veiðivötn originates from Barðabunga, located 100km north of the fissure, which are injected via lateral dyke propagation into the Torfajökull silicic centre (Blake 1984; Larsen 1984; McGarvie 1984; McGarvie et al. 1990; Zellmer et al. 2008). Axial rifts are, structurally, the extension of the Mid-Atlantic Ridge and are associated with tholeiitic magmatism, consistent with the geochemical properties of the samples originating from Veiðivötn. The tholeiites from the ERZ are derived from higher degrees of partial melting in the spinel-lherzolite stability fields (Gast 1968; O'nions et al. 1976; Jaques and Green 1980; Elliott et al. 1991; Shorttle and Maclennan 2011), they show LILE-enrichment and evolved with extensive fractionation of olivine-plagioclase-clinopyroxene at low pressures (Grove and Bryan 1983; Macdonald et al. 1990a; Yang et al. 1996). In contrast, flank zone volcanism produces more alkaline basalts, identified as a member of the magmatic system underlying Torfajökull (McGarvie 1984; Macdonald et al. 1990a; McGarvie et al. 1990), which show higher LILE/HFSE enrichment

suggesting smaller degrees of partial melt in the garnet-lherzolite stability field (O'nions et al. 1976; Macdonald et al. 1990; Shorttle and Maclennan 2011). The source of the two types of basalts found at Torfajökull is contentious; whilst Zellmer et al. (2008) attributes the variation in basaltic composition of Veiðivötn from alkali-basaltic to tholeiitic to the southwest propagation of the ERZ, McGarvie (1984) suggests that the mixing array requires an olivine basalt component, part of the Torfajökull magma system, and a tholeiitic component from the fissure. Olivine basalts form in smaller volumes at greater depths and would inject into the shallow silicic body from underneath (McGarvie 1984) whilst the interaction between tholeiitic and silicic magmas is thought to take place at shallower levels within the crust. Earlier models suggested the rhyolites formed by extensive fractional crystallisation (Macdonald et al. 1990a) however studies have suggested that significant shifts in $\delta^{18}O$ in the most evolved lavas suggest rhyolites to have originated from melting of a young and hydrothermally altered basaltic crust (Gunnarsson et al. 1998; Martin and Sigmarsson 2007; Zellmer et al. 2008). Due to the unique tectonic conditions in Iceland, high temperature basaltic magmas accumulate at shallow depth underneath rift zones and beneath central volcanoes, allowing heating and melting of the crust (Gunnarsson et al. 1998; Zellmer et al. 2008). The resulting rhyolitic melts are thought to accumulate in crustal reservoirs where they undergo crystallisation.

It has been suggested that the onset of major mixed eruption at Torfajökull started ~6800 BP and this was associated with decreasing volume of erupted rhyolites (McGarvie et al. 1990). In AD 871 and 1477, the last two silicic eruptions of Torfajökull, rhyolites erupted simultaneously with tholeiites along a single fissure, strongly suggesting the presence of a tectonic link between the magma plumbing systems of Torfajökull and the Veiðivötn fissure (Zellmer et al. 2008). Seismological techniques have not been able to identify areas of molten volumes underneath Torfajökull, suggesting that a large shallow magma chamber is not present (Soosalu and Einarsson 2004), however the western area of the caldera provides evidence for a ~4km mostly solidified magma body at a depth of 8km (Soosalu and Einarsson 2004). Nevertheless abundant low-frequency earthquakes and geothermal activity in the south part of the caldera may reflect the presence of shallow active magma (Soosalu et al. 2006). The interaction between basaltic and rhyolitic melts represents movement of rift zone magmas towards the more evolved central volcano plumbing system, and acts as a trigger for eruptions at Torfajökull. Nevertheless previous studies were focussed on whole rock data and end-member compositions and therefore a more detailed understanding of hybrid samples and the depth, extent and timescales of the interactions between the two systems remains unexplored.

The magmatic histories of crystal cargoes from the 871AD and 1477 eruptions of Torfajökull are investigated here using whole rock textures, crystal microtextures description and interpretation and crystal chemistry variations, with a focus on plagioclase crystals and hybrid compositons. Crystal chemistry and textures are used to determine storage and crystallisation conditions. Zoning in

plagioclase crystals is used to better understand magmatic interactions and extrapolate diffusion timescales and eruption triggers mechanisms.

RESULTS

Erupted products

This study focuses on the Hrafntinnuhraun (HRN - 871AD) and Laugahraun/ Namshraun (LGH/NSM - 1477) eruptions. These are the most recent eruptions of Torfajökull with an estimated VEI of 2-3 (Larsen et al. 2015) and present interesting mingling and mixing features. A range of lavas from the 871AD and 1477 eruptions were collected by Dave McGarvie (McGarvie 1984; Macdonald et al. 1990a; McGarvie et al. 1990). All whole rock data from McGarvie (1984), Macdonald et al. (1990a) and McGarvie et al. (1990) is available in Supplementary Data File 1. For simplicity, the main characteristics of the samples selected for this study are summarised in table 1, where samples were selected to represent both end member compositions and a variety of hybrid products. The 871AD eruption produced the Hrafntinnuhraun (HRN) lava in the SW area of the volcanic centre (fig. 1) (Larsen et al. 2015). The Laugahraun (LGH), Namshraun (NMS), Stutshraun (STU) and Frostadavatn (FRO) flows (STU & FRO belonging to the postglacial basalt flows in figure 1) were produced in the 1477 eruption (Larsen et al. 2015). The first two flows are located within and adjacent to the SE Torfajökull caldera rim whilst the latter two are further out on the Veiðivötn fissure (fig. 1). Whilst the 871AD eruption showcases a variety of lavas including both glassy aphyric and phyric rhyolites, mafic inclusions hosted in a rhyolitic groundmass and basaltic lavas (table 1), the products of the 1477 eruption include tholeiitic basalts (STU and FRO), phyric rhyolites (LGH) and mafic inclusions hosted in a brown rhyolitic matrix (NMS-2) (table 1).

Sample*	Eruption*	Flow*	TAS classification*	Macrotextures	Ves %	Ol	Cpx	Plg
HRN-1	871AD	Hrafntinnuhraun	Transitional basalt	-	22	7	9	54
HRN-9	871AD	Hrafntinnuhraun	Trachyte	-	33	*5*	*2*	*30*
HRN-10	871AD	Hrafntinnuhraun	Peralkaline rhyolite	-	2	*0*	*0*	*52*
HRN-26 (b)	871AD	Hrafntinnuhraun	Transitional basalt	Mafic inclusion	2	9	17	24
HRN-26 (r)	871AD	Hrafntinnuhraun	Peralkaline rhyolite	Brown filaments	3	*0*	*0*	*18*
STU-6	1477	Stutshraun	Tholeiitic basalt	-	38	4	11	28
FRO-1	1477	Frostadavatn	Tholeiitic basalt	-	26	1	4	12
NMS-2 (r)	1477	Namshraun	Trachyte	Hosts inclusions	3	*0*	*0*	*14*
NMS-2 (b1)	1477	Namshraun	Tholeiitic basalt	Mafic inclusion	6	4	2	*7*
NMS-2 (b2)	1477	Namshraun	Transitional basalt	Mafic inclusion	4	3	4	9
NMS-5	1477	Namshraun	Trachyte	-	5	*0*	*1*	*15*
NMS-6	1477	Namshraun	Trachyte	-	4	*1*	*1*	*11*
LGH-4	1477	Laugahraun	Peralkaline rhyolite	-	25	*0*	*0*	*32*

Table 1: Selected samples descriptions from the 871AD and 1477 eruptions used in this study. * indicates information retrieved from publications (McGarvie 1984; Macdonald et al. 1990a; McGarvie et al. 1990). Point counting results. Ol is olivine, Cpx is clinopyroxene and Plg is plagioclase. 1000 counts were counted for aphyric samples and 1500 for phyric samples. Mineral proportions are expressed in mass fraction, calculated from dense rock counts, vesicles % calculated from total counts. (r) and (b) represent the rhyolitic and basaltic component of the samples when mafic enclaves are present. Raw point counts are presented in Appendix 1.

Mineralogy

Mineral proportions and vesicularity estimated by point counting are summarised in table 1. The 871AD basalts (HRN-1 and HRN-26b) are plagioclase, clinopyroxene and olivine phyric containing proportions of 24-54%, 9-17% and 7-9%, respectively. Rhyolitic samples (HRN-9, HRN-10 and HRN-26r) contain abundant plagioclase 18-52%, with small amounts of biotite 2% and rarely include olivine and clinopyroxene xenocrysts <2%. The 1477 basalts (STU-6 and FRO-1) are olivine, plagioclase and clinopyroxene phyric with abundances of 1-4%, 7-27% and 2-4%, respectively. The rhyolites and trachytes (LGH-4, HRN-10, HRN-9, NMS-6, NMS-5) contain plagioclase (up to 32%) and biotite (2%). Minor clinopyroxene, olivine and alkali feldspar (<1%) are also present in trachytes.

Crystal mass fractions vary substantially between basaltic samples but more crystal poor samples (FRO-1, NMS-2 b2) show proportions similar to the ~11:6:3 proportions calculated for a three-phase gabbro eutectic crystallising at low pressures (Yang et al., 1996). It is important to note that the more phyric samples (e.g. HRN-1. STU-6, HRN-16b) have higher plagioclase proportions than expected.

Olivine crystals are mostly euhedral and up to 0.5mm in length (fig. 2a). In some cases they exhibit resorped, embayed edges (e.g. HRN-1, HRN-9, NMS-2). Analysed olivine crystals in transitional

basalt HRN-1 are normally zoned with cores of $Fo_{83.4\text{-}77.6}$ and rims of $Fo_{83.3\text{-}76.6}$. Clinopyroxene crystals are euhedral to subhedral and up to 0.5mm in length (fig. 2b). Crystals range from fresh to resorped and some show evidence for thin rims (e.g. HRN-1, HRN-9). Analysed clinopyroxene crystals in transitional basalt HRN-1 show zoning patterns similar to olivines, characterised by cores of Mg# 82.1-73-5 and rims of 81.5-77.0%.

Plagioclase is the most abundant phase in all samples and ranges from 0.5mm-1.5mm in length. It appears both as euhedral, stubby skeletal crystals and as elongate laths. Crystal edges are often resorbed and show embayments. Plagioclase crystals in all samples also display a variety of microtextures; mainly zoning (fig. 2c,d), fine sieving, and resorbed cores. Crystals can be found in the samples as isolated crystals or as glomerophyric clusters (fig. 2c,d). Isolated plagioclase crystals display an abrupt zoning patter close to the crystal edge, where a lighter rim is present. Larger plagioclase crystals, and those part of glomerophyric clusters, sometimes show more complex zoning patterns including areas of oscillatory zoning. The plagioclase crystals in tholeiitic basalts (e.g. HRN-26b and mafic enclave in NMS-2) are normally zoned and display relatively homogenous cores of $An_{92.8}$ and rims of $An_{73.9}$. Tholeiite HRN-26 also hosts isolated boxy-shaped plagioclase crystals of An20 which don't present zoning, but instead show intense fine sieving at the crystal edge, with no evidence for a fresh crystallised rim (Fig. 2). In contrast, transitional basalts (e.g HRN-1) display plagioclase with homogeneous cores of An_{88} followed by abrupt zoning in the crystal rim to An_{60}. This zoning pattern is shared to the same extent by large crystals in glomerophyric clusters and isolated phenocrysts. The main textural difference between the latter two crystal types is that large clustered plagioclase crystals also show textural evidence for oscillatory zoning in the crystal cores and mantle. In transitional basalt HRN-1, isolate plagioclase crystals of An_{40} are also present, and these show dissolution features at the crystal edge. Plagioclase crystals hosted trachytic samples (e.g. HRN-9, NMS-2 and NMS-6) show are both normally zoned i.e. $An_{40\text{-}20}$ and reversely zoned from An_{20} in the cores to An_{35} in the rims (e.g. NMS-6). Normally zoned and homogeneous crystals at $An_{35\text{-}30}$ can also display oscillatory zoning. Trachytic sample HRN-9 also hosts plagioclase crystals with affinities to those in transitional basalt HRN-1. Rhyolitic samples hosts plagioclase crystals with Anorthite ranges similar to those of the trachytes (37-17 mol.%), but zoning is normal and minor, and rare oscillatory zoning is observed in some crystals.

Samples HRN-26 and NMS-2 show large proportions of mafic inclusions within a silicic groundmass, such as mafic blobs or more angular inclusions (fig. 2g,h). Transitional basalt inclusions are characterised by olivine content and vesicularity up to 3.8%, which increases towards the edge of the enclave (fig. 2h, enclave 2). Tholeiitic inclusions, in contrast, are plagioclase rich, highly vesicular (up to 6%) and show a hybrid layer at the contact with the silicic host (fig. 2g and 2h enclave 1). Sample HRN-26 also displays glassy bands and swirls close to the basalt-rhyolite contact (fig. 2g).

198 **Crystal Size Distribution (CSD)**

199 Plagioclase CSDs were calculated using CSDCorrections (Higgins 2000, 2002) and given in
200 Supplementary Data File 2. CSDs across a range of samples from the 871AD and 1477 eruptions
201 show distinct CSD profiles (Fig. 3). The CSDs of FRO-1 (tholeiite), NMS-5 and NMS-6
202 (hybrid/mingled products), HRN-10 and LGH-4 (rhyolites) (fig. 3a-e) show straight profiles
203 suggesting that the crystals all underwent the same crystallisation history. HRN-1 (transitional
204 basalt), HRN-9 (trachyte) and STU-6 (tholeiite) show kinked profiles (fig. 3f-h) indicating the
205 presence of two distinct populations of plagioclase phenocrysts (Cashman and Marsh 1988; Higgins
206 1996). Samples HRN-26 and NMS-2 were excluded from CSD analyses due to the presence of mafic
207 enclaves. Olivine and clinopyroxene CSD profiles were not generated due to their low abundance in
208 all samples.

209 **Geochemical Methods: LA-ICP-MS and SIMS**

210 For samples in table 2, for which hand specimen were available, major and trace element
211 concentrations were determined for olivine, clinopyroxene and plagioclase using the LA-ICPMS at
212 Royal Holloway University of London, which combines a Resonetics ArF 193nm laser with a two
213 volume cell with an Agilent 7500 ICPMS as outlined in Müller et al. (2009), using the parameters in
214 table 2. These samples were selected for geochemical analyses in order to characterised a range of
215 end-member compositions (tholeiites, transitional basalts and rhyolites) as well as a series of hybrid
216 and mingled products. The selection of the samples was also limited by the availability of hand
217 specimens.

ICPMS- Agilent 7500ce/cs	
RF power	1280-1320 (optimised during tuning)
Carrier gas flow	~0.5 ml/min (optimised during tuning)
Coolant gas flow	15 l/min
Aux gas flow	1 l/min
Sampler/skimmer cones	Ni
Extraction lenses	ce
Laser ablation system	
Energy density (fluence) on target	27mj/cm^2
ThO+/Th+	~0.2%
He gas flow	850 ml/min
N2 gas flow	6 ml/min
Laser repetition rate	5Hz (cpx) 8Hz (ol, plag)
Spot size	74µm (ol) 57 µm (plag, cpx)

218 Table 2: ICPMS and ablation system settings and parameters used for mineral analyses.

219 Major element data were normalised using matrix matched standards (San Carlos olivine NMNH
220 111312-44, plagioclase anorthite NMNH 137041, plagioclase labradorite NMNH 115900 and augite
221 NMNH 164905) and corrected using correlations generated from electron microprobe data for a wide
222 range of mineral compositions and stoichiometric relationships resulting in a 100% total. Trace
223 element concentrations were normalised using NIST612 (Thirlwall and Manning, in prep). Samples

were analysed insitu from thin sections and a minimum number of 58 grains was attempted for the more porphyritic samples (e.g. HRN-1) in order to have a 95% certainty that no significant population was missed (Vermeesch 2004). Nevertheless this was not always possible due to grain abundance, size and fresh surfaces; the number of successful analyses for each sample and phase is shown in table 3. For glasses analyses, the same acquisition method as for clinopyroxene was used, with the exception of Al_2O_3, and analysing ATHO-G rhyolite and St Helen's dacite as standard glasses alongside the NIST glasses. LA-ICP-MS data is found in Supplementary Data File 3.

Plagioclase grains from population 2 (HRN-1, HRN-9), and some from population 3 and 5, (HRN-1, NMS-6) showed pronounced zoning patterns in LA-ICP-MS results and were therefore picked to be analysed by SIMS to obtain high resolution core to rim Mg and Sr profiles (fig. 6). SIMS data was collected at the NERC Ion Microprobe Facility at the University of Edinburgh. Major and trace elements analyses on plagioclase crystals were made using a 10kV primary O^- ion beam with a beam current of 5nA and a secondary accelerating voltage of 4500V minus a 75V offset on a Cameca IMS-4f ion microprobe (Hinton 1990). Profiles from core to rim were initially measured using a spot size of 15µm moving the sample under the beam in 10µm steps. Higher resolution profiles were then acquired focussing a low primary beam into a 2µm spot, moving the sample in smaller 2µm steps. Repeat analyses of plagioclase standards SPH-1 (Irving and Frey 1984) and Lake County (Meyer et al. 1974) were carried out in order to estimate precision and indicated a determination of trace elements with a relative precision of ±5%. The following number of analyses was carried out: HRN-1, 9 grains; HRN-1.2, 7 grains; HRN-9, 4 grains; HRN-26, 7 grains; NMS-6, 2 grains. According to grain size and zoning patterns, tracks varied in length from ~300 µm to ~50 µm. The data is found in Supplementary Data File 4.

Sample	Number of successful analyses		
	Olivine	Plagioclase	Clinopyroxene
HRN-1	22	80	30
HRN-9		29	
HRN-10		17	
HRN-26		22	
NMS-2		44	
NMS-6		39	
LGH-4		34	

Table 3: list of samples and number of successful grain analyses by LA-ICP-MS. Successful analyses refer to the data which was used for interpretation, including both cores and rims, whose totals where within ~99.5 and 100.5 and/or were not affected by cracks and inclusions on the analysed surface.

Crystal Chemistry

Olivine and clinopyroxene crystals abundant and large enough to be analysed by LA-ICP-MS were only present in transitional basalt HRN-1. Olivine crystal cores show forsterite contents ranging from 83.4 to 77.6 Fo mol.% whilst the rims range from 83.3 to 76.6 Fo mol.% (fig. 4a). The crystals do not show a distinct zoning pattern and the difference between core and rim forsterite is minor (<2%). Nickel and Chromium concentrations show an overall decreasing trend consistent with magmatic evolution. At high forsterite (83.3-83.5%) olivines Ni and Cr concentrations are lower than that of 80.9 mol.% Fo crystals. Nb and Y are incompatible in olivine and therefore their ratio is not affected by crystallisation processes. Nb/Y vs. forsterite content shows an overall decreasing trend and large variations at Fo 83.3-83.5% and 80%. Clinopyroxene crystals are all diopsides and show a similar behaviour to olivine. The Mg# of the cores range from 82.1 to 73.5% and that of the rims from 81.5 to 77.0% (Fig. 4). Clinopyroxenes do not show distinct compositional zoning patterns different from those expected from fractional crystallisation and REE ratios do not vary significantly. Chromium concentrations at Mg# 79-81% show large variations ranging from 463 ppm to 3449 ppm. It is important to note that the highest Mg# and Fo% contents are found in larger crystals hosted in the glomerophyric cluster and these crystals are circled in fig. 4 (fig. 2c).

LA-ICP-MS core and rim analyses of plagioclase crystals were analysed for selected hybrid and end-member composition samples spanning the 871AD and 1477 eruptions (fig. 5). Across all samples anorthite ranges from Anorthite to Oligoclase with An_{93} to An_{17}. Equilibrium anorthite was calculated and plotted alongside each sample using the method by Namur et al. (2012). Tholeiitic and transitional basalts contain plagioclases which range from $An_{92.8}$-$An_{73.9}$ mol.% (HRN-26, NMS enclaves and a postglacial tholeiite I326), and An_{88}-$An_{38.5}$ mol.% (HRN-1 and HRN-9), respectively. Rhyolitic and trachytic samples contain plagioclases which range from An_{37}-$An_{16.9}$ mol.% (HRN-10, HRN-26 and LGH-4), and $An_{39.2}$-$An_{19.7}$ mol.% (HRN-9, NMS-2, NMS-6), respectively. The overall trend of plagioclase chemistry is that expected during fractional crystallisation, with an increase in Sr and TiO_2 up to $An_{50.5}$ and An_{62} respectively, followed by a sharp decrease in Sr concentration towards $An_{16.9}$, a steady decrease in Mg, and an overall increase in incompatible elements Eu and La/Y and Ba. Nevertheless, at a smaller scale, the relationship between anorthite, TiO_2 and trace elements in plagioclase is more complex. Bimodality in Sr concentration is present at anorthite >80 mol.% where one distinct population (HRN-26, NMS-2 and tholeiite i326) presents low Sr 211-275 pm, low TiO_2 (<0.04 wt.%) as well as low Ba, Eu and La/Y compared to a different population (HRN-1 and HRN-9) showing high Sr (566-750 ppm), higher TiO_2 (>0.04 wt.%), higher Ba, Eu and La/Y (fig. 5). Mg displays the opposite behaviour being >1000 ppm in the first population and <1000 in the latter. Wide ranges in all elements are also observed at An_{61-64} and $An_{16.9-40}$, however no clear groups can be distinguished from the plots alone (fig. 5). LILE and REE provide strong

evidence for depletion in tholeiites (HRN-26, NMS-2 and tholeiite i326) compared to transitional basalts at high anorthite (HRN-1, HRN-9).

SIMS analyses for transitional basalt HRN-1 and trachyte HRN-9 plagioclases most commonly show sharp normal zoning from An_{79-84} to ~An_{67-58}. Consistent with decreasing An, Sr concentrations increase from core to rim from 580 ppm to 670 ppm. Mg concentrations vary from 850 ppm to 614 ppm in the core to 800 ppm to 982 in the rim, in contrast to the expected relationship with decreasing anorthite. Most grains show similar profile shapes, but absolute concentrations vary between grains suggesting inter-crystalline disequilibrium. Of the analysed grains, two of the HRN plagioclases show reverse zoning from low An_{30} cores to An_{50} rims with variations in Mg and Sr concentrations of 200-570 ppm and 650-541 ppm, respectively. Trachyte hosted evolved plagioclases show minor reverse zoning in anorthite from 25 to 30 mol.%, a change in Mg concentration from 120-80 ppm and Sr from 564-1074 ppm (population 5 plagioclase). Grains hosted in tholeiitic sample HRN-26 show minor reverse zoning in An_{70-75} accompanied by an Mg core to rim variations of 1100-1260 ppm and virtually flat Sr profile 213-251 ppm. One plagioclase hosted in a glomerocryst show more complex zoning patterns, with three significant zones showing reverse and normal zoning. Cores of An_{82} abruptly change to mantles of An_{87} and finally rims of An_{74}, similar to the rims composition of the other grains. The pattern is matched by Mg profiles with core-mantle-rim concentrations of 1300-1100-1350 ppm and a virtually flat Sr profile between 200-250 ppm.

The main geochemical characteristics displayed by plagioclases populations are summarised as:

1. High anorthite >An_{80}, low TiO_2, Sr, Ba, Eu and La/Y, high Mg. Crystals are euhedral and don't display characteristic microtextures such as zoning or disequilibrium features. Exception for large crystals hosted in glomerophyric clusters in sample HRN-26 which display complex and oscillatory zoning in the mantle and rim.
2. Zoned anorthite ~An_{80-60}, high TiO_2 and Sr, intermediate Ba, Eu, La/Y and Mg. Crystals show an abrupt compositional zonation at the rim, cores don't display characteristic microtextures. Exception for larger crystals in glomerophyric clusters which can show oscillatory zoning.
3. Intermediate anorthite ~An_{40-60}, high Sr, intermediate TiO_2 and Mg (lower than population 2), intermediate Ba, Eu and La/Y (higher than population 2). Crystals show disequilibrium features, in particular dissolution at the crystal edge.
4. Low anorthite ~$An_{<40}$, normal zoning, high Sr, Ba, Eu and La/Y, low Mg. Some crystals display intense fine sieving at the crystal edge.
5. Low anorthite ~$An_{<40}$, minor reverse zoning, high Sr, Ba, Eu and La/Y, low Mg.

It is important to note that in population 4 and 5 there is large scatter in all trace elements and no distinction can be made except for the zoning in anorthite.

DISCUSSION

Equilibrium assemblages

The model by Namur et al. (2012) allows for modelling plagioclase-melt equilibrium in low pressure and low water systems, applicable for the differentiation of basaltic reservoirs in Iceland with a 10% error. Comparison of plagioclase anorthite to calculated equilibrium anorthite from whole rock shows rhyolitic and tholeiitic samples to be in equilibrium whilst both the trachytes and Torfajökull basalts exhibit significant mineral-melt disequilibrium. Samples I326 (tholeiite), LGH-4, and HRN-10 (rhyolites) also show textural data that is consistent with a normal equilibrium crystal cargo and displaying straight CSD profiles (fig. 3). In contrast HRN-1, HRN-9, HRN-26, NMS-2 and NMS-6 show kinked CSD profiles (fig. 3) and/or contain crystals displaying a wide range of disequilibrium textures (fig. 2a,b,f) beyond what would be expected from a normal equilibrium cargo. These lavas indicate the presence of more than one population of the same mineral suggestive of complex processes during shallow level magma ascent, evolution and storage.

Comparison of Sr_{plag}/Sr_{WR} with partition coefficient curves calculated using the model of Blundy and Wood (1991) and the anorthite model (fig. 7) by Namur et al. (2012) show chemical variation in excess of that expected from a standard equilibrium assemblage (fig. 7a). Population 2 high-anorthite cores (>80 mol.%) in samples HRN-1 and HRN-9 (transitional basalt and trachyte) plot above any reasonable partition coefficient curve and there is a large spread at low anorthite concentrations involving crystals from populations 3, 4 and 5 (samples NMS-2, NMS-6, LGH-4 and HRN-10). Of the samples that show textural data consistent of an equilibrium assemblage, only plagioclase compositions from tholeiite I326 lie within error of a single equilibrium line suggesting that a small degree of chemical disequilibrium is also present in the basaltic samples. Both rhyolites LGH-4 and HRN-10 in fact deviate from equilibrium lines to a similar degree (fig. 7a) as samples that show kinked CSD profiles (fig. 3) and contain crystals with chemical disequilibrium features.

Fig. 7b shows how calculated partition coefficients for Mg (Bindeman et al. 1998) for individual SIMS analyses differ from known partitioning behaviour. Fractional crystallisation is expected to reduce the xAn of a plagioclase accompanied by an increase in RTlnD Mg following a trend similar to that of calculated equilibrium. The sole variable in this model is plagioclase anorthite and therefore other magmatic variables such as melt composition and temperature would not affect the plotting in the graph. For processes such as entrainment and magma mixing, intra-plagioclase disequilibrium would be present due to differences in composition between core and rim, therefore prompting diffusion modification if held enough time at magmatic temperatures. NaSi-CaAl diffusion in plagioclase is slow: 1-10 x 10^{-21} between An_{70}-An_{90} at 1200 °C (Grove and Baker 1984), therefore diffusive processes are likely to cause vertical displacement away from equilibrium instead. This is

observed in the relatively subparallel trends observed in crystal cores at anorthite ~50-80 mol.%. Moreover, entrainment and mixing could result in fast disequilibrium rim growth, which is observed in the displacement to lower RTlnD Mg of the rims.

The mineral-melt disequilibrium highlighted in fig. 7a,b could be due to the following processes:

- Plagioclase Accumulation: this would result in an increase in Sr_{WR} and therefore cause a reduction in Sr_{plag}/Sr_{WR} at a given Anorthite content. No effects on Mg-An partitioning behaviour.
- Fractional Crystallisation: crystallisation and magmatic evolution should follow the Sr partition coefficient curve (Blundy and Wood 1991, fig. 7a) where Sr compatibility increases with decreasing anorthite and where temperature drops as fractionation proceeds, instead population 2 plagioclase at $An_{\sim 80\text{-}60}$ and populations 4 and 5 between anorthite 40-20 mol.% appear to be following an opposite trend. High water concentrations in the melt could cause a shift to higher anorthite in the crystallising plagioclase. Shallow level decompression instead would reduce the anorthite composition shifting it away from the partition coefficients curves (Couch et al. 2003). The Mg-An behaviour in plagioclase should follow equilibrium lines, with increasing RTlnD Mg at lower anorthite (fig. 7b).
- Magma Mixing: the introduction of new melts into the system would affect the Sr_{plag}/Sr_{WR} according to their concentration. Higher Sr melts would decrease the Sr_{plag}/Sr_{WR} ratio and vice versa. The intra-plagioclase Mg-An equilibrium would be affected by diffusion equilibration between cores and rims causing modified RTlnD Mg.
- Entrainment: depending on the Sr concentration of the plagioclase being entrained this processes could both increase and decrease the Sr_{plag}/Sr_{WR}. However Sr concentrations in plagioclase are likely to be higher than those of the host melt therefore most likely causing an increase in Sr_{plag}/Sr_{WR}. Diffusion modification would affect the compositional boundary between melt and rims, and between cores and rims causing a vertical displacement in RTlnD Mg.

These processes are individually discussed in the following section.

Accumulation and Fractional Crystallisation

Published whole rock data from Torfajökull (fig. 8) shows trends consistent with significant fractional crystallisation with a decrease in CaO and Sr with decreasing MgO at the onset of plagioclase crystallisation. Similarly a sharp decrease in TiO_2 is associated with magnetite crystallisation. Nevertheless extensive plagioclase crystallisation is expected to reduce the Al_2O_3 content of the melt and this is not seen is fig. 8, instead the Al_2O_3 content increases with decreasing MgO. Accumulation of crystals during cooling in lava flows can produce samples that contain

significant enrichment in their equilibrium assemblage. This in turn alters the whole rock geochemistry, producing compositions pointing towards the compositions of the accumulated phase. Point count data suggests high plagioclase proportions in transitional basalts (HRN-1), tholeiitic basalts (HRN-26b and STU-6) compared to tholeiite FRO-1 (table 1). Similarly rhyolites and trachytes LGH-4, HRN-10 and HRN-9 are plagioclase porphyritic compared to HRN-26r and NMS-6. Of these samples HRN-1 and HRN-9 contain assemblages that show limited variation in crystal compositions as well as high proportions of a more primitive assemblages. Modelling of whole rock compositions suggests that the compositions of HRN lavas could have been significantly altered by up to 40% accumulation of plagioclase. The density of anorthite plagioclase is ~ 2.760 g/cm^3 (Robie et al. 1967), lower than that of basaltic melts (~2.8 g/cm^3 (Stolper and Walker 1980)), and it is therefore likely that high anorthite plagioclase would float in its host melt. In contrast an assemblage including other mineral phases, such as olivine or clinopyroxene with density of ~3.2136 g/cm^3 and 3.277 g/cm^3 respectively (Robie et al. 1967), would be denser than plagioclase alone and could sink in primitive melts. Whilst variations in whole rock Sr, CaO and to a lesser extent TiO_2 could be explained by accumulation, it does not explain the higher Al_2O_3 in more evolved compositions. This is consistent with interpretations that the high abundance of Al_2O_3 in Torfajökull rhyolites suggested formation through crustal melting (Gunnarsson et al. 1998; Zellmer et al. 2008) and therefore would not be replicated by accumulation or fractional crystallisation models.

Petrolog3 (Danyushevsky and Plechov 2011) was used to carry out forward crystallisation models from the most evolved tholeiite and transitional basalt whole rock compositions available (McGarvie 1984; Macdonald et al. 1990a; McGarvie et al. 1990), involving an ol + plag + cpx + mt crystalline assemblage, as observed from basalt point counts, at pressures of 0.001, 2, 4 and 6 kbar as crystallisation pressures estimated for Icelandic volcanic systems (Neave and Putirka 2017). Liquid lines of descent were plotted alongside whole rock data (fig. 9) and equilibrium plagioclase compositions during fractional crystallisation were plotted on mineral data diagrams (fig. 10). At primitive compositions, the range of Torfajökull lavas and plagioclase mineral compositions follows the same trend as that observed in the fractional crystallisation model. Nevertheless a large difference is observed for modelled Al_2O_3 and Sr trajectories suggesting that, as previously proposed, extensive fractionation of plagioclase to produce rhyolites is not a viable process at Torfajökull (Gunnarsson et al. 1998; Zellmer et al. 2008). Zellmer et al. (2008) also suggested that the rhyolite hosted crystals formed shortly before eruption and are therefore representative of a phenocryst population. It also possible that the model is not able to replicate fractional crystallisation at evolved compositions, as well as the fact that using mineral-melt partition coefficients to predict the trace element behaviour implies that the modelling is limited by the quality of the partitioning model utilised.

It was not possible to generate an appropriate plagioclase composition using the same parent as for the whole rock model. Instead a more primitive composition was utilised and whilst the Mg trend

could not be modelled, a similar trend for Sr, but with slightly lower concentrations was observed suggesting that high anorthite plagioclase does not crystallise from composition similar to those producing the equilibrium assemblages observed and that the variations observed can only partly be associated to fractional crystallisation. Similarly to whole rock, the trends of more evolved plagioclase compositions cannot be obtained in the Petrolog3 models using either start compositions. This suggests that FC alone cannot generate the large geochemical range observed in both whole rock and plagioclase composition.

Crystallisation Conditions

As previously shown the majority of samples contain plagioclase assemblages that display a range of Sr and Mg partition coefficients that deviate from calculated equilibrium lines on Sr_{plag}/Sr_{WR} and RTlnD Mg vs. calculated xAn plots (fig. 7a,b). These deviations could represent changes in crystallisation conditions. Anorthite in plagioclase is strongly affected by temperature where a 100 °C increases anorthite by ~5 mol.% at stable pressure and water content (Lange et al. 2009). Melt water content is also known to strongly affect plagioclase anorthite which varies by ~2 mol.% per 1 wt.% of melt H_2O (Panjasawatwong et al. 1995). It has been argued that the mantle under Iceland is wet (Schilling et al. 1983; Nichols et al. 2002; Guilbaud et al. 2007), however water contents are still below ~1.64 wt.% (Nichols et al. 2002) and therefore should not affect anorthite composition by more than ~3 mol.%. Shallow level decompression by 1 kbar and crystallisation at shallower depths would cause a reduction of anorthite by ~2 mol.% (Danyushevsky 2001), nevertheless the composition of already crystallised high anorthite plagioclase crystals would not be affected by this process, moreover decompression would also cause coarse sieving in plagioclase however this is not observed in the plagioclase cargoes. Plagioclase chemistry does show a sharp decrease in population 2 HRN-1 and HRN-9 plagioclase anorthite between core and rim of ~10-20 mol.%, and therefore a decompression by 5-10 kbar would be required, nevertheless this would not explain the displacement of the plagioclase cores. Crystallisation conditions of the plagioclase crystals have been calculated using the equations of (Putirka 2008) and tested possible equilibrium melts. High-anorthite cores suggest crystallisation depths of ~4 kbar, in agreement with the seismically determined depth of ~8 km (Soosalu and Einarsson 2004) whilst lower anorthite rims show shallower crystallisation depths ~2 kbars (fig. 11). Crystals with anorthite <60 mol.% were left out of the analyses as the model only performs well at temperatures larger than 1100 °C (Putirka 2005, 2008). The melt composition for disequilibrium assemblages was calculated using mineral compositions and partition coefficients (Blundy and Wood 1991; Bindeman et al. 1998) and tested with the model's An-Ab equilibrium (Putirka 2008), nevertheless large errors are associated with the model. A clear record of two different depths of crystallisation between the cores and the rims is highlighted. Population 2 cores were crystallised in a reservoir ~4 kbar in the crust before being carried to shallower depths ~2 kbar where rims of lower anorthite crystallised prior to eruption. Plagioclase population 1 crystals show

evidence for having crystallised at shallower depths. As a comparison, clinopyroxene thermobarometry was calculated for crystals hosted in sample HRN-1 (fig. 4) as well as an average range of clinopyroxene pressures calculated from Icelandic samples (Neave and Putirka 2017). These models show that deeper pressures are in agreement with those calculated using plagioclase.

Mixing

Previous studies predominantly based on whole rock chemistry and textures identified magma mixing and mingling as dominant processes producing hybrid products at Torfajökull (Blake 1984; McGarvie 1984; Mørk 1984a; Macdonald et al. 1990a). These studies recognised the presence of three mixing components: Veiðivötn fissure tholeiites, Torfajökull mildly alkaline or transitional basalts and Torfajökull rhyolites (Blake 1984; McGarvie 1984; Mørk 1984a; Macdonald et al. 1990a), with common rhyolite-basalt and rhyolite-rhyolite interactions. The Torfajökull lavas in this study display a variety of rock macrotextures and whole rock geochemistry. Simple mass balance binary mixing models have been carried out using published data (McGarvie 1984; Macdonald et al. 1990a; McGarvie et al. 1990) between tholeiite-rhyolite and transitional basalt-rhyolite and show that the trachyte compositions (e.g. HRN-9, NMS-6) can be generated by mixing between ~60-85% rhyolitic component with ~40-15% basaltic component, consistent with the 80:20 rhyolite:basalt ratio calculated by McGarvie (1984). Crystal cargoes also point to extensive mixing within the system through higher than equilibrium plagioclase proportions, (table 1), kinked CSD profiles (fig. 3), disequilibrium compositions and textures and zoned plagioclase crystals. Even in circumstances where plagioclase anorthite appears to be in equilibrium with the host rock (trachytic and rhyolitic lavas), trace element concentrations show large variations and mafic enclaves are found in more evolved lavas suggesting mixing processes also affected these samples. Mixing processes at Torfajökull are discussed in two different sections, magma mixing and entrainment, where the former describes processes in which two distinct melts are interacting whilst the latter describes the transfer of crystals between different magmas without substantial involvement of their original melt.

Magma mixing

The initial phase of magma mixing is represented by a physical dispersion (mingling) of one magma inside its host, during this mingling phase no chemical exchange occurs. Experimental studies have shown that during such mingling processes the intruding magma is composed of both active and coherent regions (Perugini et al. 2003, 2006). The former is represented by the formation of macrotextural filaments and swirls while in the latter no dispersion has taken place (Perugini et al. 2003, 2006). Whilst melt and volatiles are miscible, crystals are mechanically transferred during magma mixing and therefore may not be homogeneously distributed in the resulting products (Ubide et al. 2014). Crystals may also be exchanged between end-members at the enclave/host interface (Plail et al. 2018) and upon enclave disaggregation (Tepley et al. 1999). Both samples from the

871AD and 1477 eruptions contain enclaves present as discrete blebs of mafic material hosted within a rhyolitic or trachytic groundmass (fig. 2g,h). Sample NMS-2 contains two distinct blebs of mafic material hosted in a trachytic groundmass (fig. 2h). The tholeiitic enclave (enclave 1) is rounded, phenocryst rich and presents a high abundance of vesicles towards the hybrid rim at the contact with the host groundmass the compositions of the plagioclase crystals are consistent with that of plagioclase population 1 and plot within the same fields in fig. 5. The second bleb presents mineralogical affinities to that of transitional basalts, being darker in colour, crystal and vesicle poor presenting few, large euhedral olivine crystals (enclave 2). This latter enclave is more elongated in shape and does not have a hybrid rim, suggesting the two enclaves potentially represent separate sources. Sample HRN-26, a glassy rhyolite, contains a tholeiitic enclave; at the contact between the two there is a hybrid layer (fig. 2g) and the mafic enclave contains both population 1 plagioclase crystals and heavily sieved low anorthite (~20 mol.%) population 4 and 5 feldspars inherited from the host melt (fig. 2f,g). Both types of enclaves present a tabular crystal population, suggesting that the magma was already crystallised prior to incorporation and was rapidly quenched due to the large temperature difference to the host silicic melt (Eichelberger 1980; Coombs et al. 2000; Plail et al. 2018). The rhyolite in contact with the basalt presents filaments and most crystal phases are aligned as if by a flow (fig. 2g). These fluidal features are likely to have formed by superheating of the rhyolite as it came in contact with the hotter basaltic melt (Sparks et al. 1977; Kouchi and Sunagawa 1983; McGarvie et al. 1990). Whilst these could have been assimilated into their evolved host as solid material from the walls of the conduit, textural evidence suggests they were molten at the time of assimilation.

Mixing between compositionally distinct magmas has long been found to be difficult due to large differences in thermodynamic properties (Sparks and Marshall 1986; Bateman 1995; Perugini and Poli 2005). Complete mixing can only occur when the mafic end member is high in proportion with respect to the evolved member (>50%) or when the two mixing components present small geochemical differences (e.g. <10 wt% SiO_2) (Kouchi and Sunagawa 1983; Bacon 1986; Sparks and Marshall 1986; Tepley et al. 1999). The textural morphologies of mafic enclaves have been used to infer the mode of formation and two distinct mechanisms of mafic injection have been proposed. A turbulent flow of mafic magma may enter a chamber, causing fountaining which eventually disaggregates into mafic blebs presenting a chilled margin (Eichelberger 1980; Coombs et al. 2000; Rutherford and Devine 2003; Holness et al. 2005) and is a proposed method of formation for enclave 1 in NMS-2 and the enclave in sample HRN-26 (fig. 2g,h). If the mafic flow is instead low in energy and volume, the magma ponds at the bottom of the chamber (Holness et al. 2005; Plail et al. 2014, 2018). As the mafic layer cools and crystallises, the melt becomes vapour saturated and starts to exsolve H_2O (Tepley et al. 1999; Holness et al. 2005; Plail et al. 2018). Trapped volatile phases, evidenced by an increase in vesicle density towards the basalt-rhyolite interface, will decrease the

density of the intruded mafic magma (Holness et al. 2005). Once the density becomes similar or smaller to that of the host, mafic upwells into the silicic host and mafic material is dispersed within the chamber (Tepley et al. 1999; Holness et al. 2005; Plail et al. 2018). This mechanism results in the formation of glassy and highly vesicular mafic enclaves, which lack a chilled margin (Tepley et al. 1999). If resident for long enough in the silicic host these enclaves could disintegrate due to shearing and disperse primitive minerals into the host (Tepley et al. 1999). The lack of chilled margin in the mafic enclaves has also been suggested to indicate a smaller temperature difference between the mafic and silicic magma, which would facilitate chemical exchange during quenching (Bacon 1986; Plail et al. 2014, 2018). This magma injection process and enclave formation is consistent with the petrological observations of enclave 2 (fig. 2h). Plail et al. (2018) suggested that ceased mafic injection would result in larger and more hybridised enclaves. It is therefore likely that these enclaves were instead formed by a single injection of basaltic melt resulting in smaller sizes and basaltic compositions. Recent studies support a rapid mechanism for the formation of smaller enclaves, with timescales of 0.1-1 day (Plail et al. 2018). Moreover, both enclaves in NMS-2 (fig. 2h) are highly vesicular, suggesting exsolution of volatiles, which could drive further upwelling through gas expansion, potentially acting as an eruption trigger (Holness et al. 2005). Whilst magma mixing results in heating of the rhyolitic host, it enhances syn-eruptive degassing which causes slower magma expansion and therefore reducing the explosivity of the eruption (Ruprecht and Bachmann 2010). The enclave in the 871AD eruption (HRN-26, fig. 2g) differs from those of the 1477 eruption (NMS-2, fig. 2h) as it is less vesicular, 2% compared to 6%. The 871AD eruption produced a 0.18 km^3 lava flow (Hrafntinnuhraun) and 0.4 km^3 of tephra (HRN) in the SW area of the volcanic centre whilst the 1477 eruption was effusive and resulted volumetrically smaller flows (0.05 to 0.01 km^3) (Larsen et al. 2015). It is therefore possible that degassing mechanisms caused by mafic injection during the 871AD eruption were not as extensive as those of the 1477 eruption, resulting in a more explosive eruption compared to the lava flows characterising the latter eruption.

Interestingly, the evidence for magma mixing between rhyolites and basalts in the crystal cargo chemistry is limited. Reverse zoning in evolved plagioclase grains is only found in a very limited number of NMS-6 and HRN plagioclase, and therefore most evidence relies on mechanical mixing and mingling features between the end member compositions. However, crystal cargos provide evidence for frequent rhyolite-rhyolite mixing at Torfajökull. Pockets of rhyolite are thought to frequently mix and mingle with previously segregated pockets whilst stored in the crust (Gunnarsson et al. 1998). Frequent injections of basalt in the crust is also thought to result in smaller but more frequent eruptions of rhyolite (Gunnarsson et al. 1998), resulting in hybrid eruption and impeding the accumulation of large volumes of rhyolite in the crust, as observed for the 871 AD and 1477 eruptions (McGarvie et al. 1990). This model also explains the Sr disequilibrium and the wide variations in both compatible and incompatible trace elements between An_{20-40} observed in rhyolite

hosted low anorthite plagioclase populations 4 and 5 in samples LGH-4 and HRN-10 (fig. 7a). These plagioclases occasionally show resorped edges, as well as compositional zoning (e.g. NSM-6), suggesting they were mixed and crystallised in a new melt (Viccaro et al. 2010; Renjith 2014). Mg in particular shows a very wide range at low anorthite. Mg diffusion in plagioclase is fast (Bindeman et al. 1998) and therefore changes in Mg concentrations would affect the crystal faster than the equilibrium growth of a new rim. These compositional characteristics are shared by the evolved plagioclase of trachytes (fig. 7a), as these were originally stored in a rhyolitic chamber prior to interaction with a basaltic melt.

Entrainment

Samples HRN-9 and HRN-1 also show high proportions of plagioclase (table 1), but in contrast to samples which display magma mixing they show CSD profiles with increased number of larger, and therefore older, crystals (fig. 3). These large crystals are enriched in compatible and incompatible trace element chemistry, similar to population 2 plagioclase, and exhibit high anorthite cores ~80 mol.% anorthite (fig. 5, 6) and a sharp zoning profile to anorthite ~50-60 mol,% in the rim. Cores ~anorthite 80 mol.% show disequilibrium with their host melt, and a trace element pattern different to that expected by fractional crystallisation (fig. 7a,b). Similar grains have been found in trachytic samples (e.g. HRN-9), suggesting that the entrainment of population 2 crystals occurred in the basaltic end member of the trachytes. Alongside high anorthite plagioclase, these samples contain high forsterite olivine crystals, including those hosted in glomerophyric clusters, and high Mg# clinopyroxene (fig. 2c). Many studies have identified primitive phenocryst phases hosted in basaltic melts as entrained crystals from a disaggregated crystal mush (Rhodes et al. 1979; Lange et al. 2013; Neave et al. 2014, 2017) and this process has been recognised in basaltic systems across a variety of geological settings (Hansen and Grönvold 2000; Ridley et al. 2006). Entrainment of mush crystals can be recognised in rock macro-textures (Higgins 1996; Holness 2007) and their presence affects whole rock chemistry and its variability (Salaün et al. 2010; Passmore et al. 2012; Neave et al. 2014). It is now a widely accepted idea that magmas reside in the crust in vertically extensive magmatic systems, where different magma chambers are interconnected by mushy necks. Different levels of crystallisation within the crust (fig. 11) support the idea that, rather than large basaltic magma chamber, a partially mushy reservoir is present underneath Torfajökull. Seismic studies have in fact struggled to find evidence for large bodies of molten material within the Torfajökull's crust (Soosalu and Einarsson 2004) as smaller pods of melt are more difficult to detect, and more mature systems would transmit seismic waves at velocities similar to that of solid rock, due to the elastic strength caused by interconnected networks of crystals (Singh et al. 1998).

These observed textural features could be formed by solid assimilation from the walls of the plumbing system. However it would seem more difficult to disaggregate intergrown crystals from a

603 solid cumulate and rather easier to entrain them from a loosely packed mush. Microphotographs of
604 entrained crystals show, as well as solitary zoned plagioclase crystals, clots mostly composed of
605 plagioclase with minor olivine and clinopyroxene (fig. 2c,d). The microstructure of these clots
606 suggests that these crystals were hosted in a mushy environment as melt pores and films can be
607 identified at plagioclase-plagioclase boundaries (fig. 2e). Compared to clusters formed by synneusis,
608 Torfajökull glomerocrystic crystals are randomly oriented creating a framework that promotes
609 porosity and therefore trapping of melt during early stages of formation (Holness et al. 2005, 2012).
610 Moreover, planar crystal faces in large glomerocrystic plagioclases indicate that they were able to
611 grow into the melt within the crystal mush (Cabane et al. 2005) and abrupt zoning similar to that of
612 the lone phenocryst is present in the glomerocrystic crystals in contact with the groundmass (fig. 2d,
613 fig. 6). Whilst solitary plagioclase crystals present a single compositional variation boundary
614 between core and rim, consistent with a population 2 composition, the larger glomerocrystic
615 plagioclase crystals display more complex zoning patterns, including oscillatory zoning (fig. 2d).
616 This suggests a longer residence time within the mush allowing for a more complex magmatic
617 history. Olivine and clinopyroxene associated with clots show higher forsterite% and Mg#,
618 respectively, and different trace element compositions (fig. 4), a large range in Nb/Y in olivine and
619 lower Dy/Yb in clinopyroxene.

620 Little geochemical evidence is found of the mush liquid as its small proportions may have
621 homogenised with the carrier liquid (Costa et al. 2010) or it just remains present as small melt
622 inclusions and pores ~30 μm in size whose composition is unknown (fig. 2e). Nevertheless the high
623 anorthite plagioclase composition hosted in the mush suggests an MgO content of ~7 wt.% using
624 plagioclase-melt partition coefficients (Bindeman et al. 1998), whilst a ~10 wt% is required for the
625 high anorthite olivine hosted in the glomerophyric cluster, as calculated from Mg partitioning in
626 olivine (Beattie 1994). Interstitial mush liquid composition can vary in different parts of the mush
627 chamber (Costa et al. 2010) and therefore diffusive exchange between mineral and interstitial melt
628 led to the formation of plagioclases with different Mg concentrations within the same mush (fig. 6).

629 It is suggested that the entrainment and crystallisation of the low anorthite rim in plagioclase 2
630 population (HRN-1, HRN-9) is caused by the arrival of a new more evolved mildly alkali melt from
631 a deeper region of the Torfajökull system caused disruption of the mush network, leading to
632 entrainment of solitary crystals and crystal clots into the replenishing melt where plagioclase
633 crystallised a new more evolved rim ~An_{50-60}. Entrainment of new crystals in a new melt can cause
634 rapid disequilibrium growth of plagioclase, which could cause crystals to have different
635 compositions at the contact with the groundmass (fig. 6, 7b) therefore producing rims of different
636 composition (fig. 6). The low abundance of olivine and clinopyroxene mush crystals could be due to
637 the fact that they were separated from the melt with respect to plagioclase, the latter being more
638 buoyant than both olivine and clinopyroxene. Compared to HRN-1 and HRN-9 plagioclase

population 2, population 1 HRN-26 plagioclases display a depletion in TiO_2, in compatible trace elements like Sr and in incompatible trace element Eu and La/Y, and an enrichment in Mg at high anorthite ~ 80 mol.% (fig. 5). This suggests they originate from a tholeiitic melt and calculated melt composition using partition coefficients (Bindeman et al. 1998) suggest an original melt MgO of ~11 wt.%. A higher anorthite mantle compared to the core of the crystal (HRN-26. figure 6) could indicate that these crystals were subject to replenishment events from a more primitive melt, causing disequilibrium and crystallisation (fig. 8). These crystals present similar characteristics as mush crystals from Torfajökull and therefore may have had undergone similar processes, nevertheless they belong to a different system and therefore a different mush storage region. Unfortunately not enough samples were analysed for the tholeiitic plagioclase and clots, therefore this conclusion remains speculative.

Entrainment of low anorthite grains into basaltic melts is observed in sample HRN-26 (fig. 2g) where an An_{20} plagioclase (fig. 2f) is found within a tholeiite. Intense fine sieving close to the crystal's rim suggests prolonged disequilibrium caused by contact with a hotter, CaO rich melt (Renjith, 2014; Viccaro, 2010). The lack of a re-equilibrated rim suggests its residence time in the basaltic melt prior to eruption was short.

Timescales

We have utilised a range of methods to better understand the timescales of processes occurring within the Torfajökull-Veiðivötn system. Diffusion chronometry based on Mg diffusion in plagioclase can estimate re-equilibration timescales in the region of days to 100s of years (Costa et al. 2003, 2010; Druitt et al. 2012). We modelled diffusion re-equilibration of plagioclase using compositional profiles obtained by SIMS (fig. 6) of HRN-1 and HRN-9 population 2 plagioclase. The results summarised in table 4 suggest that mush crystals were entrained in a new melt, where they crystallised in the shallow crust for ~10 days prior to eruption. Diffusion re-equilibration between crystal cores and rims is also shown in fig. 7b where cores and rims are displaced from Mg equilibrium lines. Due to the dependence of the diffusion coefficient on plagioclase compositions meaning that these timescales can't be constrained with confidence <1 year, these results still qualitatively suggest a very quick mixing to eruption time. These crystals also show kinked CSD profiles (fig. 3) representing larger assimilated grains and smaller grains. These smaller crystals are thought to have grown at the same time as the rim of the larger assimilated phenocrysts therefore their residence reflects the time of rim growth, and therefore assimilation to eruption time, of the inherited mush phenocrysts. The gradient of a CSD through a single population (equation 24, Marsh 1988) can be used to estimate the residence time of a crystal population using $residence\ time = -1/G * slope$ where the slope can be obtained from CSD plot (Armienti et al. 1994; Higgins and Roberge 2007; Fornaciai et al. 2015; Neave et al. 2017). Using a crystal growth rate of $0.5\text{-}5x10^{-7}$

mm/s observed from other basaltic systems (Orlando et al. 2008; Agostini et al. 2013; Neave et al. 2017) we calculate that mush plagioclases were resident in the new carrier melt for 5-53 days prior to eruption, loosely in accordance with timescales calculated for the same samples using diffusion chronometry (table 4), nevertheless large errors are present due to the large range of inferred crystal growth rate, and the errors associated with the calculation of CSD profiles.

Due to little effect on the crystal cargoes, the timescales of mixing between basaltic and rhyolitic melts were more difficult to constrain. Experimental studies and the observation of natural samples have shown that chaotic magma mixing causes stretching and folding of compositionally different melts generating a fractal distribution of compositional gradients (Perugini et al. 2003, 2004; Costa et al. 2008). As the mingling process continues and the physical dispersion is increased, chemical exchange between the melts starts following the principles of diffusion and this is recorded once the magma quenches (Perugini et al. 2003). The chemical mobility of elements during chaotic mixing has been experimentally investigated by Perugini et al. (2013) and used to develop the Concentration Variance Decay (CVD) technique to obtain timescales of dynamic mixing processes (Perugini et al. 2015). Torfajökull's sample HRN-26 presents a mafic enclave and a hybrid layer, which shows filament-like features (fig. 2g). The host rhyolite also shows bands of glass of different colours however LA-ICP-MS analyses of the groundmass have shown them to present very small compositional variation. In contrast, larger compositional differences have been measured across the tholeiite-hybrid-rhyolite boundary (fig. 12). These results have been used to calculate CVD rate of the homogenisation process and resulted in a mixing to quenching time of 12 minutes. This method is able to calculate very fast mixing to eruption timescales and our results, on the scale of minutes, are similar to those obtained from natural samples from the original study (Perugini et al. 2015). However uncertainty arises from the temperature at which the experiments were carried out as 1200 °C may not be a realistic temperature in basaltic-rhyolitic mixing environments causing an underestimation of the speed of elemental homogenisation. Therefore rather than absolute timescales, these should be regarded qualitatively as an indication of very fast basalt-rhyolite mixing times impeding hybridisation of the two end member compositions.

Sample	Eruption	Grain	Timescale (days)	Temperature (°C)
HRN-1	871AD	5	$2.73^{+11.6}_{-0.68}$	1150
HRN-1	871AD	2	$1.3+^{5.78}_{-0.34}$	1150
HNR-1	871AD	8	$2.8+^{11.90}_{-0.70}$	1150
HRN-1.2	871AD	4	$0.49^{+2.08}_{-0.12}$	1150
HRN-1.2	871AD	5	$2.73^{+10.07}_{-0.59}$	1150
HRN-9	871AD	8	$2.01^{+8.54}_{-0.50}$	1150
HRN-9	871AD	3	$0.48^{+2.52}_{-0.36}$	1150
HRN-9	871AD	4	$1.01^{+5.30}_{-0.76}$	1150
HRN-9	871AD	1	$2.73^{+11.60}_{-0.68}$	1150
Average max	871AD	-	~10	-
HRN-26*	871AD	-	$98.65^{+419.26}_{-24.66}$	1150
NMS-6*	1477	3	$3.5^{+14.88}_{-0.88}$	900

Table 4: Diffusion chronometry results for plagioclase hosted in lavas from the 871AD eruption using the one dimensional finite-element solution model using the method by Costa et al. (2003). We used an An-dependent experimentally determined Mg diffusion coefficient (LaTourrette and Wasserburg 1998) and incremental steps of 2μm. Initial and equilibrium concentrations were determined by 1) calculating the partition coefficient for Mg using measured An contents (Bindeman et al. 1998) and temperature conditions determined by plagioclase thermobarometry (Putirka 2008); 2) using the calculated partition coefficient and measured Mg concentrations to determine the MgO content of the melts in equilibrium with the core and the rim; and 3) calculating equilibrium Mg concentrations for the host melts. Sources of error: error on partition coefficient calculations for Mg is between 8-10%; the largest error associated with diffusion is temperature estimation. The plagioclase thermobarometer (Putirka 2008) estimates a 20-30 °C error on temperature, a ±25 °C variation in the model leads to a relative error of 45-75%. Errors associated with the diffusion can change the result to up to a factor of three. *is not taken into account into the average as it is not a Torfajökull but a Veiðivötn basalt. Average max. indicates the average maximum error residence time calculated.

CONCLUSIONS

Plumbing system model

Previous work has shown interactions between products of Torfajökull and Veiðivötn (McGarvie 1984; Mørk 1984b; Macdonald et al. 1990a; Zellmer et al. 2008). This study has provided quantitave constrains on the interactions between different melts, their storage conditions and the timescales of magmatic interaction and eruption trigger mechanisms. This information has been used to produce a detailed plumbing system model (fig. 13). Samples from the 871AD eruption have highlighted the presence of a mush reservoir underneath Torfajökull at a depth of ~8-13 km, consistent with seismological studies (Soosalu and Einarsson 2004). This reservoir is tapped, and mush crystals entrained, following recharge by a deeper crystal poor evolved Torfajökull transitional basalt. Diffusion chronometry of mush plagioclase grains has shown this processes to be fast, an average of 10 days (table 4), in which the new mush rich magma is stored in the shallow crust following entrainment, and therefore indicates magma recharge and mush chamber replenishment as an

736 eruption triggering mechanism at Torfajökull. An estimated ascent rate for the new mush rich magma
737 has been calculated at ~0.9 cm s^{-1}, consistent with the values of 0.5-1 cm s^{-1} minimum ascent
738 velocities reported for the formation of plagioclase ultraphyric lavas (Lange et al. 2013). MORBs
739 have shown evidence for occurrence of xenocrysts more primitive than their host basalt, and mixing
740 of an evolved phenocryst poor magma and a primitive crystal rich melt has been identified as a
741 common process in Icelandic systems (Costa et al. 2010; Passmore et al. 2012; Neave et al. 2014,
742 2017). Petrological studies have shown that complex textures and geochemistry in igneous rocks
743 cannot be explained by melt fractionation alone, but instead indicating physical and chemical
744 processes occurring in mushy systems between crystal residues and new melts (Paterson et al. 2011;
745 Cashman and Blundy 2013; Humphreys et al. 2013; Thomson and Maclennan 2013; Caricchi and
746 Blundy 2015). Mush entrainment has also been found to play a key role in the large geochemical
747 variability of lavas erupted at Torfajökull, both in basalt variability and in trachyte hybrids (fig. 8).
748 Trachyte HRN-9 shows evidence of mush crystals; it is suggested that upon ascent of a mush rich
749 Torfajökull basalt, a pocket of rhyolite melt was encountered in the crust producing a hybrid sample.
750 Veiðivötn tholeiite is present in the 871AD eruption as a mafic enclave in sample HRN-26 (fig. 2g).

751 The 1477 eruption shows evidence for mingling of basalts and rhyolites. Trachytic samples (e.g.
752 NMS-6, fig. 2h) have shown to be produced by mixing of 60-85% rhyolite and 40-15% basalt,
753 similarly to sample HRN-9, although no high anorthite plagioclase is present. Instead both
754 Torfajökull basalts and Veiðivötn tholeiites are present as mafic enclaves hosted in a trachytic
755 groundmass (fig. 2h). The different morphologies displayed by the two type of enclaves suggest
756 different mechanisms of formation. The tholeiite enclaves are rimmed and we suggest they were
757 formed by high energy and turbulent mixing of fissure basalts upon later injection into a rhyolite
758 pocket underneath Torfajökull. This caused fountaining of basaltic material into the rhyolite and
759 formation of mafic enclaves present a hybrid rim. The Torfajökull basalt is instead thought to have
760 entered the rhyolitic melt from below, in smaller volumes and lower energy flow, ponding at the
761 bottom of the chamber and slowly allowing for chemical diffusion, aided by the smaller temperature
762 difference between rhyolite and evolved transitional basalt.

763 **Past and current activity**

764 80% of Icelandic historical eruptive events happened within the Eastern Volcanic Zone, of which
765 ~14% are attributed to the Barðabunga–Veiðivötn system and <~3% to Torfajökull (Thordarson and
766 Larsen 2007) . Veiðivötn is part of the second most active system in Iceland (Larsen 2002), and it
767 has been reported to having been particularly active since the settlement of Iceland ~870 AD,
768 erupting ~10km^3 of lava and tephra in the last 1100 years (Thordarson and Larsen 2007). The latest
769 eruption, in 1477, occurred on an ice-free part of the system along a >60 km long vents fissure
770 producing 5–10 km^3 of tephra and lava flows (Larsen 2002), therefore alternating explosive and

771 effusive activity. As discussed earlier, the SW tip of the fissure intersected the plumbing system of
772 Torfajökull resulting in simultaneous mixed eruptions (Larsen 1984; McGarvie 1984; Mørk 1984b;
773 McGarvie et al. 1990; Zellmer et al. 2008). It is suggested that for volcanic system located in
774 correspondence of the Icelandic mantle plume/anomaly, activity is high, alternating low and high
775 frequency eruptive periods that can last 40-80 years. During high frequency periods, such as the
776 1477 eruption, Veiðivötn has also been associated with major rifting episodes (Thordarson and
777 Larsen 2007).

778 At Torfajökull, seismic studies have failed to image an active magma chamber (Soosalu and
779 Einarsson 2004) nevertheless a low frequency cluster of earthquake events has been detected in the
780 southern part of the caldera (Soosalu and Einarsson 2004; Lippitsch et al. 2005; Soosalu et al. 2006).
781 These events occur in swarms and have been associated to the presence of active magma, in the form
782 of a shallow rising cryptodome (Soosalu et al. 2006). This is further supported by the intense
783 geothermal activity in the area surrounding these events (Soosalu and Einarsson 2004; Soosalu et al.
784 2006) as well as ground movements showing alternate periods of inflation and deflation which can
785 last several years (Larsen et al. 2015). In the western parts of the Torfajökull caldera, high frequency
786 earthquakes happen in an area where an inferred 8 km deep cooling magma chamber (Soosalu and
787 Einarsson 2004), in agreement with the presence of mush rich eruptive products in the western part
788 of the caldera. With the 1477 eruption being limited to the northern part of the caldera, at the
789 intersection with the fissure, this supports the idea that the lateral tholeiite injection did not encounter
790 the mush zone, resulting in the lack of mush-derived products in the 1477 eruption.

791 Understanding pre-eruptive processes is key to determining the hazard posed by volcanic centres.
792 Whilst this study is specific to the twinned eruptions of Torfajökull, the varied petrological
793 expressions of magma mixing processes, their extent and their timing is applicable to other volcanic
794 systems where similar magmatic interactions are present.

795 **REFERENCES**

796 Agostini C, Fortunati A, Arzilli F, et al (2013) Kinetics of crystal evolution as a probe to
797 magmatism at Stromboli (Aeolian Archipelago, Italy). Geochim Cosmochim Acta 110:135–
798 151. doi: 10.1016/j.gca.2013.02.027

799 Anderson DL (2005) Large Igneous Provinces : Consequences. Elements 1:259–263. doi:
800 10.2113/gselements.1.5.265

801 Annen C, Blundy JD, Sparks RSJ (2006) The genesis of intermediate and silicic magmas in deep
802 crustal hot zones. J Petrol 47:505–539. doi: 10.1093/petrology/egi084

803 Armienti P, Pareschi MT, Innocenti F, Pompilio M (1994) Effects of magma storage and ascent on
804 the kinetic of crystal growth. Contirb Miner Pet 115:402–414

805 Bacon CR (1986) Magmatic inclusions in silicic and intermediate volcanic rocks. J Geophys Res
806 91:6091. doi: 10.1029/JB091iB06p06091

807 Bateman R (1995) The interplay between crystallization, replenishment and hybridization in large
808 felsic magma chambers. Earth Sci Rev 39:91–106. doi: 10.1016/0012-8252(95)00003-S

809 Beattie P (1994) Systematics and energetics of trace-element partitioning between olivine and
810 silicate melts: Implications for the nature of mineral/melt partitioning. Chem Geol 117:57–71.
811 doi: 10.1016/0009-2541(94)90121-X

812 Bindeman IN, Davis AM, Drake MJ (1998) Ion microprobe study of plagioclase-basalt partition
813 experiments at natural concentration levels of trace elements. Geochim Cosmochim Acta
814 62:1175–1193. doi: 10.1016/S0016-7037(98)00047-7

815 Björnsson A, Saemundsson K, Einarsson P, et al (1977) Current rifting episode in north Iceland.
816 Nature 266:318–323. doi: 10.1038/266318a0

817 Blake S (1984) Magma mixing and hybridization processes at the alkalic, silicic, Torfajökull
818 central volcano triggered by tholeiitic Veidivötn fissuring, south Iceland. J Volcanol
819 Geotherm Res 22:1–31. doi: 10.1016/0377-0273(84)90033-7

820 Blundy JD, Wood BJ (1991) Crystal-chemical controls on the partitioning of Sr and Ba between
821 plagioclase feldspar, silicate melts, and hydrothermal solutions. Geochim Cosmochim Acta
822 55:193–209. doi: 10.1016/0016-7037(91)90411-W

823 Cabane H, Laporte D, Provost A (2005) An experimental study of Ostwald ripening of olivine and
824 plagioclase in silicate melts: Implications for the growth and size of crystals in magmas.
825 Contrib to Mineral Petrol 150:37–53. doi: 10.1007/s00410-005-0002-2

826 Caricchi L, Blundy J (2015) The temporal evolution of chemical and physical properties of
827 magmatic systems. Geol Soc London, Spec Publ 422:1–15. doi: 10.1144/SP422.11

828 Cashman K, Blundy J (2013) Petrological cannibalism: The chemical and textural consequences of
829 incremental magma body growth. Contrib to Mineral Petrol 166:703–729. doi:
830 10.1007/s00410-013-0895-0

831 Cashman K V., Stephen R, Sparks J (2013) How volcanoes work: A 25 year perspective. Bull Geol
832 Soc Am 125:664–690. doi: 10.1130/B30720.1

833 Cashman C V, Marsh BD (1988) Crystal size distribution (CSD) in rocks and the kinetics and
834 dynamics of crystallisation II: Makaopuhi lava lake. Contrib to Mineral Petrol 99:277–291.
835 doi: 10.1007/BF00371933

836 Coombs ML, Eichelberger JC, Rutherford MJ (2000) Magma storage and mixing conditions for
837 the 1953-1974 eruptions of Southwest Trident volcano, Katmai National Park, Alaska.
838 Contrib to Mineral Petrol 140:99–118. doi: 10.1007/s004100000166

839 Costa F, Chakraborty S, Dohmen R (2003) Diffusion coupling between trace and major elements
840 and a model for calculation of magma residence times using plagioclase. Geochim
841 Cosmochim Acta 67:2189–2200. doi: 10.1016/S0016-7037(02)01345-5

842 Costa F, Coogan LA, Chakraborty S (2010) The time scales of magma mixing and mingling
843 involving primitive melts and melt-mush interaction at mid-ocean ridges. Contrib to Mineral
844 Petrol 159:371–387. doi: 10.1007/s00410-009-0432-3

845 Costa F, Dohmen R, Chakraborty S (2008) Time Scales of Magmatic Processes from Modeling the
846 Zoning Patterns of Crystals. Rev Mineral Geochemistry 69:545–594. doi:
847 10.2138/rmg.2008.69.14

848 Couch S, Harford CL, Sparks RSJ, Carroll MR (2003) Experimental constraints on the conditions
849 of formation of highly calcic plagioclase microlites at the Soufrire Hills Volcano, Montserrat.
850 J Petrol 44:1455–1475. doi: 10.1093/petrology/44.8.1455

851 Danyushevsky L V. (2001) The effect of small amounts of H2O on crystallisation of mid-ocean
852 ridge and backarc basin magmas. J Volcanol Geotherm Res 110:265–280. doi:
853 10.1016/S0377-0273(01)00213-X

854 Danyushevsky L V., Plechov P (2011) Petrolog3: Integrated software for modeling crystallization
855 processes. Geochemistry, Geophys Geosystems 12:. doi: 10.1029/2011GC003516

856 Druitt TH, Costa F, Deloule E, et al (2012) Decadal to monthly timescales of magma transfer and
857 reservoir growth at a caldera volcano. Nature 482:77–80. doi: 10.1038/nature10706

858 Eichelberger JC (1980) Vesiculation of mafic magma during replenishment of silicic magma
859 reservoirs. Nature 288:446–450. doi: 10.1038/288446a0

860 Elliott TR, Hawkesworth CJ, Grönvold K (1991) Dynamic melting of the Iceland plume. Nature
861 351:201–206. doi: 10.1038/351201a0

862 Fornaciai A, Perinelli C, Armienti P, Favalli M (2015) Crystal size distributions of plagioclase in
863 lavas from the July–August 2001 Mount Etna eruption. Bull Volcanol 77:. doi:
864 10.1007/s00445-015-0953-8

865 Foulger GR (2002) Plumes, or plate tectonic processes? Astron Geophys 43:19–23. doi:
866 10.1046/j.1468-4004.2002.43619.x

867 Foulger GR, Anderson DL (2005) A cool model for the Iceland hotspot. J Volcanol Geotherm Res
868 141:1–22. doi: 10.1016/j.jvolgeores.2004.10.007

869 Foulger GR, Pritchard MJ, Julian BR, et al (2000) The seismic anomaly beneath Iceland extends
870 down to the mantle transition zone and no deeper. Geophys J Int 142:1–5. doi:
871 10.1046/j.1365-246X.2000.00245.x

872 Gast PW (1968) Trace element fractionation and the origin of tholeiitic and alkaline magma types.
873 Geochim Cosmochim Acta 32:1057–1086. doi: 10.1016/0016-7037(68)90108-7

874 Gravley DM, Wilson CJN, Leonard GS, Cole JW (2007) Double trouble: Paired ignimbrite
875 eruptions and collateral subsidence in the Taupo Volcanic Zone, New Zealand. Bull Geol Soc
876 Am 119:18–30. doi: 10.1130/B25924.1

877 Grove TL, Baker MB (1984) Phase equilibrium controls on the tholeiitic versus calc-alkaline
878 differentiation trends. J Geophys Res 89:3253–3274. doi: 10.1029/JB089iB05p03253

879 Grove TL, Bryan WB (1983) Fractionation of pyroxene phyric MORB at low pressure: An
880 experimental study. Contrib Miner Pet 84:293–309

881 Gudmundsson A (2000) Dynamics of volcanic systems in Iceland: example of tectonism and
882 volcanism at juxtaposed hot spot and mid ocean ridge systems. Annu Rev Earth Planet Sci
883 28:107–140

884 Gudmundsson A, Andrew REB (2007) Mechanical interaction between active volcanoes in
885 Iceland. Geophys Res Lett 34:1–5. doi: 10.1029/2007GL029873

886 Gudmundsson A, Lecoeur N, Mohajeri N (2014) Dike emplacement at Bardarbunga , Iceland ,
887 induces unusual stress changes , caldera deformation , and earthquakes. 1–7. doi:
888 10.1007/s00445-014-0869-8

889 Guilbaud MN, Blake S, Thordarson T, Self S (2007) Role of Syn-eruptive Cooling and Degassing
890 on Textures of Lavas from the ad 1783-1784 Laki Eruption, South Iceland. J Petrol 48:1265–
891 1294. doi: 10.1093/petrology/egm017

892 Gunnarsson B, Marsh BD, Taylor HP (1998) Generation of Icelandic rhyolites: silicic lavas from
893 the Torfajokull central volcano. J Volcanol Geotherm Res 83:1–45. doi: 10.1016/S0377-
894 0273(98)00017-1

895 Hansen H, Grönvold K (2000) Plagioclase ultraphyric basalts in Iceland: The mush of the rift. J
896 Volcanol Geotherm Res 98:1–32. doi: 10.1016/S0377-0273(99)00189-4

897 Hartley ME, Thordarson T (2013) The 1874-1876 volcano-tectonic episode at Askja, North
898 Iceland: Lateral flow revisited. Geochemistry, Geophys Geosystems 14:2286–2309. doi:
899 10.1002/ggge.20151

900 Higgins MD (2000) Measurement of crystal size distributions. Am Mineral 85:1105–1116

901 Higgins MD (2002) Closure in crystal size distributions (CSD), verification of CSD calculations,
902 and the significance of CSD fans. Am Mineral 87:1242–1243. doi: 10.2138/am-2002-0118

903 Higgins MD (1996) Magma dynamics beneath Kameni volcano, Thera, Greece, as revealed by
904 crystal size and shape measurements. J Volcanol Geotherm Res 70:37–48. doi: 10.1016/0377-
905 0273(95)00045-3

906 Higgins MD, Roberge J (2007) Three magmatic components in the 1973 eruption of Eldfell
907 volcano, Iceland: Evidence from plagioclase crystal size distribution (CSD) and
908 geochemistry. J Volcanol Geotherm Res 161:247–260. doi: 10.1016/j.jvolgeores.2006.12.002

909 Hildreth W (2004) Volcanological perspectives on Long Valley, Mammoth Mountain, and Mono
910 Craters: Several contiguous but discrete systems. J Volcanol Geotherm Res 136:169–198.
911 doi: 10.1016/j.jvolgeores.2004.05.019

912 Hinton RW (1990) Ion microprobe trace-element analysis of silicates: Measurement of multi-
913 element glasses. Chem Geol 83:11–25. doi: 10.1016/0009-2541(90)90136-U

914 Holness MB (2007) Textural immaturity of cumulates as an indicator of magma chamber
915 processes: infiltration and crystal accumulation in the Rum Eastern Layered Intrusion. J Geol
916 Soc London 164:529–539. doi: 10.1144/0016-76492006-021

917 Holness MB, Humphreys MCS, Sides R, et al (2012) Toward an understanding of disequilibrium
918 dihedral angles in mafic rocks. J Geophys Res Solid Earth 117:. doi: 10.1029/2011JB008902

919 Holness MB, Martin VM, Pyle DM (2005) Information about open-system magma chambers
920 derived from textures in magmatic enclaves: the Kameni Islands, Santorini, Greece. Geol

921 Mag 142:637. doi: 10.1017/S0016756805001172

922 Humphreys MCS, Edmonds M, Plail M, et al (2013) A new method to quantify the real supply of
923 mafic components to a hybrid andesite. Contrib to Mineral Petrol 165:191–215. doi:
924 10.1007/s00410-012-0805-x

925 Irving AJ, Frey FA (1984) Trace element abundances in megacrysts and their host basalts:
926 Constraints on partition coefficients and megacryst genesis. Geochim Cosmochim Acta
927 48:1201–1221. doi: 10.1016/0016-7037(84)90056-5

928 Jaques AL, Green DH (1980) Anhydrous melting of peridotite at 0-15 Kb pressure and the genesis
929 of tholeiitic basalts. Contrib to Mineral Petrol 73:287–310. doi: 10.1007/BF00381447

930 Kouchi A, Sunagawa I (1983) Mixing basalt and dacitic magmas by forced convection-Kouchi
931 Sunagawa-Nature-1983.pdf. Nature 304:527–528

932 Lange AE, Nielsen RL, Tepley FJ, Kent AJR (2013) The petrogenesis of plagioclase-phyric basalts
933 at mid-ocean ridges. Geochemistry, Geophys Geosystems 14:3282–3296. doi:
934 10.1002/ggge.20207

935 Lange RA, Frey HM, Hector J (2009) A thermodynamic model for the plagioclase-liquid
936 hygrometer/thermometer. Am Mineral 94:494–506. doi: 10.2138/am.2009.3011

937 Larsen G (2002) A brief overview of eruptions from ice-covered and ice-capped volcanic systems
938 in Iceland during the past 11 centuries: frequency, periodicity and implications. Geol Soc
939 London, Spec Publ 202:81–90. doi: 10.1144/GSL.SP.2002.202.01.05

940 Larsen G (1984) Recent volcanic history of the Veidivotn fissure swarm, southern Iceland - an
941 approach to volcanic risk assessment. 22:

942 Larsen G, Gudmundsson MT, Vogfjörð K, et al (2015) The Torfajokull volcanic system. In:
943 Ilyinskaya, Larsen and Gudmundsson (eds.): Catalogue of Icelandic Volcanoes. IMO, UI,
944 CPD-NCIP.

945 LaTourrette T, Wasserburg GJ (1998) Mg diffusion in anorthite: implications for the formation of
946 early solar system planetesimals. Earth Planet Sci Lett 158:91–108. doi: 10.1016/S0012-
947 821X(98)00048-X

948 Lippitsch R, White RS, Soosalu H (2005) Precise hypocentre relocation of microearthquakes in a
949 high-temperature geothermal field: The Torfaj??kull central volcano, Iceland. Geophys J Int
950 160:370–387. doi: 10.1111/j.1365-246X.2005.02467.x

951 Lundin ER, Dore AG (2005) NE Atlantic break-up: a re-examination of the Iceland mantle plume
952 model and the Atlantic-Arctic linkage. In: Petroleum Geology:North-West EuropeandGlobal

953 Perspectives—Proceedingsof the 6thPetroleum Geology Conference. pp 739–754

954 Macdonald R, McGarvie DW, Pinkerton H, et al (1990a) Petrogenetic evolution of the torfajökull
955 volcanic complex, Iceland I. Relationships between magma types. J Petrol 31:461–481. doi:
956 10.1093/petrology/31.2.461

957 Macdonald R, McGarvie DW, Pinkerton H, et al (1990b) Petrogenetic Evolution of the Torfajokull
958 Volcanic Complex , Iceland I. Relationship Between the Magma Types. J Petrol 31:461–481.
959 doi: 10.1093/petrology/31.2.461

960 Manning CJ, Thirlwall MF (2014) Isotopic evidence for interaction between Torfajökull mantle
961 and the Eastern Rift Zone, Iceland. Contrib to Mineral Petrol 167:1–22. doi: 10.1007/s00410-
962 013-0959-1

963 Marsh BD (1988) Crystal size distribution (CSD) in rocks and the kinetics and dynamics of
964 crystallisation I: Theory. Contrib to Mineral Petrol 99:277–291. doi: 10.1007/BF00371933

965 Martin E, Sigmarsson O (2007) Crustal thermal state and origin of silicic magma in Iceland: The
966 case of Torfajökull, Ljósufjöll and Snæfellsjökull volcanoes. Contrib to Mineral Petrol
967 153:593–605. doi: 10.1007/s00410-006-0165-5

968 McGarvie DW (1984) Torfajökull : A volcano dominated by magma mixing. Geology 12:685–688.
969 doi: 10.1130/0091-7613(1984)12<685

970 McGarvie DW, Macdonald R, Pinkerton H (1990) Petrogenetic Evolution of the Torfajokull
971 Volcanic Complex , Iceland II . The Role of Magma Mixing. J Petrol 31:461–481

972 Meyer CJ, Anderson DH, Bradley JG (1974) Ion microprobe mass analysis of plagioclase from
973 “non-mare” lunar samples. Proc Fifth Lunar Conferece, (supplement 5, Geochemica
974 Cosmochim Acta) 1:685–706

975 Mørk MBE (1984a) Magma mixing in the post-glacial veidivötn fissure eruption, southeast
976 Iceland: a microprobe study of mineral and glass variations. Lithos 17:55–75. doi:
977 10.1016/0024-4937(84)90006-9

978 Mørk MBE (1984b) Magma mixing in the post-glacial veidivötn fissure eruption, southeast
979 Iceland: a microprobe study of mineral and glass variations. Lithos 17:55–75. doi:
980 10.1016/0024-4937(84)90006-9

981 Müller W, Shelley M, Miller P, Broude S (2009) Initial performance metrics of a new custom-
982 designed ArF excimer LA-ICPMS system coupled to a two-volume laser-ablation cell. J Anal
983 At Spectrom 24:209. doi: 10.1039/b805995k

984 Murphy MD, Sparks RSJ, Barclay J, et al (2000) Remobilization of Andesite Magma by Intrusion

985 of Ma c Magma at the Soufriere Hills Volcano, Montserrat, West Indies. J Petrol 41:21–42

986 Namur O, Charlier B, Toplis MJ, Vander Auwera J (2012) Prediction of plagioclase-melt equilibria
987 in anhydrous silicate melts at 1-atm. Contrib to Mineral Petrol 163:133–150. doi:
988 10.1007/s00410-011-0662-z

989 Neave D a, Maclennan J, Hartley ME, et al (2014) Crystal Storage and Transfer in Basaltic
990 Systems : the Skuggafjoll Eruption , Iceland. 55:2311–2346. doi: 10.1093/petrology/egu058

991 Neave DA, Buisman I, MacLennan J (2017) Continuous mush disaggregation during the long-
992 lasting Laki fissure eruption, Iceland. Am Mineral 102:2007–2021. doi: 10.2138/am-2017-
993 6015CCBY

994 Neave DA, Putirka KD (2017) A new clinopyroxene-liquid barometer, and implications for magma
995 storage pressures under Icelandic rift zones. Am Mineral 102:777–794. doi: 10.2138/am-
996 2017-5968

997 Nichols ARL, Carroll MR, Höskuldsson A (2002) Is the Iceland hot spot also wet? Evidence from
998 the water contents od undegassed submarin and subglacial pillow lavas. Epsl 202:77–87. doi:
999 Islande fluides

1000 O'nions RK, Pankhurst RJ, Gronvold K (1976) Nature and development of basalt magma sources
1001 beneath Iceland and the reykjanes ridge. J Petrol 17:315–338. doi:
1002 10.1093/petrology/17.3.315

1003 Orlando A, D'Orazio M, Armienti P, Borrini D (2008) Experimental determination of plagioclase
1004 and clinopyroxene crystal growth rates in an anhydrous trachybasalt from Mt Etna (Italy). Eur
1005 J Mineral 20:653–664. doi: 10.1127/0935-1221/2008/0020-1841

1006 Panjasawatwong Y, Danyushevsky L V., Crawford AJ, Harris KL (1995) An experimental study of
1007 the effects of melt composition on plagioclase-melt equilibria at 5 and 10 kbar: implications
1008 for the origin of magmatic high-An plagioclase. Contrib to Mineral Petrol 118:420–432. doi:
1009 10.1007/s004100050024

1010 Passmore E, Maclennan J, Fitton G, Thordarson T (2012) Mush disaggregation in basaltic magma
1011 chambers: Evidence from the ad 1783 Laki eruption. J Petrol 53:2593–2623. doi:
1012 10.1093/petrology/egs061

1013 Paterson SR, Okaya D, Memeti V, et al (2011) Magma addition and flux calculations of
1014 incrementally constructed magma chambers in continental margin arcs: Combined field,
1015 geochronologic, and thermal modeling studies. Geosphere 7:1439–1468. doi:
1016 10.1130/GES00696.1

1017 Perugini D, De Campos CP, Dingwell DB, Dorfman A (2013) Relaxation of concentration
1018 variance: A new tool to measure chemical element mobility during mixing of magmas. Chem
1019 Geol 335:8–23. doi: 10.1016/j.chemgeo.2012.10.050

1020 Perugini D, De Campos CP, Petrelli M, Dingwell DB (2015) Concentration variance decay during
1021 magma mixing: a volcanic chronometer. Sci Rep 5:14225. doi: 10.1038/srep14225

1022 Perugini D, Petrelli M, Poli G (2006) Diffusive fractionation of trace elements by chaotic mixing
1023 of magmas. Earth Planet Sci Lett 243:669–680. doi: 10.1016/j.epsl.2006.01.026

1024 Perugini D, Poli G (2005) Viscous fingering during replenishment of felsic magma chambers by
1025 continuous inputs of mafic magmas: Field evidence and fluid-mechanics experiments.
1026 Geology 33:5–8. doi: 10.1130/G21075.1

1027 Perugini D, Poli G, Mazzuoli R (2003) Chaotic advection, fractals and diffusion during mixing of
1028 magmas: Evidence from lava flows. J Volcanol Geotherm Res 124:255–279. doi:
1029 10.1016/S0377-0273(03)00098-2

1030 Perugini D, Ventura G, Petrelli M, Poli G (2004) Kinematic significance of morphological
1031 structures generated by mixing of magmas: A case study from Salina Island (southern Italy).
1032 Earth Planet Sci Lett 222:1051–1066. doi: 10.1016/j.epsl.2004.03.038

1033 Plail M, Barclay J, Humphreys MCS, et al (2014) Chapter 18 Characterization of mafic enclaves in
1034 the erupted products of Soufriere Hills Volcano, Montserrat, 2009 to 2010. Geol Soc London,
1035 Mem 39:343–360. doi: 10.1144/M39.18

1036 Plail M, Edmonds M, Woods AW, et al (2018) Mafic enclaves record syn-eruptive basalt intrusion
1037 and mixing. Earth Planet Sci Lett 484:30–40. doi: 10.1016/j.epsl.2017.11.033

1038 Putirka KD (2008) Thermometers and Barometers for Volcanic Systems. Rev Mineral
1039 Geochemistry 69:61–120. doi: 10.2138/rmg.2008.69.3

1040 Putirka KD (2005) Igneous thermometers and barometers based on plagioclase + liquid equilibria:
1041 Tests of some existing models and new calibrations. Am Mineral 90:336–346. doi:
1042 10.2138/am.2005.1449

1043 Renjith ML (2014) Micro-textures in plagioclase from 1994-1995 eruption, Barren Island Volcano:
1044 Evidence of dynamic magma plumbing system in the Andaman subduction zone. Geosci
1045 Front 5:113–126. doi: 10.1016/j.gsf.2013.03.006

1046 Rhodes JM, Dungan MA, Blanchard DP, Long PE (1979) Magma mixing at mid-ocean ridges:
1047 Evidence from basalts drilled near 22° N on the Mid-Atlantic Ridge. Tectonophysics 55:35–
1048 61. doi: 10.1016/0040-1951(79)90334-2

1049 Ridley IW, Perfit MR, Smith MC, Fornari DJ (2006) Magmatic processes in developing oceanic
1050 crust revealed in a cumulate xenolith collected at the East Pacific Rise, 9°50′N.
1051 Geochemistry, Geophys Geosystems 7:1–25. doi: 10.1029/2006GC001316

1052 Robie RA, Bethke PM, Beardsley KM (1967) Selected X-ray Crystallographic Data Molar
1053 Volumes, and Densities of Minerals and Related Substances. Geol Surv Bull 1248:

1054 Roeder PL, Emslie RF (1970) Olivine-liquid equilibrium. Contrib to Mineral Petrol 29:275–289.
1055 doi: 10.1007/BF00371276

1056 Ruprecht P, Bachmann O (2010) Pre-eruptive reheating during magma mixing at Quizapu volcano
1057 and the implications for the explosiveness of silicic arc volcanoes. Geology 38:919–922. doi:
1058 10.1130/G31110.1

1059 Ruprecht P, Bergantz GW, Cooper KM, Hildreth W (2012) The crustal magma storage system of
1060 volcán quizapu, chile, and the effects of magma mixing on magma diversity. J Petrol 53:801–
1061 840. doi: 10.1093/petrology/egs002

1062 Rutherford MJ, Devine JS (2003) Magmatic Conditions and Magma Ascent as Indicated by
1063 Hornblende Phase Equilibria and Reactions in the 1995-2002 Soufriere Hills Magma. J Petrol
1064 44:1433–1453. doi: 10.1093/petrology/44.8.1433

1065 Salaün A, Villemant B, Semet MP, Staudacher T (2010) Cannibalism of olivine-rich cumulate
1066 xenoliths during the 1998 eruption of Piton de la Fournaise (La Réunion hotspot):
1067 Implications for the generation of magma diversity. J Volcanol Geotherm Res 198:187–204.
1068 doi: 10.1016/j.jvolgeores.2010.08.022

1069 Schilling JG, Zajac M, Evans R, et al (1983) Petrologic and geochemical variations along the Mid-
1070 Atlantic Ridge from 29oN to 73oN. Am. J. Sci. 283:510–586

1071 Schindelin J, Arganda-Carreras I, Frise E, et al (2012) Fiji: An open source platform for biological
1072 image analysis. Nat Methods 9:676–682. doi: 10.1038/nmeth.2019.Fiji

1073 Shorttle O, Maclennan J (2011) Compositional trends of Icelandic basalts: Implications for short-
1074 length scale lithological heterogeneity in mantle plumes. Geochemistry, Geophys Geosystems
1075 12:. doi: 10.1029/2011GC003748

1076 Shorttle O, Maclennan J, Piotrowski AM (2013) Geochemical provincialism in the Iceland plume.
1077 Geochim Cosmochim Acta 122:363–397. doi: 10.1016/j.gca.2013.08.032

1078 Sigurdsson H, Sparks RSJ (1978) Rifting episode in north iceland in 1874-1875 and the eruptions
1079 of askja and sveinagja. Bull Volcanol 41:149–167. doi: 10.1007/BF02597219

1080 Singh SC, Kent GM, Collier JS, et al (1998) Melt to mush variations in crustal magma properties

1081 along the ridge crest at the southern East Pacific Rise. Nature 394:874–878. doi:
1082 10.1038/29740

1083 Smith VC, Blundy JD, Arce JL (2009) A temporal record of magma accumulation and evolution
1084 beneath Nevado de Toluca, Mexico, preserved in plagioclase phenocrysts. J Petrol 50:405–
1085 426. doi: 10.1093/petrology/egp005

1086 Soosalu H, Einarsson P (2004) Seismic constraints on magma chambers at Hekla and Torfajökull
1087 volcanoes, Iceland. Bull Volcanol 66:276–286. doi: 10.1007/s00445-003-0310-1

1088 Soosalu H, Lippitsch R, Einarsson P (2006) Low-frequency earthquakes at the Torfajökull
1089 volcano, south Iceland. J Volcanol Geotherm Res 153:187–199. doi:
1090 10.1016/j.jvolgeores.2005.10.012

1091 Sparks RSJ, Marshall LA (1986) Thermal and mechanical constraints on mixing between mafic
1092 and silicic magmas. J Volcanol Geotherm Res 29:99–124. doi: 10.1016/0377-
1093 0273(86)90041-7

1094 Sparks SRJ, Sigurdsson H, Wilson L (1977) Magma mixing: A mechanism for triggering acid
1095 explosive eruptions. Nature 267:315–318. doi: 10.1038/267315a0

1096 Stolper E, Walker D (1980) Melt density and the average composition of basalt. Contrib to Mineral
1097 Petrol 74:7–12. doi: 10.1007/BF00375484

1098 Tait SR, Jaupart C, Vergniolle S (1989) Pressure, gas content and eruption periodicity of a shallow
1099 crystallizing magma chamber [abs.]. Eos, Trans Am Geophys Union v. 69:1465. doi:
1100 10.1016/0012-821x(89)90025-3

1101 Tepley FJ, Davidson JP, Clynne M a (1999) Magmatic interactions as recorded in plagioclase
1102 phenocrysts of Chaos Crags, Lassen Volcanic Center, California. J Petrol 40:787–806. doi:
1103 10.1093/petrology/40.5.787

1104 Thirlwall MF, Upton BGJ, Jenkins C (1994) Interaction between Continental Lithosphere and the
1105 Iceland Plume — Sr-Nd-Pb Isotope Geochemistry of Tertiary Basalts, NE Greenland. J Petrol
1106 35:839–879

1107 Thomson A, Maclennan J (2013) The distribution of olivine compositions in icelandic basalts and
1108 picrites. J Petrol 54:745–768. doi: 10.1093/petrology/egs083

1109 Thordarson T, Larsen G (2007) Volcanism in Iceland in historical time: Volcano types, eruption
1110 styles and eruptive history. J Geodyn 43:118–152. doi: 10.1016/j.jog.2006.09.005

1111 Trønnes RG (2002) Geology and geodynamics of Iceland. Unpub Ms

1112 Tuffen H, McGarvie DW, Pinkerton H, et al (2008) An explosive - Intrusive subglacial rhyolite
1113 eruption at Dalakvisl, Torfajokull, Iceland. Bull Volcanol 70:841–860. doi: 10.1007/s00445-
1114 007-0174-x

1115 Ubide T, Gale C, Larrea P, et al (2014) The relevance of crystal transfer to magma mixing: A case
1116 study in composite dykes from the central pyrenees. J Petrol 55:1535–1559. doi:
1117 10.1093/petrology/egu033

1118 Vermeesch P (2004) How many grains are needed for a provenance study? Earth Planet Sci Lett
1119 224:441–451. doi: 10.1016/j.epsl.2004.05.037

1120 Viccaro M, Giacomoni PP, Ferlito C, Cristofolini R (2010) Dynamics of magma supply at Mt.
1121 Etna volcano (Southern Italy) as revealed by textural and compositional features of
1122 plagioclase phenocrysts. Lithos 116:77–91. doi: 10.1016/j.lithos.2009.12.012

1123 Walker GPL (1974) Eruptive Mechanisms in Iceland. In: Kristjansson L. (eds) Geodynamics of
1124 Iceland and the North Atlantic Area. NATO Advanced Study Institutes Series (Series C —
1125 Mathematical and Physical Sciences), vol 11. Springer, Dordrecht

1126 Wood BJ, Blundy JD (1997) A predictive model for rare earth element partitioning between
1127 clinopyroxene and anhydrous silicate melt. Contrib to Mineral Petrol 129:166–181. doi:
1128 10.1007/s004100050330

1129 Yang H-J, Kinzler RJ, Grove TL (1996) Experiments and models of anhydrous, basaltic olivine-
1130 plagioclase-augite saturated melts from 0.001 to 10 kbar. Contrib to Mineral Petrol 124:1–18.
1131 doi: 10.1007/s004100050169

1132 Zellmer GF, Rubin KH, Dulski P, et al (2011) Crystal growth during dike injection of MOR
1133 basaltic melts: Evidence from preservation of local Sr disequilibria in plagioclase. Contrib to
1134 Mineral Petrol 161:153–173. doi: 10.1007/s00410-010-0518-y

1135 Zellmer GF, Rubin KH, Gronvold K, Jurado-Chichay Z (2008) On the recent bimodal magmatic
1136 processes and their rates in the Torfajokull-Veidivotn area, Iceland. Earth Planet Sci Lett
1137 269:387–397. doi: DOI 10.1016/j.epsl.2008.02.026

1138 Zellmer GF, Sparks RSJ, Hawkesworth CJ, Wiedenbeck M (2003) Magma Emplacement and
1139 Remobilization Timescales Beneath Montserrat: Insights from Sr and Ba Zonation in
1140 Plagioclase Phenocrysts. J Petrol 44:1413–1431. doi: 10.1093/petrology/44.8.1413

1141

1142

1143

APPENDIX 1

Point counting method and raw results

Point counting was carried out in order to determine crystal phase proportions and vesicularity for each sample. Thin sections were mounted on a mechanical slide holder fixed to a petrographic microscope at a magnification of 4x and, when necessary, 10x and moved in steps of 0.3~0.5 mm in the x and y direction. 1000 points were counted for more aphyric samples whilst 1500 were counted for crystal rich samples. Size threshold was set at 150 μm, therefore crystals with long axes below this number were counted as groundmass. Crystal textures where not taken into account during point counting, with crystals only being discriminated in terms of mineral phases.

Sample	Point counting %				Mass fractions (%)		
	Ol	Cpx	Plg	Ves	Ol	Cpx	Plg
HRN-1	2.2	2.6	19.4	21.9	7.2	8.5	53.8
HRN-9	1.5	0.6	7.1	32.3	*4.8*	*1.9*	*19.7*
HRN-10	0	0	18.7	1.8	*0*	*0*	*52*
HRN-26 (b)	2.6	5.3	8.5	1.8	8.6	17.4	23.7
HRN-26 (r)	0	0	6.3	3.4	*0*	*0*	*17.5*
STU-6	2.9	8.7	25.6	37.8	3.6	10.6	27.4
FRO-1	0.4	2.9	10.2	25.6	0.5	3.9	11.5
NMS-2 (r)	0	0	12	3.0	*0*	*0*	*14.0*
NMS-2 (b1)	3.4	1.2	7.1	6.0	4.0	1.5	7.1
NMS-2 (b2)	2.1	3.1	8.1	3.8	2.7	4.1	9.1
NMS-5	0	0.8	13.3	5.4	*0*	*1.1*	*15.1*
NMS-6	0.4	0.6	9.9	3.9	*0.5*	*0.8*	*11.0*
LGH-4	0	0	28.9	25.0	*0*	*0*	*31.9*

Point counting results. Ol is olivine, Cpx is clinopyroxene and Plg is plagioclase. 1000 counts were counted for aphyric samples and 1500 for phyric samples. Mineral % was calculated from dense rock counts, vescicles % from total counts. (r) and (b) represent the rhyolitic and basaltic component of the samples when mafic enclaves are present.

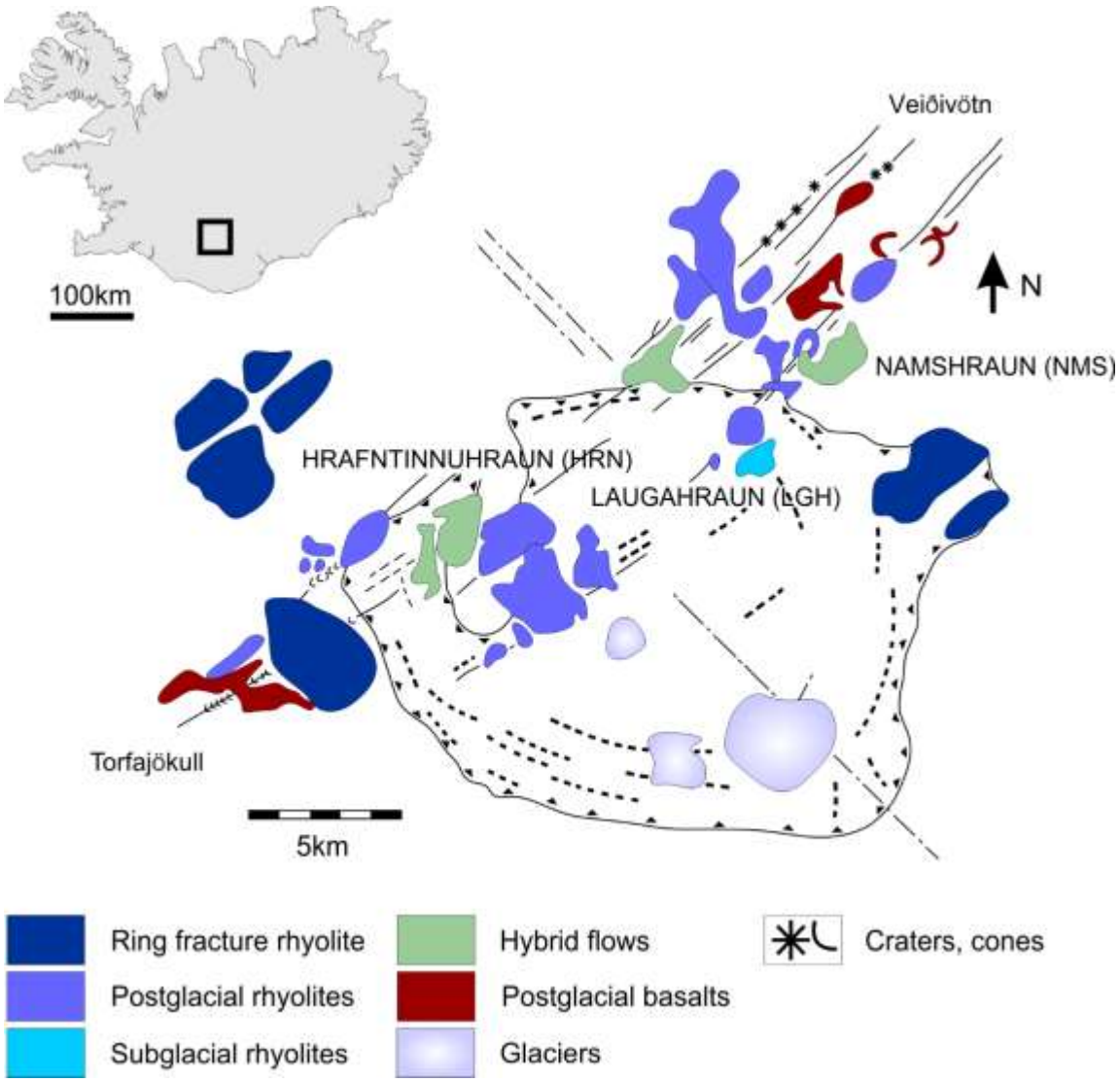

Fig. 1: simplified map of Iceland indicating the location of the Torfajökull and sketch geological map of Torfajökull highlighting the location of the erupted products and the name of the flows from the 871AD and 1477 eruptions (modified from Mcgarvie (1984)).

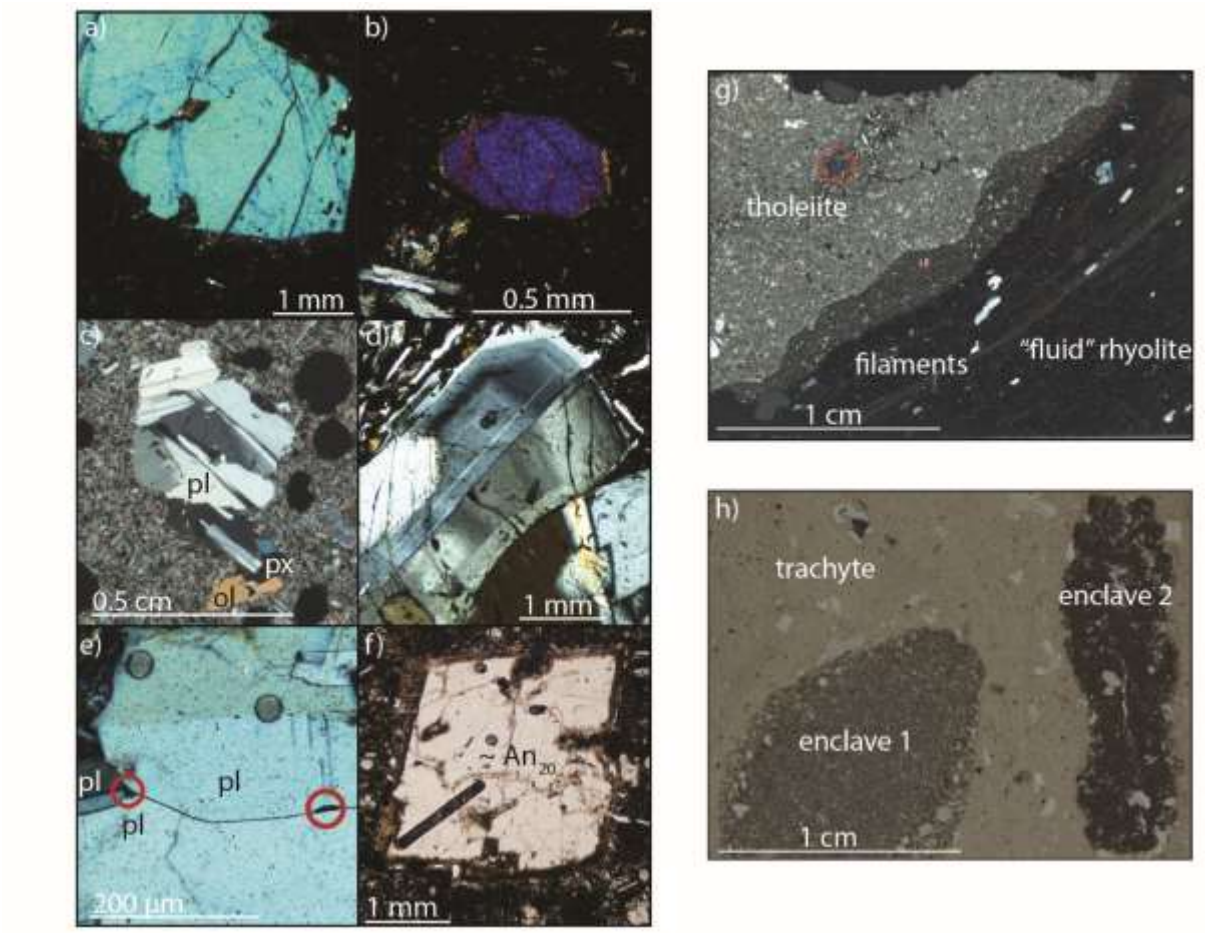

Fig. 2: a) olivine crystal showing embayments; b) clinopyroxene showing a thin disequilibrium rim; c) glomerophyric cluster composed of mostly plagioclase (pl) with minor olivine (ol) and clinopyroxene (px), hosted in a mafic groundmass; d) complex zoning in plagioclase; e) enlargement of c, pl-pl-pl and pl-pl junction; f) boxy shaped plagioclase hosted in a mafic groundmass showing abundant fine sieving at the crystal edge; g) xpl microphotograph of sample HRN-26, mafic enclave hosted in a glassy rhyolite from the 871AD eruption showing hybrid layers and filament structures. Red circle indicates the location of the xenocrystal low anorthite plagioclase from Fig. 2f; h) ppl microphotograph of NMS-2, a trachytic sample from the 1477 eruption hosting 2 different mafic enclave.

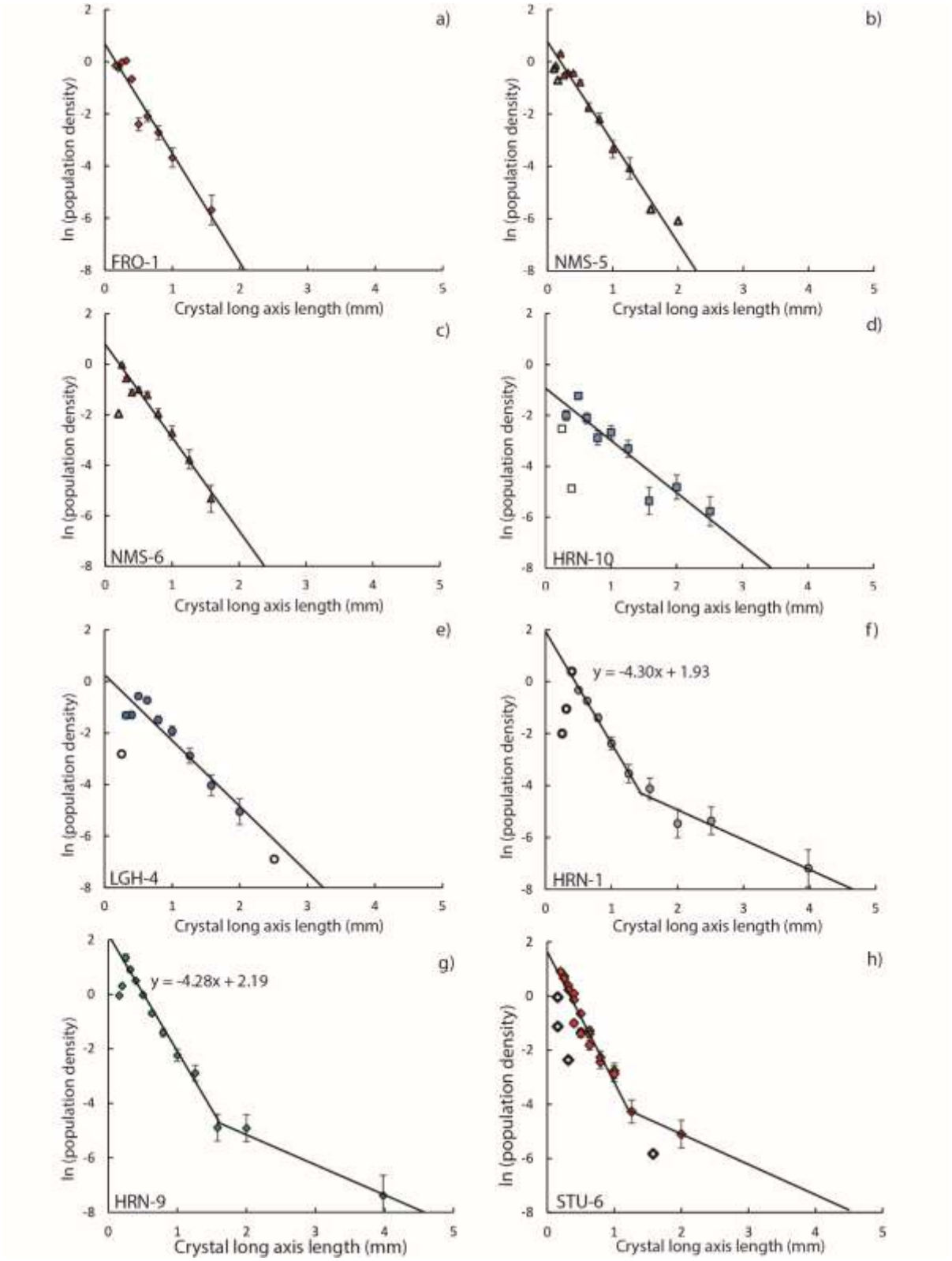

Fig. 3: CSD size distribution plots from the 871AD and 1477 eruptions. Plagioclase CSDs were calculated for the Torfajökull lavas using thin section photographs. Acquired size data using ImageJ (Schindelin et al. 2012) was then converted to true crystal size distribution using CSDCorrections (Higgins 2000, 2002).

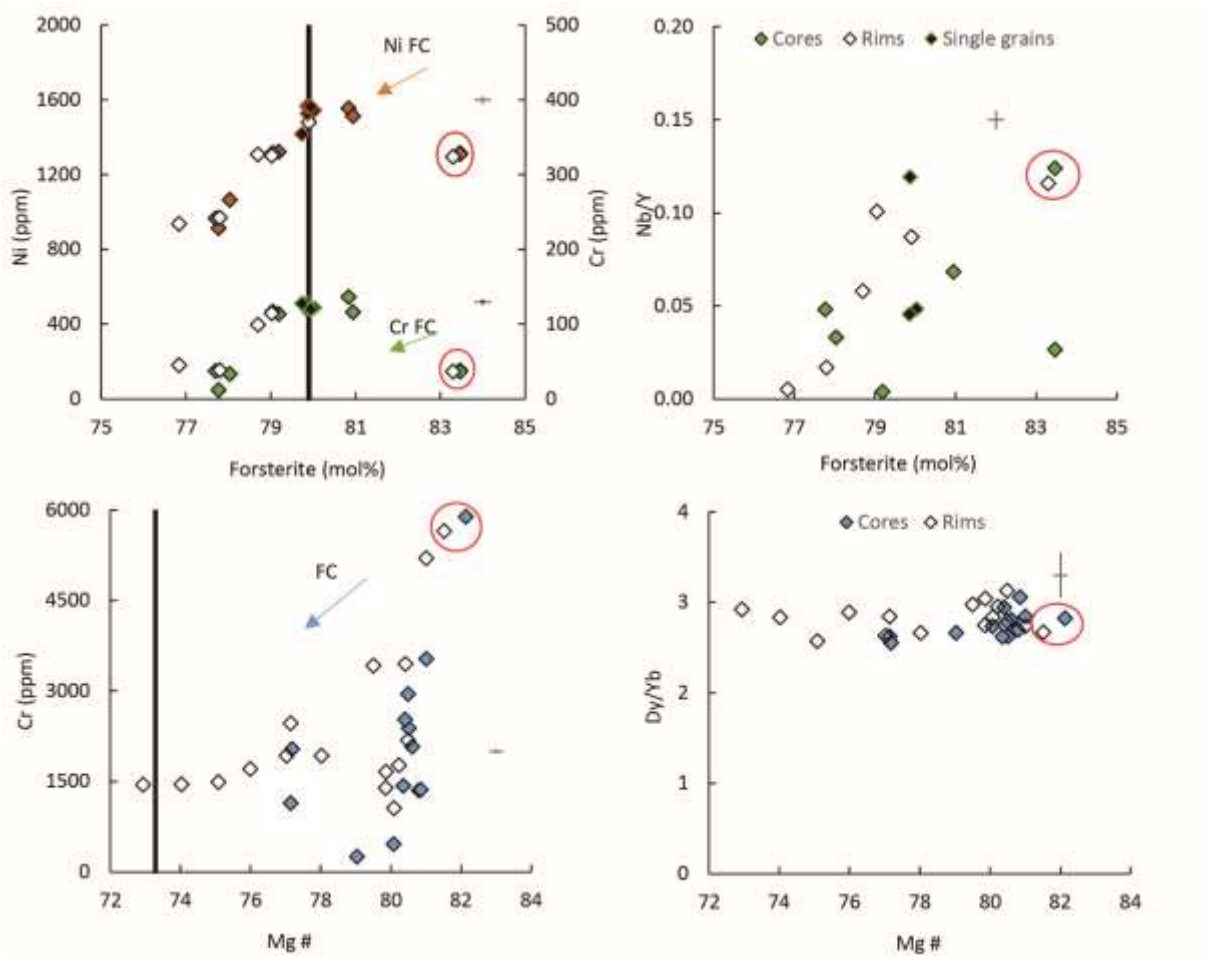

*Fig. 4: LA-ICP-MS analyses of olivine and clinopyroxene crystals hosted in sample HRN-1. Single grain analyses were carried out when the crystal was too small to accommodate two laser spots. Red circles indicate analysis of crystals hosted in the glomerophyric cluster. Black solid line is the calculated forsterite and Mg# (=100*atomic Mg/(Mg+Fe^{2+})) in equilibrium with the whole rock using a constant partitioning of Fe-Mg between olivine and liquid of 0.3 (Roeder and Emslie 1970) and equations by Wood and Blundy (1997). Errors are 2sd.*

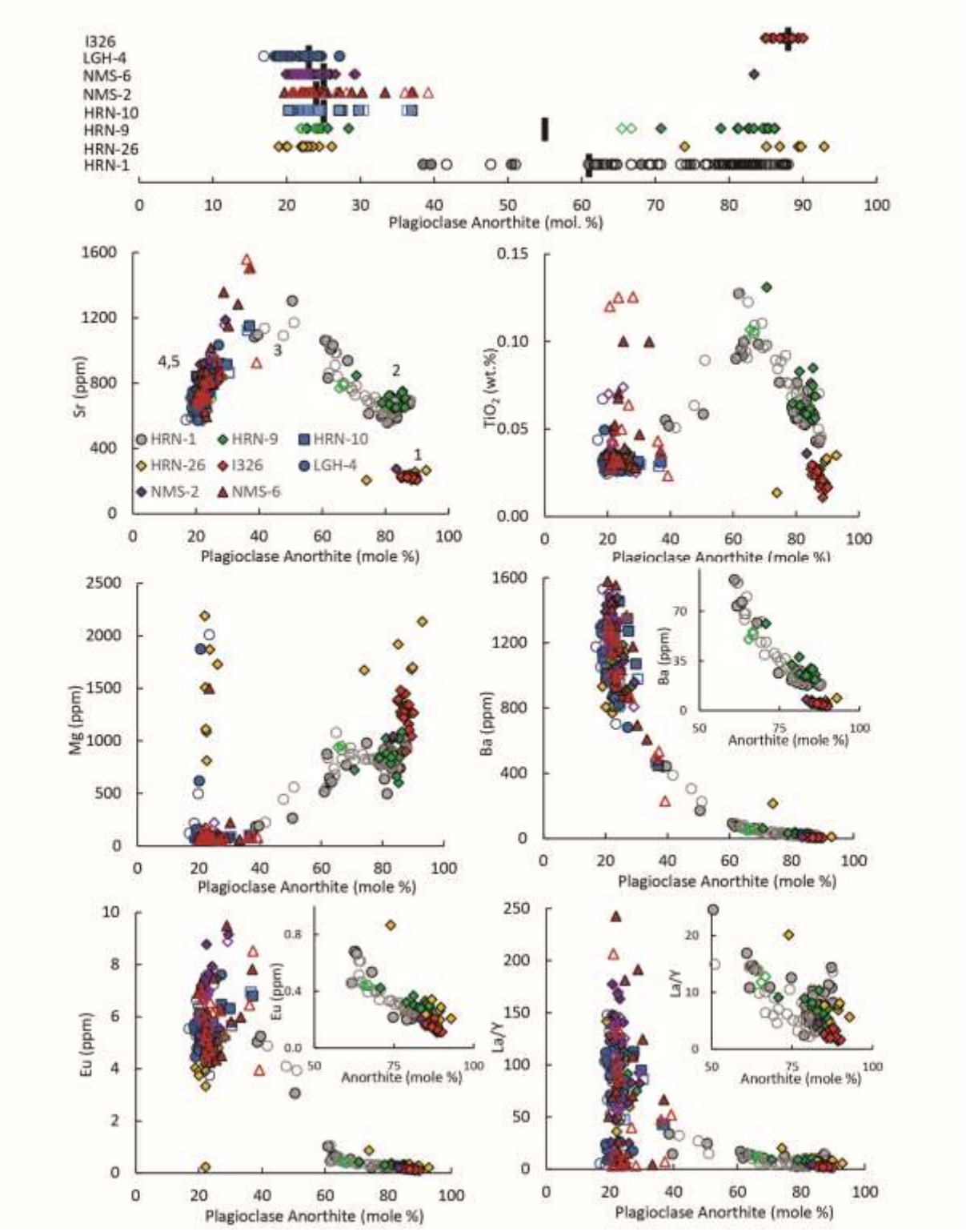

Fig. 5: LA-ICP-MS analyses for plagioclase crystals over a range of samples from the 1477 and 871AD eruptions. Black solid line is the calculated anorthite in equilibrium with the whole rock using the model by Namur et al. (2012). The tholeiitic sample I326 is a Veiðivötn basalt from Manning and Thirlwall (2014), plagioclase data is unpublished. Numbers 1-5 on the Sr vs An plot shows the geochemical range of the different populations. The 2sd error is smaller than the data points.

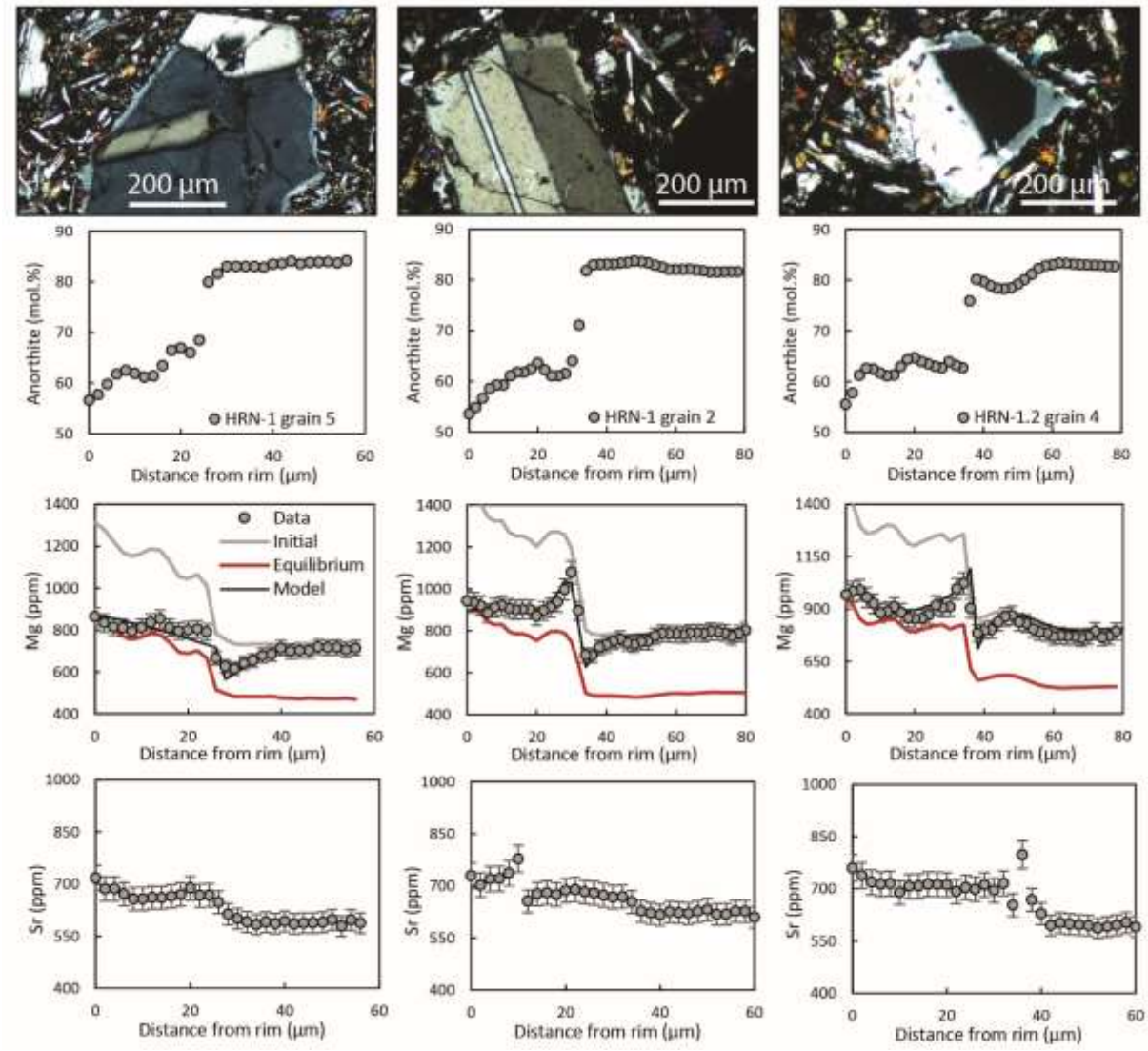

Fig. 6: SIMS analyses of plagioclase core to rim transects from the 871AD eruption. Grey dots are the data points, red lines the initial Mg profiles and grey lines the equilibrium profiles calculated using partition coefficients (Bindeman et al. 1998). Black solid line is the diffusion model calculated for Mg using the method by Costa et al. (2003).

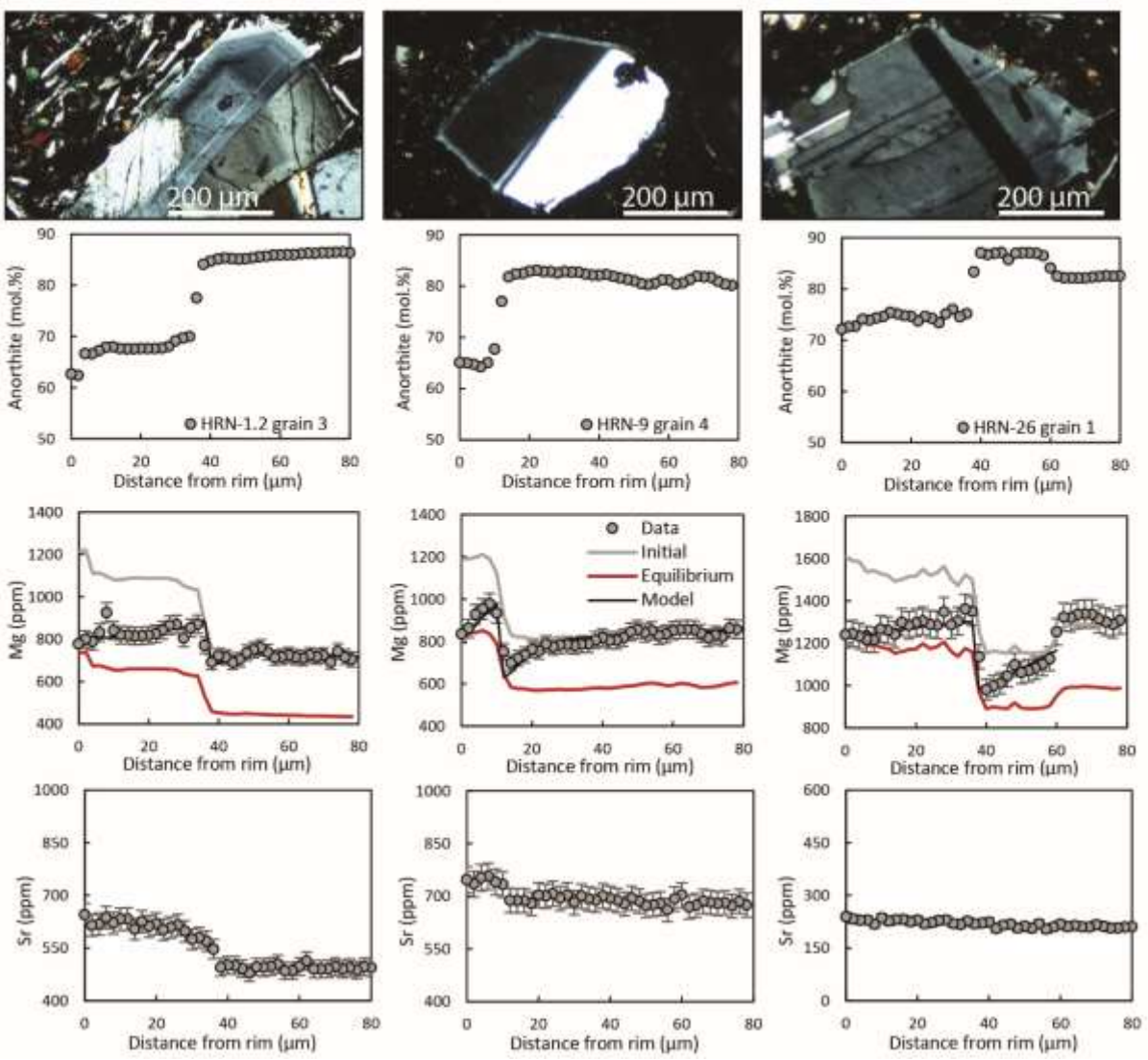

Fig. 6: continued

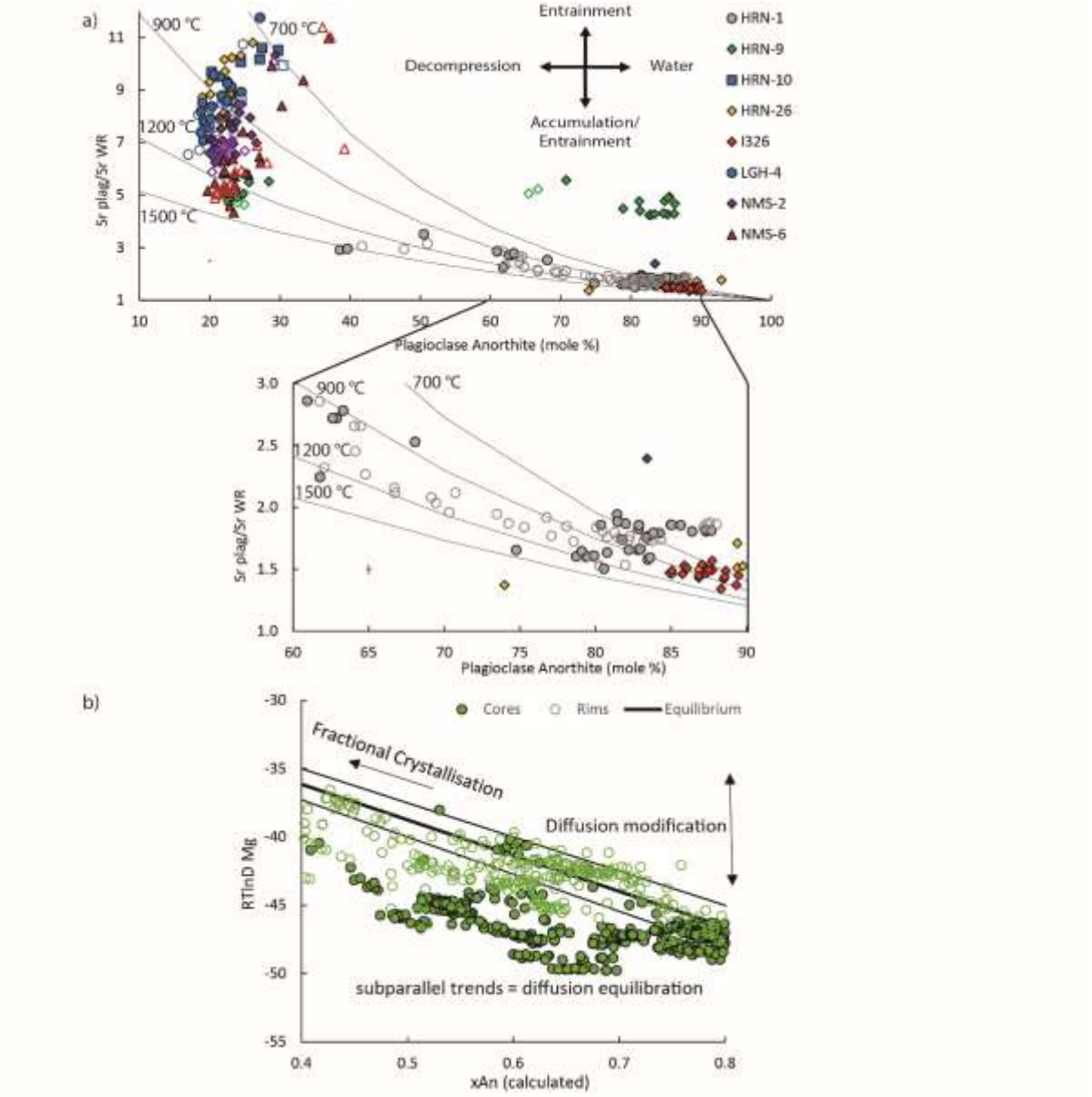

Fig. 7: a) Sr partition coefficients curved plotted against Anorthite (mol.%) and compared to LA-ICP-MS plagioclase data. Arrows indicate the likely displacement of the data caused by different magmatic processes or characteristics. The tholeiitic sample I326 is a Veiðivötn basalt from Manning and Thirlwall (2014), plagioclase data is unpublished. Error on partition curves is of 10% (Blundy and Wood 1991). b)Mg partitioning behaviour modelling (RTlnD Mg) (Bindeman et al. 1998) versus calculated xAn from plagioclase CaO (Zellmer 2003) highlighting the direction of fractional crystallisation and diffusion modification processes resulting in subparallel trends. Black lines are equilibrium trends with calculated errors. The model is only reliable for 0.4<xAn<0.8 (Bindeman et al. 1998).

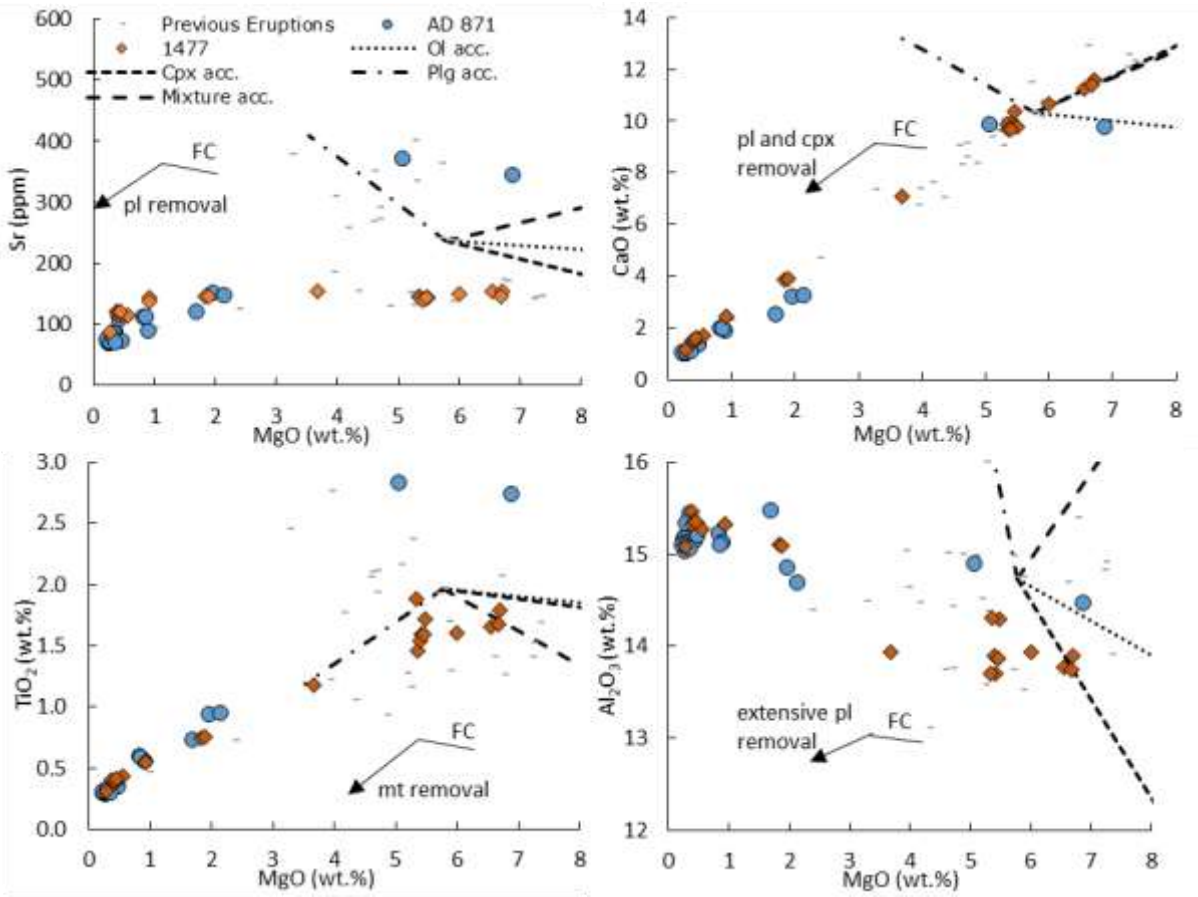

Fig. 8: Sr vs MgO, CaO vs MgO, TiO_2 vs MgO and Al_2O_3 vs MgO plots highlighting published whole rock data from the 871AD (blue) and 1477 (orange). Black lines indicate assimilation of up to 40% olivine, clinopyroxene, plagioclase and a pl+ol+cpx mixture. Fractional crystallisation trends arrows are also indicated (FC). Published data from Mcgarvie (1984), Macdonald et al. (1990), Mcgarvie et al. (1990).

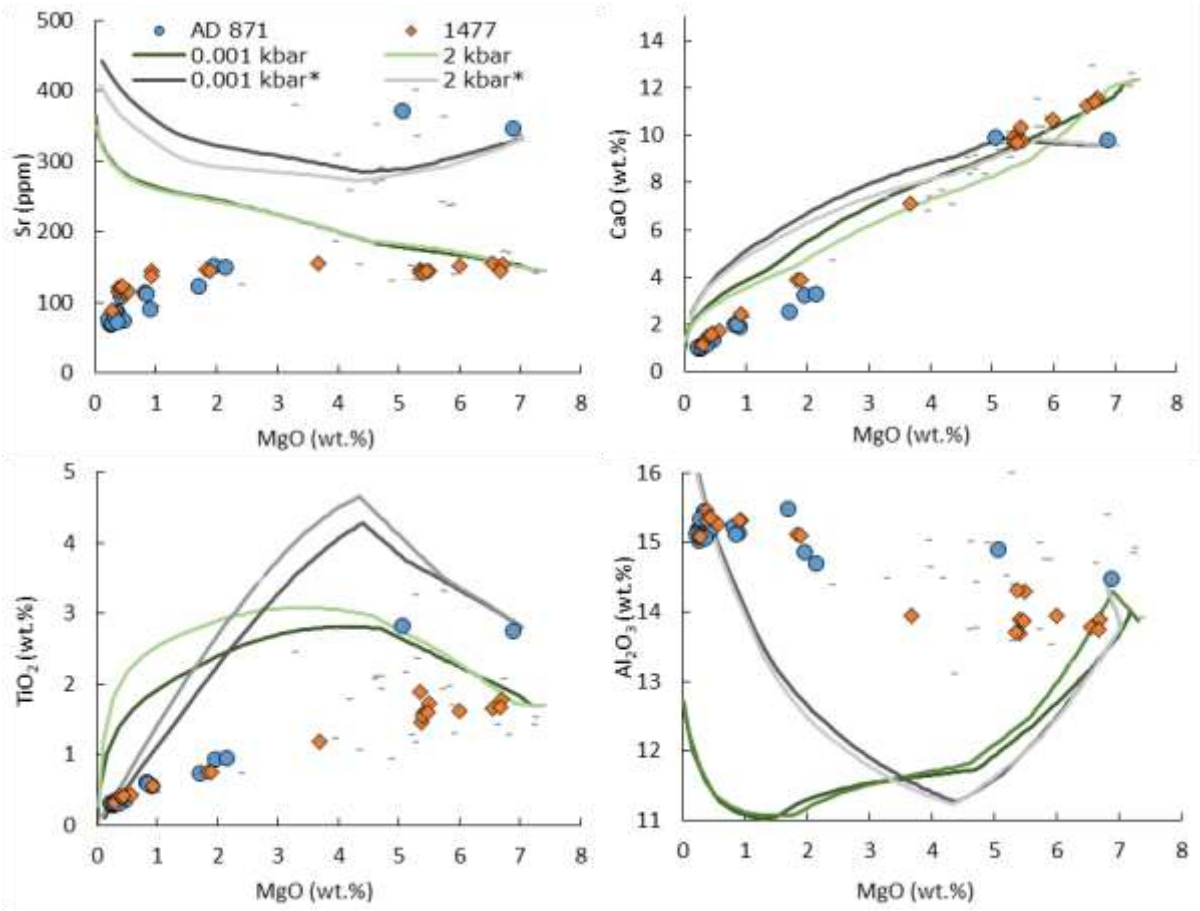

*Fig. 9: liquid line of descent (FC) models on Torfajökull Harker diagrams at 0.001 and 2 kbar (4 and 6 kbar not shown due to poor matches) with a melt MgO start composition of 7.34 wt.%, (tholeiite) and 6.88 wt.% (transitional basalt, marked with *) 100% fractionation of olivine, clinopyroxene, plagioclase and magnetite in 0.01% steps.*

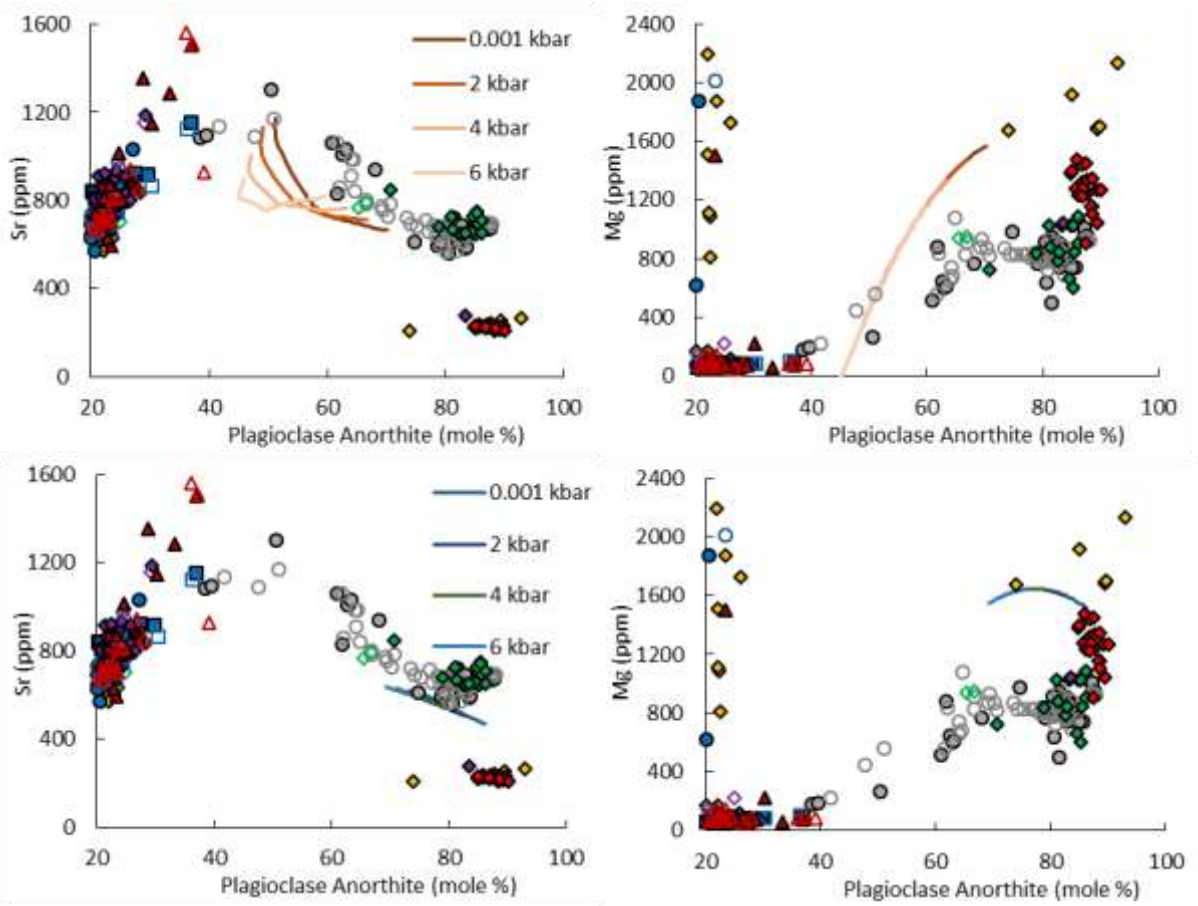

Fig. 10: equilibrium plagioclase compositions calculated during FC trajectories illustrated in Fig. 9. The top models are for whole rock basalt start composition used to reproduce the whole rock models MgO 7.34 wt.%, whilst the model at the bottom models evolution from a more primitive transitional basalt composition with MgO 9.06 wt.%. The Sr model used is that of Blundy and Wood (1991).

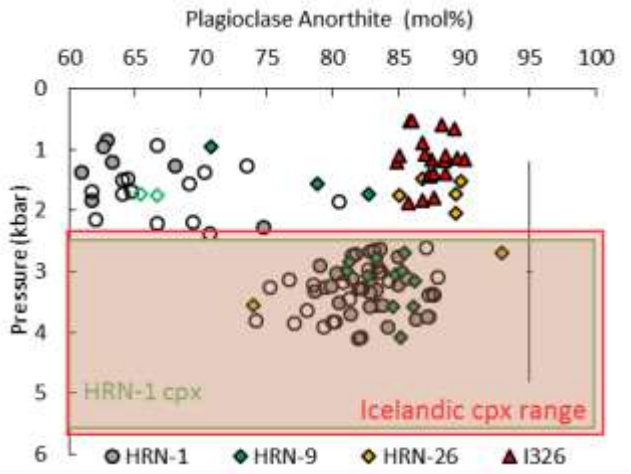

Fig. 11: modelled pressure of crystallisation plotted against plagioclase anorthite (mol.%) using the method by Putirka (2005, 2008), error is ~1.8 kbar. The tholeiitic sample I326 is a Veiðivötn basalt from Manning and Thirlwall (2014), plagioclase data is unpublished. The green field indicates the pressures calculated by HRN-1 clinopyroxene thermobarometry (Neave and Putirka 2017), the red field is the range of average clinopyroxene pressures calculated for a series of Icelandic samples (Neave and Putirka 2017).

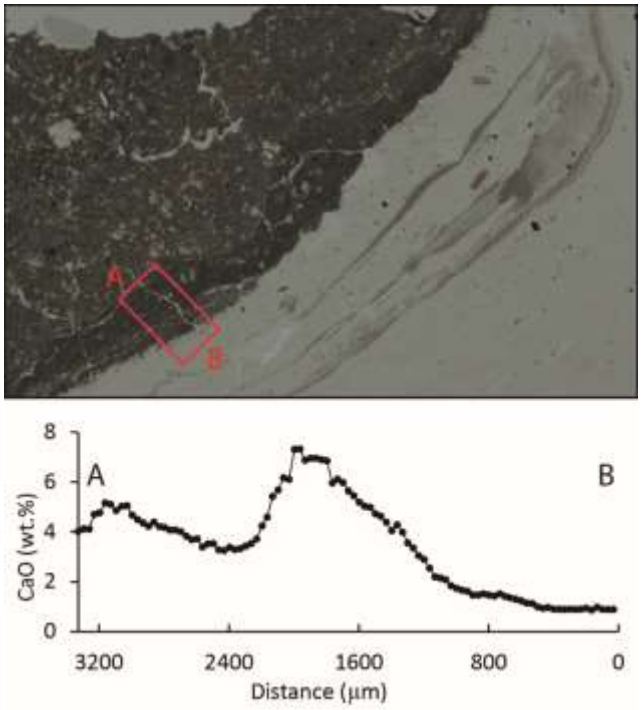

Fig. 12: LA-ICP-MS groundmass track across the hybrid layer, mafic enclave and rhyolite contact. The A-B profile location is represented by the red box.

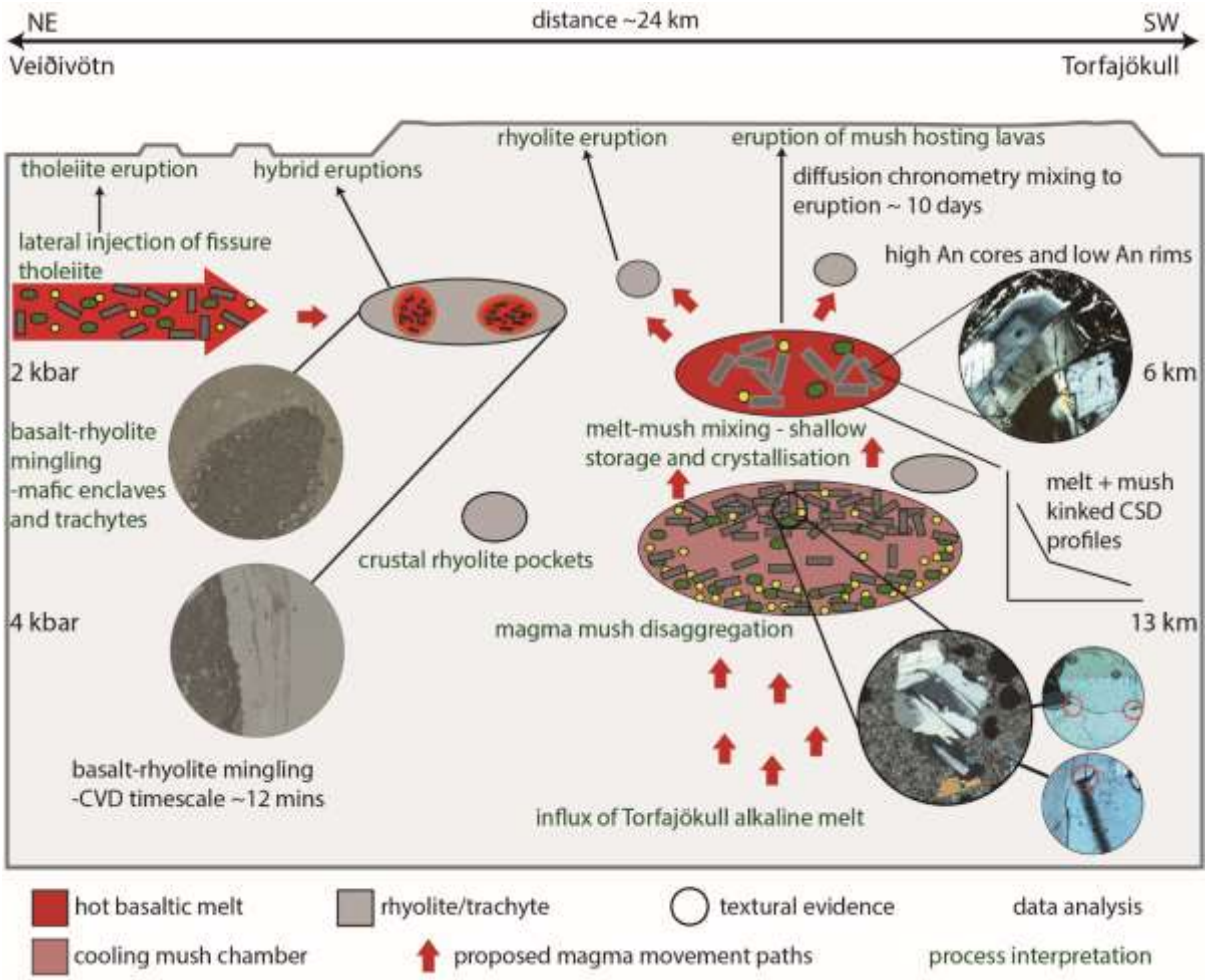

Fig. 13: schematic plumbing system model for Torfajökull reconstructed using the crystal cargo chemistry and macrotextures in this study.

Chapter 4

4. The effects of magma mixing, assimilation, ascent and amphibole fractionation on the crystal cargoes of arc magmas: a study from Salina, Aeolian Islands.

This chapter is presented in paper format and will be submitted to Contributions to Mineralogy and Petrology.

C.L. Imarisio wrote the manuscript, collected the samples plotted and interpreted the data. C.J. Manning contributed to the writing of the manuscript. C.L Imarisio and C.J. Manning analysed the samples at RHUL. F. Lucchi contributed to the manuscript providing additional samples, field and volcanological background. All the authors made suggestions and comments on the manuscript. Zoë Matthews carried out thin section binarisation for CSD analyses.

Supplementary Files are attached to the thesis.

Camilla L. Imarisio[1*]; Christina J. Manning[1]; Federico Lucchi[2]

The effects of magma mixing, assimilation, ascent and amphibole fractionation on the crystal cargoes of arc magmas: a study from Salina, Aeolian Islands.

[1]Department of Earth Sciences, Royal Holloway University of London, Egham Hill, TW20 0EX, UK.

[2]Dipartimento di Scienze Biologiche, Geologiche e Ambientali, Alma Mater Studiorum, Università di Bologna, Piazza di Porta S. Donato 1, 40126 Bologna, Italy.

*corresponding author: camilla.imarisio.2010@live.rhul.ac.uk;

Abstract

Magmas erupted at volcanic arcs rarely represent primitive geochemical signatures as they are subject to a variety of processes during ascent and storage in the crust where fractional crystallisation, magma mixing, storage conditions and crustal assimilation processes play a key role in the geochemical and textural development of arc magmas. The crystal cargoes of basalts, andesites and dacites from Salina, in the Aeolian Islands, have been utilised to better quantify and disentangle these processes. We show that Salina's magmas are affected by amphibole fractionation in basalts, which becomes a cryptic phase at more evolved composition, where it is present as breakdown anhydrous assemblages. As recorded by plagioclase and clinopyroxene, frequent magma mixing and recharge events affect both intermediate compositions at shallow depths and basaltic compositions deeper in the crust, where melts evolve prior to ascent to shallower levels. Evidence of solid crustal assimilation is present in the crystal cargoes under the form of disequilibrium glomerophyric clusters and gabbroic enclaves. Magma ascent and associated decompression also affects the composition of the cargo and suggest relatively slow ascent rates ~ 0.01-0.1m/s. These processes are shared to a different extent by all analysed samples, suggesting that the heterogeneity of crystal cargoes in Salina's magmas may represent the occurrence of mixing, assimilation and fractionation processes at different stages for the different samples.

Keywords

magma mixing; volcanic arc; crystal cargo; amphibole; petrology

INTRODUCTION

Shallow magmatic evolution at volcanic arcs

Magmas erupted at subduction zones are known to present explosive behaviour and a significant volcanic hazard (Davidson et al. 2007). Volcanic arcs form above subducted oceanic slabs (Tatsumi et al. 1989; Hawkesworth et al. 1993; Macdonald et al. 2000; Davidson et al. 2007) and their mechanism of magmagenesis involves the mantle wedge (Arculus and Wills 1980; Tatsumi et al. 1989), subducted sediments (e.g. Plank and Langmuir 1998 and references therein) and shallow crustal material (e.g. Davidson 1987; Macdonald et al. 2000). As a result, volcanism in volcanic arc environments is characterised by LILE enrichment relative to LREE and HFSE (e.g. Davidson 1987; Tatsumi et al. 1989; Hawkesworth et al. 1993; Macdonald et al. 2000), high oxidation states and increased water contents (e.g. Pearce and Peate 1995; Plank et al. 2013).

Primary magmas in arc settings are thought to pond and evolve in interconnected magma reservoirs systems within the crust at depths of ~20-30 km (Annen et al. 2006; Solano et al. 2012). Shallow chambers underlie volcanoes and host more evolved andesitic and dacitic magmas which are thought to evolve in the later stages of the island arc system, where crustal thickness reaches 20-25 km and enables magma ponding. The presence of shallow magma chambers has implications for shallow crustal magmatic evolution, which is subject to extensive fractional crystallisation of plagioclase-olivine-clinopyroxene–orthopyroxene–magnetite±amphibole. Extensive residence times in the crust also allow for frequent magma mixing and recharge event, crustal assimilation and contamination processes, and decompression and degassing (Grove and Kinzler 1986; Grove et al. 1988, 2002, 2003; Hildreth and Moorbath 1988; Rogers and Hawkesworth 1989; DePaolo et al. 1992; Annen et al. 2006; Solano et al. 2012). Primary mantle derived magmas in volcanic arcs range in composition from basaltic to magnesian-andesite, the latter suggested to generate in the upper mantle (Arculus and Wills 1980; Tatsumi et al. 1989), with variable water contents (e.g. Carmichael 2002; Grove et al. 2002). These primitive magmas are only a minor component of islands arcs. This is party due a density filtering of ascending magmas in the crust which promotes the presence of more evolved magmas (Annen et al. 2006; Solano et al. 2012), but also due to multiple shallow magma plumbing processes which affect the composition of the lavas erupted at the surface, as well as that of their crystal cargo.

The Aeolian volcanic arc and the island of Salina

The Aeolian Islands volcanoes have been active for 1.3 Ma (Lucchi et al. 2013). The Aeolian volcanic arc is comprised of seven volcanic islands, Alicudi, Filicudi, Salina, Lipari, Vulcano, Panarea and Stromboli, and several seamounts. An interplay between collision zone processes and an extensional regime caused by mantle upwelling is responsible for the large volcanological and structural variations found along the arc. The geochemical variability of incompatible trace elements

and radiogenic isotopes (Peccerillo et al. 2013) is currently attributed to the presence of a depleted mantle source (Francalanci et al. 1993; Peccerillo et al. 2013) which is modified by the addition of subducted components in the mantle wedge through hydrous fluids and silicate melts (Zamboni et al. 2016).

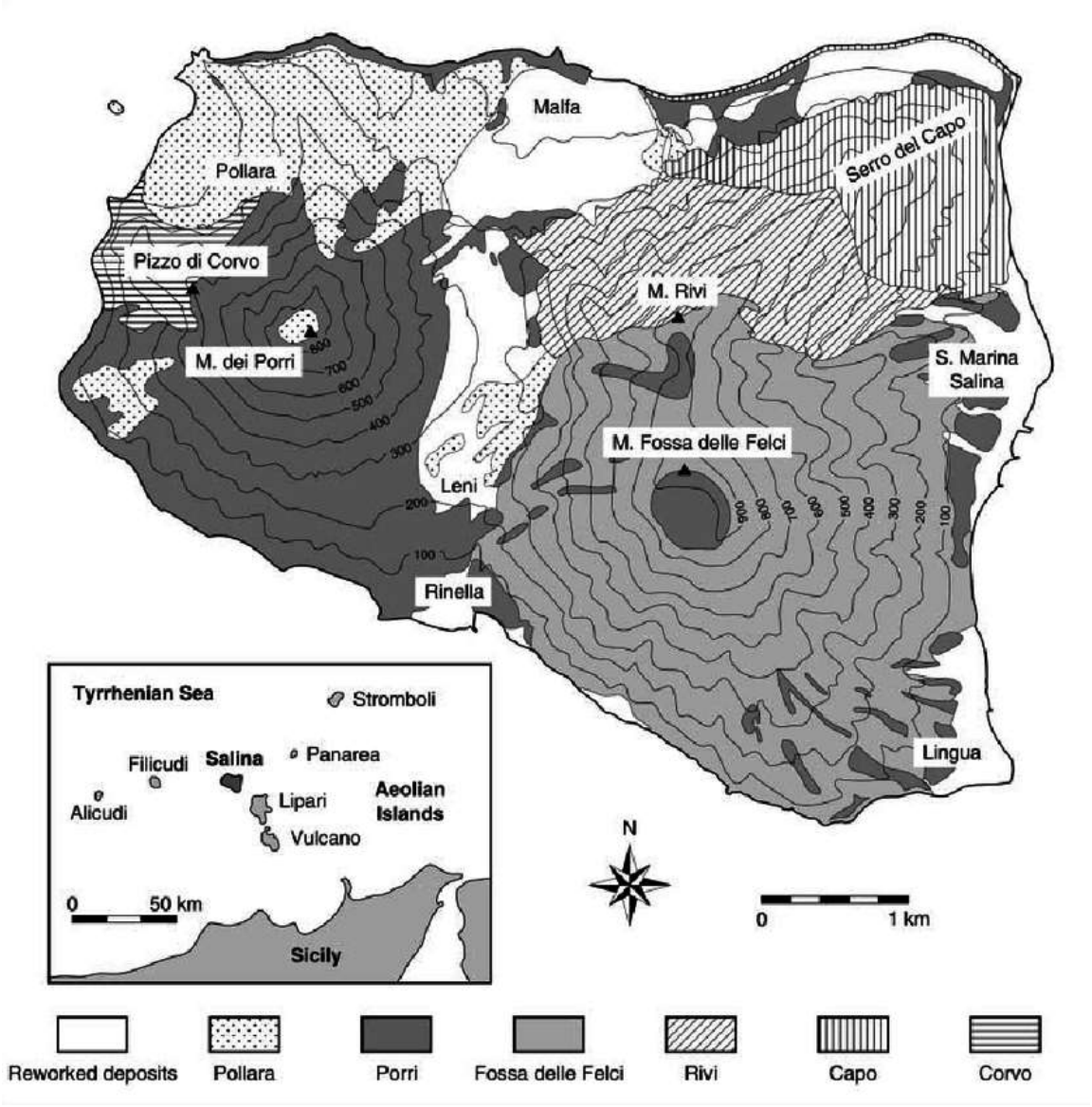

Figure 1: simplified location and sketch map of the island of Salina, highlighting the location of the main eruptive centres (from Gertisser and Keller 2000).

The island of Salina is located in northernmost part of the central sector of the archipelago along the NNW-SSE trending Tindari-Letojanni Fault System. The island is thought to have formed between ~244 and 15.6 ka (Lucchi et al. 2013) over 6 eruptive Epochs where a wide range of compositions from sub-alkaline basalts to rhyolites were erupted at the surface. Basalts are most common in the earliest stages of volcanism, whilst the latest eruptive episodes of the island see the appearance of more evolved compositions. Six volcanic centres, Corvo, Rivi, Capo, Fossa delle Felci, Porri and Pollara, show a progressive east to west shift of active vents which is also accompanied by an

evolution from calc-alkaline basalts and andesites to high-K dacites and rhyolites. Previous whole rock studies have attributed this largely to fractional crystallisation, magma mixing and mingling, and crustal assimilation processes (Calanchi et al. 1993; Gertisser and Keller 2000; Perugini et al. 2004; Lucchi et al. 2013). Extensive whole rock analyses have been carried out on the eruptive products of Salina (Ellam et al. 1989; Ellam and Harmon 1990; Calanchi et al. 1993; Gertisser and Keller 2000; Peccerillo et al. 2004; Lucchi et al. 2013). Trace elements patterns, normalised to primordial mantle (Sun and McDonough 1989), show enrichment of LILE relative to HREE and HFSE exhibiting a pattern typical of subduction related rocks (Ellam et al. 1989; Ellam and Harmon 1990; Gertisser and Keller 2000; Lucchi et al. 2013). Radiogenic isotope ratios have also been explored in detail. $^{87}Sr/^{86}Sr$ and $^{143}Nd/^{144}Nd$ show a negative correlation with ranges of 0.70409-0.70506 and 0.51267-0.51282 respectively and a systematic isotopic difference is observed with degree of evolution of the rocks. The highest radiogenic Sr ratios are found in the dacites and rhyolites of Epoch 6 whilst the lowest $^{87}Sr/^{86}Sr$ and highest $^{143}Nd/^{144}Nd$ is found in basalts and basaltic andesites. A large range in $^{208}Pb/^{204}Pb$ and $^{206}Pb/^{204}Pb$ is observed in Epochs 1-3 (Ellam et al. 1989; Ellam and Harmon 1990; Gertisser and Keller 2000; Lucchi et al. 2013) and $\delta^{18}O$ values have been found to be particularly elevated in andesites and dacites, showing an overall positive correlation with SiO_2 (Ellam et al. 1989; Ellam and Harmon 1990; Gertisser and Keller 2000; Lucchi et al. 2013). The wide ranges in magmatic compositions on Salina and their variation through time has been attributed, in previous studies, to a subduction modified mantle source and extensive polybaric fractional crystallisation processes involving olivine, clino- and orthopyroxene, plagioclase, oxides and amphibole. Magma mixing processes and crustal assimilation during storage and ascent in the crust have also been associated to the compositional variability, the latter largely influencing isotopic compositions (Ellam et al. 1989; Ellam and Harmon 1990; Gertisser and Keller 2000; Lucchi et al. 2013).

This paper presents a crystal cargo study aimed at the volcanic products affected by shallow magma plumbing system processes, in particular magma mixing and crustal assimilation. Whilst the suite of rocks present on Salina is large, here we focus on erupted andesites and dacites (common in Monte Fossa delle Felci) and the products of basalt-rhyolite mixing, present in the Pollara eruption.

Samples were collected during a field season in 2016 and consist of 13 crystalline lavas from the 4 latest eruptive Epochs of Salina, as classified by Lucchi et al. (2013). Where possible, efforts were made to collect from a fresh surface, to avoid flow fronts and possible areas of post eruption crystal accumulation and settling. A further 4 samples, whose outcrops could not be accessed, were donated by Federico Lucchi from the University of Bologna. Sample information are detailed in Table 1. Only four samples were selected for further textural and geochemical analyses. These are andesites and dacites from Epoch 4, and products of the Punta Fontanelle eruption in Epoch 6. This choice was made in order to focus this study on magma mixing and crustal assimilation processes.

SAMPLE COLLECTION

Sample	Epoch	Edifice	Formation	Age (ka)
MFF-2	3	Monte Fossa delle Felci	Vallone dei Zappini	~160-131
MFF-3	3	Monte Fossa delle Felci	Vallone dei Zappini	~160-131
MFF-1	3	Monte Fossa delle Felci	Caldara	~160-131
SAL-92*	4	Monte Fossa delle Felci	Falconiera	~147-121
SAL-64*	4	Monte Fossa delle Felci	Paolonoce	~147-121
MFF-8	4	Monte Fossa delle Felci	Serro Favarolo	~147-121
MP-1	5	Monte dei Porri	Punta di Megna	~70-57
RI-3	5	Monte dei Porri	Punta di Megna	~70-57
RI-4	5	Monte dei Porri	Punta di Megna	~70-57
RI-5	5	Monte dei Porri	Punta di Megna	~70-57
RI-7	5	Monte dei Porri	Punta di Megna	~70-57
RI-8	5	Monte dei Porri	Punta di Megna	~70-57
MFF-7	5	Monte dei Porri	Serra di Sciarato	~70-57
PO-1	5	Monte dei Porri	Serra di Sciarato	~70-57
MA-1	5	Monte dei Porri	Piano del Vescovo	~70-57
LP-7*	6	Pollara	Punta Fontanelle	~30-15.6
LP-12*	6	Pollara	Punta Fontanelle	~30-15.6

Table 1: Sample list for this study. Samples marked * were donated by Federico Lucchi. Information on eruptive Epoch, edifice, formation and age was retrieved from Lucchi et al. (2013). A comprehensive database of whole rock data retrieved from the literature can be found in Supplementary data file 1. A map and GPS location of the sample is also included in the supplementary files.

ANALYTICAL METHODS

Whole-rock samples presented in table 1 were analysed by XRF (X-Ray Fluorescence) at Royal Holloway University of London using the method by Thirlwall et al. (2000). Major elements were analysed on glass fusion disc where ~0.7g of rock powder was ignited at 1100 °C to determine LOI (loss on ignition) then fused with a lithium tetraborate flux at a 1:6 sample to flux ratio. Trace elements were analysed on pressed powder pellets made using a polyvinyl alcohol binder solution and pressed in an aluminium cup using a hydraulic press at 0.6 tons/cm^2. The analyses were carried out on a PANalytical Axios sequential X-ray fluorescence spectrometer with a 4kW Rh-anode X-ray tube.

Single grain core and rim analyses were performed *insitu* on thin sections by LA-ICP-MS at Royal Holloway University using a Resonetics 193nm ArF excimer laser coupled to an Agilent 8900 ICP-QQQ ICPMS. External standards for anorthite and labradorite (NMNH 137041, NMNH 115900), and chromium augite (NMNH 164905) were used to normalise major element data, which was corrected using correlations generated from electron microprobe data and stoichiometric relationships resulting in a 100% total. NIST glass 612 (Jarosewich 2002) was run alongside the samples to normalise trace element concentrations (Thirlwall and Manning, in prep).

Analyses were carried out using the following ICP-MS and laser parameters (Table 2):

ICPMS- Agilent 8900 ICP-QQQ	
RF power	1280-1320 (optimised during tuning)
Carrier gas flow	~0.5 ml/min (optimised during tuning)
Coolant gas flow	15 l/min
Aux gas flow	1 l/min
Sampler/skimmer cones	Ni
Extraction lenses	ce
Laser ablation system	
Energy density (fluence) on target	27mj/cm^2
ThO+/Th+	~0.2%
He gas flow	850 ml/min
N2 gas flow	6 ml/min
Laser repetition rate	5Hz (cpx) 8Hz (plag)
Spot size	57 μm (plag, cpx)

Table 2: Laser and ICP-MS run parameters

RESULTS

Whole Rock Chemistry and Petrology

The Salina volcanic suite spans a wide range of compositions, basalts - basaltic andesites - andesites - dacites. Whole rock major and trace element compositions are shown in Figure 2 alongside published datasets for the island of Salina from Supplementary Data file 1 (Ellam et al. 1989; Ellam and Harmon 1990; Gertisser and Keller 2000; Lucchi et al. 2013). Samples from Salina show SiO_2 content that ranges from 49.3 to 71.6 wt.%, and correlates strongly with K_2O to produce a continuous calc-alkaline to high-K calc-alkaline series (Figure 2). Overall, the range of erupted products increases in evolution with Epochs, with the older products showing less compositional variability than the youngest products. This is consistent with island arcs' volcanic and tectonic evolution, and the development of shallow crustal reservoirs with time.

Analyses from this study lie within the same range as published data from the same eruptive units and exhibit strong correlations between SiO_2 and most major and trace elements. Strong correlations are observed between SiO_2 and other major elements. MgO shows a steep decreasing trend with increasing SiO_2 followed by a shallower trend, whilst Al_2O_3 and TiO_2 show an initial steep increase with increasing SiO_2 followed by a decreasing trend, consistent with the onset of plagioclase and magnetite crystallisation respectively. Similar trends are observed in whole rock trace elements where increasing SiO_2 is associated with a sharp decrease in Ni concentration and a constant decrease in Sr concentrations (Figure 3). Incompatible trace elements such as Zr increase with increasing SiO_2 (Figure 3) but large variations are observed for incompatible trace elements ratios with decreasing SiO_2. La/Yb ratios show an overall increase with increasing SiO_2 whilst Dy/Yb ratios show an opposite trend decreasing with increasing SiO_2.

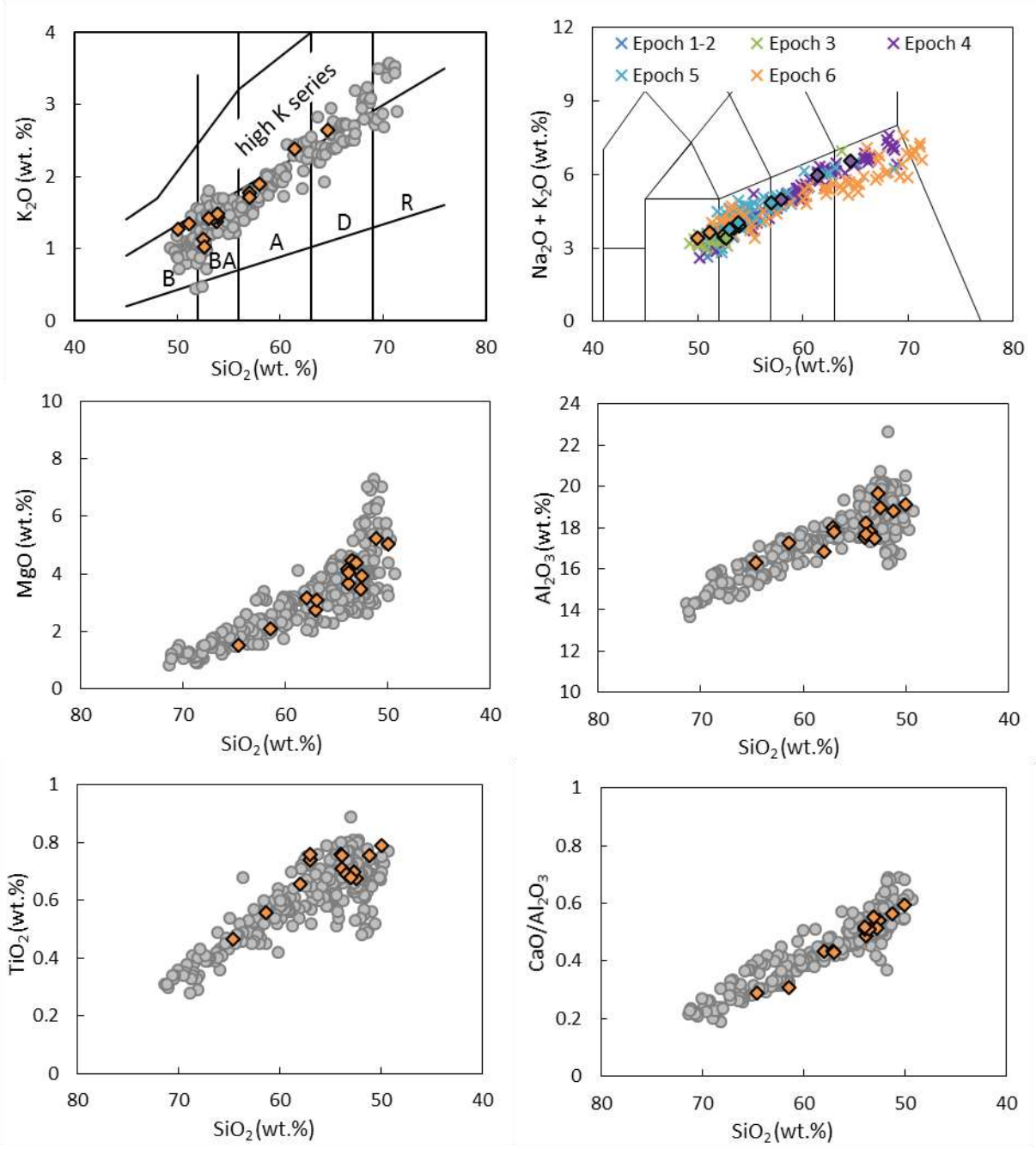

Figure 2: whole rock classification and major elements variations within the Salina volcanic suite. Grey circles are representative of previously published datasets (compiled by Lucchi et al. (2013)) – Supplementary Data file 1, and the orange diamonds represent the samples collected for this study as presented in table 1. Total Alkali Silica (TAS) diagram shows the range of composition observed across the different eruptive Epochs. Crosses indicate previously published data whilst rimmed diamonds are the samples from this study, which lie in the same ranges as those of previously published data. Error is smaller than data point.

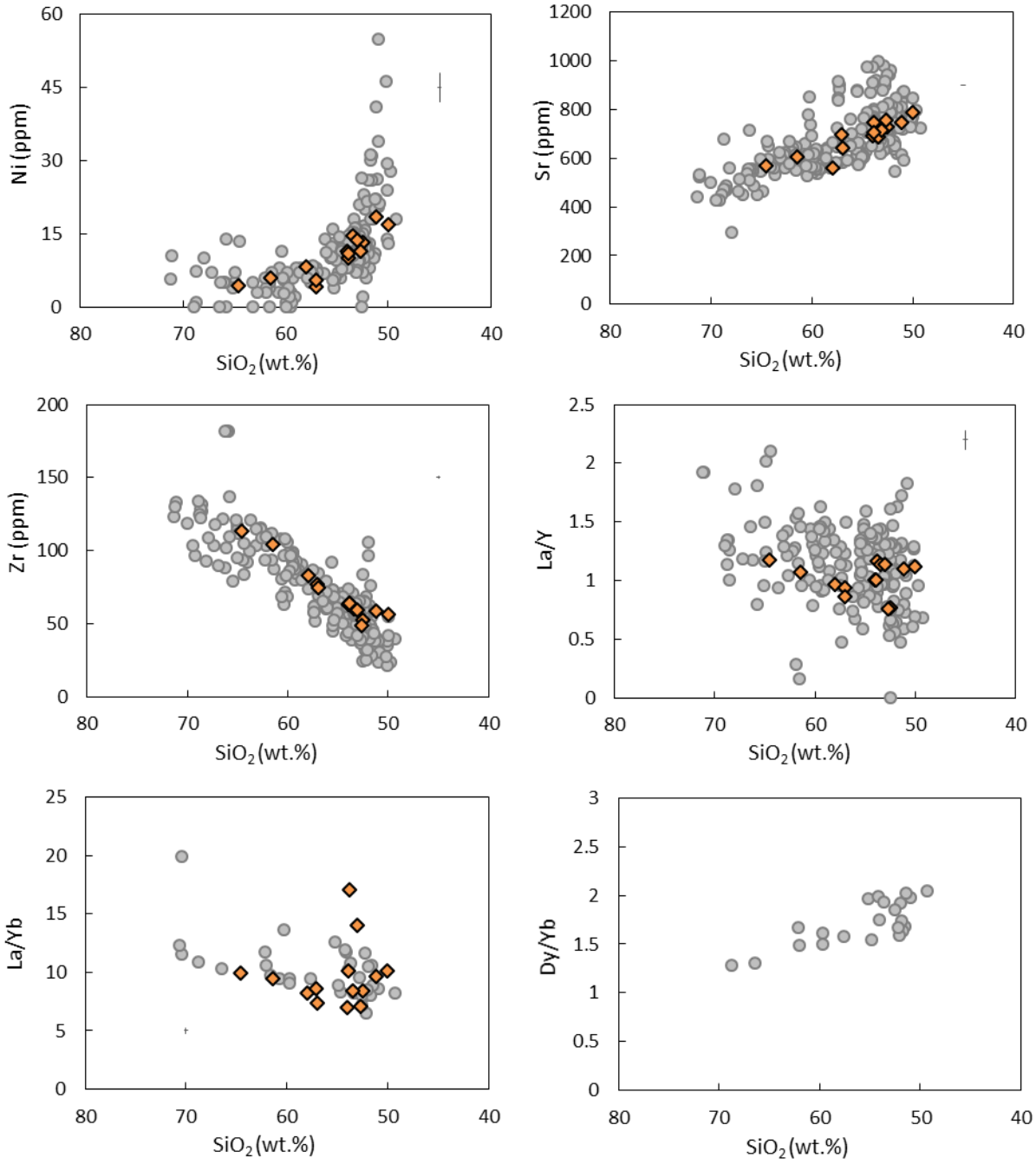

Figure 3: whole rock trace elements variations within the Salina volcanic suite. Grey circles are representative of previously published datasets (compiled by Lucchi et al. (2013)) – Supplementary Data file 1, and the orange diamonds represent the samples collected for this study as presented in Table 1.

Mineralogy

Basaltic samples (LP-7 and LP-12), a scoria and grey juvenile from Punta Fontanelle (Lower Pollara, Epoch 6 (Lucchi et al. 2013)), contain assemblages of olivine, clinopyroxene and plagioclase phenocrysts hosted in a fine-grained groundmass, with total crystallinity of 45% (Table 3). Crystal sizes in the both samples range from ~0.5 mm in olivine and 0.1-1 mm in clinopyroxene and plagioclase. Large clinopyroxene crystals (10-13%) are typically euhedral and sometimes show

minor normal zoning (Figure 4 a) whilst smaller crystals can show embayed edges. Plagioclase crystals are abundant (24-25%) and often show coarsely sieved cores (Figure 4 b). Zoning patterns vary considerably from minor zoning towards the rim to complex zoning patterns in larger plagioclase crystals (Figure 4 b), including oscillatory zoning. Oxides are common (up to 3%) and often present in ~0.5mm crystal clots comprising small (~0.1-0.2mm) plagioclase and clinopyroxene crystals ± olivines and oxides. In addition to this, LP-12 presents lower vesicularity than LP-7 (4% compared to 16%) and higher abundance of green amphiboles (~7%) up to 1.5 mm in length (Figure 4 c). In LP-12 the amphiboles are euhedral and display no or little sign of disequilibrium as reaction rims are either <14μm or not present (Figure 4 c). In sample LP-7 the amphiboles are smaller, less abundant and display a black opacitic reaction rim ~50 μm (Figure 5-LP-7). In contrast to LP-12, LP-7 amphiboles are found in glomerophyric clusters together with coarse sieved plagioclase crystals (Figure 5 LP-7 and LP-12).

Basaltic andesites present similar petrological characteristics of those of the basalts, but have more abundant (up to ~40%) plagioclase, and less abundant clinopyroxene and olivine (~5% and ~3%, respectively) (Table 3). Minerals are mostly present as large euhedral to subhedral crystals. Some basaltic andesites also show minor orthopyroxene (~2%) and high vesicularity ~17%, alongside olivines showing large dissolution and disequilibrium textures (Figure 4 d). These are less porphyritic with crystallinity ranging from 21% to 50%.

Andesites are plagioclase rich (29-34%) and have no or very low vesicularity, with crystallinity ranging from 32-47% (Table 3). Plagioclase crystals range from 0.5 to 3.4 mm in size and exhibit occasional reverse zoning towards the crystal edge (Figure 4 h). Plagioclase textures vary between samples, from euhedral crystals with minimal resorption textures (MFF-8, Figure 4 f) to crystals with completely resorbed cores (SAL-64, Figure 4 e). The abundance of clinopyroxene within the andesitic samples is low and crystals are often small, with MFF-8 showing the highest abundance and largest crystal sizes (8% and ~1.4 mm, respectively) which also show embayed edges (Figure 4 g, h).

Dacite SAL-92 (Falconiera, Epoch 4 (Lucchi et al. 2013)) has no vesicularity and high plagioclase abundance (~15%) Total crystallinity is lower compared to other samples, at 21% (Table 3). Plagioclase is present both as ~0.2-2 mm elongated laths or more boxy-shaped crystals. Plagioclase often presents coarse sieves (Figure 4 h) and embayed edges. Fresher rims are present around the sieved cores and zoning is sometimes visible (Figure 4 h). Smaller plagioclase crystals ~0.1mm are fresh and show no sieves, although some show a thin zone at the crystal edge. Clinopyroxene crystals up to 1.4 mm in size are present in small amounts (4%) and whilst most are unzoned, some show disequilibrium textures (Figure 4 i) and a thin rim at the crystal edge (Figure 4 h).

Crystal clots and enclaves

Sample LP-12 (Epoch 6 basalt) also presents a gabbroic enclave ~1 cm in size mostly composed of plagioclase and clinopyroxene. The boundary between the enclave and the host rock is sharp and the crystals on the edge of the enclave present embayed edges and poorer subhedral shapes (Figure 5).

SAL-64 (andesite) contains large ~0.5mm glomerophyric clots composed of mainly plagioclase with minor clinopyroxenes and oxides (Figure 4 g, Figure 5). Plagioclase clots are also present in MFF-8 but are less common and comprise of bigger ~0.2mm plagioclase crystals often showing oscillatory zoning. Olivine is sometimes present as a minor phase <1% and displays disequilibrium textures (Figure 5).

SAL-92 contains glomerophyric clusters ~0.5mm in size and mostly composed of plagioclase crystals with clinopyroxene and oxides (Figure 5). Glomerocrysts of intensively sieved large plagioclase crystals are also present (Figure 5).

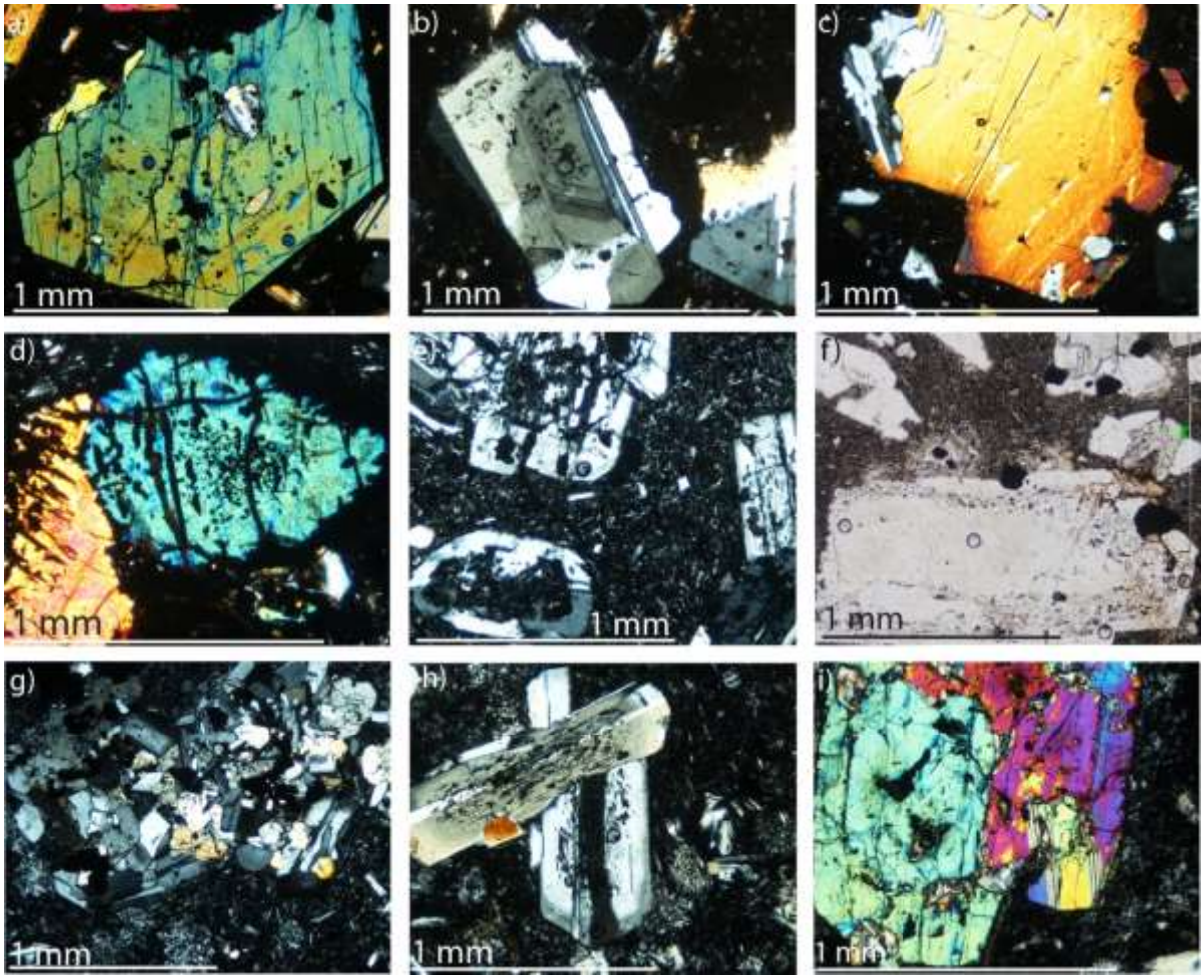

Figure 4: microphotographs of lavas from Salina (xpl, except f which is in ppl): a) large euhedral broken clinopyroxene crystal, b) zoned plagioclase with moderate coarse sieving, c) amphibole, d) disequilibrium olivine, e) coarse sieving and resorped cores in plagioclase, f) fine sieving in

plagioclase, g) glomerocryst of plagioclase, clinopyroxene and oxides, h) coarse sieving in plagioclase with fresh crystal rims, i) disequilibrium clinopyroxene crystals.

Point counting results for selected samples are shown in Table 3.

Mineral abundance and vesicularity from point counts (%)									
Sample	**Ol**	**Cpx**	**Opx**	**Plag**	**Oxide**	**Hb**	**Bi**	**Vs**	**Gmass**
MFF-2 (ba)	3	4	0	26	2	0	0	14	51
MFF-3 (ba)	3	4	0	31	2	0	0	14	46
MFF-1 (ba)	3	5	0	29	2	0	0	16	46
SAL-92 (d)	0	4	0	15	3	0	0	0	78
SAL-64 (a)	1	4	0	29	2	0	0	0	64
MFF-8 (a)	1	8	0	34	3	0	0	2	52
MP-1 (ba)	3	5	0	39	3	0	0	12	38
RI-3 (ba)	2	5	2	27	3	0	0	17	45
RI-4 (ba)	3	5	0	40	3	0	0	13	36
RI-5 (ba)	3	5	0	38	2	0	0	13	40
RI-7 (ba)	3	5	0	40	3	0	0	14	36
RI-8 (ba)	2	4	1	29	3	0	0	17	43
MFF-7 (ba)	3	5	0	30	2	0	0	17	43
PO-1 (a)	1	8	0	35	3	0	0	0	54
MA-1 (a)	0	3	0	27	2	0	0	14	54
LP-7 (b)	4	13	0	24	3	1	0	16	39
LP-12 (b)	1	10	0	25	3	7	0	4	51

Table 3: point counting results for a range of samples from the Salina volcanic suite. Abbreviations are as follows: ol, olivine; cpx, clinopyroxene; opx, orthopyroxene; plag, plagioclase; hb, hornblende; bi, biotite; vs, vesicle; gmass, groundmass. Next to sample name, in brackets, is the rock type: b, basalt; ba, basalt andesite; a, andesite; d, dacite; r, rhyolite. All values are calculated % from 1500 point counts per slide (not dense rock equivalent).

Crystal Size Distribution

Crystal size distributions (CSDs) for four selected samples, amphibole bearing basalt (LP-12), andesites (MFF-8 and SAL-64), and dacite SAL-92, (Figure 6) were calculated using thin section maps, assumed to be representative of the whole sample. Plagioclase and clinopyroxene size data was acquired using ImageJ (Schindelin et al. 2012) and converted to true crystal size distribution using CSDCorrections (Higgins 2000b, 2002a).

Epoch 4 dacitic and andesitic samples SAL-64, SAL-92 and MFF-8 show similar CSDs trends for both plagioclase and clinopyroxene (Figure 6). The CSD profile is “kinked” in two distinct points, at the highest and lowest crystal sizes (Figure 6), suggesting the presence of populations with different crystallisation histories (Cashman and Marsh 1988; Higgins and Roberge 2007). In contrast, Epoch 6 basalt LP-12 shows a concave down trend, which becomes shallower towards larger crystal sizes for both plagioclase and clinopyroxene (Figure 6).

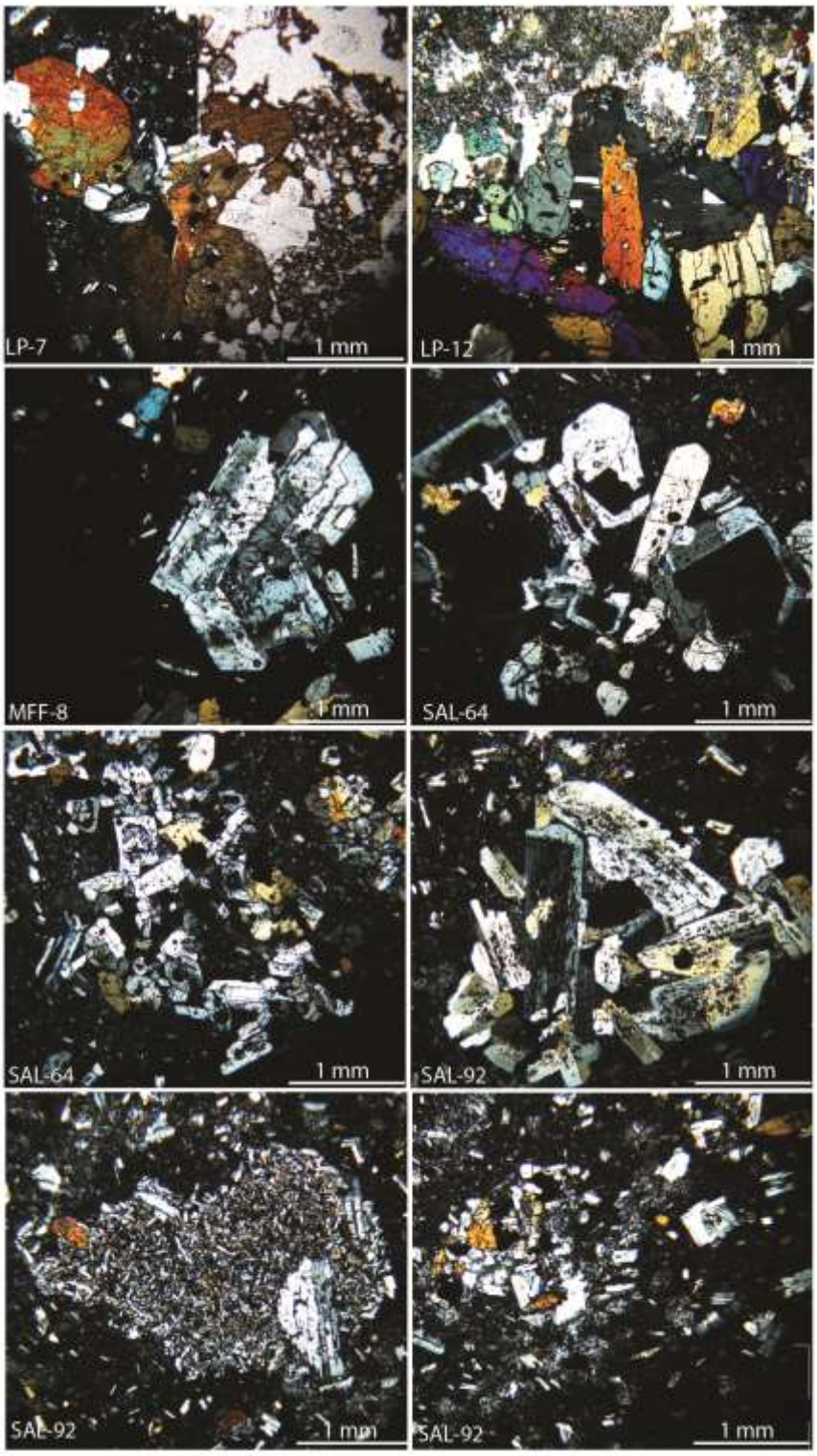

223

224 Figure 5: Variety of crystal clots types found in Salina's lavas.

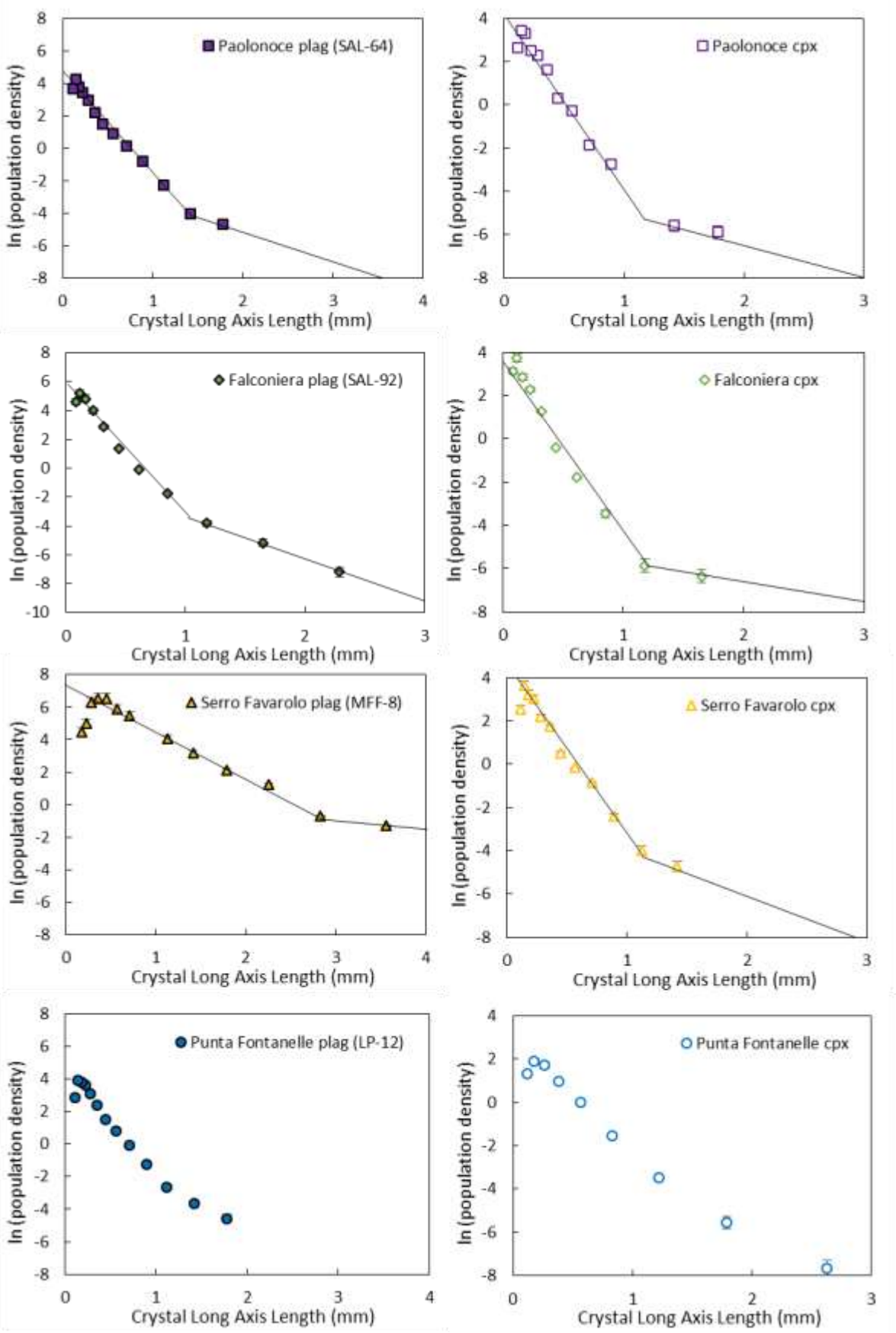

225

226 Figure 6: crystal size distribution graphs for SAL-64, SAL-92, MFF-8 and LP-12. Full symbols are
227 plagioclase whilst empty symbols are clinopyroxene CSDs.

CRYSTAL CARGO CHEMISTRY

Samples SAL-92 (dacite), SAL-64 and MFF-8 (andesites) show a plagioclase mineral assemblage displaying microtextures such as coarse and fine sieving, suggestive of disequilibrium conditions (Viccaro et al. 2010; Renjith 2014). They also present glomerophyric clusters that, together with microtextures, can be indicative of a series of magmatic processes including mixing and assimilation. Similarly, basaltic sample LP-12 hosts a gabbroic assemblage and a large variation of clinopyroxene, plagioclase and amphibole sizes. These samples were selected for core and rim mineral geochemical analyses carried out by LA-ICP-MS. Plagioclase crystals are present in all samples and were therefore most targeted for this study. Clinopyroxene crystals were only abundant and large enough to be analysed in sample LP-12 and MFF-8.

All clinopyroxene crystals in LP-12 and MFF-08 are augites, and show distinct ranges in Mg#. Those in LP-12 show higher Mg# between 78.4 and 75.7 and those in MFF-8 lower Mg# between 75.7 and 71.0 (Figure 7 a). Minor reverse zoning between cores and rims of ~2-3% Mg# is sometimes present in both samples (Figure 7 a-h). Compatible element concentrations decrease with decreasing Mg#, 224-437 ppm (LP-12) and 132-485 ppm (MFF-8) for V and 3-48 ppm (LP-12) and 2-71 ppm (MFF-8) for Ni (Figure 7 b,c). For both elements large variations are present at Mg# ~78 and ~75. Eu/Eu*, Dy_N/Yb_N and Sm_N/Yb_N ratios show an overall decreasing trend with Mg#, nevertheless they are relatively flat within single samples (Figure 7d-f).

Clinopyroxene REE patterns normalised to chondrite (Nakamura 1974) for MFF-8 and LP-12 show distinct trends (Figure 7 g,h). LP-12 clinopyroxene shows a strong LREE depletion compared to MREE and HREE, with a pronounced negative Eu anomaly, which increases with increasing REE concentrations Figure 7 g). In contrast MFF-8 shows two different trends. One with depletion in LREE and relative flat MREE and HREE, and one with LREE enrichment compared to flat MREE and HREE (Figure 7 h). Similarly to LP-12, a strong Eu anomaly is present and increases with increasing concentrations. In both samples, there is no clear distinction between core and rim chemistry, LP-12's most primitive and most evolved clinopyroxenes' compositions are from core analyses (Figure 7 g) whilst for MFF-8 the most evolved and most primitive compositions are those of clinopyroxene rims, with the exception of the two core analyses with enriched LREE (Figure 7 h).

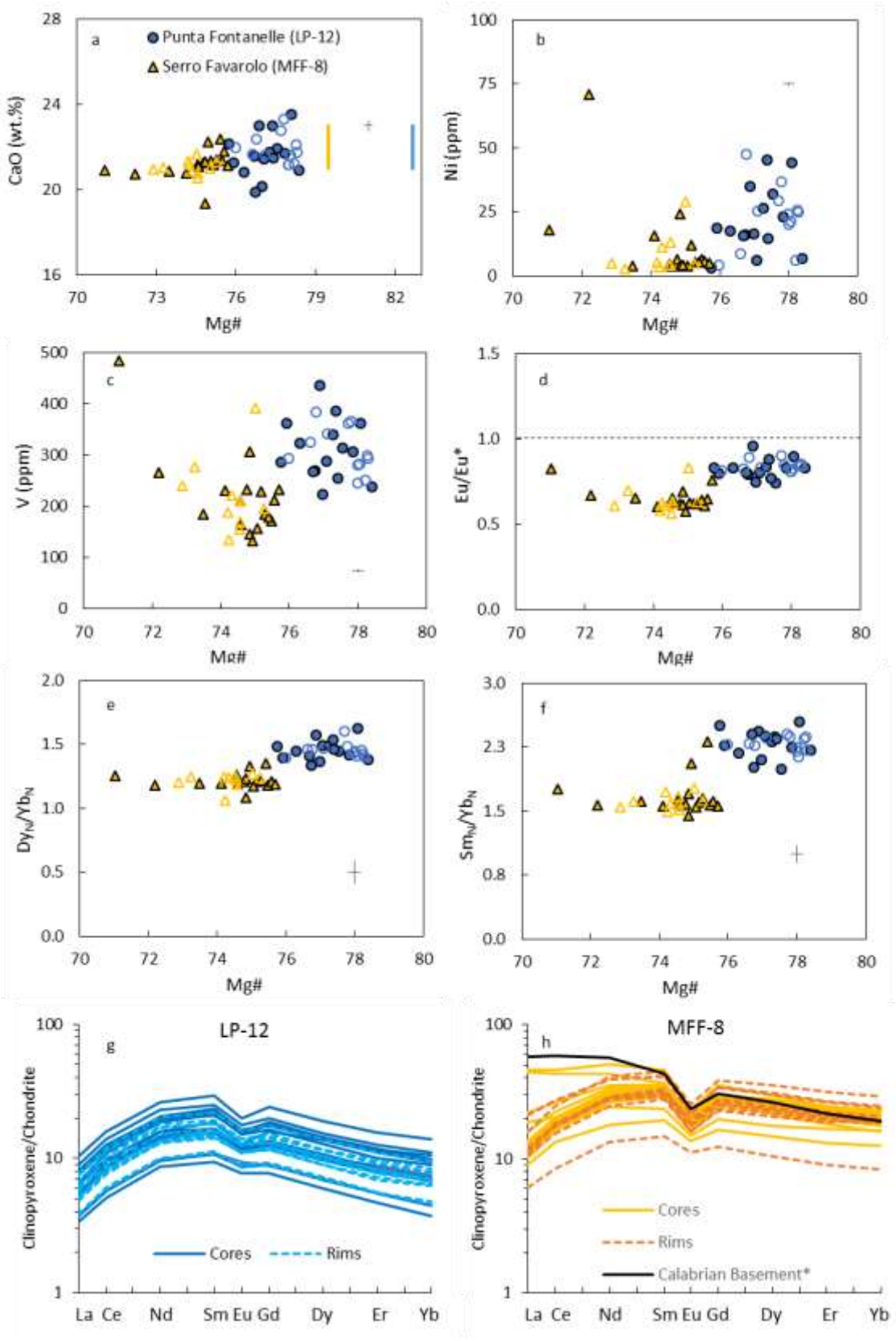

Figure 7: clinopyroxene chemistry for samples MFF-8 and LP-12. The yellow and blue lines represent calculated equilibrium Mg# from whole rock (Wood and Blundy 1997) for MFF-8 and LP-12. Error bar is 2sd. Clinopyroxene REE concentrations normalised to chondrite (Nakamura 1974). Calabrian basement composition from (Francalanci et al. 1993). Closed and open symbols represent core and rim analyses respectively.

Plagioclase crystals were analysed for four selected samples giving ranges from Anorthite to Labradorite, with $An_{83-96,}$ $An_{55-82,}$ An_{57-88} and An_{52-87} in LP-12, SAL-64, SAL-92 and MFF-8, respectively (Figure 8 a). Compatible elements (Sr, Ba) show general increases with decreasing anorthite (Figure 8 b,d,g). Sr in LP-12 (Epoch 6 basalt) shows the lowest and least variable compatible element concentrations with no significant overlap with compositions from other samples, consistent with the higher An% of the LP-12 plagioclases (Figure 8 b). LP-12 plagioclase population shows ranges of 703-1172ppm and 20-82ppm for Sr and Ba respectively, with no significant difference in composition between core and rim analyses. This is consistent with the textural characteristics of these crystals (Figure 4b) which show small scale oscillatory zoning but no abrupt zoning between cores and rims. The inner core and zones of LP-12 plagioclase sometimes display coarse sieving (Figure 4b). Despite their different degree of evolution, Epoch 4 SAL-64 (andesite), SAL-92 (dacite) and MFF-8 (andesite) all show significant overlap in plagioclase An% ranges but showing varying degrees of overlap in compatible element concentrations. All samples show very similar concentrations of Ba at a given An%, but each sample delineates a separate trend between Sr ppm and An% which ranges from 857-2034ppm, 1143-1851ppm and 735-1516ppm, for SAL-64, SAL-92 and MFF-8 respectively (Figure 8 b). LP-12, SAL-64 and SAL-92 show a steep increase in Sr at higher anorthite $>An_{77}$ followed by a less sharp but steady increase towards lower anorthite values. In contrast, SAL-92 (dacite) shows a steep increase at high anorthite (1143-1541 ppm) followed by a relatively flat trend in Sr (1514-1530 ppm) between $An_{76.7-58.0}$ mol.%. Moreover, SAL-92 appears to show a systematic decrease in anorthite, and Sr concentration, between cores and rims whilst such distinction is not observed in the other samples (Figure 8 b). These crystals often display fine sieves around the crystal edge, or resorbed and intensively sieved cores (Figure 4e, 4h, 4f), and can show reverse zoning where fresh, less evolved rims are present. Ba, TiO_2 and La/Y show similar increasing trends with decreasing anorthite, but sample SAL-92 shows lower TiO_2 (0.007-0.024 wt.%) than the other samples at the same anorthite (SAL-64: 0.008-0.039 wt.% and MFF-8: 0.009-0.036 wt.%) (Figure 8 f). La/Y instead shows large variations at all anorthite contents. For LP-12 and SAL-64 La/Y range 4.17-14.76 and 1.82-25.45 respectively with no clear variations between cores and rims (Figure 8 h). MFF-8 plagioclases display lower La/Y in the rims (average 12.42) than in the cores (13.29) at the same anorthite, whilst SAL-92 displays the lowest values in the high anorthite cores (5.86-9.03) and similar ranges across lower anorthite cores (10.83-21.82) and rims (6.98-19.80) Figure 8h). Mg concentrations are relatively flat and vary between 131 and 319 ppm between the highest and the lowest anorthite, only sample SAL-92 shows a slight overall increasing trend and large variations between 131-579 ppm are observed for LP-12 at $\sim An_{90}$. Fe_2O_3/Al_2O_3 and Sm/Eu ratios show similar decreasing patterns with decreasing anorthite contents, nevertheless large variations are observed for LP-12 (0.015-0.025 and 0.15-0.65 respectively). MFF-8 appears to show higher Fe_2O_3/Al_2O_3 and Sm/Eu ratios in the rims (0.016-0.023 and 0.23-0.52) compared to the cores (0.015-0.022 and 0.23-0.38) at $An_{<70}$ mol.% (Figure 8 e,g) and SAL-92 shows

systematically lower Sm/Eu ratios at low anorthite than the other samples on average ~0.38 (Figure 8 g).

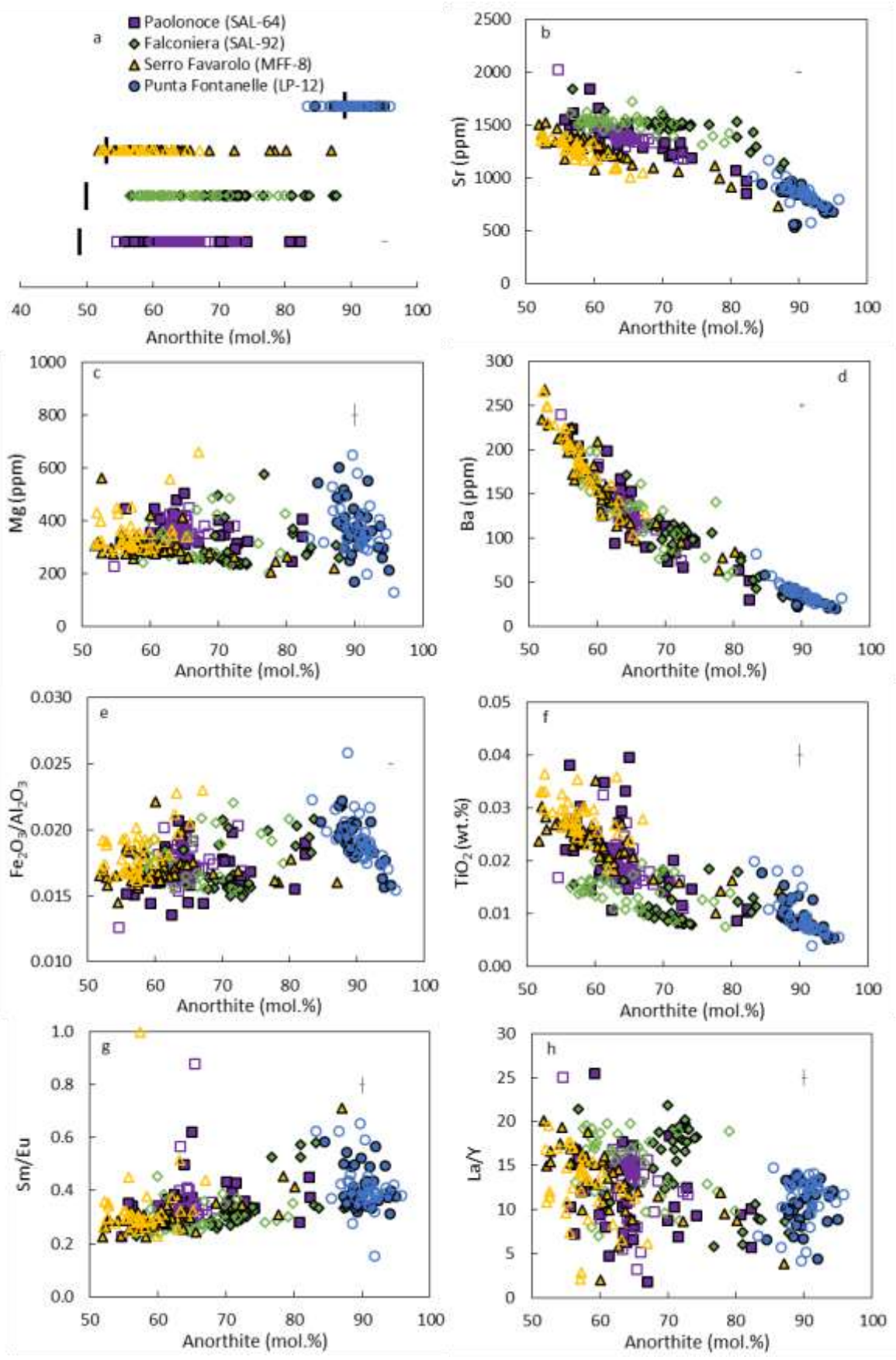

302

303 Figure 8: plagioclase chemistry for cores (full symbols) and rims (empty symbols). Solid black lines
304 in "a" are calculated equilibrium anorthite values from whole rock (Namur et al. 2012). Error is 2sd.

DISCUSSION

Crystal Cargoes Assemblages

The large range of mineralogy and textures (Figure 9) observed suggest that these samples have undergone a range of processes resulting in a heterogeneous crystal cargo that contains equilibrium and disequilibrium assemblages. Disequilibrium features, such as sieving and resorption (Figure 4), as well as kinks in the CSD profiles of samples SAL-64, SAL-92 and MFF-8 (Figure 6) suggest that the observed assemblages are not solely composed of primary cargoes. Equilibrium plagioclase anorthite and clinopyroxene Mg# (Figure 8 a, Figure 7 a) calculated from whole rock compositions (Wood and Blundy 1997; Namur et al. 2012) indicate that the LP-12 plagioclase crystals are in equilibrium with the host rock (Figure 8a), whilst the clinopyroxenes have lower Mg# than the equilibrium value (Figure 7a). Samples SAL-64, SAL-92 and MFF-8 display wider ranges of anorthite (Figure 8). SAL-64 and SAL-92 appear to be in disequilibrium, with plagioclase exhibiting higher anorthite than calculated equilibrium values, whilst MFF-8 appears to have lower anorthite rims in equilibrium with the calculated value (Figure 8). MFF-8 clinopyroxenes also present clinopyroxene Mg# lower than equilibrium (Figure 7). A caveat of models using whole rock to calculated equilibrium assemblage is that they require the host rock to be the original melt from which the crystals formed, therefore resulting in errors for xenocrystal populations and earlier formed phenocrysts.

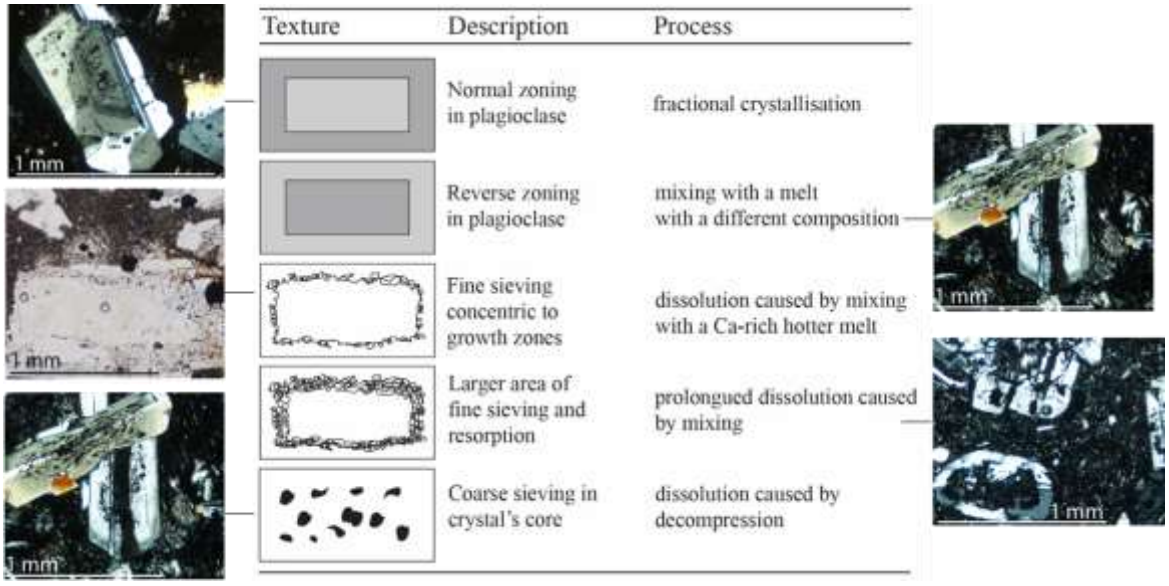

Figure 9: summary of plagioclase textures and interpretation (modified from Renjith (2014)) alongside sample pictures from Figure 4.

Comparison of expected $Sr_{plag\text{-}WR}$ partitioning behaviour with changing anorthite and observed Sr_{plag}/Sr_{WR} was utilised to assess the degree of disequilibrium (Blundy and Wood 1991) (Figure 11). Comparison of plagioclase compositions with partition coefficient lines show that not all plagioclase lie in the equilibrium areas within the calculated Sr_{plag}/Sr_{WR} lines. Andesite samples SAL-64 and

MFF-8 show trends that lie parallel to the partitioning curves (Figure 11). It is important to note that MFF-8 cores and rims appear to be following parallel trends between anorthite ~50-70 mol.% (Figure 11) suggesting a change in crystallisation conditions between cores and rims. Instead, dacite SAL-92 plagioclases lie mostly off any reasonable partition coefficient trend, with all cores analyses being offset to higher $Sr_{plag}/Sr_{melt,}$ moreover a relatively flat Sr_{plag}/Sr_{melt} is observed between anorthite ~80-55 mol.%. Basalt LP-12, which shows equilibrium in the anorthite model (Figure 8a) (Namur et al. 2012), lies displaced to lower Sr_{plag}/Sr_{melt} than equilibrium (Figure 11). One of the limitations of this model is that we have used whole rock compositions. LP-12 is a highly porphyritic rock, with high proportions of plagioclase compared to clinopyroxene and olivine (Table 3) and it is therefore likely that the displacement to lower $Sr_{plag\text{-}WR}$ (Figure 11) could be caused by crystal accumulation. In fact modelling of the whole rock composition by subtracting variable proportions of plagioclase shows that removal of 20% plagioclase results in Sr_{plag}/Sr_{melt} of 1.6, which would plot within the equilibrium lines.

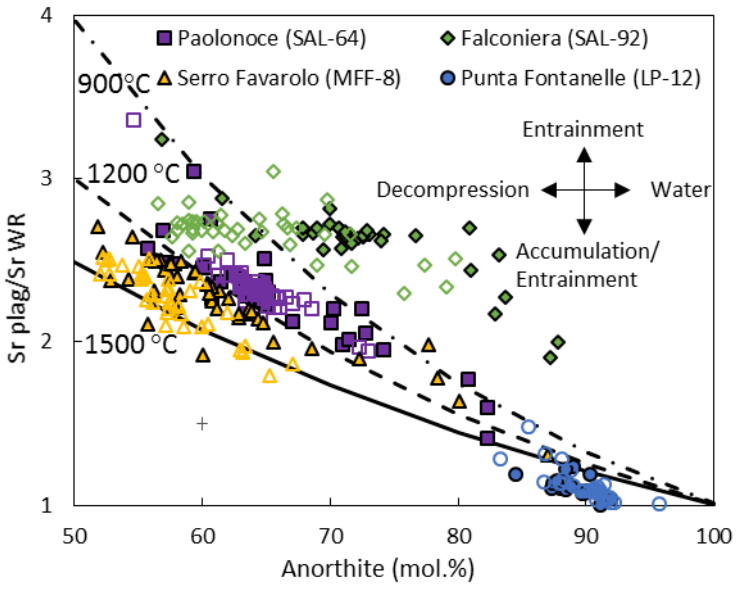

Figure 10: [Sr plag]/[Sr melt] vs anorthite plot with calculated Sr partition coefficients curves (Blundy and Wood 1991). Error on partition lines is 10%.

Further displacement from partition coefficient lines in Figure 11 could be caused by a variety of reasons. Horizontal displacement of SAL-92 plagioclase could indicate variation in crystallisation conditions. Experimental results have shown that plagioclase crystals with high anorthite content ~90 mol.% can be crystallised from a hydrous tholeiite with melt water ~5wt.% at a pressure of 2-3 kbar (Takagi et al. 2005) and that an increase in melt water by 1 wt.% would result in a ~2 mol.% increase in anorthite (Sisson and Grove 1993; Panjasawatwong et al. 1995; Takagi et al. 2005). Salina is situated in a volcanic arc setting, where previous studies found melt water content on Salina of ~0.5-3.7 wt.% (Nazzareni et al. 2011) and 4-4.5 wt.% in the most felsic compositions (Donato et al. 2006), and therefore it is likely that high melt water contents may affect the mineral chemistry. The

plagioclase hygrometer model by Putirka (2008) was used to provide an estimation of the water content of plagioclase crystals and the results show that for crystals with anorthite contents >80 mol.% melt water varies between 1.3-4.6 wt.% (Figure 11) suggesting a possible maximum increase in anorthite by ~9 mol.%. The model used for equilibrium anorthite (Namur et al. 2012) does not take into account water content and it is therefore possible that the high anorthite contents of LP-12 and the calculated anorthite disequilibrium shown by SAL-64 and SAL-92 high anorthite grains may be due to elevated water content in the melt (Takagi et al. 2005). Shallow level decompression and ascent from depth are also known to decrease anorthite content in plagioclase (Couch et al. 2003a, b). Coarse sieves in plagioclase cores are observed in all samples (Figure 4) which are thought to form as a response to decompression (Viccaro et al. 2010; Renjith 2014). A decrease in pressure of ~1 kbar would result in degassing and an decrease in anorthite of ~2 mol.% (Danyushevsky 2001), inducing the crystallisation of more evolved rims. This could be a reason for the systematic anorthite variations between cores and rims in SAL-92, but it does not account for the lack of variations in $Sr_{plag\text{-}WR}$ and no systematic differences in pressure and temperature conditions are observed from thermobarometry modelling results (Figure 11). Displacement to higher and lower $Sr_{plag\text{-}WR}$ can instead be caused by entrainment through assimilation and magma mixing processes, depending on whether the assimilating melt has a higher or lower Sr content, but it is more likely to increase the $Sr_{plag\text{-}WR}$ as plagioclase Sr concentrations are usually higher than those of the whole rock. Entrainment in a melt with higher Sr than that the crystal formed in would cause a decrease in $Sr_{plag\text{-}WR}$, and could explain the upward translation of SAL-64, MFF-8 and SAL-92 plagioclase >An_{75}. Further evidence for these processes is given by the complex zoning patterns observed in crystals (Figure 4) and reverse chemical zoning (Figure 7, Figure 8). The different shallow plumbing system processes which could be affecting the cargo, and their equilibrium conditions, are discussed individually and in further detail in the sections below.

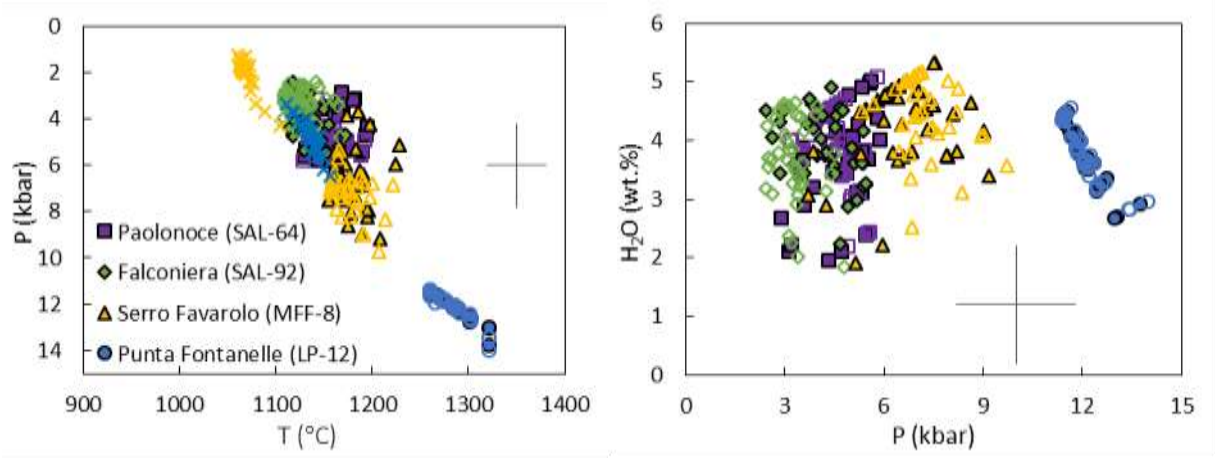

Figure 11: left) plagioclase thermobarometry (Putirka 2008). Yellow and blue crosses are clinopyroxene barometry calculations for MFF-8 and LP-12 respectively (Neave and Putirka 2017); right) plagioclase water content (wt.%) calculated using the Putirka (2008) hygrometer.

Magma mixing

Pollara (LP)

Interaction between different melts on Salina has been identified through mafic inclusions in more evolved lavas, zoned deposits in the lower Pollara sequence and banded pumices (Calanchi et al. 1993; Perugini et al. 2004; Donato et al. 2006; Lucchi et al. 2013). Mineral disequilibrium textures have also been identified, such as zoning and sieving in plagioclase (Calanchi et al. 1993; Lucchi et al. 2013; Nicotra et al. 2014), but the extent of magma mixing in generating the geochemical variability observed in the lavas of Salina and its effect on the crystal cargo is still poorly constrained.

The Punta Fontanelle eruptive sequence, Lower Pollara, resulted in an inversely stratified explosive eruption where dark basalts and andesites were overlain by light coloured andesitic to rhyolitic pumices (Calanchi et al. 1993; Lucchi et al. 2013). Samples LP-7 and LP-12 represent a black scoria and a juvenile grey clast respectively, from the basaltic section of the eruptive sequence (Lucchi et al. 2013). In sample LP-12, the high anorthite plagioclase is in equilibrium with the host whole rock composition (Figure 8) and clinopyroxene chemistry is associated to basaltic compositions (Figure 7), however clinopyroxene Mg# is lower than that calculated for equilibrium Mg# ~82 (Figure 7) (Wood and Blundy 1997). Samples LP-12 and LP-7 plot as basalts on the TAS diagram (Figure 2) and contain amphibole crystals with little or no sign of disequilibrium (Figure 4, Figure 5).

There are three possible scenarios for the presence of amphibole in basaltic samples; 1) the amphibole is of mantle origin, 2) the amphibole is co-genetic to the magma it is hosted in and 3) the amphibole is xenocrystal.

The possibility of mantle amphibole being entrained by rising melts (e.g. Best 1974) is not viable, as such prolonged decompression during ascent would cause substantial disequilibrium reaction rims which are not observed (Figure 4, Figure 5).

The other possibility is that the amphibole crystallised in equilibrium with the basalt, as proposed by Calanchi et al. (1993). It was suggested that increasing La/Yb and decreasing Dy/Yb with increasing SiO_2 in arc magmas indicates amphibole crystallisation in the crust (e.g. Macdonald et al. 2000; Davidson et al. 2007; Smith 2014). Figure 3 shows that increasing La/Yb trends are observed for more evolved rocks, and decreasing Dy/Yb ratios. The decreasing trend with decreasing SiO_2 reaches out to more evolved compositions and a similar trend is observed for more primitive compositions at SiO_2 ~49-52 wt.%, and is reflected in clinopyroxene chemistry (Figure 7), suggesting that amphibole fractionation plays a role in the petrogenesis of Salina's magmas. The lack of disequilibrium features and the size of the largest amphiboles suggest that they were hosted in equilibrium conditions just prior to eruption. Large clinopyroxene phenocrysts and plagioclase crystals are observed alongside amphiboles and oxides in LP-12 and LP-7 (Figure 4, Figure 5), and

the latter contains glomerophyric clusters of amphibole and plagioclase (Figure 5). Plagioclase and clinopyroxene CSDs (Figure 6) present a trend indicative of coarsening (Schiavi et al., 2009; Higgins, 2011) and complex zoning patterns in plagioclase crystals (Figure 4 b) could suggest that these large crystals could be antecrysts part of a basaltic chamber crystal mush or cumulate zone, subject to frequent basaltic replenishment. Cumulate entrainment is a common process in arc magmas (Dungan and Davidson 2004; Larocque and Canil 2010; Smith 2014) and it is suggested that amphibole bearing assemblages are more prone to assimilation compared to clinopyroxene dominated assemblages (Dungan and Davidson 2004). Assimilated cumulates could have been formed by crystallisation of an anhydrous olivine, clinopyroxene and plagioclase assemblage through the injection of different magmas in a deep crustal reservoir. The following crystallisation of amphibole as water became more concentrated in the melt could have occurred at the expense of either clinopyroxene or olivine crystals (Smith 2014), nevertheless the low abundance of olivine compared to clinopyroxene in LP-12 (Table 3) suggests amphibole could have progressively replaced olivine in the equilibrium assemblage. This is also supported by the abundance of oxides which suggests a higher degree of magmatic evolution. Experimental studies have shown that amphibole can crystallise from basaltic melts hosting olivine, plagioclase and clinopyroxene under specific temperature (<~1040 °C), pressure (~5-15 kbar) and water content (~2.5-4.5 wt.% melt H_2O) (Barclay and Carmichael 2004; Müntener and Ulmer 2006; Krawczynski et al. 2012). Others suggest that temperatures up to 1130 °C and pressures ~15 kbar could result in the crystallisation of calcic amphiboles from natural basaltic magmas (Ridolfi and Renzulli 2012). LP-12 clinopyroxene thermobarometry modelling (Figure 11) suggested a crystallisation temperature of ~1135 °C at a pressure of 4.8 kbar and the plagioclase hydrometer suggested an average melt water contents of ~3.80 wt.% (Figure 11). The calculated pressure and water contents are in agreement with published amphibole stability experiments (Barclay and Carmichael 2004; Müntener and Ulmer 2006; Krawczynski et al. 2012) and whilst associated calculated temperatures are too high, it is likely that the crystallisation of amphibole followed or replaced that of clinopyroxene (Smith 2014) or olivine therefore crystallising from a melt with potentially lower temperatures.

It is also possible that the amphibole was assimilated from a more evolved magma. The Punta Fontanelle sequence is known to have formed due to mixing between a basaltic and a silicic end member (Calanchi et al. 1993; Lucchi et al. 2013). Amphibole in Salina's lavas has been found as andesite hosted mafic inclusions (Lucchi et al. 2013), and as phenocrysts in the Monte Fosse delle Felci andesites and dacites (Gertisser and Keller 2000) and products of the Upper Pollara eruption (Lucchi et al. 2013). It is therefore possible that the amphibole crystallised in a more evolved reservoir which was erupted following basaltic recharge. This would have caused heating of the silicic melt causing disequilibrium, however it was suggested that heating between 1-50 °C under experimental conditions forms reaction rims in 3-48h (De Angelis et al. 2015) therefore very fast

453 recharge to eruption times in the scale of days (Browne and Gardner 2006) would be needed to erupt
454 fresh amphiboles as observed in LP-12 (Figure 4 c). However no other indication of mixing with an
455 evolved melt is found in the other mineral phases of LP-12. Neither plagioclase nor clinopyroxene
456 crystals show significantly lower anorthite or Mg# in their rims (Figure 7, Figure 8) and, whilst some
457 show reverse zoning, the difference is small ~2 mol.% and not the variation expected from mixing
458 between a basalt and a rhyolite. Plagioclase crystals in LP-12 present coarse sieving in the cores
459 (Figure 4 b), associated with decompression and ascent from depth (Renjith 2014), nevertheless this
460 process was not prolonged as most of the crystal remains unaffected. The cause of the lack of other
461 evolved crystal phases such as lower anorthite plagioclase is difficult to constrain, however one
462 possibility is that the specific gravity of amphibole is higher than that of plagioclase and therefore
463 the two phases would have been distributed to different parts of the reservoir. Calanchi et al. (1993)
464 reported plagioclase compositions of An_{64-83} for the andesitic products of the eruption suggesting a
465 degree of hybridisation between the two end-members, therefore suggesting that it would be possible
466 for more evolved plagioclase to have been erupted during a different stage of the zoned Pollara
467 eruption (i.e. in the pumices).

468 Whilst the origins of the amphibole remains difficult to constrain, the textures observed in the erupted
469 basaltic products LP-12 and LP-7 suggest that fast ascent and eruption times (3-48h) were necessary
470 in order to maintain fresh amphiboles with little or no disequilibrium rim, which would be expected
471 both in the case of mixing and decompression (De Angelis et al. 2015). Moreover it also remains
472 unclear why the amphiboles in LP-7 (Figure 5) show more disequilibrium features compared to LP-
473 12 (Figure 4 c), one possibility is that since LP-12 erupted before LP-7, as shown in field
474 observations (Lucchi et al. 2013), the amphibole would have remained in disequilibrium conditions
475 for longer in LP-7 therefore developing thicker disequilibrium rims than in LP-12 in slower ascent
476 rate conditions.

477 The minor reverse zoning and oscillatory zoning observed in plagioclase hosted in LP-12 is
478 consistent with the previously suggested hypothesis that continuous replenishment of deep basaltic
479 reservoirs contributed to keeping a fairly constant basalt range on Salina for the first 100 ka of
480 volcanic activity (Calanchi et al. 1993; Lucchi et al. 2013; Nicotra et al. 2014), and with the idea of
481 a partially mushy chamber generating the Punta Fontanelle basaltic products (Calanchi et al. 1993).
482 The reverse zoning observed can be obtained with 40-60% mixing between an LP-basalt and a less
483 evolved melt such as basalts with MgO up to ~7% and Sr ~731 ppm (Figure 12, supplementary data
484 file 1) which have been reported for Epochs 1-3 (Gertisser and Keller 2000; Lucchi et al. 2013). It is
485 therefore possible that the eruption of LP-12 was due to mafic recharge of a pre-existing basaltic
486 reservoir and mush. LP-12 also shows evidence for a gabbroic-like textured xenolith (Figure 5),
487 showing that entrainment of crustal material is a common process during magmatic ascent (Dungan
488 and Davidson 2004). Nevertheless, trace element zoning patterns in LP-12 do not appear to follow a

consistent correlation and end member compositions are therefore difficult to constrain (Figure 12). LP-12 clinopyroxene REE concentrations (Figure 7) show a trend consistent with fractional crystallisation, and the lack of systematic variations between cores and rims suggest mixing of magmas. The Eu anomaly (Figure 7) indicates plagioclase crystallisation occurred either before or alongside that of clinopyroxene and the similar pattern in REE (Figure 7) also indicates a similar parental composition suggesting that the source of the recharging melt remained constant. Varied La/Y in plagioclase ratios (Figure 8) could therefore be related to different degrees of melting of the mantle source.

Two different eruptive triggering scenarios have previously been proposed for the Lower Pollara eruption. Calanchi et al. (1993) suggested that the eruption was triggered by the injection of a silicic magma from deeper into the crust into a shallower basaltic, partially mushy, chamber. Lucchi et al. (2013) instead suggested the opposite mechanism by which a basaltic magma intruded a shallow crustal evolved reservoir. Variations in magma discharge rate during explosive eruptions allows for the eruption of denser underlying layers through the overlying more silicic layers (Blake and Ivey 1986), producing the Punta Fontanelle eruptive sequence observed in the field (Calanchi et al. 1993; Lucchi et al. 2013). The crystal cargo hosted in LP-12 suggests deep crystallisation and frequent replenishment as suggested by the complex zoning patterns in plagioclase (Figure 4 b), and the chemical zoning in both plagioclase and clinopyroxene (Figure 7, Figure 8). It has also been previously suggested that the evolution of shallow crustal reservoirs is associated with the appearance of more evolved compositions on Salina (Nazzareni et al. 2001). Moreover, deep crustal hot zones beneath volcanic arcs setting have been proposed to contribute to the appearance of silicic melts, formed by incomplete crystallisation of hydrous basalts, alongside minor amounts of crustal melting (Annen et al. 2006). As well as supporting the idea of compositional variations in deep seated basalts, the silicic melts are thought to segregate from mush zones and rise to shallower levels (Solano et al. 2012), suggesting that the eruption of the mush rich LP samples would have required triggering from a basaltic source at depth, which encountered a shallower silicic reservoir on the way to the surface.

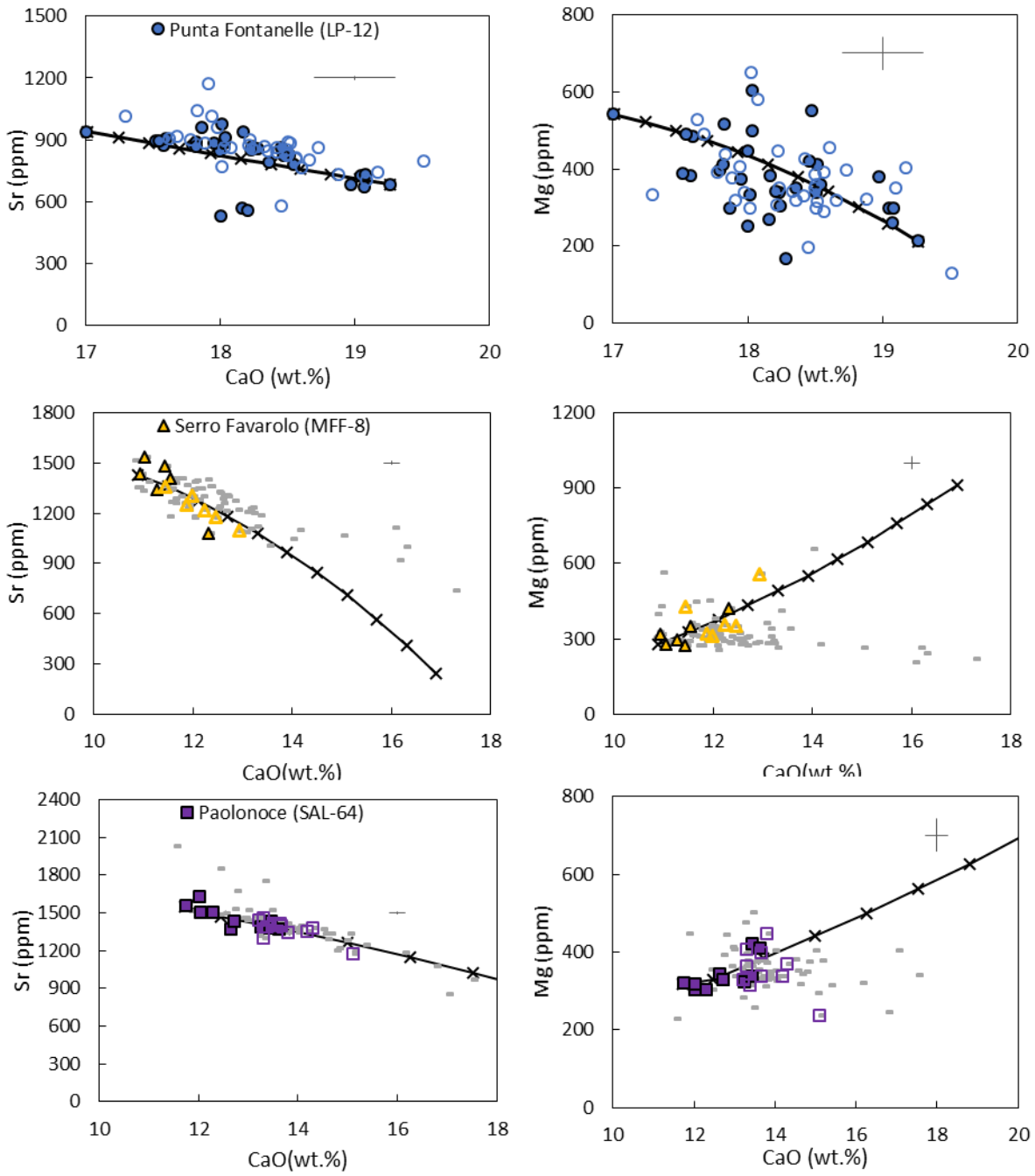

Figure 12: binary mixing models for LP-12, MFF-8 and SAL-64. For MFF-8 and SAL-64 only data for reverse zoned crystals is shown, and grey data points are the remaining analyses. Error is 2sd. For MFF-8 and SAL-64, coloured samples are the ones which were modelled for mixing as they displayed reverse zoning. The remaining normal zoned crystals are displayed in grey. Possible mixing end-members for samples MFF-8 and SAL-64 were selected from the whole rock database in supplementary file 1, showing that 10-20% could account for the reverse zoning observed in the crystals. For LP-12, mixing was carried out utilising the most primive crystal composition (parent calculated at 7wt.% MgO, using partition coefficients and whole rock database in the supplementary files).

Monte Fossa delle Felci (SAL-64 & MFF-8)

In the intermediate products of Monte Fossa delle Felci (Epoch 4) andesites SAL-64 and MFF-8, evidence for magma mixing can be seen through plagioclase textures and zoning patterns. MFF-8

displays plagioclase crystals with large areas covered in fine sieves (Figure 4 f), resulting from the interaction with a hotter Ca-rich melt (Renjith 2014). In both samples, intensively sieved plagioclase cores are surrounded by fresher rims (Figure 4 e,f) of An_{60}. Plagioclase CSDs exhibit a kinked CSD profile, with a shallower gradient at higher crystal size and a steep drop at the lowest crystal sizes (Figure 6). Whilst this is sometimes indicative of textural coarsening (Higgins 2000a; Schiavi et al. 2009), it is only the last bin size in which the largest grains exhibit a shallower trend, rather than a progressive shallowing of the right hand side of the trend. This kinked profile has previously been described as a response to magma mixing and recharge events (Cashman and Marsh 1988), where injection of a hotter melt causes resorption and stunted growth for a period of time before re-equilibration and crystallisation continues. This causes a concave down pattern in the smallest crystals, as nucleation rate drops, and a shallower gradient at high crystal sizes which resume growth after equilibration (Higgins and Roberge 2007). Where core and rim analyses were possible, plagioclase crystals show reverse zoning of up to 8 mol.% anorthite between $An_{\sim 52}$ and $An_{\sim 70}$, accompanied by an increase in Mg and decrease in Sr concentrations (Figure 8). Increase in Fe_2O_3 in the rims of zoned crystals, and therefore an increased Fe_2O_3/Al_2O_3 ratio, has been suggested to be an indicator of magmatic recharge (Ginibre et al. 2007). This is also supported by higher Mg concentrations in the rims, associated with more primitive melts (Figure 8 c,e). Binary mixing models were carried out with whole rock compositions (Figure 12), using calculated Sr and Mg partition coefficients (Blundy and Wood 1991; Bindeman et al. 1998) to obtain equilibrium plagioclase compositions, and 10-20% mixing can account for the difference in composition between plagioclase cores and rims (Figure 12). The mixing basalt composition required is of ~5 wt.% MgO and ~800 ppm Sr, similar to that of basalts from Monte Fossa delle Felci (Lucchi et al. 2013). Mixing and entrainment of more primitive antecrystal grains processes are also seen in clinopyroxene chemistry with distinctively different REE patterns observed within the MFF-8 population (Figure 7), where no systematic variation is observed between cores and rims, and where the most primitive clinopyroxene REE concentration belongs to a rim (Figure 7).

Whilst mixing models explain the reverse zoning in crystals, they are not able to explain the trends of the remaining plagioclase core-rim relationships. The remaning variations and normal zoning can be associated to fractional crystallisation, and high anorthite crystal cores $\sim An_{77-82}$ in both MFF-8 and SAL-64 are part of large glomerophyric clusters (Figure 5) and are therefore likely to be entrained antecrysts.

MFF-8 also shows systematic variations in composition between plagioclase cores and rims which are not explained by the mixing models, where most rims lie to higher Mg, Fe_2O_3/Al_2O_3 and Sm/Eu, as opposed to La/Y and Sr concentrations which are mostly lower in the rims than in the cores (Figure 8 b,c,e,g,h). Increasing Fe_2O_3/Al_2O_3 ratios in plagioclase have also been associated with increasing oxygen fugacity, suggesting that the crystallisation of the MFF-8 rims partly occurred due to

565 decompression driven crystallisation driven by H_2O degassing (Humphreys et al. 2006). Release of
566 H_2 from the melt promotes oxidising conditions which increase plagioclase-melt Fe partitioning
567 (Wilke and Behrens 1999), hence increasing Fe_2O_3/Al_2O_3, but decreases Eu partitioning and has little
568 effect on Sm (Drake and Weill 1975; Wilke and Behrens 1999; Burnham et al. 2015) resulting in
569 higher Sm/Eu ratios as seen in MFF-8 rims (Figure 8 g). MFF-8 rims also shows evidence for
570 decreasing pressure with associated decreasing H_2O wt.% (Figure 11). Decompression driven events
571 are in agreement with the abundant coarse sieving present in the plagioclase crystals (Figure 4) and
572 by the "higher temperature" rims observed in figure 10 as a result of latent heat released upon rims
573 crystallisation. It is therefore possible that bimodality in MFF-8 crystal chemistry is partly due to
574 magma recharge and mixing events at depth, as well as a decompression event resulting in the
575 systematically distinct rim chemistry. In contrast, heavily resorped crystal cores (Figure 4 e) and no
576 systematic variations in trace elements concentrations between cores and rims could suggest that
577 frequent mixing episodes followed by fractional crystallisation dominate the disequilibrium features
578 in SAL-64, supported by a large vertical variations in La/Y at $An_{\sim 60\text{-}65}$ (Figure 8).

579 **Crustal Assimilation, Entrainment and Ascent from Depth**

580 Crustal assimilation has long been recognised as an important process in the evolution of arc
581 magmas. On the island of Salina, and the Aeolian Islands in general, this process is highlighted by
582 correlating isotopic signatures and SiO_2 (e.g. Ellam et al. 1989; Ellam and Harmon 1990; Gertisser
583 and Keller 2000; Lucchi et al. 2013), as well as the presence of xenoliths and assimilated solid
584 material, such as crystal clots, in the lavas (e.g. Calanchi et al. 1993; Gertisser and Keller 2000;
585 Perugini et al. 2004; Lucchi et al. 2013). All samples contain enclaves or clots of gabbroic minerals
586 exhibiting a range of shapes, texture and mineral proportions (Figure 5). LP-12 hosts a gabbroic
587 assemblage (Figure 5), MFF-8 crystal clots comprise mostly of plagioclase exhibiting coarse sieving
588 in the core. Samples SAL-64 and SAL-92 contain crystal clots with significant proportions of
589 pyroxene and oxides in addition to plagioclase. SAL-64 clots occasionally present olivine.
590 Variations among glomerophyric clots could suggest multiple mechanisms for formation: 1)
591 aggregation of phenocrysts during convection, 2) assimilation and/or entrainment of
592 cumulate/crystal mush or wall rock material and 3) crystalline assemblages formed by the breakdown
593 of amphibole.

594 1) Glomerophyric clusters in MFF-8 are mostly composed of intensively sieved plagioclase crystals.
595 Renjith (2014) suggested that glomerocrysts could form as a response to suturing of spatially close
596 resorbed crystals. The composition of the plagioclase in some of the clots is similar to that of the
597 other phenocrysts suggesting that they are co-genetic. The two clinopyroxene crystal cores with
598 enriched LREE (Figure 7) are found in crystal clots. Fluid derived LREE enrichment is a common
599 process at volcanic arcs (Stalder et al. 1998; Peccerillo et al. 2013; Chen et al. 2017) and a recognised

process affecting Salina's magmas (Peccerillo et al. 2013; Zamboni et al. 2016). Clinopyroxene is refractory and would preserve its original signature even if hosted in a severely altered rock (Bizimis et al. 2000), suggesting that these LREE enriched crystals would have crystallised from a previously modified melt. The REE pattern (Figure 7) shows a trend similar to that of the Calabrian crust composition (Francalanci et al. 1993), suggesting they are xenocrystal and could have been entrained upon ascent.

2) Other crystals present more primitive compositions and as discussed above are likely to have been entrained. The clots in SAL-64 occasionally contain olivine, and this is not present as a isolated phenocryst phase. Moreover the size and mineralogy of the crystals in the clots of SAL-64 is varied thus suggesting that they could have different origins (Figure 5). Plagioclase crystals hosted in the clots is often sieved and or zoned suggesting that it was subject to growth in an open system chamber, suggesting they are of antecrystal nature. The crystal clusters observed in SAL-64 are therefore likely to be products of cumulate entrainment by the host melt. The cluster in LP-12 has a gabbroic appearance and could have been entrained from a more solid portion of the mush (Figure 5). The clusters in SAL-92 are more difficult to constrain. Glomerophyric clusters dominated by large sieved plagioclase crystals (Figure 5), similar to those hosted in SAL-64, are present and their chemistry is similar to that of phenocrysts suggesting they were also entrained from a co-genetic cumulate.

3) A third type of crystal clot is present in SAL-92, these clots have a regular outline, they are fine grained and composed of mostly plagioclase alongside pyroxene and oxide, all of similar crystal size and shape (Figure 5). Plagioclase crystals large enough to be analysed by LA-ICP-MS display more primitive compositions than the remaining populations and at ~An_{80} plot to relatively higher Mg, Fe_2O_3 and TiO_2 (Figure 8, Figure 13) with respect to the expected trend, and are therefore not thought to be antecrystal. As opposed to the other populations in the same samples, these crystals do not show microtextures or compositional zoning and are therefore unlikely to have formed and entrained as part of a cumulate or by clustering of phenocrysts. Regular shaped clusters of very fined grained, microlitic sized, crystals are also present (Figure 5) but due to their size they could not be targeted for geochemical analyses.

The fate of amphibole in Salina's magmas

Among other origins, crystal clots in intermediate arc lavas have previously been associated with the breakdown of amphibole (e.g. Stewart 1975). The limited stability field of amphibole, and its susceptibility to decompression and heating, often results in reaction rims forming on the outer crystal. Amphiboles are not present in any of the 3 intermediate samples discussed in this section, they have however previously been identified in other Salina lavas (Lucchi et al. 2013), in the Monte Fossa delle Felci products (Gertisser and Keller 2000) and, as previously discussed, play an

important role in the petrogenesis of Salina (Figure 3, Figure 4). It was previously described that amphibole disequilibrium rims could be of either opacitic or gabbroic nature (Rutherford and Hill 1993; Browne and Gardner 2006) with the latter being associated with amphibole breakdown and resorption. Experimental results (De Angelis et al. 2015) have shown that disequilibrium conditions in amphibole result in the breakdown of the rim into microlites of plagioclase, pyroxene and oxides. Prolonged residence in such disequilibrium conditions at higher temperatures and/or shallower depths results in the breakdown of amphibole into a pseudomorph clot of plagioclase ± pyroxene ± oxide (Stewart 1975; De Angelis et al. 2015), similar to the characteristics of the fine grained clots observed in SAL-92 (Figure 5). Moreover elevated Mg, Fe_2O_3 and TiO_2 concentrations in the plagioclase could reflect the availability of these elements provided by the breakdown of amphibole (Figure 13). However, if this was the case, it is challenging to assess whether the cause of disequilibrium was caused by decompression or heating. Whilst it has been suggested that higher proportions of clinopyroxene with respect to orthopyroxene in the clots is caused by heating (De Angelis et al. 2015), clinopyroxene dominated clots are also closely linked to calc-alkaline volcanism (Buckley et al. 2006) which is found on Salina. Moreover in all samples large plagioclase crystals show abundant coarse sieving textures in the cores, suggesting dissolution due to ascent from depth (Renjith 2014). These crystal clots may present the mineralogical characteristics of possible amphibole breakdown products, nevertheless due to the lack of other amphibole crystals, or pseudomorphs, this remains a speculative observation. Another possible explanation for these clots, containing plagioclase crystals with elevated Mg, Fe_2O_3 and TiO_2 concentrations, could be that of them being magmatic enclaves resulted from mixing with a more primitive melt. Quick quenching of the basaltic magma, supported by the lack of chilled margin, could also suggest that no major geochemical disruption would have affected the more evolved melt. Similar clots and textures have been identified in the dacites of Kameni Islands (Martin et al. 2006).

Geothermobarometry modelling has been applied to plagioclase crystals (Putirka 2008) and clinopyroxene (Neave and Putirka 2017) where available (Figure 11). Previous studies suggested the presence of two distinct reservoirs underneath Salina, at >12.7km and 1.7-4.7 km respectively (Nazzareni et al. 2001; Zanon and Nikogosian 2004), with the shallower reservoir developing towards Epochs 3-4 in association with the appearance of more evolved intermediate compositions. Whilst errors on plagioclase barometry are large, a qualitative relationship is observed between deeper basalts (LP-12) and shallower intermediate compositions (SAL-64, SAL-92 and MFF-8). More robust clinopyroxene geobarometry modelling (Neave and Putirka 2017) was carried out on samples LP-12 and MFF-8 and indicate crystallisation depths of 4-6 kbar and 1-4 kbar, respectively, (Figure 11) in agreement with previous studies (Nazzareni et al. 2001; Zanon and Nikogosian 2004). The results indicate that more primitive plagioclases crystallise at depth, whilst intermediate anorthite compositions, often present in the rims of the intensively coarse-sieved crystals, formed at

shallower depths following decompression. SAL-92 plagioclase core and rims in particular show rims to have crystallised at lower pressure, with lower pressure being associated to lower H_2O wt.% (Figure 11). This suggests that ascent from depth is a common process in the intermediate lavas of Salina and could support the case for possible amphibole breakdown as a result of prolonged disequilibrium due to decompression. In water saturated systems, the degrees of dissolution of the plagioclase cores are thought to be directly proportional to the rate of magmatic ascent and that the effect should increase with increased water content (Viccaro et al. 2010). The coarse sieving observed in plagioclase cores suggest they formed as a response to intermediate ascent rates before residence in shallower reservoirs. The chemistry of SAL-92 hosted plagioclase also suggests prolonged decompression at moderate ascent rates. As previously mentioned, crystallisation at lower pressures lowers the anorthite content in plagioclase (Danyushevsky 2001; Couch et al. 2003a; Blundy et al. 2006). Pressure however has been found to have minor effects on Sr partitioning behaviour between plagioclase and melt, with magma chemistry being the dominant control (Blundy and Wood 1991; Bindeman et al. 1998). As reported in previous studies (Zellmer et al. 2003), it is therefore likely that the flat Sr trend observed in SAL-92 plagioclase (Figure 8, Figure 10), and the systematic variation in anorthite between cores and rims, is caused by decompression and ascent through the crust. Plagioclase CSDs (Figure *6*) have been used to calculate growth time (Cashman and Marsh 1988; Armienti 2008; Špillar and Dolejš 2013; Neave et al. 2017) of SAL-92 rims, using growth rates from (Couch et al. 2003b), and suggest timescales of 0.7-12.4 days. Using this growth rate and the storage depth for the rims, previously calculated at 2-4 kbars (Figure 11), slow ascent rates on the scale of 0.01-0.1m/s were calculated.

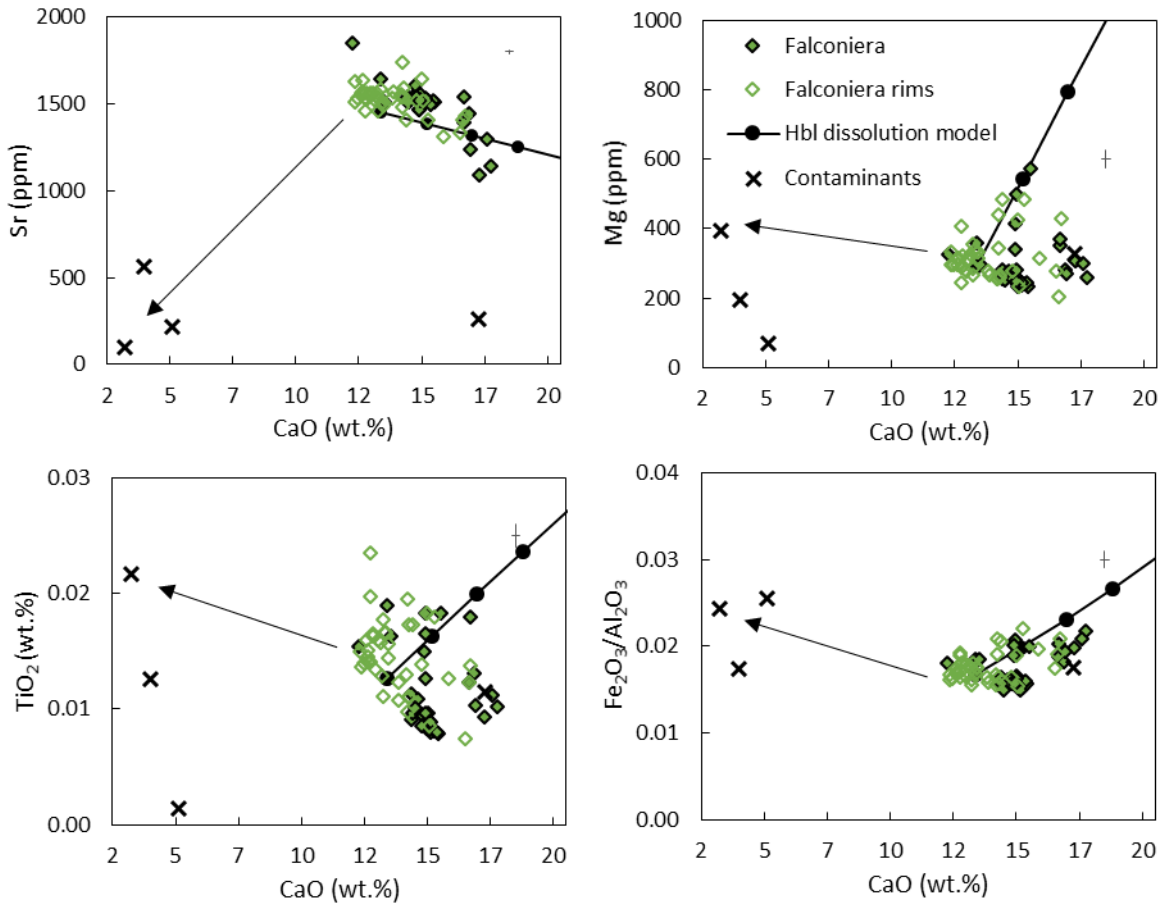

Figure 13: SAL-92 models, black lines show the modelled displacement direction towards potential Calabrian crust crustal contaminants (Caggianelli et al. 1991; Francalanci et al. 1993). Plagioclase compositions in equilibrium with the four lithologies were calculated using published whole rock data and partition coefficients and are plotted as black crosses. Modelling of crystallisation along a hornblende dissolution line is also shown to justify some compositional variation at high anorthite (high Ca) plagioclase compositions.

Crystal Contamination

The presence of xenolithic material and crystal clots different to possible amphibole pseudomorphs. mafic enclaves and cumulate entrainment (Figure 5) could suggest magmatic ascent as a viable process for assimilation of crustal material. Moreover, whole rock compositions give evidence for Assimilation – Fractional Crystallisation (AFC) (DePaolo 1981) processes with crystallisation rates of 0.05-0.1 (Ellam et al. 1989; Ellam and Harmon 1990; Gertisser and Keller 2000; Lucchi et al. 2013; Peccerillo et al. 2013) resulting in higher calc-alkaline signatures in dacites and andesites (Figure 2). In samples SAL-64 and MFF-8, plagioclase shows an overall trend of increasing Sr and decreasing Mg from $An_{\sim 80}$ to $An_{\sim 50}$ consistent with magmatic evolution, instead SAL-92 shows a relatively flat Sr trend (~1514-1530 ppm) and a slight increase in Mg (~235-316 ppm) from $An_{\sim 80}$ to $An_{\sim 58}$ (Figure 8). It is possible that the Sr trend was modified by crustal contamination, alongside prolonged degassing as previously explained. Four potential contamination sources have previously

been considered for Salina, a felsic granulite (Caggianelli et al. 1991), an Aeolian Island xenolith and two different Calabrian basement samples (Francalanci et al. 1993; Gertisser and Keller 2000).

Figure 13 shows possible displacement in the plagioclase trends caused by assimilation processes and whilst this partly responsible for the SAL-92 trend, systematically low TiO_2 and Eu enrichment is not easily explained by these trends suggesting that AFC processes are not responsible, in agreement with previous studies (Nicotra et al. 2014). As previously mentioned, Eu becomes increasingly more compatible in plagioclase in reducing conditions (Drake and Weill 1975; Wilke and Behrens 1999; Burnham et al. 2015). It is therefore possible that Eu enrichment in SAL-92 plagioclases is related to reducing conditions in a water saturated magma in agreement in relatively high calculated melt water contents ~4 wt.% (Figure 11). TiO_2 depletions in arc lavas have been proposed to be enhanced during low degrees of melting in the presence of a Ti-rich phase (Thirlwall et al. 1994), and to be further enhanced by fractional crystallisation of magnetite and amphibole (Thirlwall et al. 1994; Li et al. 2017). Clots in SAL-92 could provide evidence for resorbed amphiboles (Figure 5), which would suggest that amphibole fractionation may have occurred in the earlier evolution of the magma and it is therefore possible that it would have contributed to the TiO_2 depletion in the sample, nevertheless these are still speculations. It was also suggested that low TiO_2 arc magmas could be related to mantle wedge depletion, due to melt extraction prior to arc magma genesis in the back basin (Woodhead and Eggins 1993; Ewart et al. 1998) suggesting a potential depleted mantle source for SAL-92 as previously proposed (Peccerillo et al. 2013).

CONCLUSIONS

Crystal cargoes and Open system processes

The crystal cargoes hosted in the lavas from Salina provide an insight into the effects of open plumbing system processes on crystals microtextures and composition, which helps us quantify and better identify these processes. The main conclusions are summarised below:

- Large ranges of incompatible trace element ratios within the same flow suggests frequent recharge of primitive magmas.
- Reverse zoning in plagioclase and wide ranges in incompatible trace elements in evolved andesite and dacite compositions suggest magma mixing and recharge processes occurred in shallow reservoirs in the crust.
- Evidence for decompression as an eruptive mechanism is observed in the crystal microtextures. Breakdown of amphibole suggests ascent from depths and residence time in shallow reservoirs. Intense coarse sieving in plagioclase cores supports intermediate ascent rates.

- Quick mixing to eruption timescales is shown by lack of disequilibrium in the Lower Pollara basalts, suggesting magma mixing as an effective eruption trigger.
- The effect of crustal assimilation on the crystal cargo is represented by the presence of xenolithic glomerophyric clusters and by potentially modified trace element patterns in plagioclase crystals.
- Amphiboles are present in erupted basaltic samples, but are a cryptic phase at more evolved compositions.

Whilst these processes are better described in individual samples, the variety of microtextures in plagioclase is shared to a different extent by all samples. This suggests the presence of different populations which have been affected by these processes at different stages of their evolution, and show evidence for different crystallisation histories and location.

REFERENCES

Annen C, Blundy JD, Sparks RSJ (2006) The genesis of intermediate and silicic magmas in deep crustal hot zones. J Petrol 47:505–539. doi: 10.1093/petrology/egi084

Arculus RJ, Wills KJA (1980) The petrology of plutonic blocks and inclusions from the lesser antilles Island arc. J Petrol 21:743–799. doi: 10.1093/petrology/21.4.743

Armienti P (2008) Decryption of Igneous Rock Textures: Crystal Size Distribution Tools. Rev Mineral Geochemistry 69:623–649. doi: 10.2138/rmg.2008.69.16

Barclay J, Carmichael ISE (2004) A Hornblende Basalt from Western Mexico: Water-saturated Phase Relations Constrain a Pressure-Temperature Window of Eruptibility. J Petrol 45:485–506. doi: 10.1093/petrology/egg091

Barry TL, Pearce JA, Leat PT, et al (2006) Hf isotope evidence for selective mobility of high-field-strength elements in a subduction setting: South Sandwich Islands. Earth Planet Sci Lett 252:223–244. doi: 10.1016/j.epsl.2006.09.034

Best MG (1974) Mantle-derived amphibole within inclusions in alkalic-basaltic lavas. J Geophys Res 79:2107–2113. doi: 10.1029/JB079i014p02107

Bindeman IN, Davis AM, Drake MJ (1998) Ion microprobe study of plagioclase-basalt partition experiments at natural concentration levels of trace elements. Geochim Cosmochim Acta 62:1175–1193. doi: 10.1016/S0016-7037(98)00047-7

Bizimis M, Salters VJM, Bonatti E (2000) Trace and REE content of clinopyroxenes from supra-subduction zone peridotites. Implications for melting and enrichment processes in island arcs. Chem Geol 165:67–85. doi: 10.1016/S0009-2541(99)00164-3

Blake S, Ivey GN (1986) Magma-mixing and the dynamics of withdrawal from stratified reservoirs. J Volcanol Geotherm Res 27:153–178. doi: 10.1016/0377-0273(86)90084-3

Blundy J, Cashman K, Humphreys M (2006) Magma heating by decompression-driven crystallization beneath andesite volcanoes. Nature 443:76–80. doi: 10.1038/nature05100

Blundy JD, Wood BJ (1991) Crystal-chemical controls on the partitioning of Sr and Ba between plagioclase feldspar, silicate melts, and hydrothermal solutions. Geochim Cosmochim Acta 55:193–209. doi: 10.1016/0016-7037(91)90411-W

Browne BL, Gardner JE (2006) The influence of magma ascent path on the texture, mineralogy, and formation of hornblende reaction rims. Earth Planet Sci Lett 246:161–176. doi: 10.1016/j.epsl.2006.05.006

787 Buckley VJE, Sparks RSJ, Wood BJ (2006) Hornblende dehydration reactions during magma
788 ascent at Soufrière Hills Volcano, Montserrat. Contrib to Mineral Petrol 151:121–140. doi:
789 10.1007/s00410-005-0060-5

790 Burnham AD, Berry AJ, Halse HR, et al (2015) The oxidation state of europium in silicate melts as
791 a function of oxygen fugacity, composition and temperature. Chem Geol 411:248–259. doi:
792 10.1016/j.chemgeo.2015.07.002

793 Caggianelli A, Delmoro A, Paglionico A, et al (1991) Lower crustal granite genesis connected with
794 chemical fractionation in the continental crust of Calabria (Southern Italy). Eur J Mineral
795 3:159–180. doi: 10.1127/ejm/3/1/0159

796 Calanchi N, De Rosa R, Mazzuoli R, et al (1993) Silicic magma entering a basaltic magma
797 chamber: eruptive dynamics and magma mixing - an example from Salina (Aeolian islands,
798 Southern Tyrrhenian Sea). Bull Volcanol 55:504–522. doi: 10.1007/BF00304593

799 Carmichael ISE (2002) The andesite aqueduct: Perspectives on the evolution of intermediate
800 magmatism in west-central (105-99°W) Mexico. Contrib to Mineral Petrol 143:641–663. doi:
801 10.1007/s00410-002-0370-9

802 Cashman C V, Marsh BD (1988) Crystal size distribution (CSD) in rocks and the kinetics and
803 dynamics of crystallisation II: Makaopuhi lava lake. Contrib to Mineral Petrol 99:277–291.
804 doi: 10.1007/BF00371933

805 Chen C, Liu Y, Foley SF, et al (2017) Carbonated sediment recycling and its contribution to
806 lithospheric refertilization under the northern North China Craton. Chem Geol 466:641–653.
807 doi: 10.1016/j.chemgeo.2017.07.016

808 Couch S, Harford CL, Sparks RSJ, Carroll MR (2003a) Experimental constraints on the conditions
809 of formation of highly calcic plagioclase microlites at the Soufrire Hills Volcano, Montserrat.
810 J Petrol 44:1455–1475. doi: 10.1093/petrology/44.8.1455

811 Couch S, Sparks RJ, Carroll MR (2003b) The Kinetics of Degassing-Induced Crystallization at
812 Soufriere Hills Volcano, Montserrat. J Petrol 44:1477–1502. doi:
813 10.1093/petrology/44.8.1477

814 Danyushevsky L V. (2001) The effect of small amounts of H2O on crystallisation of mid-ocean
815 ridge and backarc basin magmas. J Volcanol Geotherm Res 110:265–280. doi:
816 10.1016/S0377-0273(01)00213-X

817 Davidson J, Turner S, Handley H, et al (2007) Amphibole “sponge” in arc crust? Geology 35:787–
818 790. doi: 10.1130/G23637A.1

819 Davidson JP (1987) Crustal contamination versus subduction zone enrichment: Examples from the
820 Lesser Antilles and implications for mantle source compositions of island arc volcanic rocks.
821 Geochim Cosmochim Acta 51:2185–2198. doi: 10.1016/0016-7037(87)90268-7

822 De Angelis SH, Larsen J, Coombs M, et al (2015) Amphibole reaction rims as a record of pre-
823 eruptive magmatic heating: An experimental approach. Earth Planet Sci Lett 426:235–245.
824 doi: 10.1016/j.epsl.2015.06.051

825 DePaolo DJ (1981) Trace element and isotopic effects of combined wallrock assimilation and
826 fractional crystallization. Earth Planet Sci Lett 53:189–202. doi: 10.1016/0012-
827 821X(81)90153-9

828 DePaolo DJ, Perry F V, Baldridge WS (1992) Crustal versus mantle sources in granitic magmas: A
829 two-parameters model based on Nd isotope studies. Trans R Soc Edinburgh 83:439–446

830 Donato P, Behrens H, De Rosa R, et al (2006) Crystallization conditions in the Upper Pollara
831 magma chamber, Salina Island, Southern Tyrrhenian Sea. Mineral Petrol 86:89–108. doi:
832 10.1007/s00710-005-0105-5

833 Drake MJ, Weill DF (1975) Partition of Sr, Ba, Ca, Y, Eu/2+/, EU/3+/, and other REE between
834 plagioclase feldspar and magmatic liquid - An experimental study. 39:689–712. doi:
835 10.1016/0016-7037(75)90011-3

836 Dungan MA, Davidson J (2004) Partial assimilative recycling of the mafic plutonic roots of arc
837 volcanoes: An example from the Chilean Andes. Geology 32:773–776. doi:
838 10.1130/G20735.1

839 Ellam RM, Harmon RS (1990) Oxygen isotope constraints on the crustal contribution to the
840 subduction-related magmatism of the Aeolian Islands, southern Italy. J Volcanol Geotherm
841 Res 44:105–122. doi: 10.1016/0377-0273(90)90014-7

842 Ellam RM, Hawkesworth CJ, Menzies MA, Rogers NW (1989) The Volcanism of Southern Italy:
843 Role of Subduction and the Relationship Between Potassic and Sodic Alkaline Magmatism. J
844 Geodyn 94:4589–4601

845 Ewart A, Collerson KD, Regelous M, et al (1998) Geochemical evolution within the Tonga-
846 Kermadec-Lau Arc-Back-arc systems: The role of varying mantle wedge composition in
847 space and time. J Petrol 39:331–368. doi: 10.1093/petroj/39.3.331

848 Francalanci L, Taylor SR, McCulloch MT, Woodhead JD (1993) Geochemical and isotopic
849 variations in the calc-alkaline rocks of Aeolian arc, southern Tyrrhenian Sea, Italy:
850 constraints on magma genesis. Contrib to Mineral Petrol 113:300–313. doi:

851 10.1007/BF00286923

852 Gertisser R, Keller J (2000) From basalt to dacite: Origin and evolution of the calc-alkaline series
853 of Salina, Aeolian arc, Italy. Contrib to Mineral Petrol 139:607–626. doi:
854 10.1007/s004100000159

855 Ginibre C, Wörner G, Kronz A (2007) Crystal zoning as an archive for magma evolution. Elements
856 3:261–266. doi: 10.2113/gselements.3.4.261

857 Grove T, Parman S, Bowring S, et al (2002) The role of an H2O-rich fluid component in the
858 generation of primitive basaltic andesites and andesites from the Mt. Shasta region, N
859 California. Contrib to Mineral Petrol 142:375–396. doi: 10.1007/s004100100299

860 Grove TL, Elkins-Tanton LT, Parman SW, et al (2003) Fractional crystallization and mantle-
861 melting controls on calc-alkaline differentiation trends. Contrib to Mineral Petrol 145:515–
862 533. doi: 10.1007/s00410-003-0448-z

863 Grove TL, Kinzler RJ (1986) Petrogenesis of Andesites. Annu Rev Earth Planet Sci 14:417–454.
864 doi: 10.1146/annurev.ea.14.050186.002221

865 Grove TL, Kinzler RJ, Baker MB, et al (1988) Assimilation of granite by basaltic magma at Burnt
866 Lava flow, Medicine Lake volcano, northern California: Decoupling of heat and mass
867 transfer. Contrib to Mineral Petrol 99:320–343. doi: 10.1007/BF00375365

868 Hawkesworth CJ, Gallagher K, Hergt JM, McDermott F (1993) Mantle and slab contributions in
869 arc magmas. Annu Rev Earth Planet Sci 21:175–204. doi:
870 10.1146/annurev.ea.21.050193.00113

871 Higgins MD (2002a) Closure in crystal size distributions (CSD), verification of CSD calculations,
872 and the significance of CSD fans. Am Mineral 87:1242–1243. doi: 10.2138/am-2002-0118

873 Higgins MD (2000a) Measurement of crystal size distributions. Am Mineral 85:1105–1116

874 Higgins MD (2000b) Measurement of crystal size distributions. Am Mineral 85:1105–1116. doi:
875 0003-004X/00/0009–1105

876 Higgins MD (2002b) A crystal size-distribution study of the Kiglapait layered mafic intrusion,
877 Labrador, Canada: Evidence for textural coarsening. Contrib to Mineral Petrol 144:314–330.
878 doi: 10.1007/s00410-002-0399-9

879 Higgins MD, Roberge J (2007) Three magmatic components in the 1973 eruption of Eldfell
880 volcano, Iceland: Evidence from plagioclase crystal size distribution (CSD) and
881 geochemistry. J Volcanol Geotherm Res 161:247–260. doi: 10.1016/j.jvolgeores.2006.12.002

882 Hildreth W, Moorbath S (1988) Crustal contributions to arc magmatism in the Andes of Central
883 Chile. Contrib to Mineral Petrol 98:455–489. doi: 10.1007/BF00372365

884 Humphreys MCS, Blundy JD, Sparks RSJ (2006) Magma evolution and open-system processes at
885 Shiveluch Volcano: Insights from phenocryst zoning. J Petrol 47:2303–2334. doi:
886 10.1093/petrology/egl045

887 Jarosewich E (2002) Smithsonian Microbeam Standards. J Res Natl Inst Stand Technol 107:681.
888 doi: 10.6028/jres.107.054

889 Krawczynski MJ, Grove TL, Behrens H (2012) Amphibole stability in primitive arc magmas:
890 Effects of temperature, H2O content, and oxygen fugacity. Contrib to Mineral Petrol
891 164:317–339. doi: 10.1007/s00410-012-0740-x

892 Larocque J, Canil D (2010) The role of amphibole in the evolution of arc magmas and crust: The
893 case from the Jurassic Bonanza arc section, Vancouver Island, Canada. Contrib to Mineral
894 Petrol 159:475–492. doi: 10.1007/s00410-009-0436-z

895 Lee CTA, Lee TC, Wu CT (2014) Modeling the compositional evolution of recharging,
896 evacuating, and fractionating (REFC) magma chambers: Implications for differentiation of
897 arc magmas. Geochim Cosmochim Acta 143:8–22. doi: 10.1016/j.gca.2013.08.009

898 Li L, Xiong XL, Liu XC (2017) Nb/Ta fractionation by amphibole in hydrous basaltic systems:
899 Implications for arc magma evolution and continental crust formation. J Petrol 58:3–28. doi:
900 10.1093/petrology/egw070

901 Lucchi F, Gertisser R, Keller J, et al (2013) Chapter 9 Eruptive history and magmatic evolution of
902 the island of Salina (central Aeolian archipelago). Geol Soc London, Mem 37:155–211. doi:
903 10.1144/M37.9

904 Macdonald R, Hawkesworth CJ, Heath E (2000) The Lesser Antilles volcanic chain: A study in arc
905 magmatism. Earth Sci Rev 49:1–76. doi: 10.1016/S0012-8252(99)00069-0

906 Martin V.M, Honless M.B, Pyle, D (2006).Textural analysis of magmatic enclaves from the
907 Kameni Islands, Santorini, Greece. Journal of Volcanology and Geothermal Research 154:89-
908 102 doi: :10.1016/j.jvolgeores.2005.09.021

909 Müntener O, Ulmer P (2006) Experimentally derived high-pressure cumulates from hydrous arc
910 magmas and consequences for the seismic velocity structure of lower arc crust. Geophys Res
911 Lett 33:1–5. doi: 10.1029/2006GL027629

912 Nakamura N (1974) Determination of REE, Ba, Fe, Mg, Na and K in carbonaceous and ordinary
913 chondrites. Geochim Cosmochim Acta 38:757–775. doi: 10.1016/0016-7037(74)90149-5

914 Namur O, Charlier B, Toplis MJ, Vander Auwera J (2012) Prediction of plagioclase-melt equilibria
915 in anhydrous silicate melts at 1-atm. Contrib to Mineral Petrol 163:133–150. doi:
916 10.1007/s00410-011-0662-z

917 Nazzareni S, Molin G, Peccerillo A, Zanazzi PF (2001) Volcanological implications of crystal-
918 chemical variations in clinopyroxenes from the Aeolian Arc, Southern Tyrrehenian Sea
919 (Italy). Bull Volcanol 63:73–82. doi: 10.1007/s004450100125

920 Nazzareni S, Skogby H, Zanazzi PF (2011) Hydrogen content in clinopyroxene phenocrysts from
921 Salina mafic lavas (Aeolian arc, Italy). Contrib to Mineral Petrol 162:275–288. doi:
922 10.1007/s00410-010-0594-z

923 Neave DA, Buisman I, MacLennan J (2017) Continuous mush disaggregation during the long-
924 lasting Laki fissure eruption, Iceland. Am Mineral 102:2007–2021. doi: 10.2138/am-2017-
925 6015CCBY

926 Neave DA, Putirka KD (2017) A new clinopyroxene-liquid barometer, and implications for magma
927 storage pressures under Icelandic rift zones. Am Mineral 102:777–794. doi: 10.2138/am-
928 2017-5968

929 Nicotra E, Viccaro M, De Rosa R, Sapienza M (2014) Volcanological evolution of the Rivi-Capo
930 Volcanic Complex at Salina, Aeolian Islands: Magma storage processes and ascent dynamics.
931 Bull Volcanol 76:1–24. doi: 10.1007/s00445-014-0840-8

932 O'Hara MJ (1977) Geochemical evolution during fractional crystallisation of a periodically refilled
933 magma chamber. Nature 266:503–507. doi: 10.1038/266503a0

934 O'Hara MJ, Mathews RE (1981) Geochemical evolution in an advancing, periodically replenished,
935 periodically tapped, continuously fractioned magma chamber. J Geol Soc London 138:237–
936 277

937 Panjasawatwong Y, Danyushevsky L V., Crawford AJ, Harris KL (1995) An experimental study of
938 the effects of melt composition on plagioclase-melt equilibria at 5 and 10 kbar: implications
939 for the origin of magmatic high-An plagioclase. Contrib to Mineral Petrol 118:420–432. doi:
940 10.1007/s004100050024

941 Pearce JA, Peate DW (1995) Tectonic Implications of the composition of Volcanic Arc Magmas.
942 Annu Rev Earth Planet Sci 23:251–285

943 Peccerillo A, Dallai L, Frezzotti ML, Kempton PD (2004) Sr-Nd-Pb-O isotopic evidence for
944 decreasing crustal contamination with ongoing magma evolution at Alicudi volcano (Aeolian
945 arc, Italy): Implications for style of magma-crust interaction and for mantle source

compositions. Lithos 78:217–233. doi: 10.1016/j.lithos.2004.04.040

Peccerillo A, De Astis G, Faraone D, et al (2013) Chapter 15 Compositional variations of magmas in the Aeolian arc: implications for petrogenesis and geodynamics. Geol Soc London, Mem 37:491–510. doi: 10.1144/M37.15

Perugini D, Ventura G, Petrelli M, Poli G (2004) Kinematic significance of morphological structures generated by mixing of magmas: A case study from Salina Island (southern Italy). Earth Planet Sci Lett 222:1051–1066. doi: 10.1016/j.epsl.2004.03.038

Plank T, Kelley KA, Zimmer MM, et al (2013) Why do mafic arc magmas contain ~4wt% water on average? Earth Planet Sci Lett 364:168–179. doi: 10.1016/j.epsl.2012.11.044

Plank T, Langmuir CH (1998) The chemical composition of subducting sediment and its consequences for the crust and mantle. Chem Geol 145:325–394. doi: 10.1016/S0009-2541(97)00150-2

Putirka KD (2008) Thermometers and Barometers for Volcanic Systems. Rev Mineral Geochemistry 69:61–120. doi: 10.2138/rmg.2008.69.3

Renjith ML (2014) Micro-textures in plagioclase from 1994-1995 eruption, Barren Island Volcano: Evidence of dynamic magma plumbing system in the Andaman subduction zone. Geosci Front 5:113–126. doi: 10.1016/j.gsf.2013.03.006

Ridolfi F, Renzulli A (2012) Calcic amphiboles in calc-alkaline and alkaline magmas: Thermobarometric and chemometric empirical equations valid up to 1,130°C and 2.2 GPa. Contrib to Mineral Petrol 163:877–895. doi: 10.1007/s00410-011-0704-6

Rogers G, Hawkesworth CJ (1989) A geochemical traverse across the North Chilean Andes: evidence for crust generation from the mantle wedge. Earth Planet Sci Lett 91:271–285. doi: 10.1016/0012-821X(89)90003-4

Rutherford MJ, Hill PM (1993) Magma Ascent Rates From Amphibole Breakdown â€™ An Experimental Study Applied to the 1980-1986 Mount St . Helens Eruptions the rates processes phenocrysts of amphibole that were is becoming increasingly important in the fields of presence of melt at depth . 98:

Schiavi F, Walte N, Keppler H (2009) First in situ observation of crystallization processes in a basaltic-andesitic melt with the moissanite cell. Geology 37:963–966. doi: 10.1130/G30087A.1

Schindelin J, Arganda-Carreras I, Frise E, et al (2012) Fiji: An open source platform for biological image analysis. Nat Methods 9:676–682. doi: 10.1038/nmeth.2019.Fiji

978 Sisson TW, Grove TL (1993) Experimental investigations of the role of H2O in calc-alkaline
979 differentiation and subduction zone magmatism. Contrib to Mineral Petrol 113:143–166. doi:
980 10.1007/BF00283225

981 Smith DJ (2014) Clinopyroxene precursors to amphibole sponge in arc crust. Nat Commun 5:1–6.
982 doi: 10.1038/ncomms5329

983 Solano JMS, Jackson MD, Sparks RSJ, et al (2012) Melt segregation in deep crustal hot zones: A
984 mechanism for chemical differentiation, crustal assimilation and the formation of evolved
985 magmas. J Petrol 53:1999–2026. doi: 10.1093/petrology/egs041

986 Špillar V, Dolejš D (2013) Calculation of time-dependent nucleation and growth rates from
987 quantitativetextural data: Inversion of crystal size distribution. J Petrol 54:913–931. doi:
988 10.1093/petrology/egs091

989 Stalder R, Foley SF, Drey GP, Horn I (1998) Mineral-aqueous fluid partitioning of trace elements
990 at 900-1200°C and 3.0-5.7 GPa: New experimental data for garnet, clinopyroxene, and rutile,
991 and implications for mantle metasomatism. Geochim Cosmochim Acta 62:1781–1801. doi:
992 10.1016/S0016-7037(98)00101-X

993 Stewart DC (1975) Crystal clots in calc-alkaline andesites as breakdown products of high-Al
994 amphiboles. Contrib to Mineral Petrol 53:195–204. doi: 10.1007/BF00372604

995 Sun S -s., McDonough WF (1989) Chemical and isotopic systematics of oceanic basalts:
996 implications for mantle composition and processes. Geol Soc London, Spec Publ 42:313–
997 345. doi: 10.1144/GSL.SP.1989.042.01.19

998 Takagi D, Sato H, Nakagawa M (2005) Experimental study of a low-alkali tholeiite at 1-5 kbar:
999 Optimal condition for the crystallization of high-An plagioclase in hydrous arc tholeiite.
1000 Contrib to Mineral Petrol 149:527–540. doi: 10.1007/s00410-005-0666-7

1001 Tatsumi Y, Otofuji Y, MAtsuda T, Nohda S (1989) Opening of the Sea of Japan back-arc basin by
1002 asthenopheric injection. Tectonophysics 166:317–329. doi: 10.1016/0040-1951(89)90283-7

1003 Thirlwall M., Singer B., Marriner G. (2000) 39Ar–40Ar ages and geochemistry of the basaltic
1004 shield stage of Tenerife, Canary Islands, Spain. J Volcanol Geotherm Res 103:247–297. doi:
1005 10.1016/S0377-0273(00)00227-4

1006 Thirlwall MF, Smith TE, Graham AM, et al (1994) High field strength element anomalies in arc
1007 lavas: Source or process? J Petrol 35:819–838. doi: 10.1093/petrology/35.3.819

1008 Ventura G (2013) Chapter 2 Kinematics of the Aeolian volcanism (Southern Tyrrhenian Sea) from
1009 geophysical and geological data. Geol Soc London, Mem 37:3–11. doi: 10.1144/M37.2

1010 Viccaro M, Giacomoni PP, Ferlito C, Cristofolini R (2010) Dynamics of magma supply at Mt.
1011 Etna volcano (Southern Italy) as revealed by textural and compositional features of
1012 plagioclase phenocrysts. Lithos 116:77–91. doi: 10.1016/j.lithos.2009.12.012

1013 Wilke M, Behrens H (1999) The dependence of the partitioning of iron and europium between
1014 plagioclase and hydrous tonalitic melt on oxygen fugacity. Contrib to Mineral Petrol
1015 137:102–114. doi: 10.1007/s004100050585

1016 Wood BJ, Blundy JD (1997) A predictive model for rare earth element partitioning between
1017 clinopyroxene and anhydrous silicate melt. Contrib to Mineral Petrol 129:166–181. doi:
1018 10.1007/s004100050330

1019 Woodhead J, Eggins S (1993) High Field Strength and Transition Element Systematics in Island
1020 arc and back-arc basalts--Evidence for multi-phase melt extraction and a DM wedge.PDF.
1021 114:491–504

1022 Zamboni D, Gazel E, Ryan JG, et al (2016) Contrasting sedimentmelt and fluid signatures for
1023 magma components in the Aeolian Arc: Implications for numerical modeling of subduction
1024 systems. Geochemistry Geophys Geosystems 17:2034–2053. doi: 10.1002/2016GC006406

1025 Zanon V, Nikogosian I (2004) Evidence of crustal melting events below the island of Salina
1026 (Aeolian arc, southern Italy). Geol Mag 141:525–540. doi: 10.1017/S0016756804009124

1027 Zellmer GF, Sparks RSJ, Hawkesworth CJ, Wiedenbeck M (2003) Magma Emplacement and
1028 Remobilization Timescales Beneath Montserrat: Insights from Sr and Ba Zonation in
1029 Plagioclase Phenocrysts. J Petrol 44:1413–1431. doi: 10.1093/petrology/44.8.1413

1030

Chapter 5

5. Introducing crystalMath, a new numerical forward model for the geochemical and textural evolution of crystal cargoes subject to magmatic open system processes.

This chapter is presented in paper format and will be submitted to a journal.

C.L Imarisio, C.J. Manning and P. Burgess equally contributed to the development of the model. C.L. Imarisio coded the geochemical calculations, P. Burgess developed the model structure and model graphical outputs, C.J Manning coded both the geochemical calculations and textural outputs. All authors made suggestions and comments on the manuscript.

Supplementary Files are attached to the thesis.

Camilla L. Imarisio[1*]; Christina J. Manning[1]; Peter M. Burgess[2]

Introducing crystalMath, a new numerical forward model for the geochemical and textural evolution of crystal cargoes subject to magmatic open system processes.

[1]Department of Earth Sciences, Royal Holloway University of London, Egham Hill, TW20 0EX, UK.

[2]School of Environmental Sciences, University of Liverpool, Brownlow St, Liverpool L3 5DA, UK.

*corresponding author: camilla.imarisio.2010@live.rhul.ac.uk; 07776 420870

Abstract

Crystal cargoes hosted in lavas have commonly been used to reconstruct magmatic histories, as they are able to record variations in crystallisation conditions in their growth zones. The textural and geochemical properties of crystal cargoes are strongly affected by open system processes, yet their modelling is difficult due to large uncertainties in thermodynamic processes which cannot easily be retrieved from natural samples. We introduce CrystalMath, a numerical forward model able to reproduce the geochemical evolution and textural zoning patterns observed in basaltic magmatic crystals. The model produces graphical outputs of the results, as well as a final thin section like output which can be compared to natural samples. The textural output and calculated crystal size distributions can be used to investigate the relationship between crystallisation and nucleation rates, and their effects on mineral proportions and melt evolution in natural samples.

Keywords

Fractional crystallisation modelling; crystal cargoes; magma mixing modelling; crystal textures; nucleation;

INTRODUCTION

The products of a volcanic eruption provide insights into volcanic behaviour and eruptive styles (Cashman et al. 2013), both of which are significantly controlled by magma composition. Whole rock data plays an important role in understanding the petrogenesis of lavas, providing information on magma composition. However whole rock is a homogenised representation of superimposed processes such as differentiation, magma mixing and crustal contamination, making it difficult to distinguish individual processes occurred during magma evolution (Davidson et al. 2007; Viccaro et al. 2010). Crystal cargoes hosted in lavas commonly include a variety of crystal populations which are the product of a number of open system processes (Davidson et al. 2007; Jerram and Martin 2008; Streck 2008). As they grow, crystals are redistributed and dispersed in different parts of the plumbing system and record pressure, temperature, composition and volatile content of the magma in which they are crystallising (Hawkesworth et al. 2004; Davidson et al. 2007; Ginibre et al. 2007; Jerram and Martin 2008; Streck 2008; Renjith 2014). Detailed geochemistry data for major and trace elements zoning patterns in crystals can therefore be used to identify the heterogeneity present in the melt and better constrain magmatic histories and evolution pathways, involving open system processes, allowing the reconstruction of magma plumbing systems structures and evolutions (Costa et al. 2003; Davidson et al. 2007; Ginibre et al. 2007; Jerram and Martin 2008; Streck 2008; Renjith 2014).

Numerical modelling in igneous petrology has evolved significantly over recent years. We now have access to highly sophisticated models able to model magma evolution under specific conditions (Ghiorso and Sack 1995; Smith and Asimow 2005; Danyushevsky and Plechov 2011). Software (e.g. MELTS and pMELTS) exist, designed to facilitate thermodynamic modelling and equilibrium in magmatic systems over a specific pressure and temperature range in order to determine the equilibrium crystallising mineral assemblage (Ghiorso and Sack 1995). However, these are focussed on whole rock and melt evolution rather than crystal cargo chemistry, and it is therefore difficult to forward model open-system processes, such as magma mixing, and their effects on the cargoes.

Efforts have been made to quantify and interpret magmatic processes based on crystal information, both chemical and textural. The Crystal Size Distribution (CSD) technique has long been used to interpret igneous textures. This technique is able to obtain the number, shape and size of the crystals which in return provide information on the physical conditions

under which the crystals nucleated, grew and the equilibrium-disequilibrium events occurred during the cooling history of a melt (e.g. Cashman and Marsh 1988; Marsh 1988; Higgins 2002; Zieg and Lofgren 2006; Armienti 2008). CSDs have also been found to be able to identify different crystal size populations within the same lava (Marsh 1988; Higgins 1996; Neave et al. 2017). Microtextures present in crystals, zoning patterns as well as sieves and other disequilibrium features, have been investigated in conjunction to geochemical variations in crystals (Nelson and Montana 1992; Davidson et al. 2007; Renjith 2014; Viccaro et al. 2016). These studies provide a qualitative and semi-quantitative description of plagioclase microtexture occurrence, however it is difficult to quantify the physical conditions under which these microtextures develop.

A necessary aspect of modelling crystallisation and magmatic evolution is the equilibrium between minerals and melt. This has been incorporated in algorithms such as MELTS and Petrolog3 (Ghiorso and Sack 1995; Smith and Asimow 2005; Danyushevsky and Plechov 2011) based on the principle of minimization of free energy (Ariskin et al. 1993) and the principle of pseudoliquidus temperatures (Nathan and Vankirk 1978). Petrolog3 (Danyushevsky and Plechov 2011) facilitates the incorporation of existing models in order to simulate melt evolution and equilibrium crystallisation during fractional crystallisation processes. Mineral-melt equilibria and measured partition coefficients between minerals and melts (Roeder and Emslie 1970; Drake and Weill 1975; Ford et al. 1983; Beattie et al. 1991; Blundy and Wood 1991, 2003; Bindeman et al. 1998; Li and Ripley 2010) have also been essential for the development of a variety of igneous thermometers and barometers, used to model the pressure and temperature conditions during crystallisation (e.g. Drake and Weill 1975; Ford et al. 1983; Beattie 1994; Putirka et al. 2003; Putirka 2005, 2008; Neave and Putirka 2017). Petrolog3 (Danyushevsky and Plechov 2011) is the most accurate model used to determine the crystallisation of an equilibrium assemblage during magmatic evolution, taking into account major and trace elements partitioning behaviour between minerals and melts, however this model is still not able to model the complexity of magma mixing and resulting in geochemically varied and mixed assemblages. Moreover model output is restricted to numerical values and does not attempt to link chemical and textural data.

This paper presents CrystalMath, a numeric forward model for magmatic evolution focussing on crystal chemistry and quantification of magmatic processes affecting the growth of crystals and their composition. CrystalMath generates an output reproducing geochemical data as well as a geometric representation of the location, orientation and size

of crystals in the "lava", providing quantitative information on crystal zoning, mineral proportions and crystal size distribution. Using geochemical and crystal size data as a means of comparison with natural samples, it provides a powerful new tool for investigating variables such as nucleation and growth rates which cannot be directly measured from a lava. With further development this model will be able to model the evolution and interaction between multiple melts to allow a better understanding of pre and syn-eruptive processes, as well as the complex relationships involved in generating the chemical variability observed in crystal cargoes.

MODEL FORMULATION

CrystalMath generates an equilibrium mineral assemblage, reproduces intra crystal compositional zoning patterns (assuming equilibrium with the surrounding melt) and macrotextural relationships formed during magmatic evolution. The geochemical model has been developed by reviewing and using a series of well-established equations published in the literature to calculate melt evolution in forward in time iterations (Figure 1). In contrast crystal size data and textural output represents a new and novel technique to investigate nucleation and growth rate processes. CrystalMath is currently optimised to crystallise an olivine ± plagioclase ± clinopyroxene assemblage.

Model source code

CrystalMath is written in MATLAB, and will run in any version 2014b or later. The model is composed of approximately 2103 lines of code, arranged in functions within a single m file. Main calling routines are at the beginning of the code, most calculations in the middle and the graphic plotting routines at the end. The function containing the main model time loop is called "crystalMathOneRun" and starts at line 76. This source code is given in Appendix 1. Comment statements are included throughout the source code to explain key details and make maintenance and development of the code easier.

Input parameters

User defined input parameters (Figure 1) include melt composition, water content and pressure of storage and crystallisation. The model requires an initial melt composition consisting of 11 major oxides SiO_2, Al_2O_3, Fe_2O_3, FeO, MgO, CaO, Na_2O, K_2O, TiO_2, MnO, P_2O_5 and water, all in weight percent (wt.%). Also required are 8 trace elements Ni, Cr, Sc, Sr, Ba, Rb, Zr, and Nb, all in ppm. Initial pressure of storage conditions can be set and

changed throughout the model run to simulate magma ascent. Temperature instead is recalculated from the melt composition at each iteration, however an arbitrary value is put in place at the start of the run to function as a placeholder within the pressure and temperature data matrix. Model run parameters such as number of iterations, maximum number of crystals and crystal size, nucleation rates and time step can also be varied and defined by the user to represent those observed from petrological observations.

Model algorithm and data structures

CrystalMath models a 40 x 20 x 10 mm volume of magma. Dimensions were selected to represent a volume the same length and width as a thin section but thicker in the z direction. This is assumed to represent a sample from the centre of a chamber with 0 mass and heat flux out of the model volume. The model is mostly deterministic, except for one stochastic element that calculates crystal nucleation points using a random number generator. The model algorithm uses both set and user defined input parameters to define initial melt conditions and initiate the crystallisation time loop, in which fractional crystallisation of an olivine ± plagioclase ± clinopyroxene assemblage is modelled (Figure 1). The crystallisation loop continues until one of the user defined maximum number of iterations, maximum crystal number or maximum crystal size is reached, at which point the crystallisation process is ended and the model outputs are generated (Figure 1). From the output it is possible to obtain further results after post processing (Figure 1). Data are stored throughout the model runs using two structure arrays. The structure array *crystConst* contains data which do not change over time as the model progresses, such as mineral type and crystal centre point coordinates. The *crystVar* data structure contains information that changes at each model time step, such as mineral composition for each growth zone. Melt major and trace elements composition are stored in matrices sized by the number of elements and number of iterations.

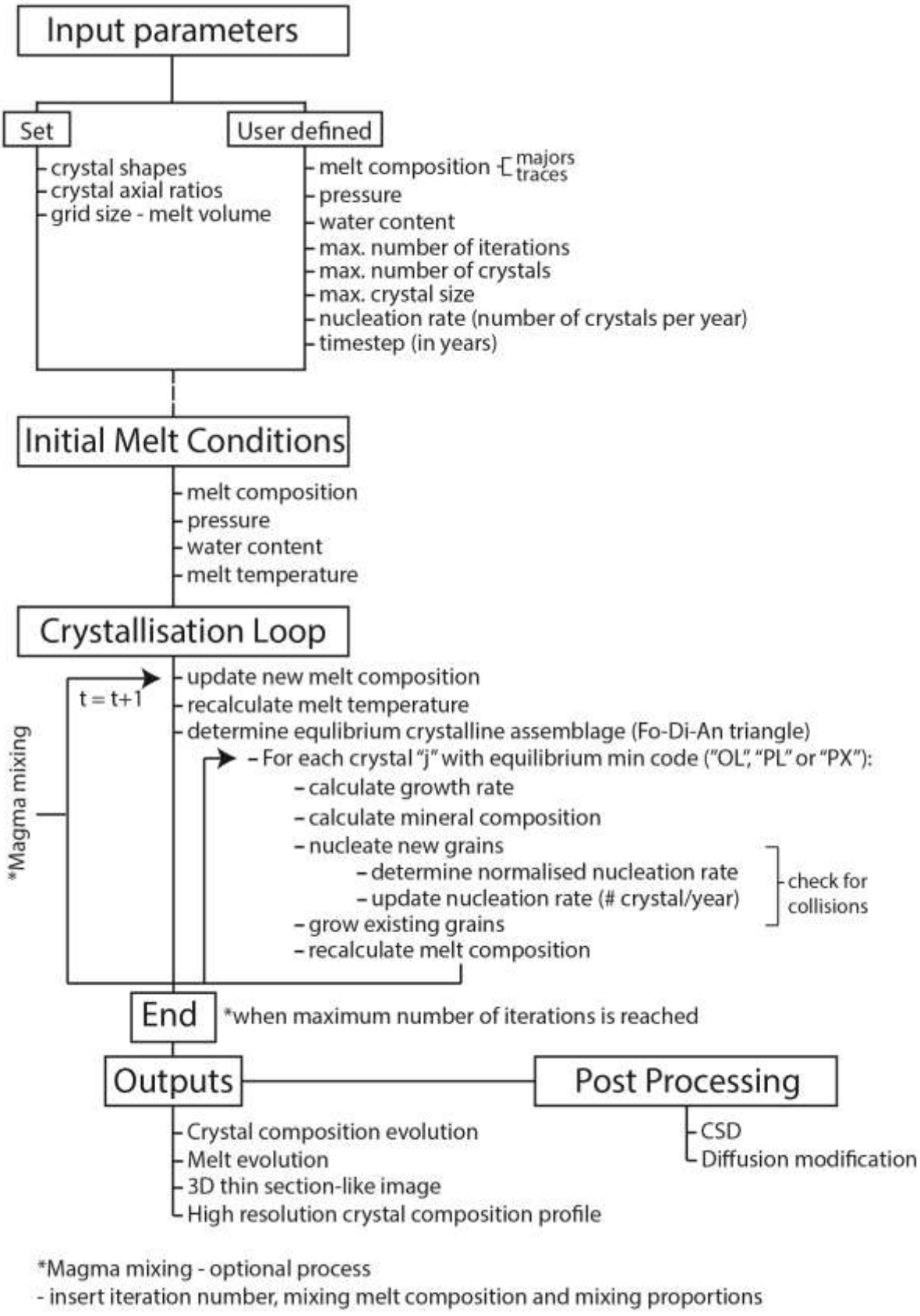

Figure 1: CrystalMath model structure and flowchart.

Modelling crystallisation and crystal growth

Following the input parameters, the crystallisation loop simulates a numerical forward model of fractional crystallisation with a typical time step of 1 year that provides good resolution of the cooling and crystallisation histories considered here. Used equations and references are in Appendix 2.

Calculation of melt composition

For the first iteration, melt composition is set by the user. For the following iterations the melt composition is recalculated using:

$$C_L = C_0 F^{Kd-1} \quad \text{Eq.1}$$

$$C_S = C_0 KdF^{Kd-1} \quad \text{Eq.2}$$

For major (eq.1) and trace elements (eq.2, (Gast 1968)) respectively where *F* is the weight fractionation of liquid remaining, *C* is the elemental concentration and *Kd* is the partition coefficient for the element in consideration. The model the equation accounts for the removal of one single mineral phase per iteration rather than the simultaneous removal of multiple phases as the model is set to crystallise and remove one crystal at a time (Figure 1).

Calculation of melt temperature

Melt temperature is calculated at the start of each iteration according to the new melt composition using the Ford algorithm (equation 3, (Ford et al. 1983)), which is based on olivine-liquid cation partitioning behaviour, where the Mg-Fe^{2+} partition coefficients equation may be used as a geothermometer with an average temperature error of ±7.85°C (Ford et al. 1983). Whilst this does not affect the forsterite content in olivine and Mg# in clinopyroxene directly, the error can have a 1% effect on plagioclase anorthite content. Fe-Mg partitioning between olivine and melt is well established at 0.3±0.03 (Roeder and Emslie 1970), making the olivine-liquid thermometer robust. Olivine is generally the first crystallising phase in a Mg-rich melt, therefore high-forsterite olivines provide the most reliable estimates for initial melt temperature. The thermometer has been developed from a range of experimental glass composition, with MgO values ranging between 22.02 and 1.43 wt.% therefore allowing temperature calculations for a wide compositional range (Ford et al. 1983).

Determination of equilibrium crystallising assemblage

The mineral type ("OL", "PL" or "PX") being crystallised at each iteration is determined using a Fo-Di-An triangle plot (Osborn and Tait 1952). CIPW norm calculations are carried out on the new melt composition and proportions of forsterite, diopside and anorthite are transformed into coordinates and plotted on the triangle plot. The built-in inpolygon function, which checks whether the point locates inside or on edge of polygonal region of the triangle plot, determines the mineral field in which the data point plots and therefore the mineral type to be crystallised from the current melt composition. Once the mineral type has been determined, all crystals with the equilibrium mineral code assigned proceed to grow and new minerals of the same type nucleate (Figure 1). The inpolygon function results in the fact that only one phase can be crystallised at any one time and therefore modelling along the cotectic line is not allowed by the model. The melt composition zig-zags across the cotectic line into different minerals stability fields but does not move across it in a straight line (Danyushevsky and Plechov 2011)).

Nucleation rates and nucleation positions

For CrystalMath runs, a set combination of crystal crystallisation rates (expressed as number of crystals per year) must be specified. The crystallisation rate for each crystal type is normalised to a nucleation rate curve function (Hort 1998) and determines the number of new crystals of that type created at each model time step. Currently the model does not allow the modelling of grain entrainment and resorption, meaning that every grain that nucleates proceeds to grow and is present in the final output. The locations for crystal nucleation are randomly determined coordinate points within the model's grid which do not correspond with the position of previously crystallised grains.

Calculation of mineral compositions

Following growth rate determination and calculation of new crystal edge coordinates, the model calculates major element equilibrium mineral compositions for olivine, plagioclase and pyroxene for each iteration using stoichiometric calculations and equilibrium end member calculations for forsterite, anorthite and clinopyroxene Mg# (Ford et al. 1983; Putirka et al. 2003; Putirka 2005). Trace element determination for each crystal is based on mineral-melt partitioning models (Blundy and Wood 1991; Bindeman et al. 1998; Li and Ripley 2010) and published partition coefficient (K_D) values from the GERM database

(Appendix 2). For elements where the value is not calculated but input directly, it is possible to vary the K_D using recommended values from the literature.

Crystal Geometry and Calculation of growth rates

Geometric information such as crystal shapes and axial ratios are determined by the crystalline structure of a mineral (Higgins 2006). These parameters (Deer et al. 2013) are currently hard-coded in the model and summarised in Table 1. Crystal shape has been simplified so that each crystal is defined in three dimensions using a reduced number of crystal apices that approximate idealised crystal geometries in 3D (Figure 2). A reduced number of apices reduces computation time during the time loop and also facilitate faster plotting. Higgins (2006) showed that calculating, recorded and plotting all the crystal apices would not significantly change calculated crystal volumes from those of a simplified mineral shape. Olivine, plagioclase and clinopyroxene are coloured in red, grey and green respectively (Figure 2) with the lightest and darkest shades representing the most primitive and most evolved composition respectively for the current model run.

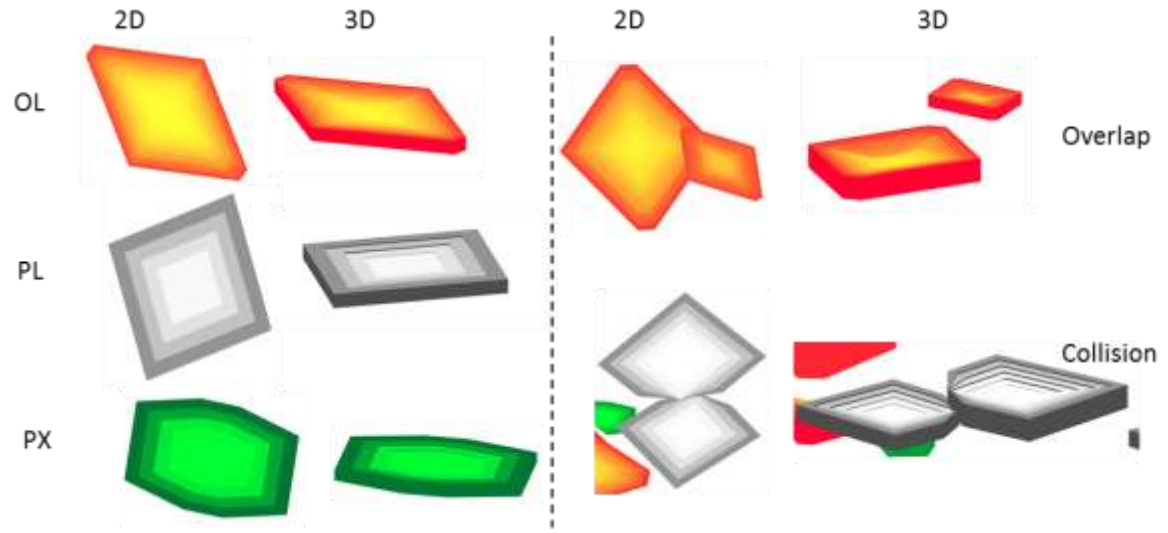

Figure 2: 2D and 3D view of olivine, plagioclase and clinopyroxene crystals alongside 2D and 3D view showing the effects of crystal overlap and crystal collision on the final model output.

Growth rates are calculated for each mineral following the growth rate equation by (Toramaru 1991, equation 7) where the growth rate is a function of temperature, concentration of crystallising components in the melt, and elemental diffusion coefficient between mineral and melt (Toramaru 1991). In all of the model runs here, temperature varies by less than 100°C, depending on the length of the model run, and therefore melt composition, and availability of crystallising components in the melt, acts as the main

control on growth rate. Once a growth rate is determined for each crystal type, growth rates for the three main axes for each crystal type are scaled by the axial ratio. Mineral composition is assumed to be in equilibrium with melt composition, so the composition of the new volume of crystal growth is recorded as the composition in equilibrium with the current melt. The new melt composition is recalculated at the end of each single mineral growth loop, where the amount of melt crystallised is determined by calculating the volume of the mineral phase being removed. Once all pre-existing crystals have been crystallised and new ones are nucleated, the model moves to the next iteration where the new melt composition is input into the model and the temperature and equilibrium crystalline assemblages are recalculated as previously mentioned and the crystal growth and crystallisation loop starts again. It is important to note that the order in which the crystals grow is randomised, in order to better replicate the compositional variety observed in rim compositions of natural samples.

As crystals grow, they may collide with other crystals. Collisions disrupt crystal geometry by blocking the growth of one of more crystal apices, leading to variations in crystal geometry (Figure 2). Collisions between crystals where crystal apices would penetrate the volume of another adjacent crystal are determined using the inpolygon function, which checks at each iteration of crystal growth whether the new crystal apex coordinates are inside another pre-existing crystal (or polygon). In the event of collision with another grain, only the colliding crystal corners will stop growing, whilst the rest of the crystal will continue to grow. Moreover, the crystals are set to be randomly oriented within the 3D grid, therefore their x-y axis view shape could be distorted, replicating the thin section - cut effect that can be observed in natural samples (Higgins, 2006).

Mineral Type	**Olivine (OL)**	**Plagioclase (PL)**	**Clinopyroxene (PX)**
X-section Crystal Shape	6-sided	4-sided	8-sided
Axial Ratios (a:b:c)	0.4663 : 1 : 0.6146	0.635 : 1 : 1.1003	1.0888 : 1 : 0.5833

Table 1: set input parameters for crystal geometry: size and axial ratios from Deer et al. (2013).

Optional processes

CrystalMath gives the user the additional option of introducing a magma mixing event at a specific iteration number, in order to simulate a recharge or magma mixing event, for example just prior to eruption. For this option the user can define the composition of the input melt and the mixing proportions. The new melt composition is then fed into the model and the crystal growth loop continues as illustrated above. Similar calculations can be implemented to simulate ascent by varying the storage pressure and water content.

Model output and post processing

Outputs

The outputs of the model comprise geochemical data plots, a 3D visualisation of all the crystals formed in the model volume, a plot of the crystals visible in a thin-section slice through the model volume, and simple CSD plots for each mineral type. The geochemical plots include a detailed compositional history of the melt, as well as pressure and temperature conditions, for each iteration. The model also generates a compositional history for each mineral phase, consisting of major and trace elements composition and equilibrium end member for each iteration. Core – rim compositional profiles for plagioclase grains are also output as a text file. Examples of all graphical outputs from the model are shown in Appendix 3.

Post processing

Diffusion modification can be applied to the compositional profile in each crystal as a post-processing calculation, using equations from (Costa et al. 2003) and a timescale determined by the user.

RESULTS

Modelling different starting melt compositions

A range of starting melt compositions (Table 2, Figure 3, Appendix 4) was used in order to test the model's sensitivity to melt composition and melt evolution through the Fo-Di-An triangle.

	TAS	Setting	MgO wt.%	Melt T (°C)	Fo %
Melt 1	Basalt	Torfajökull, Iceland	6.88	1222	80.0
Melt 2	Basalt	Salina, Aeolian Islands	5.10	1138	*81.3
Melt 3	Basaltic Andesite	Salina, Aeolian Islands	4.04	1124	*76.2
Melt 4	Andesite	Salina, Aeolian Islands	2.09	1103	*71.1
Melt 5	Rhyolite	Torfajökull, Iceland	0.29	1109	*41.9

Table 2: different starting melt compositions used to test CrystalMath, alongside model calculated melt temperature (Ford, 1981) and equilibrium Forsterite. * Indicates models where olivine was not the equilibrium crystalline assemblage at the start of the run. XRF data in appendix 1 (Icelandic compositions: (McGarvie 1984; Macdonald et al. 1990; McGarvie et al. 1990); Salina compositions from Chapter 4).

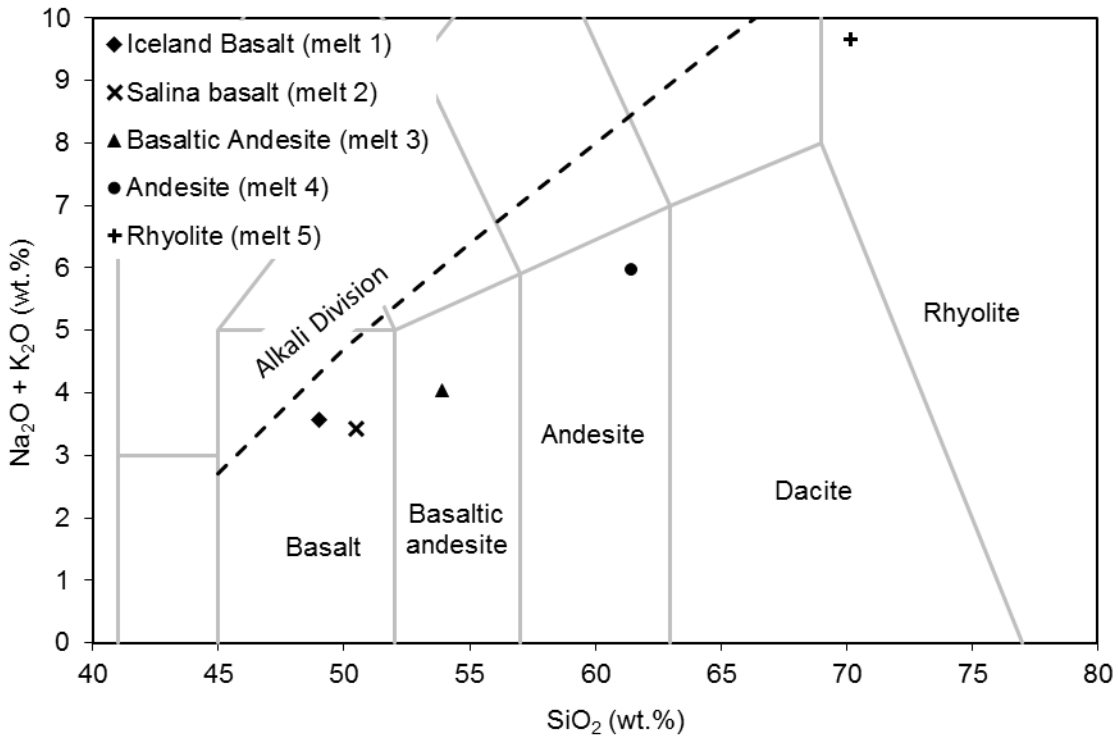

Figure 3: TAS diagram illustrating the classification of the melt compositions used to test the model. Data in appendix 1 (Icelandic compositions: (McGarvie 1984; Macdonald et al. 1990; McGarvie et al. 1990); Salina compositions from Chapter 4).

Tracking melt evolution across the Fo-Di-An triangle shows how melt chemistry is affected by nucleation and growing crystals. Two different types of basalts were modelled, one from Iceland, and one from Salina in the Aeolian Arc (Table 2). The Icelandic basalt (melt 1) follows a melt evolution consistent with that of a tholeiitic melt, where olivine crystallisation is followed by plagioclase and later clinopyroxene (Figure 4), consistent with its classification on the TAS diagram (Figure 3). The Salina basalt (melt 2) would also be expected to follow the evolution trend of a tholeiite (Figure 5). However, the melt starts its evolution in the plagioclase field, and moves to olivine and diopside, resulting in a pl-ol-pl-ol-cpx crystallisation sequence as opposed to an expected ol-pl-px sequence as observed in natural samples. This is probably due to the fact that the basalt is already relatively evolved (~5.10 wt.% MgO, Table 2) and contains high Ca and Al. In addition, calc-alkaline evolution trends are different to tholeiitic ones and the lack of Fe-Ti oxides crystallisation as well as amphibole largely affects the melt composition and its crystallisation path. Similarly, due to the model being optimised for crystallisation of ol-pl-px, basaltic andesitic, andesitic and rhyolitic melts crystallisations (3, 4 and 5) cannot be replicated. They initially plot in the anorthite field of the Fo-Di-An triangle and whilst the basaltic andesite proceeds to crystallise clinopyroxene (Figure 6), the andesite and rhyolite migrate across to the olivine

300 field therefore producing an unrealistic crystalline assemblage (Figure 7, Figure 8). The
301 rhyolitic melt (melt 5) fails to complete 40 iterations as the evolution trend approaches the
302 non-defined spinel field on the Fo-Di-An triangle and therefore the model fails to recognise
303 a crystallising phase (Figure 8). Whilst the spinel field could be added to the model, this
304 would still represent an unrealistic crystalline assemblage for a rhyolitic melt. These model
305 runs show that the model is optimized for basaltic compositions which start in the olivine
306 field, and proceed to either the plagioclase or clinopyroxene field. Basaltic andesitic
307 compositions can be used with caution, but the model is not yet suitable for felsic
308 compositions.

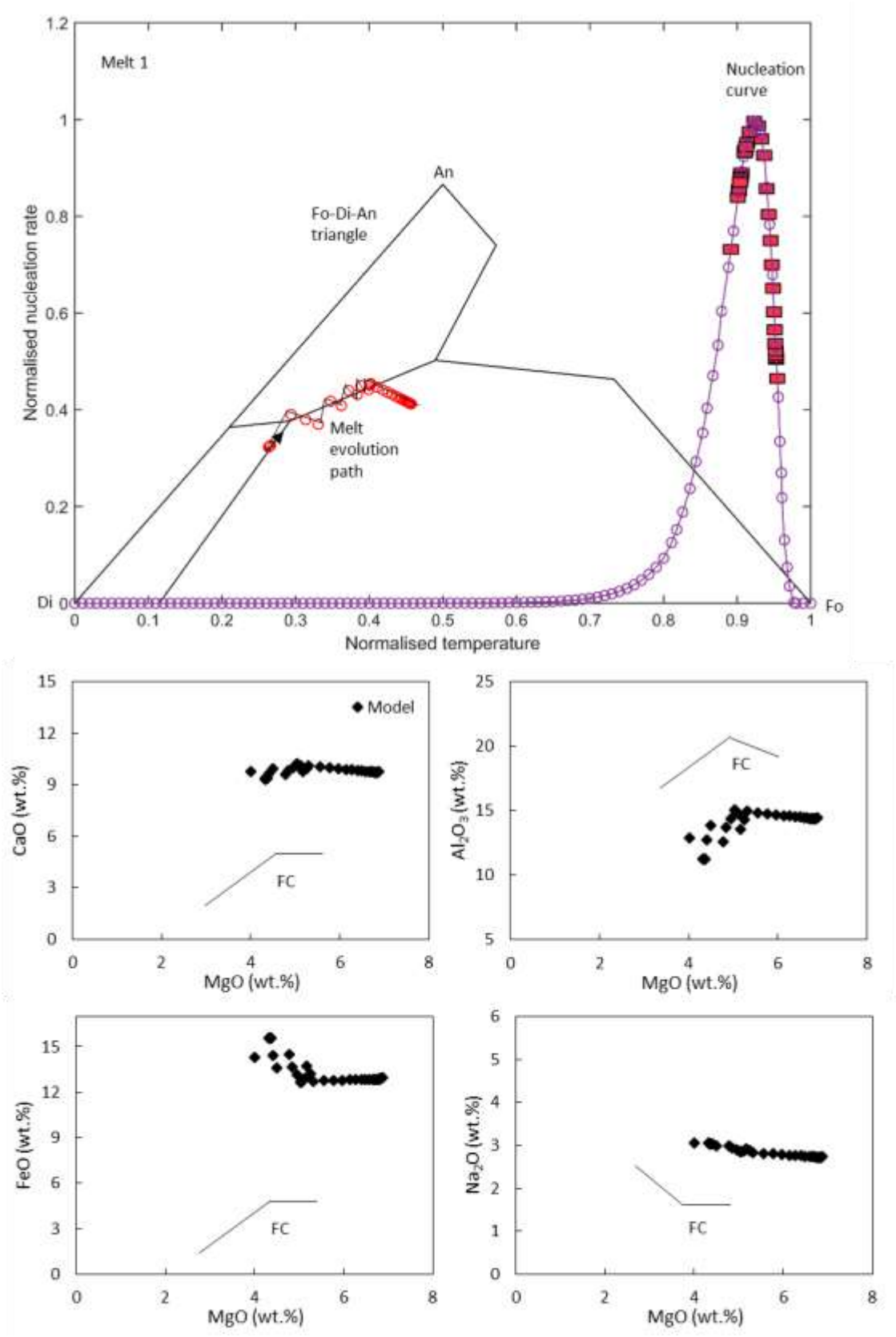

Figure 4: Melt 1 evolution along the Fo-Di-An triangle showing a tholeiitic ol-pl-px trend and major elements trends though fractional crystallisation compared to the expected trend. The x and y axis refer to the nucleation curve (generated from Hort (1998)) and do not apply to the Fo-Di-An triangle plot.

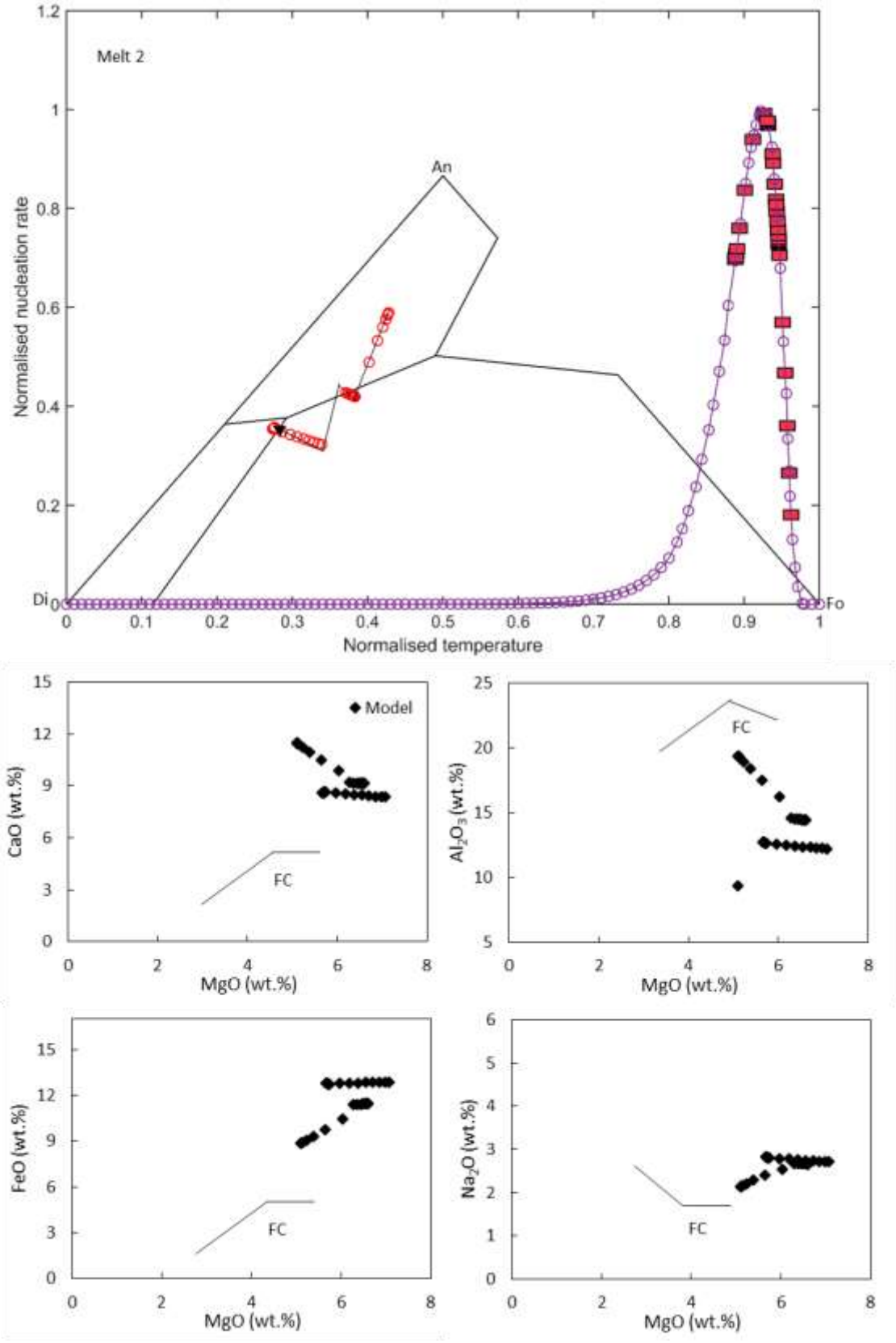

Figure 5: Melt 2 evolution along the Fo-Di-An triangle showing a pl-ol-pl-ol-px trend and major elements trends though fractional crystallisation compared to the expected trend. The x and y axis refer to the nucleation curve (generated from Hort (1998)) and do not apply to the Fo-Di-An triangle plot.

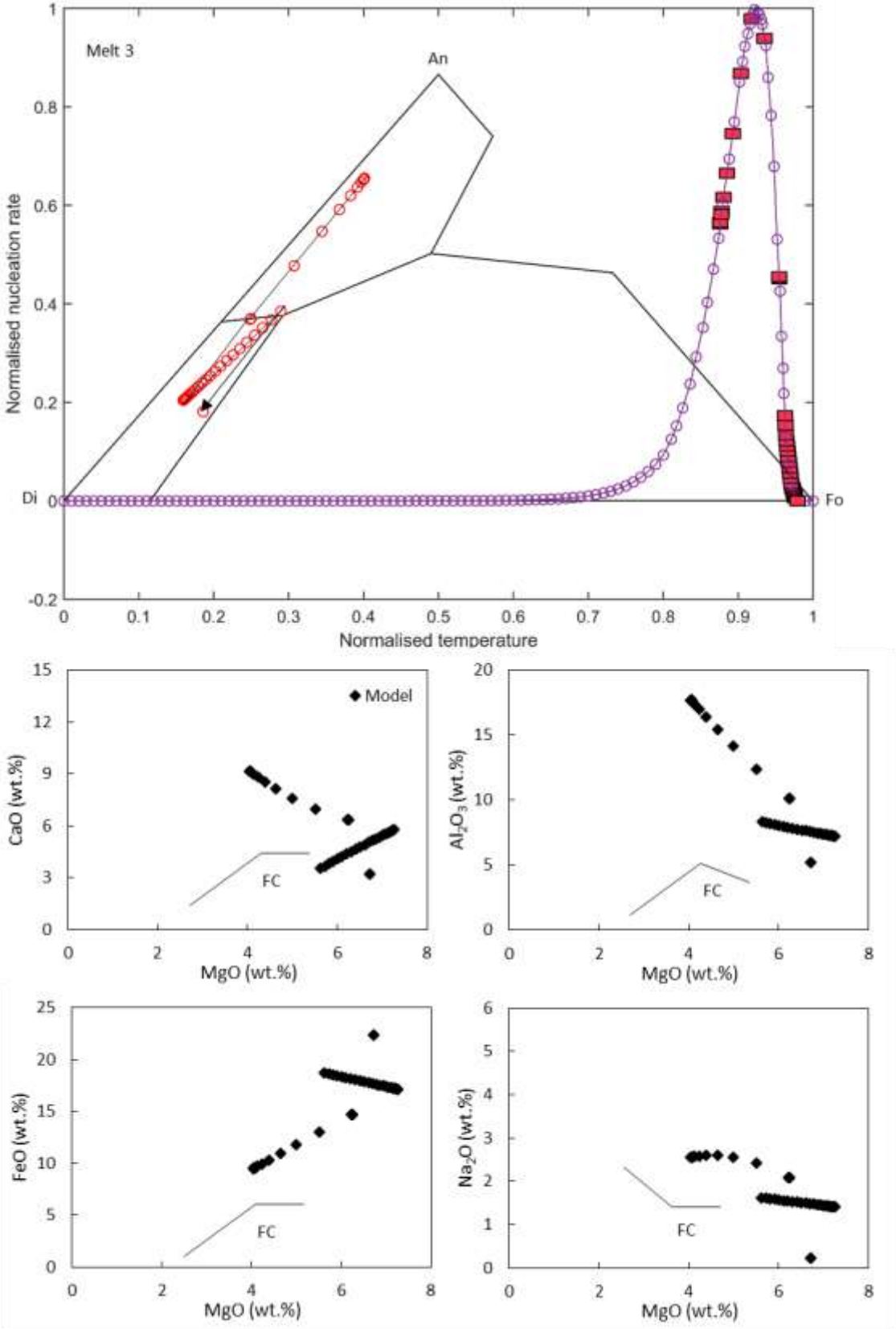

Figure 6: Melt 3 evolution along the Fo-Di-An triangle showing an pl-px trend and major elements trends though fractional crystallisation compared to the expected trend. The x and y axis refer to the nucleation curve (generated from Hort (1998)) and do not apply to the Fo-Di-An triangle plot.

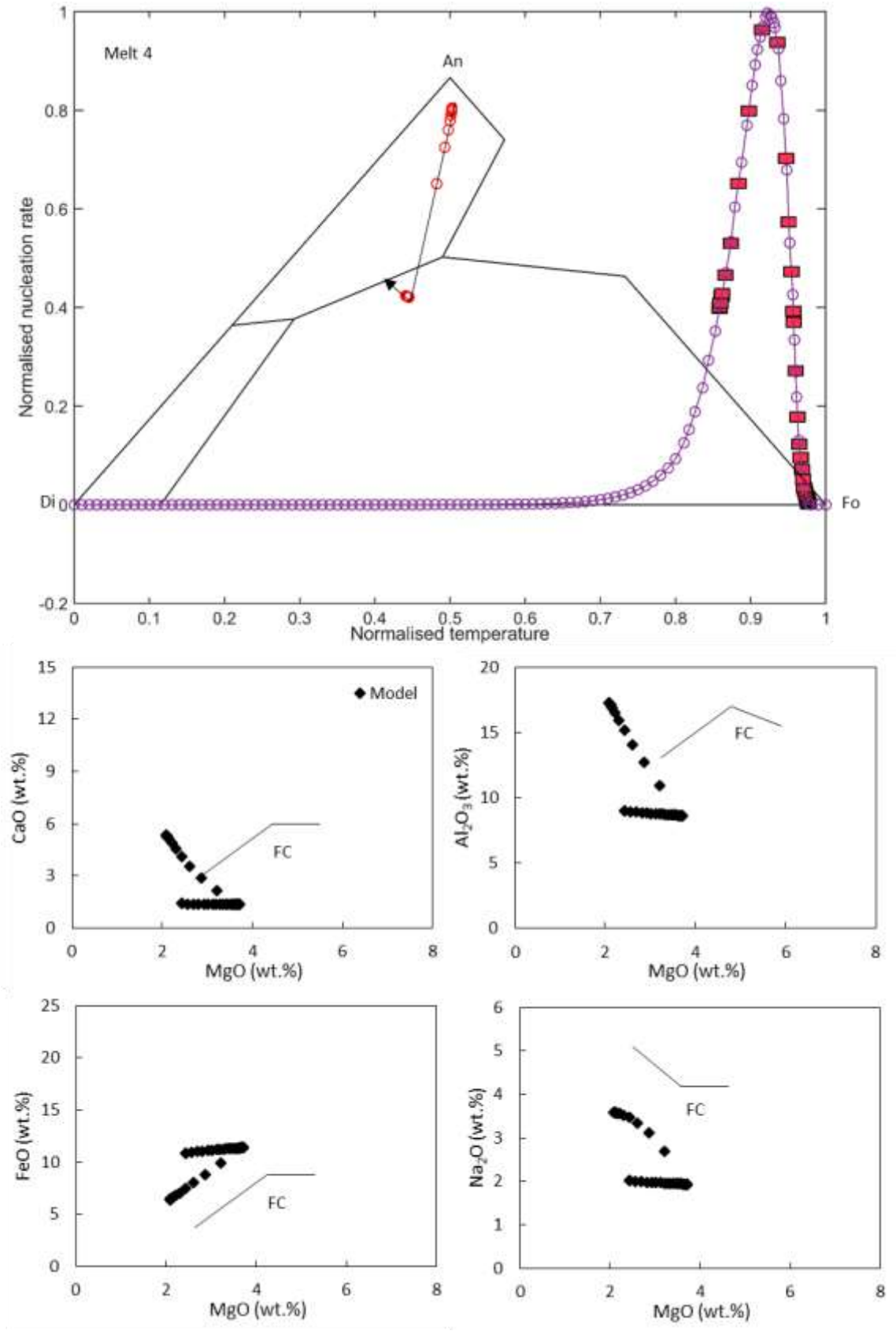

Figure 7: Melt 4 evolution along the Fo-Di-An triangle showing a pl-ol trend and major elements trends though fractional crystallisation compared to the expected trend. The x and y axis refer to the nucleation curve (generated from Hort (1998)) and do not apply to the Fo-Di-An triangle plot.

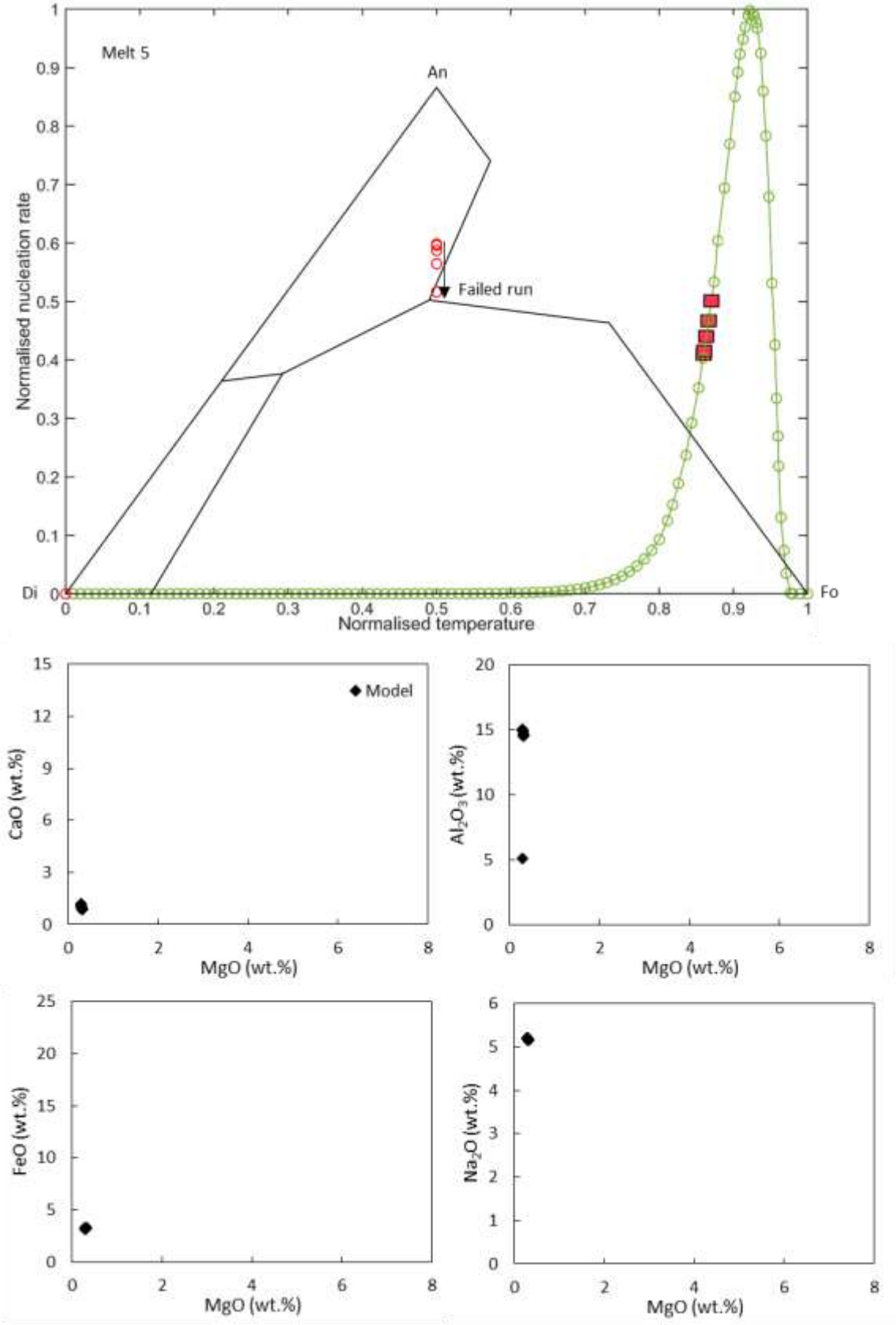

Figure 8: Melt 5 evolution along the Fo-Di-An triangle showing a failed model run due to the evolution trend entering the undefined spinel field on the Fo-Di-An triangle at iteration 5-6. The x and y axis refer to the nucleation curve (generated from Hort (1998)) and do not apply to the Fo-Di-An triangle plot.

Modelling fractional crystallisation

As previously shown, the model is optimised for a limited range of basaltic composition due to the crystalline assemblage being limited to olivine, plagioclase and clinopyroxene. Such limited range in composition is however consistent with experimental results showing the crystallisation of olivine, plagioclase and clinopyroxene happening within a limited range of SiO_2 (2-3 wt.%), temperature (~1170-1050 °C) and melt fraction (1-0.6) (Nandedkar et al. 2014; Caricchi and Blundy 2015). The results of Torfajökull basalt (melt 1) fractional crystallisation models (Figure 4, Figure 9, Table 2) have been compared to major and trace element Harker diagrams of a database of samples from Torfajökull, Iceland (Chapter 3). Major elements which are largely controlled by the crystalline assemblage (e.g. CaO and MgO) show trends consistent with those observed in published data (Figure 9). A steady decrease in olivine is controlled by olivine fractionation, and a decrease in CaO and Al_2O_3 is observed at the onset of plagioclase fractionation, which is accompanied by a drastic increase in FeO, as magnetite is not being crystallised in the model, and less prominent increase in Na_2O concentrations. Zig zag patterns observed in the trend at the onset of plagioclase crystallisation are consistent with the zig zag trends across the olivine-plagioclase cotectic (Figure 4).

Modelled trace element concentrations broadly follow the trends of the Torfajökull compositional range (Figure 9), consistent with melt 1 being a Torfajökull basalt (Figure 18, Table 2). Ni decreases rapidly with decreasing MgO, whilst Sr and Ba increase slowly with decreasing MgO. Incompatible elements such as Zr increase slowly throughout the olivine crystallisation window, with a steep increase at the onset of plagioclase crystallisation (Figure 9). Precise modelling of trace elements has been proven difficult due to the large error imposed by partition coefficients, nevertheless the overall trends are consistent with those observed in analysed and published data for Torfajökull (McGarvie 1984; Macdonald et al. 1990; McGarvie et al. 1990). Intermediate compositions (MgO ~4 wt.%) are not a good match in the model run, this is due both to the fact that the model is optimised for more primitive compositions and that the intermediate products of Torfajökull are interpreted to be a product of mixing and not fractional crystallisation (chapter 3). Equilibrium crystal cargo chemistry is calculated from the whole rock throughout the model run. Plagioclase anorthite is plotted against commonly utilised plagioclase trace elements such as Sr, Ba and Mg whose partition coefficients can be calculated using published equations (Blundy and Wood 1991; Bindeman et al. 1998) (Figure 10). Flat trends at constant anorthite against

number of iterations (during the model run) represent periods of the model run where plagioclase is not being crystallised and therefore its calculated equilibrium anorthite is not being updated in the model and should therefore be disregarded. Overall anorthite shows a decreasing trend An_{82-72} with increasing number of iterations consistent with fractional crystallisation (Figure 10). Similarly to whole rock modelling, trace element partitioning behaviour can cause large errors in plagioclase modelled compositions. Figure 10 shows Sr, Ba and Mg modelling where Sr and Ba have been tested using both the Blundy and Wood (1991) model (black) and the Bindeman et al. (1998) model (yellow). It is observed that the latter better matches the trends and concentration observed in the analysed plagioclase from Torfajökull for both Sr and Ba models (Figure 10).

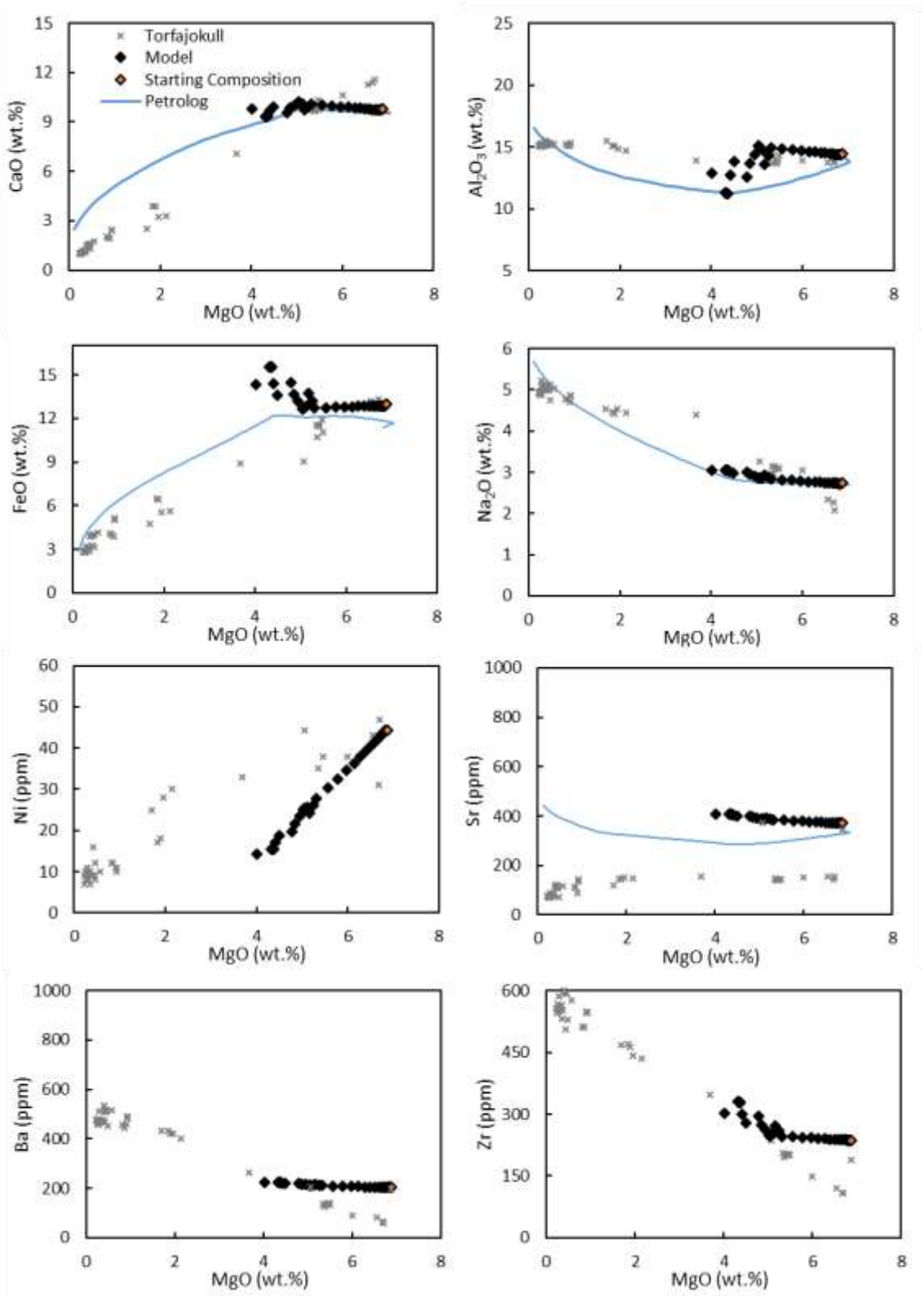

377

378 Figure 9: major and trace element Harker diagrams comparing model melt 1 fractional
379 crystallisation trends with that of published data from Iceland (McGarvie 1984; Macdonald
380 et al. 1990; McGarvie et al. 1990). The blue line indicates Petrolog3 model runs from a
381 transitional basalt composition with MgO 6.8 wt.% with a 100% fractionation of olivine,
382 clinopyroxene, plagioclase and magnetite in 0.01% steps at a pressure of 2 kbars.

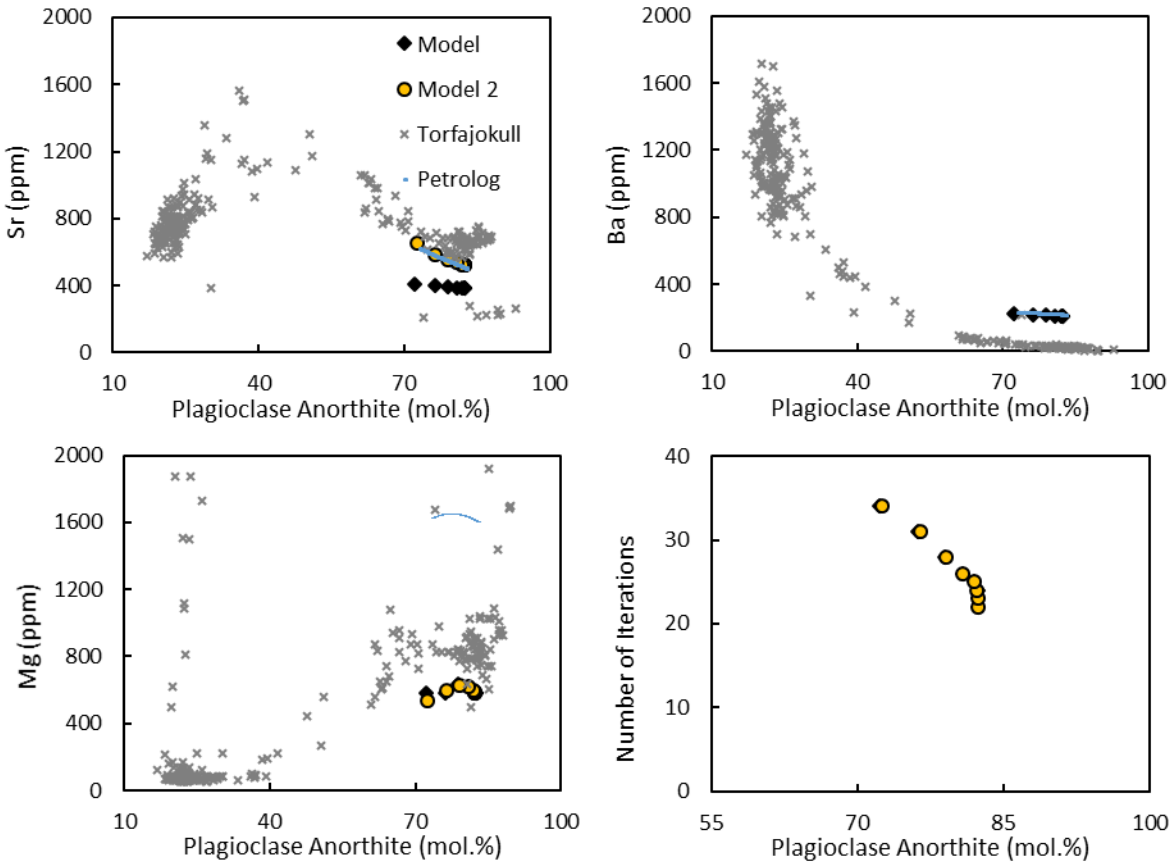

383

384 Figure 10: fractional crystallisation model results for plagioclase composition compared to
385 plagioclase laser mineral data from Iceland (Chapter 3). Black model 1 line indicates
386 partition coefficient calculations for Sr and Ba from Blundy and Wood (1991) and yellow
387 model 2 line partition coefficients for Sr and Ba from Bindeman et al. (1998). The blue line
388 indicates Petrolog3 model runs from a transitional basalt composition with MgO 6.8 wt.%
389 with a 100% fractionation of olivine, clinopyroxene, plagioclase and magnetite in 0.01%
390 steps at a pressure of 2 kbars.

391 ***Comparison with Petrolog3***

392 As a comparison, test model runs were plotted alongside fractional crystallisation model
393 runs using Petrolog3 (Danyushevsky and Plechov 2011). The models were both run using a
394 parent trachytic composition with MgO 6.8 wt.% and a pressure of 2 kbar. Petrolog3 runs
395 were carried out assuming 100% fractionation of olivine, clinopyroxene, plagioclase and
396 magnetite in 0.01% steps. Figure 9 shows that whilst initial model melt compositions are
397 comparable, the evolutionary trends are not, with the exception of CaO. This can largely be
398 attributed to the fact that, as shown by the lack of decreasing Ni, the onset of plagioclase
399 crystallisation occurs earlier on in the Petrolog3 model than in our runs. Nevertheless the
400 plagioclase composition and trends are comparable (Figure 10), with the exception of Mg.
401 Similarly, the fractionation of magnetite allowed in the Petrolog3 run allows for smoother

trends in elements such as FeO, which are not present in CrystalMath runs due to the lack of modelling for magnetite. The main difference which can be observed is the extent of fractional crystallisation reached by the Petrolog3 run which extends to rhyolites with 1 wt.% MgO. The main reason for this, and a large difference between this model and CrystalMath, is that fractional crystallisation processes are not modelled volumetrically but by percentages of phases removed. This ensures a smooth evolutionary trend extending to highly silicic compositions, nevertheless these may not be realistic, as suggested by the associated shorted plagioclase crystallisation times, which terminate at $An_{\sim 70}$.

Modelling magma mixing

Magma mixing models were carried out using Torfajökull basalt and Torfajökull rhyolite (melt 1 and Melt 5, Table 2), with mixing proportions of 0.7 and 0.3 respectively. The magma mixing event was programmed to occur at iteration 26 out of 28 total iterations in order to simulate magma mixing shortly prior to eruption, as reflected by the zoning patterns in crystals (Figure 11). The results of the mixing event are observed in all melt major and trace element compositions (Figure 12). As expected the hybrid compositions lie on a mixing line with the rhyolitic end member, and the plagioclase composition abruptly changes from An_{82} to An_{62} mol.% (Figure 13). Trace element concentrations for Sr, Ba and Mg also change to 522-658 ppm (Sr), 24-84 ppm (Ba) and 594-630 ppm (Mg) (Figure 13). The thin section like output shows plagioclase crystals with clear compositional variations, strongly changing towards the rim due to the mixing event (Figure 11). Zoomed in crystals show compositional variation from the cores to the rim, where the rims of larger crystals present the same composition as that of the cores of smaller later formed crystals (Figure 11), matching observed patterns in natural samples. Mg diffusion modification was modelled on plagioclase core to rim compositional profile for residence timescales of 10 days and 1 hour (Figure 14). In this case diffusion modelling was carried out using the one-dimensional finite-element solution model using the method by Costa et al. (2003). We used an An-dependent experimentally determined Mg diffusion coefficient (LaTourrette and Wasserburg 1998), with the equilibrium concentrations for each zone and the temperature being extracted from the model outputs at the time of the iteration where the diffusion calculations are carried out. Due to the dependence of the diffusion coefficient on plagioclase compositions meaning that these timescales can't be constrained with confidence on short timescales, nevertheless the calculations are present as placeholders in

the model and could be used to diffuse profiles for other element and crystal phases in the model.

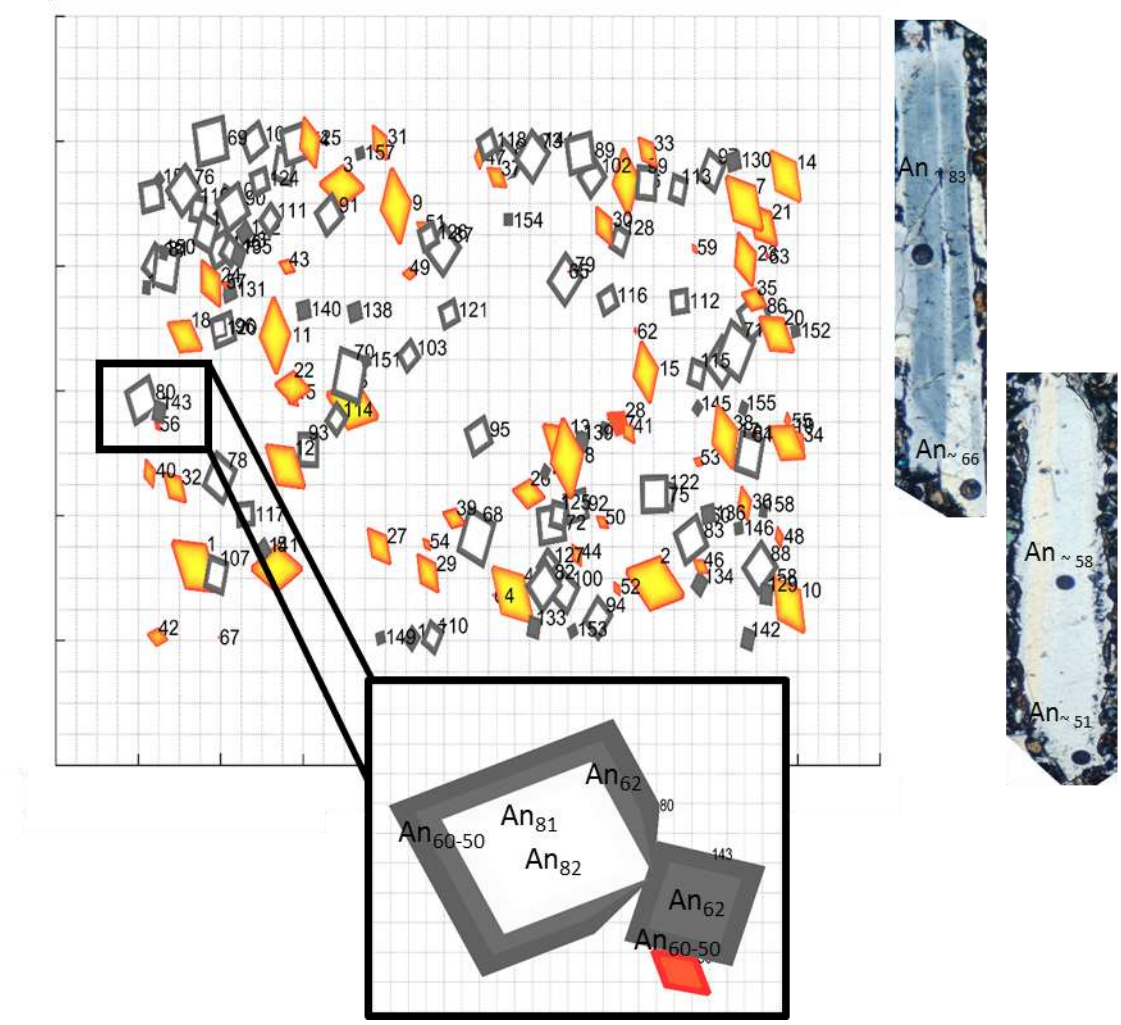

Figure 11: thin section like output for the magma mixing event displaying abrupt zoning in plagioclase crystals and different plagioclase populations, as observed in the natural samples.

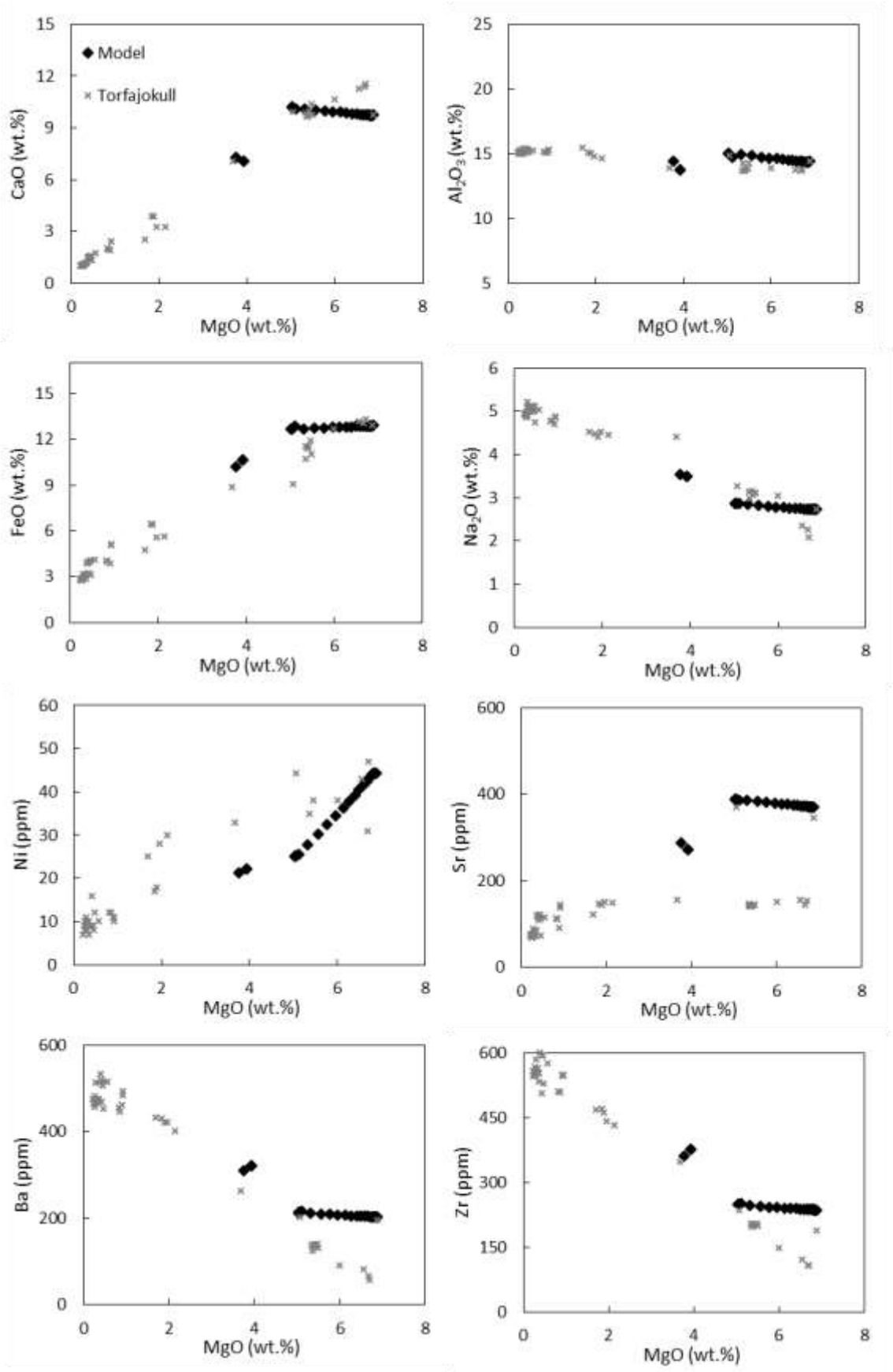

Figure 12: effects of modelled magma mixing event on the melt composition. Published data for Iceland from: (McGarvie 1984; Macdonald et al. 1990; McGarvie et al. 1990).

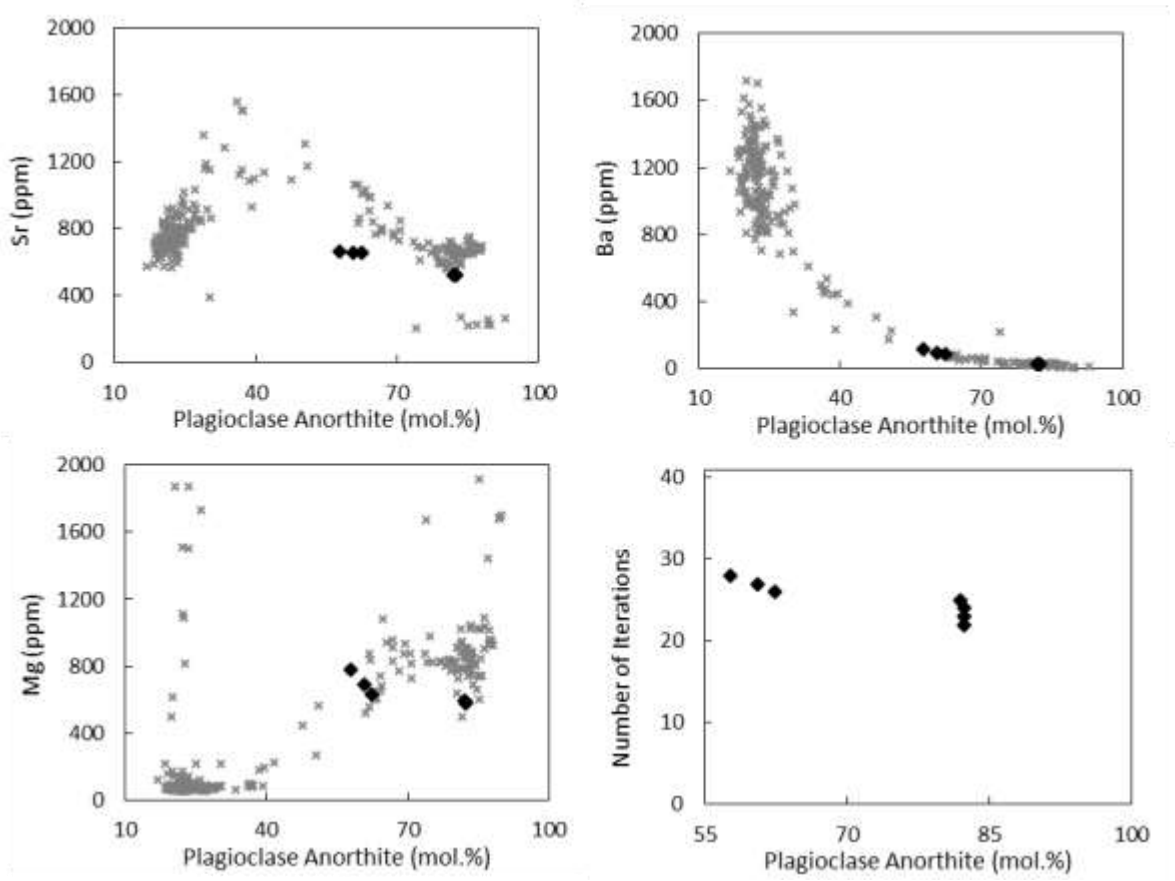

445

446 Figure 13: effects of modelled magma mixing event on plagioclase composition (Chapter
447 3).

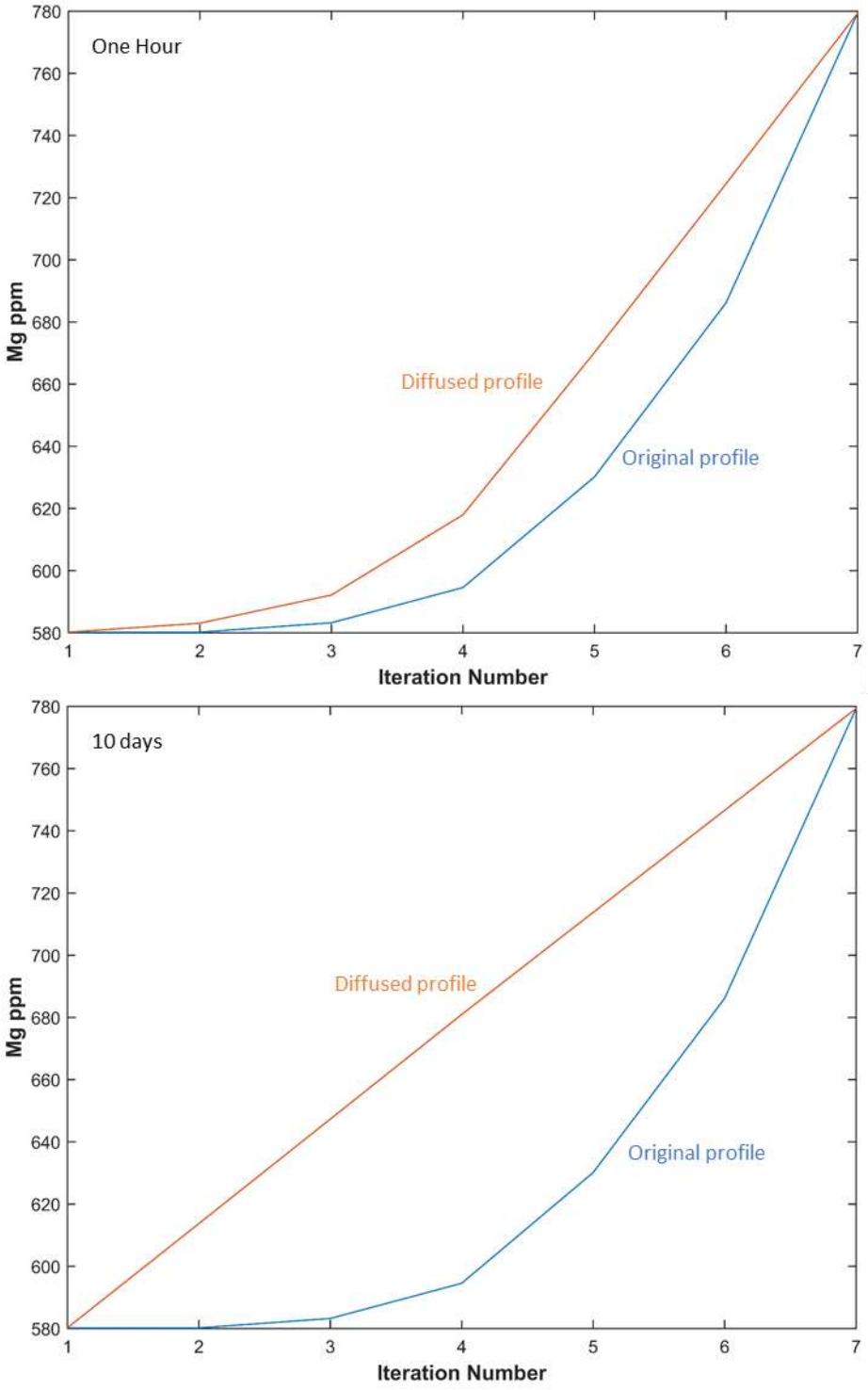

Figure 14: Mg diffusion modification modelling results at 1156 °C (model temperature at the last iteration) using the method by Costa et al. (2003) for one hour and 10 days. The original profile is that of the model output at the end of a model run, where a composition is retrieved from each crystal zone from core to rim along plagioclase long axis.

Determination of nucleation rates using multiple model runs and a parameter space plot

CSDs can be used as a tool to investigate and quantify crystal nucleation, growth and mixing (Cashman and Marsh 1988; Marsh 1988; Higgins 2000; Zieg and Lofgren 2006; Armienti 2008). The semi logarithmic CSD trend through a single population is expressed as:

$$\ln[n(L)] = \left(-\frac{L}{G\tau}\right) + \ln(n^0) \quad \text{Eq. 3}$$

Where G is the average growth rate, τ is the average crystal growth time and $n^0$is the crystal nucleation density (or intercept) (Marsh 1988). Both nucleation and growth rate processes are dependent on the degree of undercooling (e.g. Kirkpatrick 1975, 1978) and therefore the cooling history of a magma relates to its crystal population (Cashman and Marsh 1988; Marsh 1988), determining its chemical and textural evolution through time. Nevertheless rates of nucleation and growth can only be determined if magma solidification parameters are known (Cashman and Marsh 1988; Marsh 1988) and this information is difficult to retrieve from natural samples as a CSD trend can result from a range of crystal growth and nucleation rate combinations (Špillar and Dolejš 2013). In this model, crystal growth rates are known as they are calculated for each iteration (Toramaru 1991), nevertheless due to the small compositional and temperature variations throughout a single model run, growth rates do not vary drastically, therefore providing a base for the investigation of nucleation rates.

Unfortunately nucleation rates for natural minerals in magma remain largely unknown, with only theoretical and experimental information and constraints available (Brandeis et al. 1984; Cashman and Marsh 1988; Marsh 1988; Toramaru 1991; Zieg and Lofgren 2006; Armienti 2008; Pupier et al. 2008; Schiavi et al. 2009, 2010; Vinet and Higgins 2011; Špillar and Dolejš 2015; Polacci et al. 2018). Therefore these models parameters have been treated as effectively unknowns, and we devised ways to constrain them. This is done using a multiple model run approach.

The multiple model runs cover a wide range of crystallisation rates (expressed as number of crystals per year), which can be set or user defined, and outputs a file containing the number of olivine, plagioclase and clinopyroxene crystals produced by each combination of crystallisation rates. Output from the multiple runs is used to plot a "parameter space plot" (Figure 16), a 3D plot with x,y and z axes corresponding to olivine, plagioclase and clinopyroxene nucleation rates respectively. The plot is composed of a series of "boxes" of different size and colour representing the deviation of mineral proportions in the model runs

from those observed in a natural sample. The size of the box is calculated by comparing crystal count differences between model and sample, the bigger the size of the box, the better the crystal count match is. The colour coding of the boxes is based on the difference between the number of observed and modelled crystals of each type (Figure 15). Red, blue and green indicate poor matches for olivine, clinopyroxene and plagioclase respectively whilst white boxes indicate a better match. When using the parameter space plot to identify crystallisation rates for natural samples it is therefore important to focus on the white and largest boxes as they are representative of the best fit of crystallisation rates combinations.

It is important to note that nucleation rates in the model are used assuming that any nucleated grain will proceed to crystallise and grow and are therefore referred to as crystallisation rates. The interpretation of the parameter space plot function is based on the assumption that it is possible to retrieve nucleation rates from CSD plots using the slope and intercept of the crystal's CSD (e.g. Pupier et al. 2008), nevertheless the value obtained is that of a constant nucleation rate throughout the crystallisation and growth history for each phase which would result in a flat CSD trend (Figure 17a). In fact nucleation rates are not constant throughout the crystallisation history of a melt, as they are controlled by intensive parameters such as undercooling and Gibbs's energy of crystallisation (e.g. Kirkpatrick 1975; Hort 1998; Couch et al. 2003), which vary throughout the crystallisation history of a magma. In magmatic systems undercooling is a function of temperature and melt composition (Toramaru 1991) and strongly affects the shape of the nucleation curve, which peaks at lower degrees of undercooling. A dimensionless nucleation rate equation (Hort 1998) is used in the model to vary the nucleation value, obtained from the parameter space plot function, as a function of undercooling, assumed to be the difference between a maximum temperature (melting temperature of basalt), and the temperature calculated from the model at each iteration. This normalised temperature value corresponds to a set normalised nucleation value which when multiplied to the maximum nucleation value, assumed to be the crystallisation rate value obtained through the parameter space plot, provides a nucleation rate which varies at each iteration as a function of melt temperature (Figure 4). The implementation of the nucleation curve as a function of undercooling (Hort 1998), where the position of the melt on the nucleation curve is dependent on the ratio between the melting temperature (or maximum temperature) and the melt temperature (model temperature calculation), results in a CSD trend with an overall increase in ln (population density) at smaller crystal sizes (Figure 17b) rather than a flat trend (Figure 17a).

A total of 3192 CrystalMath runs were computed to span possible combinations of crystallisation rates (number of crystals/year) for olivine (1-12), plagioclase (2-20) and clinopyroxene (2-20) (Figure 16). Ranges of crystallisation rates have been calculated from CSD plots of natural samples using the nucleation density (intercept) value (Pupier et al. 2008; Špillar and Dolejš 2013) and tested in different combinations to assess the similarity of the mineral proportions in the output results to that of an equilibrium gabbroic assemblage consisting of 15:55:30 olivine:plagioclase:clinopyroxene mineral proportions (Yang et al. 1996). The resulting crystallisation rates, in conjunction with a dimensionless nucleation rate curve equation (Hort 1998), have been used to compare mineral proportions in the final output to equilibrium assemblages (Yang et al. 1996).The area of large white boxes (area 1, Figure 16) represents the area with the best combination of nucleation rates for generating an equilibrium crystal assemblage. Areas 2 and 3 (Figure 16) instead represent areas with a poor crystalline assemblage match.

Example crystallisation rates determined for area 1, 2 and 3 are summarised in Table 3 and were all run for 40 iterations using the same start composition (Torfajökull basalt, melt 1) in order to determine the effects of varying nucleation rates on melt evolution (expressed on the Fo-Di-An triangle) and the final output. The crystallisation rates from Table 3 were normalised to the nucleation rate curve (Hort 1998) for each model run. It is important to note that the parameter space plot was run prior to the addition of the nucleation curve function into the model.

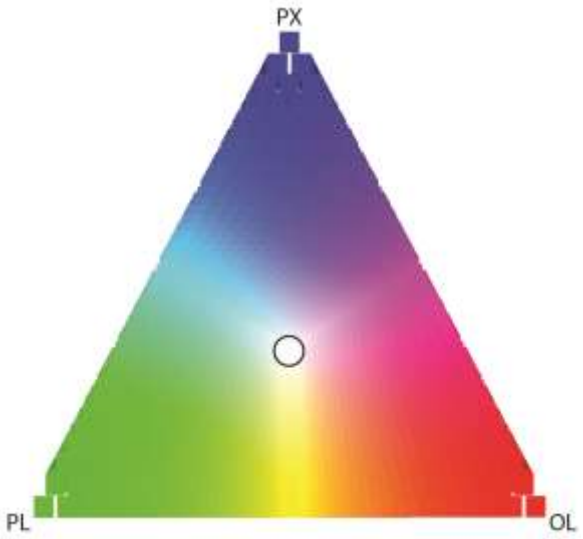

Figure 15: Parameter space plot colour scheme. Triangle sides and apices indicate poor matches between modelled and observed crystal type counts, the circle in in the middle white area indicates the best matches.

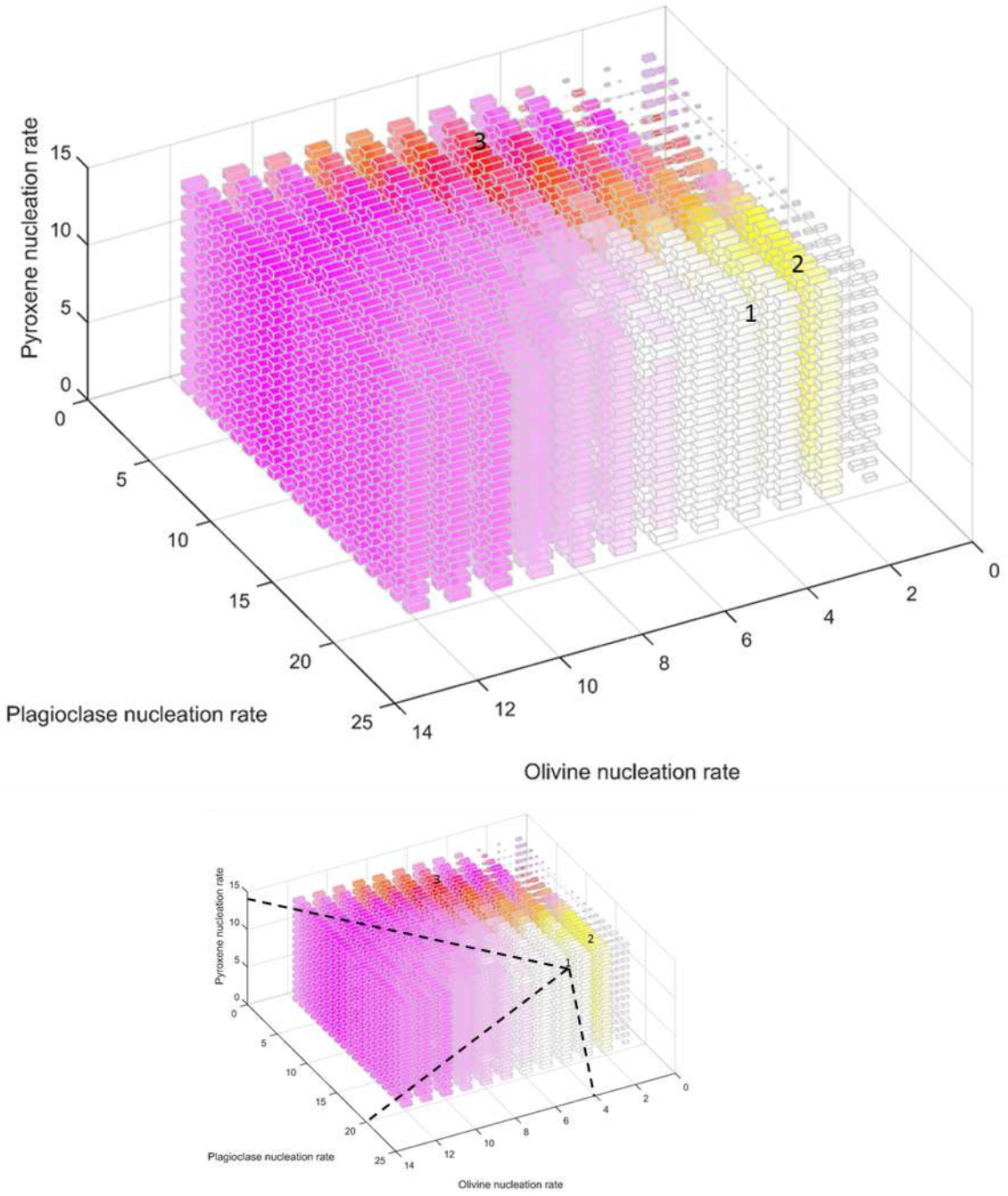

Figure 16: parameter space plot output used to determine a good fit of nucleation rates, represented in the plot by the area composed of white boxes. The bigger the box size is, the better the crystal count match is between the model run and the sample. Red, blue and green boxes, and variations in between, represent bias for the proportion of olivine, clinopyroxene and plagioclase respectively. White boxes represent the best available match in terms of mineral proportions between the model and the sample.

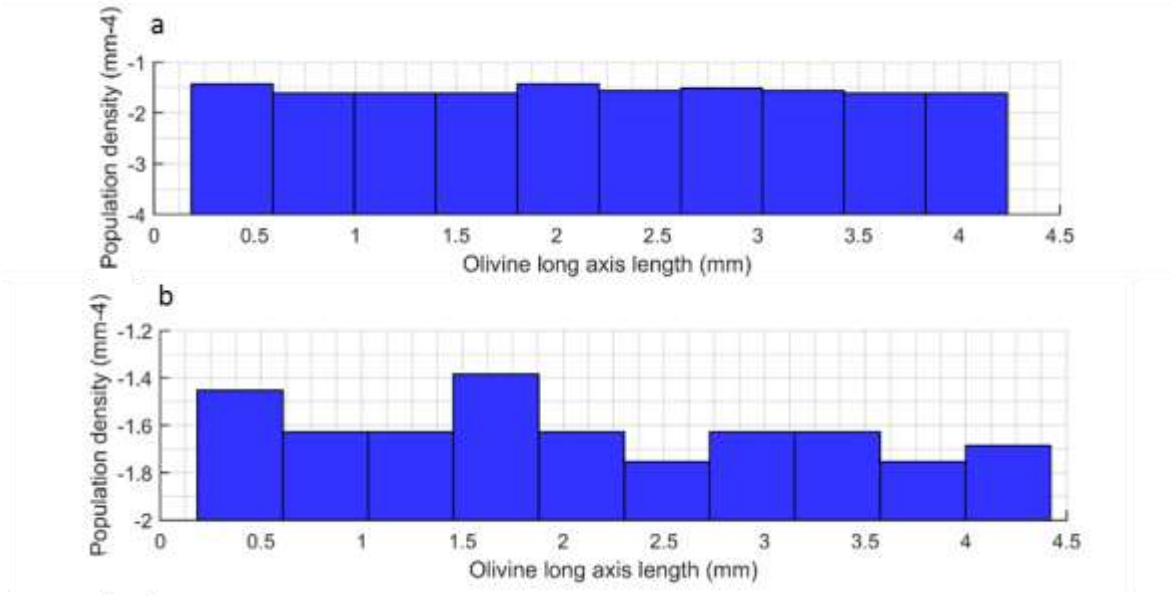

554

555 Figure 17: examples of differences in CSD trends for olivine using a constant nucleation
556 rate (a) and a normalised nucleation rate (b) using the equation by Hort (1998).

Nucleation Rate (#/year)	Olivine	Plagioclase	Clinopyroxene
Area 1	4	20	14
Area 2	2	15	14
Area 3	6	5	14

557 Table 3: combination of crystallisation rates for areas 1, 2 and 3 in Figure 16.

558 Table 4 illustrates the mineral proportions derived from model runs for each area, compared
559 to those by Yang et al. (1996). Average residuals indicates the residual of all phases for each
560 area compared to those of Yang et al. (1996), standard deviation pl-px indicated the average
561 residual for plagioclase and clinopyroxene for all areas compared to those of Yang et al.
562 (1996). In both cases the mineral proportions of Area 1 are those with the smallest error.

Mineral Proportions	Olivine	Plagioclase	Clinopyroxene	Average r.	r. pl-px
Area 1	58	61	48	11	5
Area 2	38	43	9	9	8
Area 3	76	35	39	15	7
Yang (1996)*	15	55	30	-	-

563 Table 4: mineral proportions in the output using nucleation rates from Table 3 compared to
564 the equilibrium assemblage proportions by Yang et al. (1996).

565

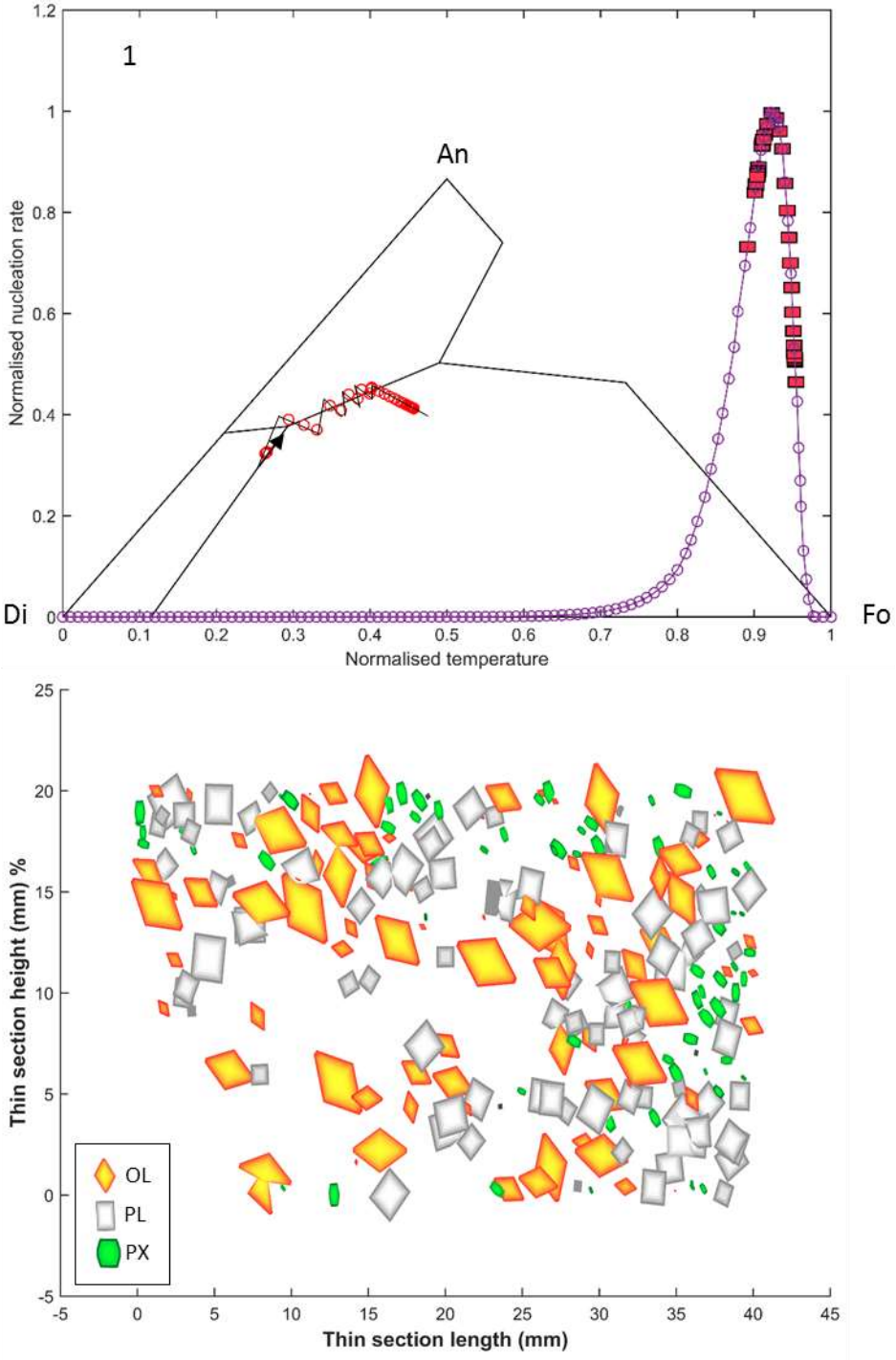

Figure 18: Area 1 melt evolution, nucleation curve and final thin section like output.

Area 1 represented the best-fit set of nucleation rates (Table 3) to reproduce a crystallising assemblage with mineral proportions similar to those expected from equilibrium crystallisation (Yang et al. 1996). The three minerals, olivine (yellow-orange); plagioclase (light grey- dark grey) and clinopyroxene (light green-dark green) are colour coded so that the lightest and darkest shade correspond to the most primitive and most evolved composition respectively.

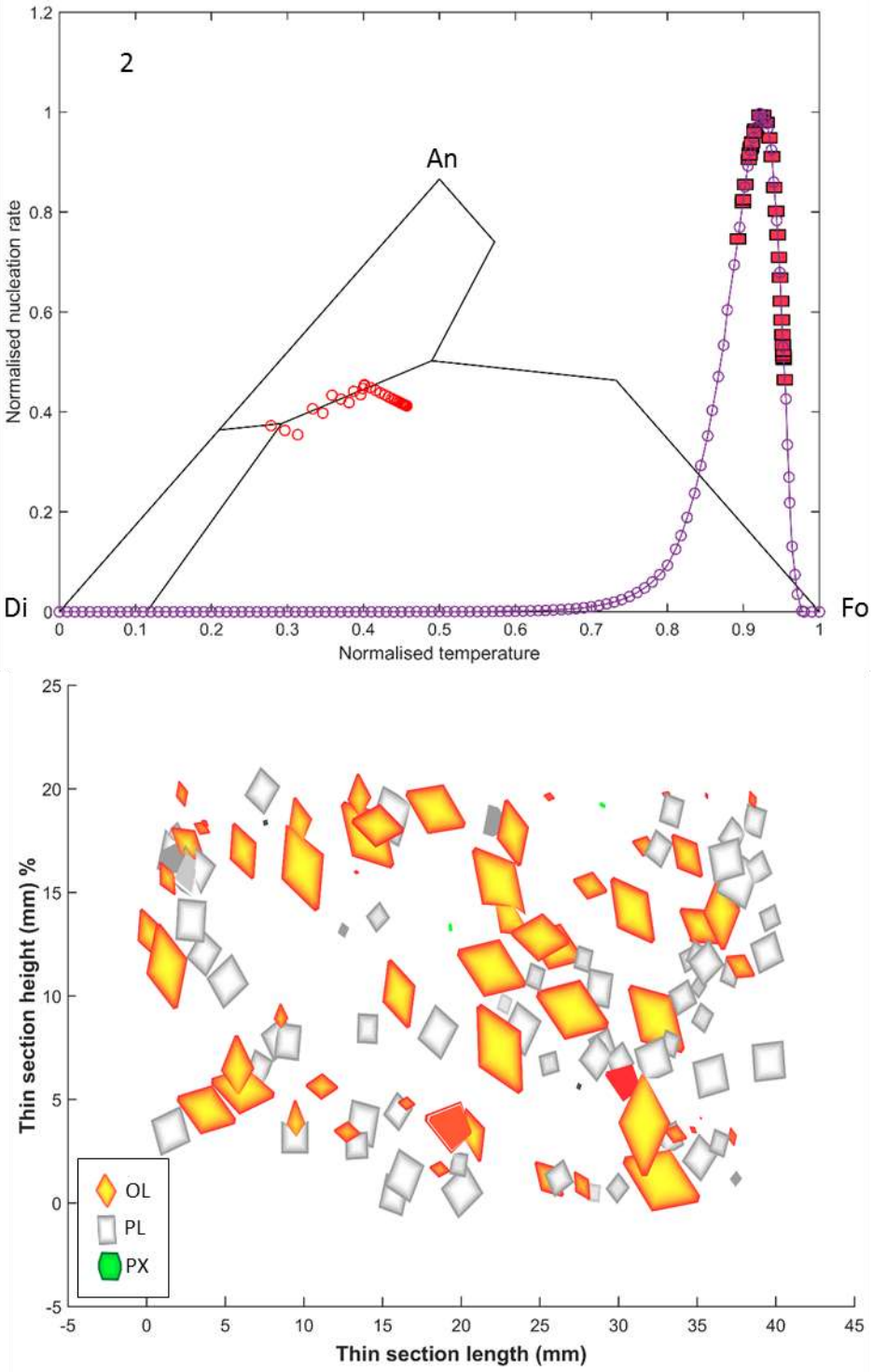

574

575 Figure 19: Area 2 melt evolution, nucleation curve and final thin section like output.

576 Area 2 represents a poor match of nucleation rates (Table 3) which are biased towards olivine
577 and plagioclase. This is observed in the final melt evolution for a single model run with these
578 nucleation rates, as the melt composition only crosses into the Diopside field for one
579 iteration (one circle on the Fo-Di-An plot) and the final output is therefore mostly composed
580 of olivine and plagioclase crystals, with very few and small clinopyroxene crystals.

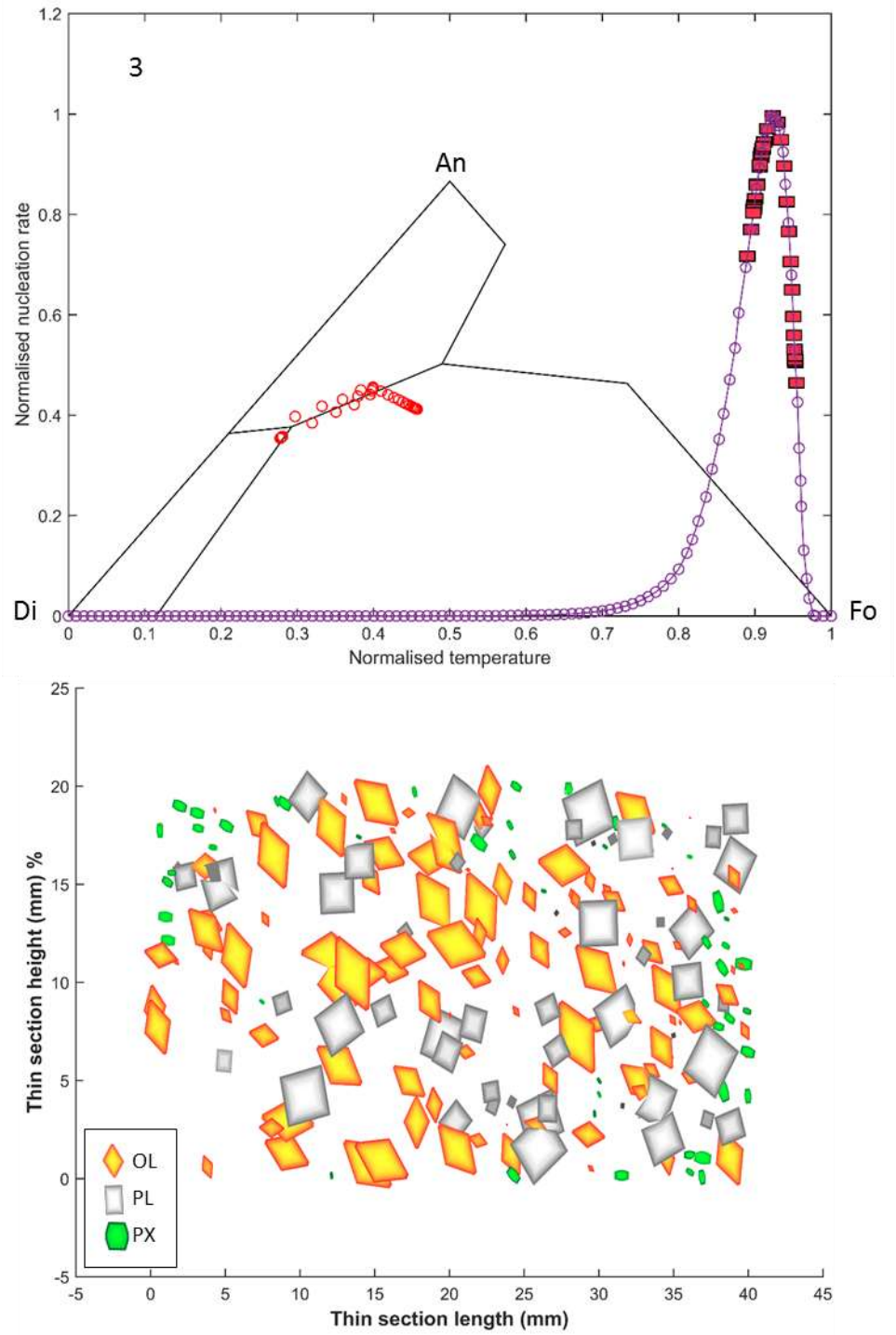

Figure 20: Area 3 melt evolution, nucleation curve and final thin section like output.

Area 3 also represents a poor combination of crystal nucleation rates (Table 3) as it is biased towards olivine. In this case, whilst the melt evolution path (Figure 20) is very similar to that of area 1 (Figure 18), the larger amount of olivine crystals nucleated at each iteration, and the smaller amount of plagioclase being nucleated at each iteration, results in a poor match for the latter, as well as a high abundance of larger olivine crystals.

Crystal Size Distributions (CSDs)

As previously shown in Figure 17, normalising the nucleation rates in Table 3 obtained from Figure 16 as a function on temperature results in a log-linear trend in the final CSD output. Nevertheless a further test for the nucleation rates obtained in Table 3 was carried out comparing the CSD outputs resulting from model runs for each Area (Figure 21), only varying the input crystallisation rates (Table 3).

The CSD profile for Area 1 in the multiple runs parameter space (Figure 21) shows an overall increase in population density towards smaller crystal sizes, followed by a drop towards smaller sizes. This is consistent with variation in nucleation during melt cooling which sees increased nucleation rates during initial cooling, to a peak nucleation rate, after which nucleation rate falls. Consistent with being a poor match for the crystalline assemblage (Figure 16), the CSD resulting from area 2 shows a trend not consistent with that of a crystallisation trend resulting in the lack of clinopyroxene crystallisation. Area 3 shows a log linear CSD trend, despite giving a bad match to mineral proportions. This could be due to the abundance of olivine in this model which gives rise to a more complete olivine CSD (Figure 21). It is also important to note that the largest olivine crystal sizes are observed in Area 2 where the lower nucleation rate means that the melt evolves more slowly and therefore stays in the forsterite field, nucleating olivines, for a larger amount of iterations as well as resulting in the presence of higher number of large olivine crystals.

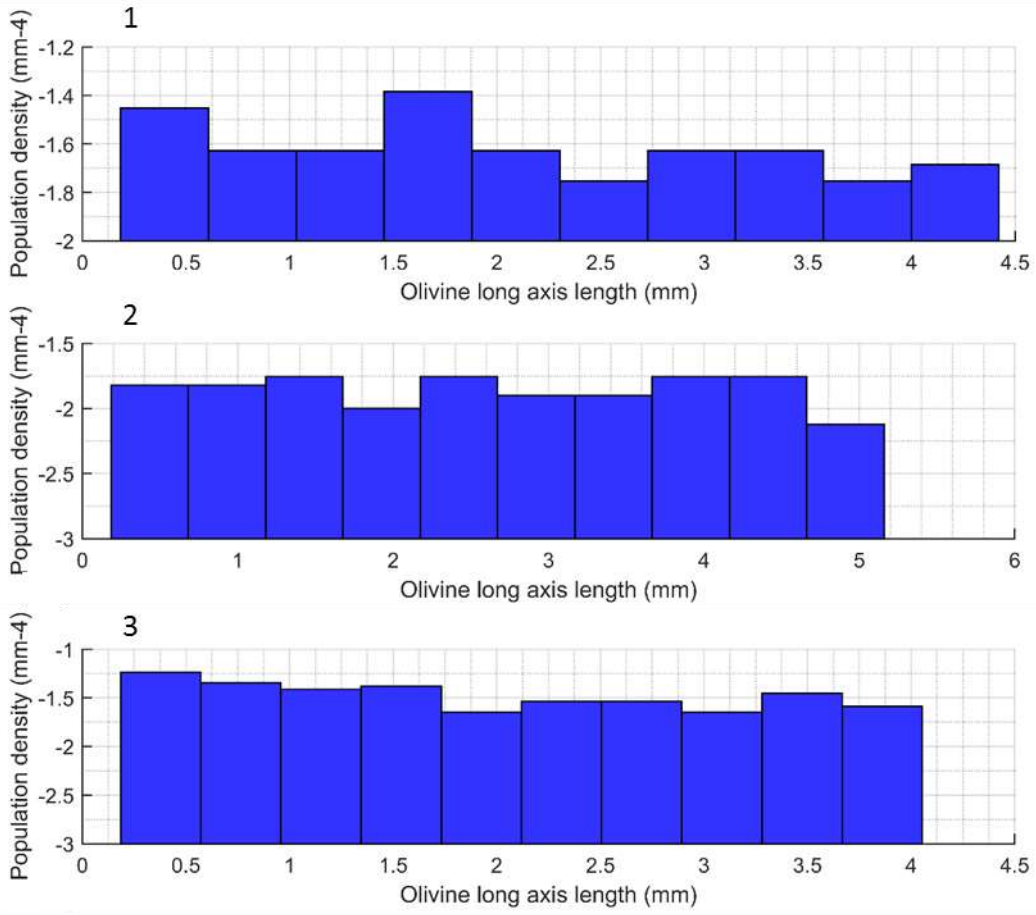

Figure 21: comparison of olivine CSD profiles for areas 1, 2 and 3 using nucleation rates from Table 3.

All results so far have been modelled using a melting temperature of 1280°C (Larsen 1929), however an increase in maximum temperature to 1400°C, results on the melt being located in the decreasing slope of the nucleation curve. This in turns affects the nucleation normalisation and the resulting CSD trend (Figure 22) which shows an opposite trend with decreasing population density with decreasing crystal size. A reverse CSD trend is not observed in nature, and whilst a progressive downward switch of lower crystal size, and associated upward translation of larger crystal size, has been associated with textural coarsening (Higgins 2002), a decreasing CSD with decreasing crystal size is unattainable as nucleation decreases faster than growth rate at the same rate of undercooling (e.g. Maaløe et al. 1989; Hort 1998).

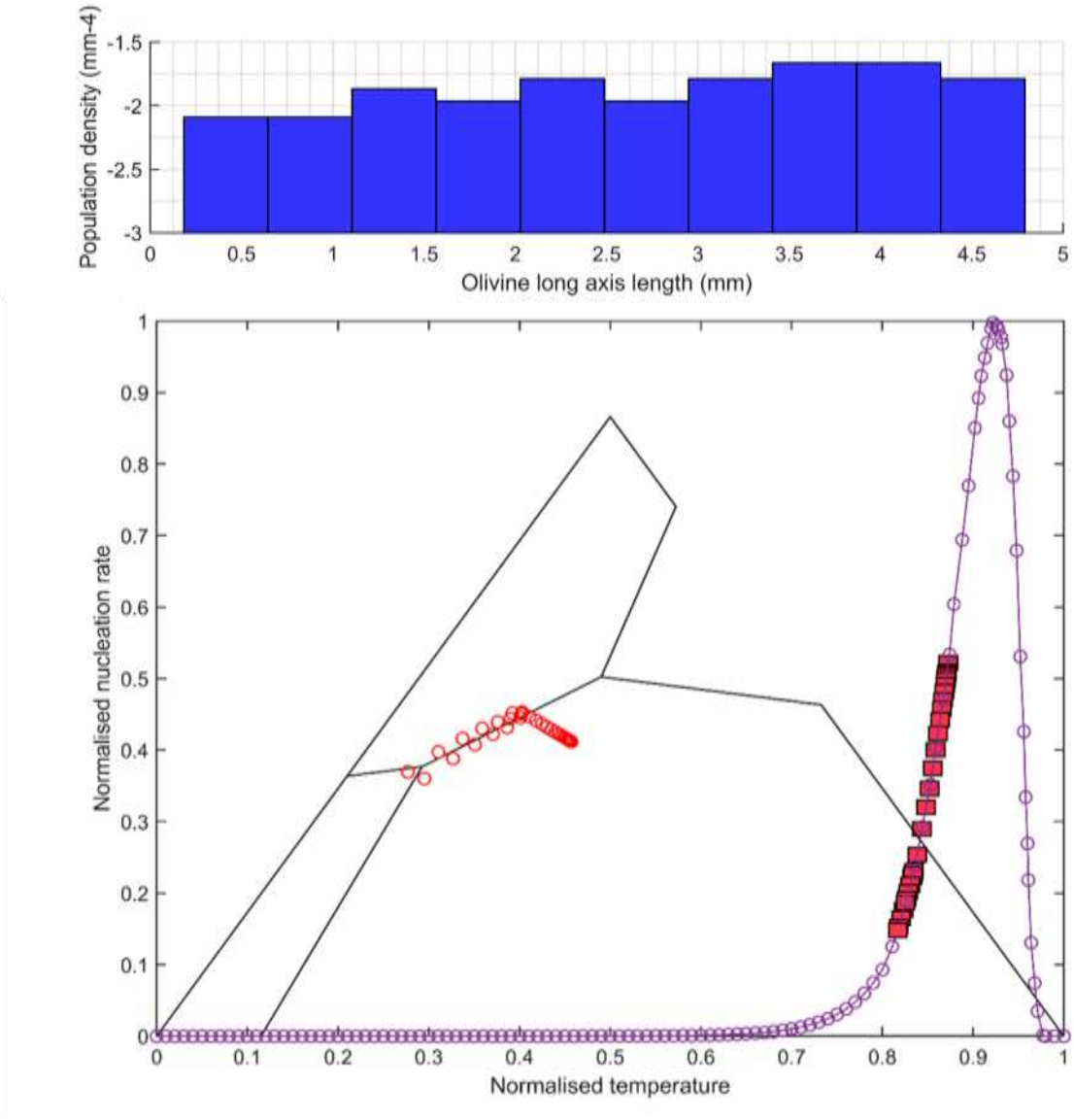

Figure 22: Effects of temperature on crystallisation and normalised nucleation rates, and melt evolution.

Manual removal of crystals

Grain settling and resorption processes are not yet included in CrystalMath, which results in every grain nucleated proceeding to grow and remaining in the model volume irrespective of its density relative to the melt. This can result in olivine abundances in excess of those observed in natural samples. Torfajökull basaltic melt 1 so far has shown to provide the most realistic crystallisation trend (Figure 4) and has therefore been used as a basis to further test the model. Five consecutive model runs were executed starting with melt 1 composition and crystallised for a small number of iterations, then using the resulting daughter melt composition as a starting point for the following run which begins with no crystals formed

633 (Table 5). This allows to test the effects of "manual removal" of olivine crystals and
634 investigate its effects on melt evolution, the final CSD and output.

Run	Iterations	Start Melt	# Olivine	# Plagioclase	# Clinopyroxene
1	10	Melt 1	26	0	0
2	10	Daughter 1	27	0	0
3	10	Daughter 2	27	0	0
4	15	Daughter 3	49	0	0
5	40	Daughter 4	84	79	37
-	40	Melt 1	87	91	22

635 Table 5: run details for olivine removal tests alongside Melt 1 single run minerals
636 proportions for comparison, daughter compositions are in Appendix 4.

637 The total number of iterations in the test runs is 85, whilst the Melt 1 runs are 40. Whilst this
638 is not directly comparable, a larger number of iterations were carried out in the test in order
639 to model the appearance of plagioclase and clinopyroxene which do not crystallise until test
640 run 5 (Table 5). The results of the removal tests show that manually removing olivine for
641 the first iterations does not significantly vary the output of the model compared to a single
642 40 iterations run of melt 1 (Figure 23). This is due to the fact that manually removing olivines
643 means that each time that the model is run with a new daughter composition, the volume of
644 crystals being removed is small as new olivines are nucleated and grow from scratch,
645 meaning that the melt evolution is slow and shows insignificant chemical differences for the
646 first 10 iterations (e.g. ~0.1 wt.% MgO), as shown in Figure 23. In contrast, model run 4,
647 where 15 iterations were run, shows larger variations (0.5 wt.% MgO). Comparing the final
648 output of model run 5 (Table 5) and the output of Melt 1 single run shows minimal
649 differences. The MgO of the former varies from 6.06 to 4.06 wt.% and that of the latter from
650 6.88 to 4.32 wt.%. Similarly, the mineral proportions resulting from the crystallisation
651 models are very similar (Table 5) and do not result in a significant reduction (and removal)
652 of olivine crystals. The CSD evolution for model run 5 and melt 1 are different with the
653 former showing a relatively flat trend and the latter a more step-like trend towards increasing
654 ln(population density) towards smaller crystal sizes and sudden drop for the smallest sizes
655 (Figure 24). This is consistent with model run 5 covering a smaller section of the nucleation
656 curve compared to melt 1 (Figure 23) therefore presenting a narrower nucleation range and
657 resulting in flatter trends compared to melt 1. The smaller nucleation range covered by

model run 5 can be explained by the fact that melt temperature would have been calculated from a more evolved melt than melt 1 (Figure 25) resulting in lower values.

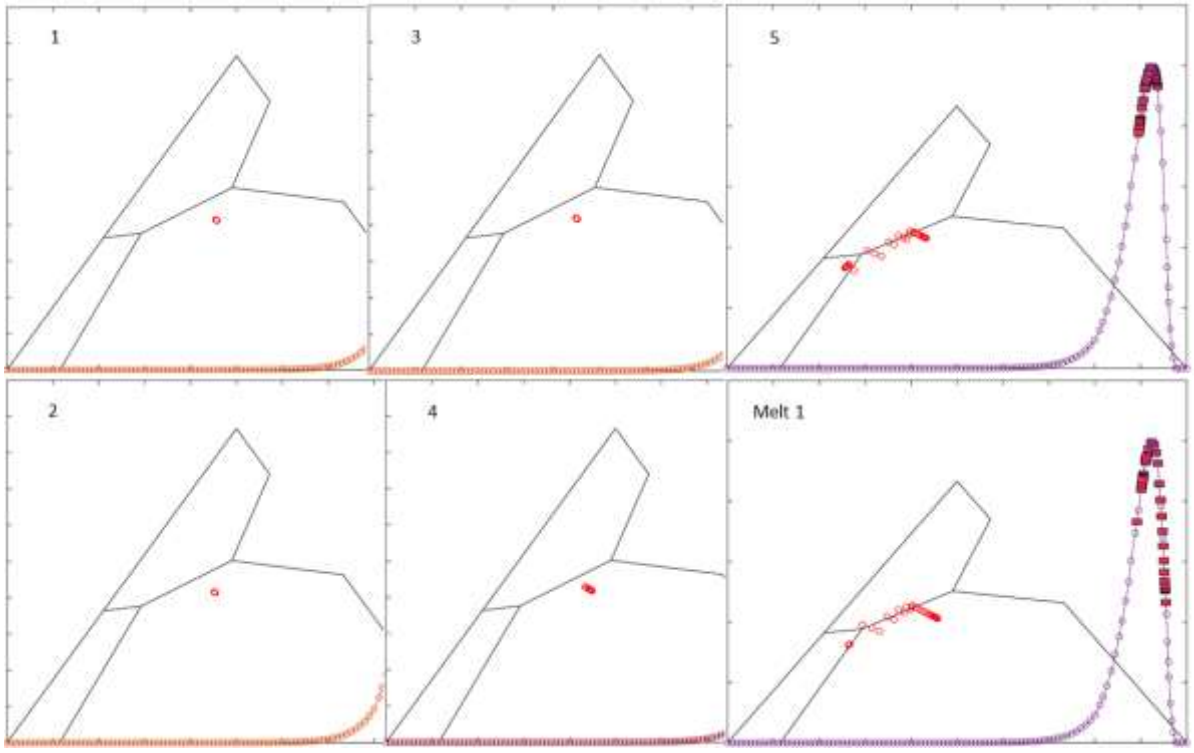

Figure 23: removal test runs (Table 5) results and comparison melt 1 Fo-Di-An triangle and melt nucleation evolution outputs.

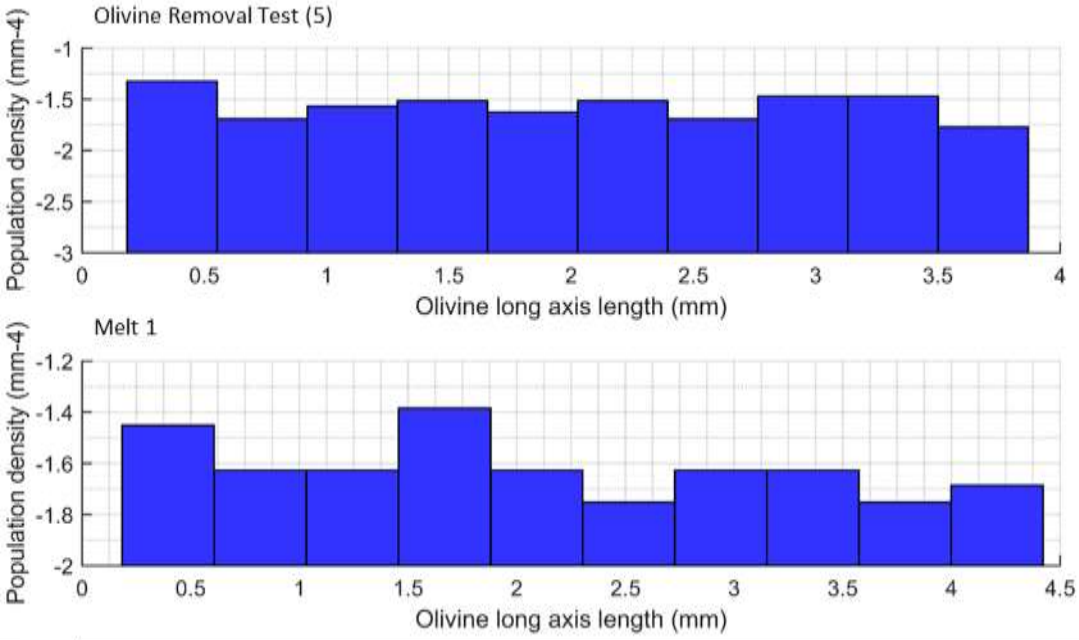

Figure 24: Olivine CSD outputs for Olivine Removal Test 5 (Table 5) and melt 1 (Table 2) for the model runs illustrated in Figure 23.

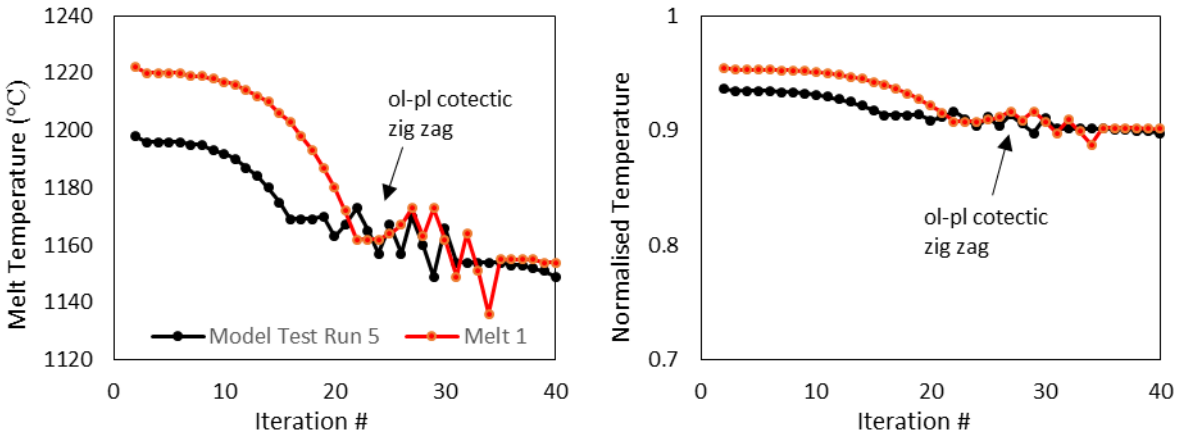

Figure 25: melt temperature and normalized temperature evolution for model test run 5 and melt 1 resulting in different melt position along the nucleation curve in Figure 23.

DISCUSSION AND FURTHER DEVELOPMENTS

Model Application to Published Data

Test runs were carried out using published Kilauea Iki lava lake basalt compositions (Vinet and Higgins 2011). The melt evolution was modelled for 40 iterations to avoid the compositional and textural effects of the zig-zag trend across the olivine-plagioclase cotectic on olivine composition and CSD output. The melt evolution follows an olivine to plagioclase evolution, the CSD shows a maximum olivine crystal size of 0.68 cm and a compositional range of forsterite 90.2-77.7 % (Figure 26, Figure 27) across a large crystallisation interval resulting in a melt MgO variation from 15.8 to 6.3 wt.% (Figure 26). The results are in agreement with the published data (Vinet and Higgins 2011), where olivines range in size from 0.93 to 0.06 cm and display three forsterite populations with Fo_{90-86}, Fo_{82-78} and Fo_{78-74}. Olivine CaO and NiO varies from 0.10-0.35 wt.% and 0.13-0.49 wt.% respectively. NiO is in good agreement with our model run, where the variation is between 0.23-0.39 wt.% (Figure 26) suggesting that the partition coefficient equation (Li and Ripley 2010) used in the model results in reliable compositions. CaO contents instead range in the model from 0.28-0.39 wt.% and show an increasing trend with decreasing forsterite (Figure 26). CaO K_D between olivine and melt was set at 0.03 and kept constant at all forsterite ranges, however no plagioclase is being crystallised in the model run, for the reasons mentioned before, and it is therefore possible that the increasing CaO trend is caused by the lack of mineral phases which would affect the CaO of the melt. Nevertheless high forsterite CaO contents are in agreement to those published in the literature (Figure 26) (Vinet and Higgins 2011).

691 The CSD trend from the model run increases towards smaller crystal sizes, with the lower
692 ln(population density) being that the largest grains ~0.68 cm (Figure 27). Nevertheless the
693 slope and intercept value for the trend differ from those calculated by Vinet and Higgins
694 (2011). Comparison of crystal size data is given in Table 6. Whilst the overall trend of the
695 CSD is comparable, the slope values are smaller, as well as presenting a narrower range.
696 Similarly the intercept values show a very narrow range compared to published results
697 (Vinet and Higgins 2011). The author invokes processes such as textural coarsening which
698 would affect the final CSD results, nevertheless the difference in the values is still too large
699 suggesting that the nucleation rates in the model span a narrower range than observed in
700 nature. The crystal residence times of the crystals in the published data set has been
701 interpreted to be between 1-60 days (Vinet and Higgins 2011) in agreement with a model
702 run of 40 years, with one year time step per iteration.

Vinet (2011)	**Length (cm)**	**Slope**	**Intercept**
Average	0.52	-2.33	0.84
Max	0.93	-1.08	4.67
Min	0.06	-16.09	-2.28
Model	**Length (cm)**	**Slope**	**Intercept**
Average	0.36	-0.6	-1.67
Max	0.68	-0.9	-1.5
Min	0.04	-0.3	-2

703 Table 6: comparison of crystal size results between published data (Vinet and Higgins 2011)
704 and model run.

705

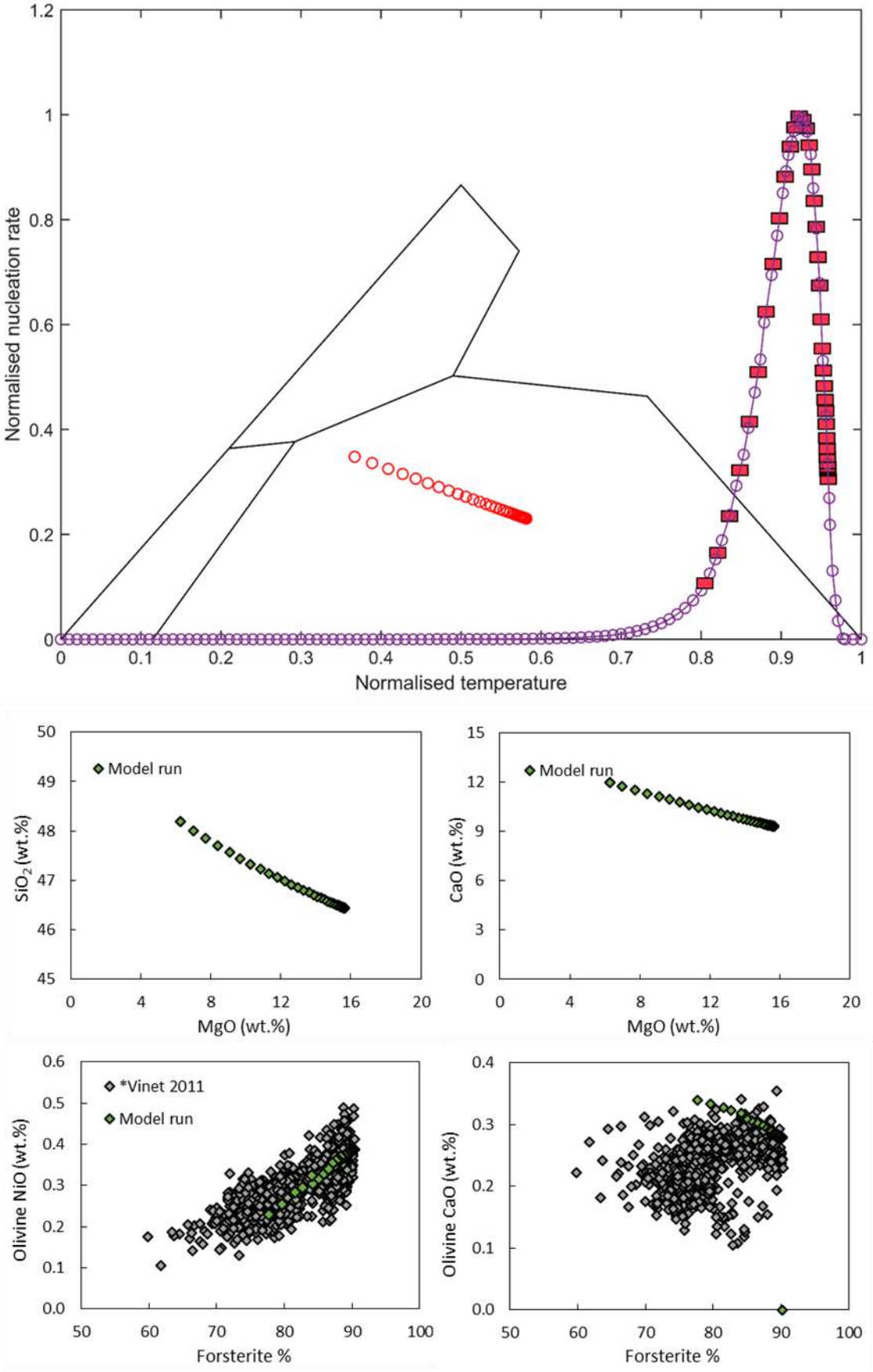

Figure 26: results of the model test using start compositions from Kilauea (Vinet and Higgins 2011).

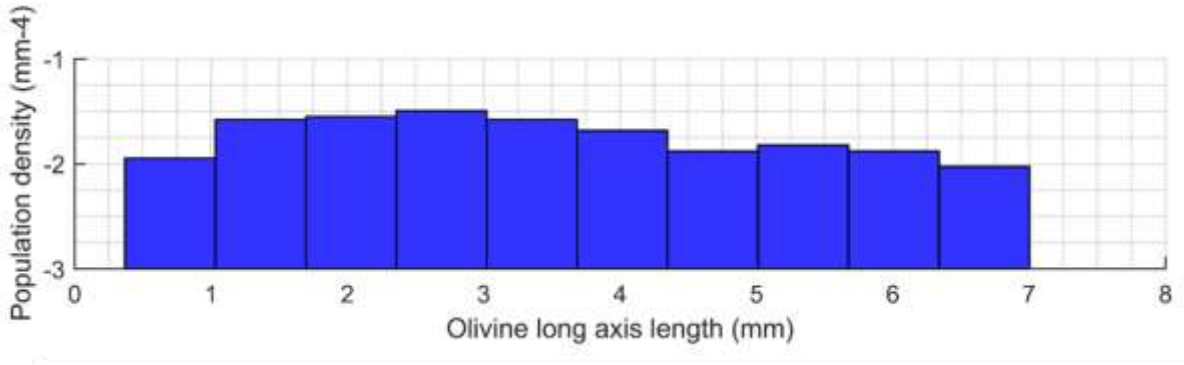

Figure 27: CSD results of the model test using start compositions from Kilauea (Vinet and Higgins 2011).

Assumptions and simplifications

Due to the wide range of processes occurring in multicomponent systems and their non-linear relationships, the full modelling of the kinetics of a crystallising magma is challenging (Jaupart and Tait 1995; Valentine et al. 2002). This model does not aim to reproduce complex thermodynamic processes, therefore crystals nucleate at randomly determined coordinate points within a 40 x 20 x 10 mm grid, scaled to represent a volume the same length and width as a thin section but thicker in the z direction. Whilst this is a stochastic representation, investigating thermal and geochemical gradients which are emplaced once crystallisation begins (Jaupart and Tait 1995) is beyond the scope of this model. The small scale over which the crystallisation process in the model is occurring allows the assumption that no significant geochemical gradient is formed adjacent to growing crystals. Nevertheless grains are crystallised incrementally and therefore grains can crystallise different rim compositions, partly reflecting the heterogeneity of melts in magma chambers (Figure 4, Appendix 3).

Modelling fractional crystallisation and magma mixing

The model has shown to be optimised for a limited range of basaltic compositions and whilst olivine, plagioclase and clinopyroxene are amongst the main igneous phases and provide important information about initial melt composition, temperature and pressure of crystallisation and magmatic processes, they do not allow for the modelling of more evolved melts, or melts, like in the case of the Salina tholeiite, which contains abundant water content ~4 wt.% and show evidence for amphibole fractionation (Chapter 4). Whilst complex mineral formulas of more evolved igneous minerals, such as amphiboles, can be incorporated in the model, this would increase the error in output compositions. Similarly,

735 the melt evolution of the model is strongly affected by the lack of magnetite crystallisation,
736 and this is shown through biased FeO compositional trends (Figure 4).

737 The Fo-Di-An triangle tests showed that failed composition model runs all started in the
738 anorthite field (Figure 5, Figure 6, Figure 7, Figure 8), therefore a possible option is to
739 incorporate a different phase equilibria triangle, such as the Diopside-Albite-Anorthite
740 triangle, which would exclude olivine as a possible crystallising phase at more evolved melt
741 compositions. Allowing the modelling of more evolved composition will also allow for
742 better modelling of magma mixing and entrainment processes, as different melts could be
743 evolved separately and mixed. This would allow for the entrainment of mineral phases,
744 therefore resulting in a more comprehensive heterogeneous crystal cargo as expected during
745 magma mixing processes.

746 *Issues with partition coefficients*

747 Small changes in partition coefficients values can result in large changes in the resulting
748 melt and crystal concentrations, posing major issues in geochemical modelling of magmatic
749 processes. Significant work has been undertaken on the quantification of the partitioning
750 behaviour of trace elements between mineral and melt and found that partitioning behaviour
751 is affected by external magmatic variable such as temperature, pressure, oxygen fugacity
752 and the concentration in the mineral and melt (e.g. Blundy and Wood 1991, 2003; Ren et al.
753 2003; Tepley et al. 2010; Bédard 2014; Laubier et al. 2014; Nielsen et al. 2017; Sun et al.
754 2017; Wagner et al. 2017). Due to the sensitivity of the model to this parameter, values have
755 been calculated from published models or carefully selected from a published database
756 (GERM) to ensure they are the most appropriate possible values for the magma being
757 modelled (Appendix 2). Choice is mostly based on the SiO_2 content of the melt and
758 temperature conditions. This is particularly important when modelling extensive fractional
759 crystallisation and mixing events, where large temperature and compositional differences
760 can be present. Figure 28 shows a comparison of plagioclase trace element models for
761 plagioclase (Blundy and Wood 1991; Bindeman et al. 1998) and fixed K_D values from
762 GERM. For compatible element Sr, larger variations in partitioning model results are
763 observed for basaltic compositions (black), whilst for Ba larger variations are observed for
764 both basaltic (black) and rhyolitic compositions (red). Incompatible element Zr shows large
765 variations at andesitic (red) and rhyolitic compositions (blue), and MgO shows larger
766 variations for basalts (black) and andesites (red). Standard deviation for each element and

767 composition are given in Table 7, and these results highlight the importance of carefully
768 picking portioning models and to regard results with care due to the large errors present.

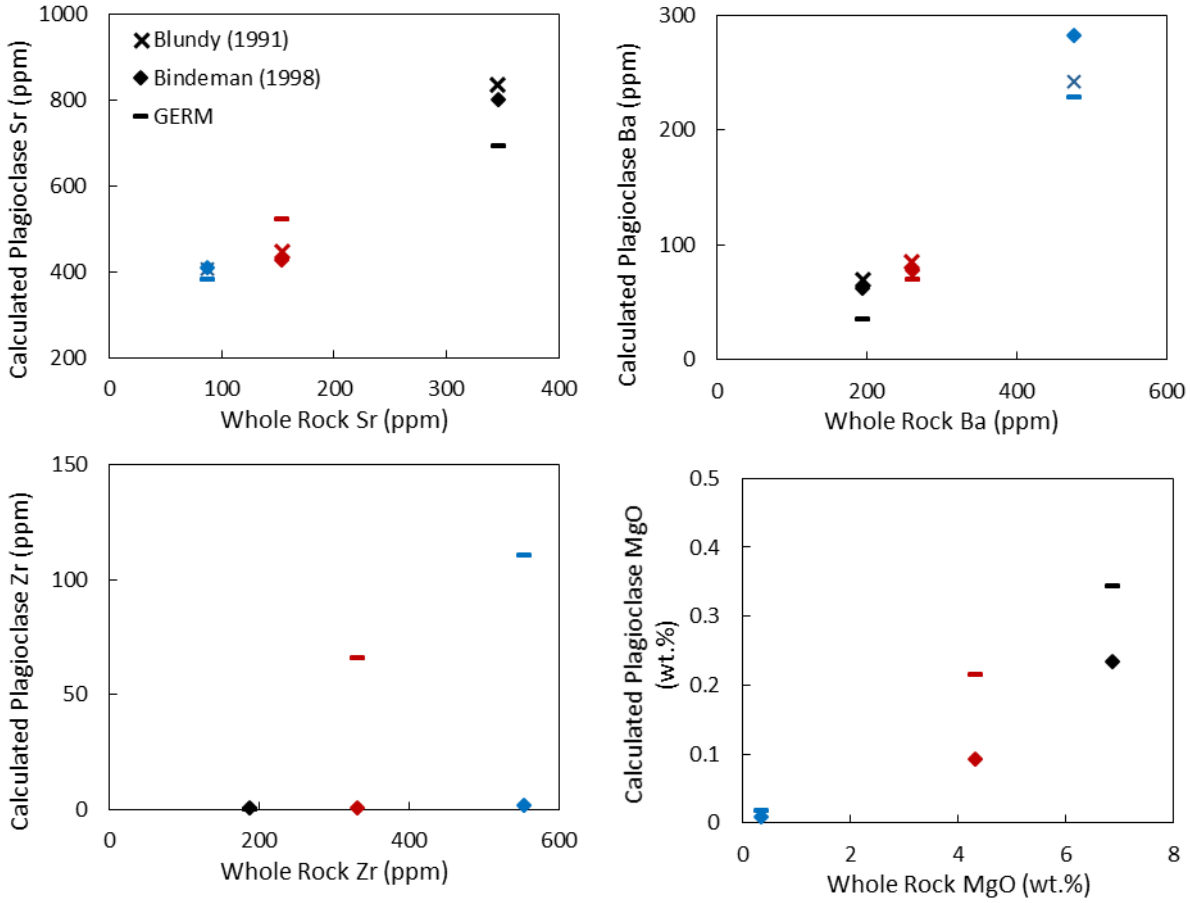

769

770 Figure 28: trace element partitioning models results for plagioclase using Blundy and Wood
771 (1991), Bindeman et al. (1998) and set values from GERM. Black symbols are for basaltic
772 compositions, red symbols for andesitic compositions and blue symbols for rhyolitic
773 compositions.

774

	Sr	Ba	Zr	MgO
Basalt	74.2	18.0	0.32	0.08
Andesite	51.0	7.2	46.4	0.09
Rhyolite	15.0	28.0	77.0	0.01

775 Table 7: standard deviations for trace element partitioning models and MgO in plagioclase.

776

777

778

779

Nucleation rates and CSDs

Efforts have been made to retrieve crystal nucleation rates from the literature. However, these are often determined by thermodynamic equations (e.g. Kirkpatrick 1975; Toramaru 1991). These include a large number of parameters whose difficulty to constrain results in large uncertainties. The determination of these parameters is beyond the scope of our model and therefore are not incorporated. Moreover published values are not scaled to a finite volume of melt, and the relationship between number of nucleated grains versus the number of grains which effectively proceed to crystallise and grow. All of these would affect the number of grains in the final output and therefore affect the population density and trend in the resulting CSD plot. The use of the nucleation curve by Hort (1998) has proven suitable for providing an increasing number of crystals at the as crystal size decreases (Figure 17), consistent with observations in natural samples, nevertheless the range of slope and intercept values in the CSD plot is narrower than those of natural samples (Figure 27, Table 6) and therefore further modifications and nucleation curve tests must be carried out.

The largest current constraint on CSDs evolution in the model is that these evolve under a controlled set of conditions (e.g. melt composition, pressure, temperature) meaning that the model is unable to account for a set of processes which affect the CSD in natural samples. This means that the model may only being able to reproduce textural changes for a portion of the crystallisation history rather than the complete story found in natural samples. In magmatic systems, larger crystals (phenocrysts) and smaller crystals (microlites) grow in different environments where the former grow in a quiescent environment prior to emplacement or eruption and are affected by coarsening and settling. Microlites on the other hand are thought to crystallise as a result of sudden pressure drops, rapid cooling and associated increase in nucleation rates prior to ascent and eruption (e.g. Cashman 1992; Hersum and Marsh 2007; Renjith 2014). This burst in nucleation results in larger numbers of small crystals which gives CSDs plots their typical steep trend at smaller sizes (e.g. Cashman 1992; Hersum and Marsh 2007; Renjith 2014). Nevertheless, our model is not able to replicate these processes and therefore results in more gradual variations in nucleation (Hort 1998), which is more similar to the evolution of plutonic bodies rather than erupted products, due to the growth rate in the model being relatively constant due to small changes in temperature and melt composition. Growth also plays a large role in controlling CSDs, it is infact rare to find igneous minerals larger than ~2-3cm. This is due to growth being limited by diffusion, where elements which are not used in crystal growth accumulate at the edges

of the crystals effectively impeding growth (Hersum and Marsh 2007) and can only be moved by diffusion. These processes and parameters however are not taken into consideration as geochemical gradients are not modelled. A further complication of modelling CSDs is that natural samples are rarely found at arbitrary rates of arrested crystallisation (Hersum and Marsh 2007), nevertheless observations of crystallisation in lava lakes (Cashman and Marsh 1988) suggests that, after the initial nucleation stage, aggregation and annealing of smaller grains to form larger crystals is observed (Cashman and Marsh 1988; Zieg and Lofgren 2006; Hersum and Marsh 2007; Schiavi et al. 2009), and associated impingement processes reduce the growth rate.

It is therefore necessary to highlight that the model is not yet able and aimed at reproducing the complexity of these magmatic evolution processes, nevertheless it provides a starting point for testing a semi-quantitative evaluation of crystallisation rates and their effects on both the textural and geochemical output, which can be compared to natural samples.

A further caveat is that, as a consequence of volumetric fractional crystallisation, constraints on nucleation rates and zig-zagging across the ol-pl cotectic, the model results in larger than observed olivine crystals in the final output. The manual removal tests carried out showed that carrying out smaller crystallisation steps does not result in a significant change in final olivine crystal number (Figure 23). A function could be added to randomly remove the oldest grains of crystals which are not currently in equilibrium with the melt as defined by the Fo-Di-An triangle plot, therefore simulating physical crystal resorption. The advantage of volumetric crystals fractionation is that it allows for mineral density calculations. Therefore crystal settling processes could be added into the model, where olivine crystals denser than the melt will sink to form a “cumulate” zone and would no longer affect the geochemical evolution of the melt. This would ensure that melt evolution proceeded in larger steps than those observed in the removal test, as the larger volume and number of olivine crystals would initially be present in the early stages of the model melt evolution.

CONCLUSIONS

- CrystalMath has been shown to be able to model fractional crystallisation in basalts, and to a certain extent, magma mixing processes and their geochemical and textural effects on both the final “lava” output and crystal cargoes. Moreover, the multiple runs model and parameter space plot provide an initial tool to investigate relationships between quantifiable crystallisation rates and magmatic evolution.
- CrystalMath has yet again highlighted the difficulties and uncertainties in modelling magmatic processes, concerning mineral-melt equilibrium, thermodynamic processes and related processes such as nucleation rates, and the complexity and heterogeneity of processes occurring in magmatic system such as crystal settling and resorption.
- CrystalMath is still in development, the current limitations include its restriction towards primitive compositions, the lack of modelling of physical process such as crystal settling and constrains on nucleation rates. Nevertheless, the ability of the model to geochemically model natural samples has been proven, and therefore the geochemistry can be used as a tie point to model these non-well constrained variables.

862 **REFERENCES**

863 Adam J, Green T (2006) Trace element partitioning between mica- and amphibole-bearing
864 garnet lherzolite and hydrous basanitic melt: 1. Experimental results and the
865 investigation of controls on partitioning behaviour. Contrib to Mineral Petrol 152:1–
866 17. doi: 10.1007/s00410-006-0085-4

867 Ariskin AA, Frenkel MY, Barmina GS, Nielsen RL (1993) Comagmat: a Fortran program
868 to model magma differentiation processes. Comput Geosci 19:1155–1170. doi:
869 10.1016/0098-3004(93)90020-6

870 Armienti P (2008) Decryption of Igneous Rock Textures: Crystal Size Distribution Tools.
871 Rev Mineral Geochemistry 69:623–649. doi: 10.2138/rmg.2008.69.16

872 Bacon CR, Druitt TH (1988) Compositional evolution of the zoned calcalkaline magma
873 chamber of Mount Mazama, Crater Lake, Oregon. Contrib to Mineral Petrol 98:224–
874 256. doi: 10.1007/BF00402114

875 Beattie P (1994) Systematics and energetics of trace-element partitioning between olivine
876 and silicate melts: Implications for the nature of mineral/melt partitioning. Chem
877 Geol 117:57–71. doi: 10.1016/0009-2541(94)90121-X

878 Beattie P, Ford C, Russell D (1991) Partition coefficients for olivine-melt and
879 orthopyroxene-melt systems. Contrib to Mineral Petrol 109:212–224. doi:
880 10.1007/BF00306480

881 Bédard JH (2014) Parameterizations of calcic clinopyroxene - Melt trace element partition
882 coefficients. Geochemistry, Geophys Geosystems 15:303–336. doi:
883 10.1002/2013GC005112

884 Bindeman IN, Davis AM, Drake MJ (1998) Ion microprobe study of plagioclase-basalt
885 partition experiments at natural concentration levels of trace elements. Geochim
886 Cosmochim Acta 62:1175–1193. doi: 10.1016/S0016-7037(98)00047-7

887 Blundy J, Wood B (2003) Partitioning of trace elements between crystals and melts. Earth
888 Planet Sci Lett 210:383–397. doi: 10.1016/S0012-821X(03)00129-8

889 Blundy JD, Wood BJ (1991) Crystal-chemical controls on the partitioning of Sr and Ba
890 between plagioclase feldspar, silicate melts, and hydrothermal solutions. Geochim
891 Cosmochim Acta 55:193–209. doi: 10.1016/0016-7037(91)90411-W

892 Brandeis G, Jaupart C, Allègre CJ (1984) Nucleation, crystal growth and the thermal
893 regime of cooling magmas. J Geophys Res 89:10161. doi: 10.1029/JB089iB12p10161

894 Caricchi L, Blundy J (2015) The temporal evolution of chemical and physical properties of
895 magmatic systems. Geol Soc London, Spec Publ 422:1–15. doi: 10.1144/SP422.11

896 Cashman K V. (1992) Groundmass crystallization of Mount St. Helens dacite, 1980-1986:
897 a tool for interpreting shallow magmatic processes. Contrib to Mineral Petrol
898 109:431–449. doi: 10.1007/BF00306547

899 Cashman K V., Stephen R, Sparks J (2013) How volcanoes work: A 25 year perspective.
900 Bull Geol Soc Am 125:664–690. doi: 10.1130/B30720.1

901 Cashman C V, Marsh BD (1988) Crystal size distribution (CSD) in rocks and the kinetics
902 and dynamics of crystallisation II: Makaopuhi lava lake. Contrib to Mineral Petrol
903 99:277–291. doi: 10.1007/BF00371933

904 Costa F, Chakraborty S, Dohmen R (2003) Diffusion coupling between trace and major
905 elements and a model for calculation of magma residence times using plagioclase.
906 Geochim Cosmochim Acta 67:2189–2200. doi: 10.1016/S0016-7037(02)01345-5

907 Couch S, Harford CL, Sparks RSJ, Carroll MR (2003) Experimental constraints on the
908 conditions of formation of highly calcic plagioclase microlites at the Soufrire Hills
909 Volcano, Montserrat. J Petrol 44:1455–1475. doi: 10.1093/petrology/44.8.1455

910 Danyushevsky L V., Plechov P (2011) Petrolog3: Integrated software for modeling
911 crystallization processes. Geochemistry, Geophys Geosystems 12:. doi:
912 10.1029/2011GC003516

913 Davidson JP, Morgan DM, Charlier BL a., et al (2007) Microsampling and isotopic
914 analysis of igneous rocks: implications for the study of magmatic systems. doi:
915 10.1146/annurev.earth.35.031306.140211

916 Deer, W. A., Howie, R. A., & Zussman, J. (1992). *An introduction to the rock-forming*
917 *minerals.* 2nd ed. Harlow, Essex, England : New York, NY: Longman Scientific &
918 Technical.

919 Drake MJ, Weill DF (1975) Partition of Sr, Ba, Ca, Y, Eu/2+/, EU/3+/, and other REE
920 between plagioclase feldspar and magmatic liquid - An experimental study. 39:689–
921 712. doi: 10.1016/0016-7037(75)90011-3

922 Duke JM (1976) Distribution of the period four transition elements among olivine, calcic
923 clinopyroxene and mafic silicate liquid: Experimental results. J Petrol 17:499–521.
924 doi: 10.1093/petrology/17.4.499

925 Dunn T, Sen C (1994) Mineral/matrix partition coefficients for orthopyroxene, plagioclase,
926 and olivine in basaltic to andesitic systems: A combined analytical and experimental
927 study. Geochim Cosmochim Acta 58:717–733. doi: 10.1016/0016-7037(94)90501-0

928 Ewart A, Griffin WL (1994) Application of proton-microprobe data to trace-element
929 partitioning in volcanic rocks. Chem Geol 117:251–284. doi: 10.1016/0009-
930 2541(94)90131-7

931 Ford CE, Russell DG, Craven JA, Fisk MR (1983) Olivine-Liquid Equilibria:
932 Temperature, Pressure and Composition Dependence of the Crystal/Liquid Cation
933 Partition Coefficients for Mg, Fe2+, Ca and Mn. J Petrol 24:256–266. doi:
934 10.1093/petrology/24.3.256

935 Gast PW (1968) Trace element fractionation and the origin of tholeiitic and alkaline
936 magma types. Geochim Cosmochim Acta 32:1057–1086. doi: 10.1016/0016-
937 7037(68)90108-7

938 Ghiorso MS, Sack RO (1995) Chemical mass transfer in magmatic processes IV. A revised
939 and internally consistent thermodynamic model for the interpolation and extrapolation
940 of liquid-solid equilibria in magmatic systems at elevated temperatures and pressures.
941 Contrib to Mineral Petrol 119:197–212. doi: 10.1007/BF00307281

942 Ginibre C, Wörner G, Kronz A (2007) Crystal zoning as an archive for magma evolution.
943 Elements 3:261–266. doi: 10.2113/gselements.3.4.261

944 Hart SR, Dunn T (1993) Experimental cpx/melt partitioning of 24 trace elements. Contrib
945 to Mineral Petrol 113:1–8. doi: 10.1007/BF00320827

946 Hawkesworth C, George R, Turner S, Zellmer G (2004) Time scales of magmatic
947 processes. Earth Planet Sci Lett 218:1–16. doi: 10.1016/S0012-821X(03)00634-4

948 Hersum TG, Marsh BD (2007) Igneous textures: On the kinetics behind the words.
949 Elements 3:247–252. doi: 10.2113/gselements.3.4.247

950 Higgins MD (2000) Measurement of crystal size distributions. Am Mineral 85:1105–1116

951 Higgins MD (2002) A crystal size-distribution study of the Kiglapait layered mafic
952 intrusion, Labrador, Canada: Evidence for textural coarsening. Contrib to Mineral
953 Petrol 144:314–330. doi: 10.1007/s00410-002-0399-9

954 Higgins, M. (2006). Quantitative Textural Measurements in Igneous and Metamorphic
955 Petrology. Cambridge: Cambridge University Press.
956 doi:10.1017/CBO9780511535574

957 Higgins MD (1996) Magma dynamics beneath Kameni volcano, Thera, Greece, as
958 revealed by crystal size and shape measurements. J Volcanol Geotherm Res 70:37–
959 48. doi: 10.1016/0377-0273(95)00045-3

960 Hort M (1998) Abrupt Change in Magma Liquidus Temperature because of Volatile Loss
961 or Magma Mixing: Effects on Nucleation, Crystal Growth and Thermal History of the
962 Magma. J Petrol 39:1063–1076. doi: 10.1093/petroj/39.5.1063

963 Jaupart C, Tait S (1995) Dynamics of differentiation in magma reservoirs to gradients
964 deveioped at the recent work has focused on the internal structure. J Geophys Res
965 100:615–617

966 Jenner GA, Foley SF, Jackson SE, et al (1993) Determination of partition coefficients for
967 trace elements in high pressure-temperature experimental run products by laser
968 ablation microprobe-inductively coupled plasma-mass spectrometry (LAM-ICP-MS).
969 Geochim Cosmochim Acta 57:5099–5103. doi: 10.1016/0016-7037(93)90611-Y

970 Jerram D a., Martin V (2008) Understanding crystal populations and their significance
971 through the magma plumbing system. doi: 10.1144/SP304.7

972 Kirkpatrick JR (1978) Nucleation and growth of plagioclase, Makaopui and Alae lava
973 lakes, Kilauea Volcano, Hawaii: Discussion. Bull Geol Soc Am 89:797–798. doi:
974 10.1130/0016-7606(1978)89<797:NAGOPM>2.0.CO;2

975 Kirkpatrick RJ (1975) Crystal Growth from the Melt : A Review. Am Miner 60:798–814

976 Larsen ES (1929) The temperatures of magmas. Am Mineral 14:81–94

977 Laubier M, Grove TL, Langmuir CH (2014) Trace element mineral/melt partitioning for
978 basaltic and basaltic andesitic melts: An experimental and laser ICP-MS study with
979 application to the oxidation state of mantle source regions. Earth Planet Sci Lett
980 392:265–278. doi: 10.1016/j.epsl.2014.01.053

Li C, Ripley EM (2010) The relative effects of composition and temperature on olivine-liquid Ni partitioning: Statistical deconvolution and implications for petrologic modeling. Chem Geol 275:99–104. doi: 10.1016/j.chemgeo.2010.05.001

Luhr JF, Carmichael ISE (1980) The Colima Volcanic complex, Mexico. Contrib to Mineral Petrol 71:343–372. doi: 10.1007/BF00374707

Maaløe S, Tumyr O, James D (1989) Population density and zoning of olivine phenocrysts in tholeiites from Kauai, Hawaii. Contrib to Mineral Petrol 101:176–186. doi: 10.1007/BF00375304

Macdonald R, McGarvie DW, Pinkerton H, et al (1990) Petrogenetic evolution of the torfajökull volcanic complex, Iceland I. Relationships between magma types. J Petrol 31:461–481. doi: 10.1093/petrology/31.2.461

Marsh BD (1988) Crystal size distribution (CSD) in rocks and the kinetics and dynamics of crystallisation I: Theory. Contrib to Mineral Petrol 99:277–291. doi: 10.1007/BF00371933

McGarvie DW (1984) Torfajökull : A volcano dominated by magma mixing. Geology 12:685–688. doi: 10.1130/0091-7613(1984)12<685

McGarvie DW, Macdonald R, Pinkerton H (1990) Petrogenetic Evolution of the Torfajokull Volcanic Complex , Iceland II . The Role of Magma Mixing. J Petrol 31:461–481

McKay GA, Weill DF (1977) KREEP petrogenesis revisited. Proc Eighth Lunar Conferece, (supplement 8, Geochemica Cosmochim Acta) 2339–2355

McKenzie D, O'Nions RK (1991) Partial melt distribution from inversion of rare earth element concentrations. J Petrol 32:1021–1091. doi: 10.1093/petrology/32.5.1021

Mysen BO (1978) Experimental determination of nickel partition coefficients between liquid pargasite, and garnet peridotite minerals and concentration limits of behaviour according to Henry's Law at high pressure and temperature. American 278:217–243

Nandedkar RH, Ulmer P, Müntener O (2014) Fractional crystallization of primitive, hydrous arc magmas: An experimental study at 0.7 GPa. Contrib to Mineral Petrol 167:1–27. doi: 10.1007/s00410-014-1015-5

1010 Nathan HD, Vankirk CK (1978) A model of magmatic crystallization. J Petrol 19:66–94.
1011 doi: 10.1093/petrology/19.1.66

1012 Neave DA, Buisman I, MacLennan J (2017) Continuous mush disaggregation during the
1013 long-lasting Laki fissure eruption, Iceland. Am Mineral 102:2007–2021. doi:
1014 10.2138/am-2017-6015CCBY

1015 Neave DA, Putirka KD (2017) A new clinopyroxene-liquid barometer, and implications
1016 for magma storage pressures under Icelandic rift zones. Am Mineral 102:777–794.
1017 doi: 10.2138/am-2017-5968

1018 Nelson ST, Montana A (1992) Sieve-textured plagioclase in volcanic rocks produced by
1019 rapid decompression. Am Mineral 77:1242–1249

1020 Neumann H, Mead J, Vitaliano CJ (1954) Trace element variation during fractional
1021 crystallization as calculated from the distribution law. Geochim Cosmochim Acta
1022 6:90–99. doi: 10.1016/0016-7037(54)90018-6

1023 Nielsen RL, Ustunisik G, Weinsteiger AB, et al (2017) Trace element partitioning between
1024 plagioclase and melt: An investigation into the impact of experimental and analytical
1025 procedures. Geochemistry, Geophys Geosystems 18:3359–3384. doi:
1026 10.1002/2017GC007080.Received

1027 Osborn EF, Tait DB (1952) The system diopside-forsterite-anorthite. Am. J. Sci.

1028 Polacci M, Arzilli F, La Spina G, et al (2018) Crystallisation in basaltic magmas revealed
1029 via in situ 4D synchrotron X-ray microtomography. Sci Rep 8:1–13. doi:
1030 10.1038/s41598-018-26644-6

1031 Pupier E, Duchene S, Toplis MJ (2008) Experimental quantification of plagioclase crystal
1032 size distribution during cooling of a basaltic liquid. Contrib to Mineral Petrol
1033 155:555–570. doi: 10.1007/s00410-007-0258-9

1034 Putirka KD (2008) Thermometers and Barometers for Volcanic Systems. Rev Mineral
1035 Geochemistry 69:61–120. doi: 10.2138/rmg.2008.69.3

1036 Putirka KD (2005) Igneous thermometers and barometers based on plagioclase + liquid
1037 equilibria: Tests of some existing models and new calibrations. Am Mineral 90:336–
1038 346. doi: 10.2138/am.2005.1449

1039 Putirka KD, Mikaelian H, Ryerson F, Shaw H (2003) New clinopyroxene-liquid
1040 thermobarometers for mafic, evolved, and volatile-bearing lava compositions, with
1041 applications to lavas from Tibet and the Snake River Plain, Idaho. Am Mineral
1042 88:1542–1554. doi: 10.2138/am.2005.431

1043 Ren M, Parker DF, White JC (2003) Partitionning of Sr, Rb, Y, and LREE between
1044 plagioclase and peraluminous silicic magma. Am Mineral 88:1091–1103

1045 Renjith ML (2014) Micro-textures in plagioclase from 1994-1995 eruption, Barren Island
1046 Volcano: Evidence of dynamic magma plumbing system in the Andaman subduction
1047 zone. Geosci Front 5:113–126. doi: 10.1016/j.gsf.2013.03.006

1048 Roeder PL, Emslie RF (1970) Olivine-liquid equilibrium. Contrib to Mineral Petrol
1049 29:275–289. doi: 10.1007/BF00371276

1050 Schiavi F, Walte N, Keppler H (2009) First in situ observation of crystallization processes
1051 in a basaltic-andesitic melt with the moissanite cell. Geology 37:963–966. doi:
1052 10.1130/G30087A.1

1053 Schiavi F, Walte N, Konsnschak A, Keppler H (2010) A moissanite cell apparatus for
1054 optical in situ observation of crystallizing melts at high temperature. Am Mineral
1055 95:1069–1079. doi: 10.2138/am.2010.3379

1056 Smith PM, Asimow PD (2005) Adiabat-1ph: A new public front-end to the MELTS,
1057 pMELTS, and pHMELTS models. Geochemistry, Geophys Geosystems 6:1–8. doi:
1058 10.1029/2004GC000816

1059 Sobolev AV, Migdisov AA, Portnyagin MV (1996) Incompatible element partitioning
1060 between clinopyroxene and basalt liquid revealed by the study of melt inclusions in
1061 minerals from Troodos lavas, Cyprus. Petrology 4:307–317

1062 Špillar V, Dolejš D (2013) Calculation of time-dependent nucleation and growth rates
1063 from quantitativetextural data: Inversion of crystal size distribution. J Petrol 54:913–
1064 931. doi: 10.1093/petrology/egs091

1065 Špillar V, Dolejš D (2015) Heterogeneous nucleation as the predominant mode of
1066 crystallization in natural magmas: numerical model and implications for crystal–melt
1067 interaction. Contrib to Mineral Petrol 169:. doi: 10.1007/s00410-014-1103-6

1068 Streck MJ (2008) Mineral Textures and Zoning as Evidence for Open System Processes.

1069 Rev Mineral Geochemistry 69:595–622. doi: 10.2138/rmg.2008.69.15

1070 Sun C, Graff M, Liang Y (2017) Trace element partitioning between plagioclase and
1071 silicate melt: The importance of temperature and plagioclase composition, with
1072 implications for terrestrial and lunar magmatism. Geochim Cosmochim Acta
1073 206:273–295. doi: 10.1016/j.gca.2017.03.003

1074 Tepley FJ, Lundstrom CC, McDonough WF, Thompson A (2010) Trace element
1075 partitioning between high-An plagioclase and basaltic to basaltic andesite melt at 1
1076 atmosphere pressure. Lithos 118:82–94. doi: 10.1016/j.lithos.2010.04.001

1077 Toramaru A (1991) Model of nucleation and growth of crystals in cooling magmas.
1078 Contrib to Mineral Petrol 108:106–117. doi: 10.1007/BF00307330

1079 Valentine GA, Zhang D, Robinson BA (2002) Modeling Complex, Nonlinear Geological
1080 Processes. Annu Rev Earth Planet Sci 30:35–64. doi:
1081 10.1146/annurev.earth.30.082801.150140

1082 Viccaro M, Barca D, Bohrson WA, et al (2016) Crystal residence times from trace element
1083 zoning in plagioclase reveal changes in magma transfer dynamics at Mt. Etna during
1084 the last 400 years. Lithos 248–251:309–323. doi: 10.1016/j.lithos.2016.02.004

1085 Viccaro M, Giacomoni PP, Ferlito C, Cristofolini R (2010) Dynamics of magma supply at
1086 Mt. Etna volcano (Southern Italy) as revealed by textural and compositional features
1087 of plagioclase phenocrysts. Lithos 116:77–91. doi: 10.1016/j.lithos.2009.12.012

1088 Villemant B, Boudon G (1998) Transition from dome-forming to plinian eruptive styles
1089 controlled by H2O and Cl degassing. Nature 392:65–69. doi: 10.1038/32144

1090 Vinet N, Higgins MD (2011) What can crystal size distributions and olivine compositions
1091 tell us about magma solidification processes inside Kilauea Iki lava lake, Hawaii? J
1092 Volcanol Geotherm Res 208:136–162. doi: 10.1016/j.jvolgeores.2011.09.006

1093 Wagner J, Haigis V, Künzel D, Jahn S (2017) Trace element partitioning between silicate
1094 melts – A molecular dynamics approach. Geochim Cosmochim Acta 205:245–255.
1095 doi: 10.1016/j.gca.2017.02.017

1096 Watson EB, Ryerson FJ (1986) Partitioning of zirconium between clinopyroxene and
1097 magmatic liquids of intermediate composition. Geochim Cosmochim Acta 50:2523–
1098 2526. doi: 10.1016/0016-7037(86)90035-9

1099 Yang H-J, Kinzler RJ, Grove TL (1996) Experiments and models of anhydrous, basaltic
1100 olivine-plagioclase-augite saturated melts from 0.001 to 10 kbar. Contrib to Mineral
1101 Petrol 124:1–18. doi: 10.1007/s004100050169

1102 Zieg MJ, Lofgren GE (2006) An experimental investigation of texture evolution during
1103 continuous cooling. J Volcanol Geotherm Res 154:74–88. doi:
1104 10.1016/j.jvolgeores.2005.09.020

1105

1106

APPENDIX 1: Source Code

Found in Supplementary Files

APPENDIX 2: model equations

Function	Equation	Reference
Fractional Crystallisation	$\frac{Cl}{Co} = F^{(D-1)}$	(Neumann et al. 1954)
Temperature	$\ln\left(\frac{X_i^{ol}}{X_i^L}\right) = C_0 + \frac{C_1}{T} + \frac{C_2(P-1)}{T} + C_3 \ln\left(1.5\left(X_{Mg}^L + X_{Ca}^L + X_{Mn}^L + X_{Cr2+}^L + X_{Ni}^L\right)\right) + C_4 \ln(3X_{Si}^L) + \sum C_j \ln(1 - X_j^L)$	(Ford et al. 1983)
An mol.%	$\frac{10^4}{T(K)} = 6.12 + 0.257 \ln\left(\frac{[An^{pl}]}{[Ca^{liq}(Al^{liq})^2(Si^{liq})^2}\right) - 3.166\,[Ca^{liq}] + 0.2166\,[H2O^{liq}] - 3.137\left[\frac{Al^{liq}}{Al^{liq}+Si^{liq}}\right] + 1.216\,[Ab^{pl}]^2 - 2.475\,x\,10^{-2}\,[P(kbar)]$	(Putirka 2005)
Growth Rate	$uR = \frac{v_c DC}{R}\left\{1 - \exp\left[\frac{2\gamma v_c DC}{kT_m}\left(\frac{1}{R} - \frac{1}{R_c}\right)\right]\right\}$	(Toramaru 1991)
Mg Diffusion	$\frac{\partial C_{Mg}}{\partial t} = \left(\mathrm{DMg} * \frac{\partial^2 C_{Mg}}{\partial x^2} + \frac{\partial C_{Mg}}{\partial x} * \frac{\partial D_{Mg}}{\partial x}\right) - \frac{A}{RT} * \left(D_{Mg} * \frac{\partial C_{Mg}}{\partial x} * \frac{\partial X_{An}}{\partial x} + C_{Mg} * \frac{\partial D_{Mg}}{\partial x} * \frac{\partial X_{An}}{\partial x} + D_{Mg} * C_{Mg} * \frac{\partial X_{An}}{\partial x^2}\right)$	(Costa et al. 2003)

APPENDIX 2: Kd values

	Basalt			Andesite			Rhyolite		
Element	**OL**	**PL**	**PX**	**OL**	**PL**	**PX**	**OL**	**PL**	**PX**
Ni	Eqn.[1]	0.122[9]	2.6[13]	Eqn. [1]	0.061[11]	4.6[11]	Eqn.[1]	1.1[12]	-
Cr	0.63[2]	Eqn.[9]	36[15]	5.14[7]	Eqn.[9]	30[14]	5.14[7]	Eqn.[9]	30[14]
Sc	0.38[2]	Eqn.[9]	1.31[16]	0.3[11]	Eqn.[9]	17[14]	-	Eqn.[9]	33[14]
Sr	5.11e-4[2]	Eqn.[9,10]	0.0479[2]	0.008[6]	Eqn.[9,10]	0.5[14]	-	Eqn.[9,10]	0.5[14]
Ba	3.2e-5[2]	Eqn.[9,10]	1.1e-4[2]	0.005[8]	Eqn.[9,10]	0.1[12]	-	Eqn.[9,10]	0.1[14]
Rb	1.8 e-4[4]	Eqn.[9]	0.011[4]	0.01[7]	Eqn.[9]	0.07[12]	-	Eqn.[9]	0.03[14]
Zr	0.001[5]	Eqn.[9]	0.046[17]	0.01[7]	Eqn.[9]	0.12[18]	-	Eqn.[9]	0.29[14]
Nb	0.0016[6]	0.01[4]	0.004[19]	0.0016[6]	1.3[12]	0.78[12]	-	0.07[12]	0.31[12]
Mg	-	Eqn.[9]	-	-	Eqn.[9]	-	-	Eqn.[9]	-

List of partition coefficients (Kd) models used for trace element calculations in the model. Where an equation is available, this is marked as "Eqn", otherwise the value given is that of the published Kd value. References are listed in order for olivine, plagioclase and clinopyroxene as indicated from the GERM website: [1] Li and Ripley 2010; [2] Beattie 1994; [3] ------; [4] McKenzie and O'Nions 1991; [5] Adam and Green 2006; [6] Dunn and Sen 1994; [7] Villemant and Boudon 1998; [8] McKay and Weill 1977; [9] Bindeman et al. 1998; [10] Blundy and Wood 1991; [11] Luhr and Carmichael 1980; [12] Ewart and Griffin 1994; [13] Mysen 1978; [14] Bacon and Druitt 1988; [15] Duke 1976; [16] Hart and Dunn 1993; [17] Sobolev et al. 1996; [18] Watson and Ryerson 1986; [19] Jenner et al. 1993.

APPENDIX 3: All model outputs

Found in Supplementary Files

APPENDIX 4: Melt compositions and run parameters

Found in Supplementary Files

Chapter 6

6. Critical Evaluation and Conclusions

A critical evaluation of the analytical techniques and models utilised, summary of key findings for this thesis and possible future research directions are outlined in this final chapter.

The overarching aim of the project presented in this thesis is to contribute to the better understanding of the range of shallow plumbing system magmatic processes and their effects on the crystal cargo, and plagioclase in particular. The focus has been put on comparing processes occurring at different tectonic settings, and in providing a more quantitative approach on their nature, extent, location and timing. In this study, a new crystal database for the latest eruptions of Torfajökull has been generated (Chapter 3). This data has provided a more holistic overview of the nature, location, timing and extent of the shallow plumbing system processes at Torfajökull, and its interactions with the adjacent fissure system. A particular emphasis was put on the basaltic product and their evidence for mush entrainment, as well as basalt-rhyolite mixing and mingling. As a comparison, a smaller crystal database was created for intermediate products from the Island of Salina, in a volcanic arc setting. These were used to provide an insight into the effects of crustal storage dynamics on the crystal cargoes, with a focus on pre-eruptive conditions and superimposed magmatic processes such as crustal assimilation and mixing. The two studies were carried out in order to better understand and most importantly quantify the effects on the crystal cargo of commonly occurring magmatic processes, such as mixing, assimilation and entrainment, across different tectonic settings, a rift-plume interaction setting (Iceland) and a volcanic arc (Aeolian Islands). In order to do this, a combination of petrology, geochemistry and numerical modelling techniques was used. Numerical modelling techniques utilised included both established published models and CrystalMath, a newly developed numerical model presented in this thesis (Chapter 5) used to replicate magmatic evolution, with a focus on crystal cargoes, used to better quantify shallow plumbing system processes as well as crystallisation conditions.

Whole rock analyses were carried out by XRF. Crystal textures were studied using optical microscopy and quantified using the CSD technique. Crystal cargo major and trace element compositions were analysed by LA-ICP-MS, but for some specific Torfajökull

products SIMS data was also utilised. The development of the forward model for crystal cargo evolution in an open system was initiated by generating a novel MATLAB code (Chapter 5).

6.1 Working with crystal cargoes

6.1.1. Why work with crystal cargoes?

Whole rock plays an important role in the understanding and study of the petrogenesis of a magma. An advantage of using whole rock is that numerical models exist that allow to quantify the extent of different processes affecting the melt composition (e.g. Ariskin 1993; Ghiorso and Sack 1995; Smith and Asimow 2005; Danyuschevsky and Plechov 2011), and relatively simple models can help quantify shallow process such as magma mixing and crustal assimilation (e.g. DePaolo 1981). Nevertheless, as previously discussed, whole rock composition is the result of homogenisation of a series of magmatic processes, such as fractional crystallisation, magma mixing and crustal assimilation which could be difficult to disentangle and study individually. This is particularly important for melts (and crystals) which are stored for a long period of time prior to eruption, where they can be subject to a variety of processes and changes in storage conditions. In contrast, crystals allow the study and identification of individual processes occurred during the evolution of a melt however, due to complex mineral-melt relationships and other issues discussed in Chapter 1, there are limitations in understanding the role of and the degree to which these magmatic processes can be quantified, and observations often remain qualitative or semi-quantitative (e.g. Humphreys et al 2006; Ginibre et al 2007; Neave et al 2014; Reinjith 2014; Bennett et al 2019). These limitations, and the ways in which these were addressed in this thesis, are discussed in the following sections.

In this study, the analysis of crystal cargoes at both volcanic settings has been able to provide a more detailed insight into the evolution of the melt prior to eruption, due to the significant textural and chemical heterogeneity which can be preserved in crystals. A holistic petrological, geochemical and numerical modelling approach has allowed for a better understanding and quantification of crystallisation conditions and eruption triggering processes at both volcanic centres.

Plagioclase crystals in particular have been proven particularly useful in reconstructing magmatic histories, as they have been found in abundance across the whole compositional

range of the samples. Plagioclase also reacts quickly to compositional, temperature and pressure changes in the environment it grows in therefore providing a detailed insight into its crystallisation histories (Viccaro et al. 2010; Renjith 2014; Tepley et al. 1999; Browne et al. 2006; Viccaro et al. 2016; Churikova et al. 2013; Couch et al. 2003; Neave et al. 2014). As previously discussed, using plagioclase also presents challenges, including complicated mineral-melt relationships, and diffusion controlled growth periods resulting in oscillatory zoning which can obscure changes in crystallisation conditions (Vance 1962; Bottinga et al. 1966). Both olivine and clinopyroxe, the latter in particular, have frequently been used in the literature to disentangle magmatic processes (e.g. Morgan et al. 2004; Shea et al. 2015; Petrone et al. 2016; Ubide & Kamber 2018). Clinopyroxene has been useful for geobarometry modelling (Putirka et al. 1996; Putirka 1999; Neave & Putirka 2017; Putirka 2008), as it is a more robust method than that of plagioclase. In this thesis clinopyroxene thermobarometry has been used as a test and support for the pressure and temperature conditions calculated using plagioclase. In the numerical model CrystalMath, plagioclase thermobarometry was used to calculate equilibrium anorthite compositons (Putirka 2005). Olivine on the other hand was rarely present, or present in too little amounts to prove useful for comparison across the same sample, eruption and volcanic centre. Nevertheless interpretations could be extrapolated as the presence of fresh olivines implies the presence of a relatively primitive crystalline assemblage and they can be used to reconstruct primitive melt compositions (Ford et al. 1983; Beattie 1994). The olivine thermometer, based of Fe-Mg relationships (Ford et al 1983), has also proven to accurately calculate melt temperature in CrystalMath. Both in the Torfajökull and Salina samples neither olivine nor pyroxene were present in high abundance to be considered to reconstruct magmatic processes at their respective volcanic system. Moreover, following petrographic observations, olivine and clinopyroxene also showed less or no textural variability compared to plagioclase.

6.1.2. Assumptions and limitations

There are several assumptions which must be taken into consideration when working with crystal cargoes. The analysis of crystals has been carried out *insitu* using thin sections. The first assumption is that the thin section used is representative of the whole sample. In order to avoid biases in connection to this, two thin sections were cut for each samples in different locations, or three if the sample presented a large degree of macroscopic variability (Figure 6. 1), for example the presence of magmatic inclusions. Each thin

section was analysed petrographically under the microscope in order to ensure the sampling of the widest range of characteristics observed. For the samples collected during fieldwork, where possible, two or more samples for each flow where collected at different locations.

A further assumption is that the crystals analysed are representative of the whole cargo hosted in the lava. One of the benefits of LA-ICP-MS analyses is that they are relatively quick and therefore allow the acquisition of large amounts of data. Nevertheless this can be limited by the size of the thin section being analysed, the size of the crystal and the area of fresh surface on the crystal on which to place the laser spot on. The production of binary images for Crystal Size Distributions analyses has allowed the count of mineral phases present in the selected samples. For the least porphyritic sample, HRN-9 from Torfajökull, 182 plagioclase grains were counted. In contrast, 1672 plagioclase crystals were counted for SAL-64, a porphyritic lava from Salina.

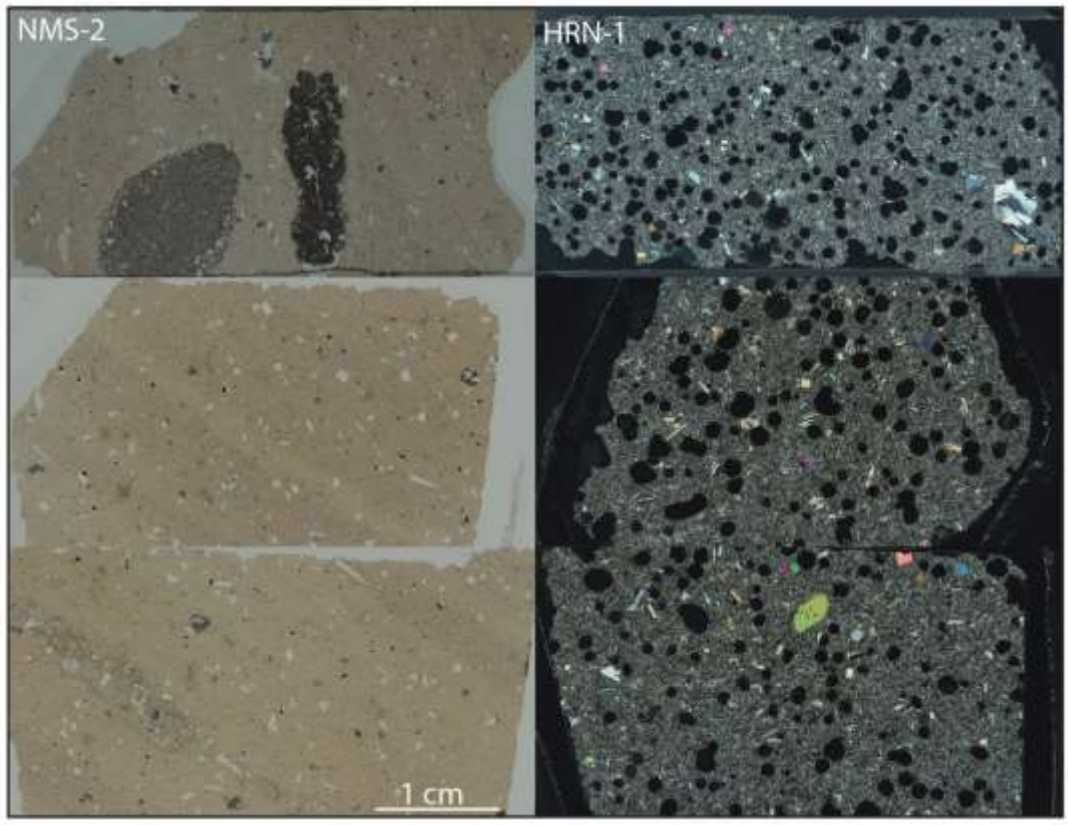

Figure 6. 1: comparison of three thin sections of the same sample (NMS-2 and HRN-1) show how different features, e.g. mafic enclaves (NMS-6) and glomerophyric clusters (HRN-1) may have been missed if only one section was analysed.

The analysis of all grains present in a single section is therefore unattainable. Vermeesch (2004) suggested that, in order to have a 95% certainty that no fraction smaller than 0.05

of the whole grain population has been missed during analysis, a number of 117 grains needs to be analysed for provenance studies. Whilst in igneous rocks this should also be considered as a factor of crystallinity of the sample, a similar approach has been attempted and considered for reconstructing magmatic histories using crystal cargoes. Where possible, core and rim analyses were taken for each crystal therefore assuming that each zone is representative of different stage of magmatic evolution and therefore, ideally, a higher numbers of analyses is required compared to provenance studies (Vermeesch 2004). Nevertheless this was not always possible (see Table 6. 1), especially for less porphyritic samples where less than 45 crystals were analysed, and therefore the lack of disequilibrium crystals in LA-ICP-MS results may not necessarily imply the fact that xenocrystal populations do not exist, but there is instead the possibility that they were not sampled and/or analysed. Nevertheless efforts were made to sample from crystals which showed petrologically distinct characteristics such as zoned and non-zoned crystals, fresh and resorbed surfaces, sieving, isolated or glomerophyric crystals etc. Moreover, some laser data was not possible to use due to poor analyses, for example when the ablation went over an inclusion, the edge of the crystal or ablated through the entire crystal therefore resulting in modified compositions.

Sample	Number of successful analyses		
	Olivine	Plagioclase	Clinopyroxene
HRN-1	22	80	30
HRN-9		29	
HRN-10		17	
HRN-26		22	
NMS-2		44	
NMS-6		39	
LGH-4		34	
SAL-64		84	
SAL-92		74	
MFF-8		80	27
LP-12		66	27

Table 6. 1: list of samples and number of successful grain analyses by LA-ICP-MS. Successful analyses refer to the data, including both cores and rims, whose totals were between ~99.5-100.5 and which were therefore used for interpretation.

Finally, whilst picking and mounting grains on polished blocks would have resulted in a larger number of analyses, given the same instrument time, it would have not provided

the same spatial resolution or core-rim relationships as *insitu* analyses. For both Icelandic and Salina samples, analyses on a larger number of samples and across a more diverse range of eruptions and flows may shed more detailed information of magmatic processes, however this was not possible within the time, and funding, of this PhD.

6.1.3 Analytical techniques – Rationale and limitations

A disadvantage of LA-ICP-MS compared to EPMA (Figure 6. 2) is the spatial resolution at which analyses are carried out. The laser spot size is of 74µm for olivine and 57µm for clinopyroxene and plagioclase. This means that only for larger crystals both core and rims analyses were possible, and the analysis of groundmass grains and microlites was not feasible. Similarly, the presence of compositional zones smaller than the laser spot size was identified under the microscope, as well as fine scale oscillatory zoning; therefore any ablation in those areas would have resulted in homogeneisation of the compositional zonation. Whilst this could be an issue, grains, and the area of the grains, targeted for analyses commonly showed optically homogeneous cores and clear rims, and did not show areas of fine zoning. SIMS data for the Torfajökull samples (Chapter 3) shows no widespread evidence for oscillatory zoning, except for large glomerocryst-hosted crystals (i.e. HRN-26) and rhyolitic sample NMS-6 (Figure 6. 3). Similarly, SIMS profiles across plagioclase crystals carried out for diffusion modelling suggest that no significant zoning patterns are observed in the core and more central zones of the crystal. The only significant zone and abrupt change in composition is observed at the edge of the crystal, and this is also observed in LA-ICP-MS data (Chapter 3). Unfortunately, this is not the case for the Salina samples (Chapter 4) which show much more complex zoning patterns as well as a wider range of populations within the same sample. Whilst these crystals would have benefit from higher spatial resolution analyses, it was not possible in the timeframe of this project. Overall, further analyses on more samples and higher resolution analyses on the Salina samples would have allowed for a better constrained magmatic history and plumbing system reconstruction of this volcanic system. Nevertheless, LA-ICP-MS data still enabled the identification of different populations within the sample and to highlight distinct geochemical signature across the different samples.

The reliability of plagioclase major and trace element concentrations obtained through LA-ICP-MS was assessed by comparing the results of the same grains analysed by EPMA (Electron Probe Microanalysis) at the University of Edinburgh for sample HRN-1, and the results show that the data is comparable (Figure 6. 2). Larger variations in anorthite

and trace and major elements at $An_{\sim 55\text{-}65}$ are observed but are nevertheless within error. The good correlations observed between EPMA and LA-ICP-MS data at high anorthite suggest that in terms of analytical precision the two methods are comparable. Whilst the error for Sr is smaller by LA-ICP-MS, the errors for major elements, such as Fe_2O_3, is higher than EPMA. Nevertheless it is important to note that the differences in elemental concentrations resulting from the two methods are still within error of each other and, of significance to this thesis, they reproduce a similar and comparable trend between datasets.

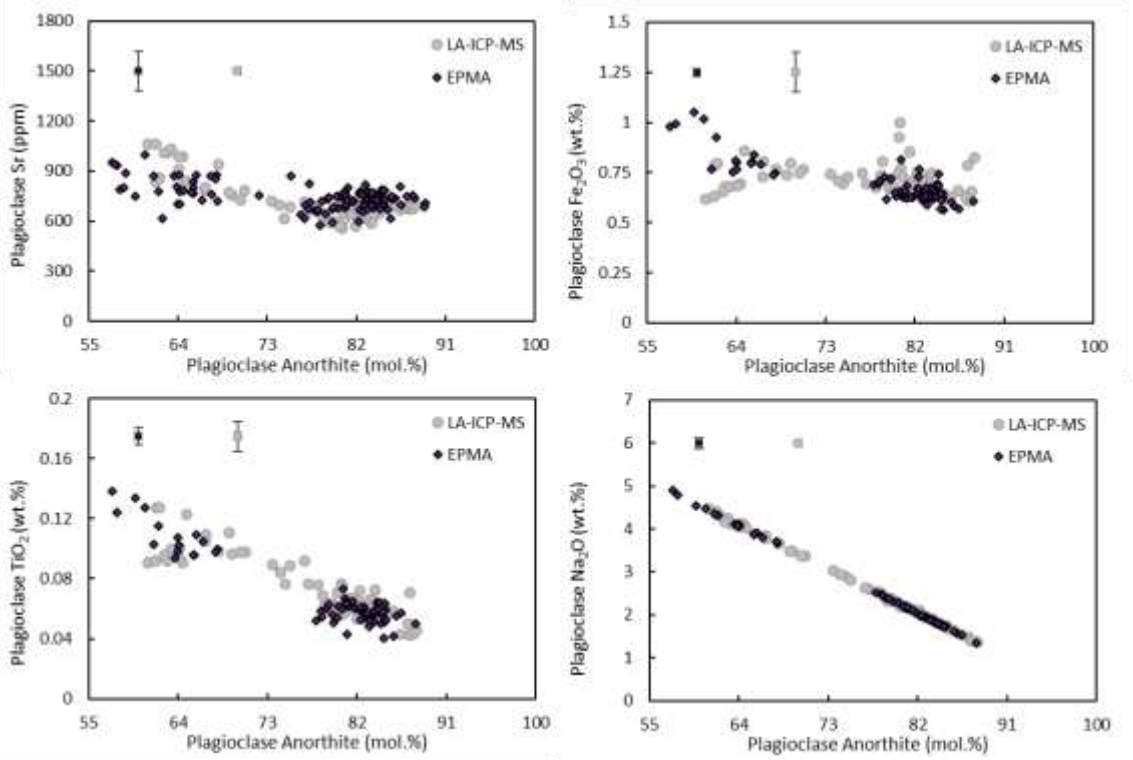

Figure 6. 2: comparison of LA-ICP-MS and EPMA plagioclase mineral data for sample HRN-1 for trace element Sr and major elements Fe_2O_3, TiO_2 and Na_2O against anorthite, suggesting that the two methods are comparable in terms of analytical precision. Error bars are shown in the top left corner of each plot.

Attempts were made, throughout the 1st and 2nd year of this PhD project, to analyse Sr isotopic compositions of plagioclase hosted in the Torfajökull samples. Whilst analysing whole grains could have resulted in heterogeneity of the different isotopic signatures, a large amount of grains (~20) would have resulted in a trend plotting towards any potentially distinct compositional end-member.

Picked whole plagioclase grains were prepared and loaded on to beads which were mounted in a turret for TIMS analyses using the method by Charlier et al. (2006). Each

beaker was cleaned in concentrated HCl and HNO_3 prior to use. Sample digestion was carried out by adding HCl and then HNO_3 and HF, leaving the sealed beakers onto a hotplate at ~150 ℃. The lids were then removed to evaporate the samples to dryness. The sample was then passed through columns using Sr spec resin. After pre-cleaning, 5 drops of Sr spec resin were pipetted directly into each column. Further cleaning of the columns was then ensured using varying concentrations of HNO_3. The samples were then loaded and eluted with 8M HNO_3. The resulting Sr fraction was collected in cleaned beakers and left to dry overnight. Once dry, the samples were loaded on the beads using H_3PO_4, burning off any remaining acid from the filament by increasing the current to 2A. Once loaded onto the turret, the samples were analysed using the Royal Holloway VG 354 TIMS.

Working with a very small amount of material, as single feldspar grains weighted around ~0.5mg, it was found that the standard sample preparation method (Charlier et al. 2006) routinely used in the TIMS laboratory was not working for these samples as the ionisation was not enough for analyses. Possible reasons could have been: 1) the material was not dissolving properly during the dissolution phase, 2) the loss of Sr during column chemistry separation, 3) low ionisation due to the spread of material on the filament rather than it being concentrated in the centre of the bead and 4) low ionisation due to inadequate separation inhibiting Sr ionisation, possibly impeded by Ca. These issues were attempted to be resolved by 1) digesting the sample in HF and HNO_3 4 molar as well as loading it for column chemistry in 4M and by crushing the sample into finer powder rather than attempting to dissolve it as a whole grain, 2/4) testing column chemistry solutions for each step by ICP-MS, finding that acid molarity played a major role in Sr retention, where at 8M Sr uptake is at his highest and is efficiently separated from Ca (Horwitz et al. 1992), 3) loading samples on the filament using a parafilm dam, which ensured the sample was loaded in the middle of the filament (where the beam is focussed) but which also burnt off as the voltage was turned on. Nevertheless none of these solutions attempted throughout the two years improved our results and therefore Sr isotopic analyses could not be carried out in the timescales of this project.

6.2 Using whole rock & mineral-melt disequilibrium

The results of crystal cargoes studies for both the Torfajökull and Salina volcanic system point to a wide diversity of magmatic processes occurring and affecting the composition of the final erupted product. When crystal chemistry was compared to host whole rock

composition, it became clear that the degree of disequilibrium present meant that utilising whole rock alongside crystal chemistry would have resulted in errors in the interpretation and calculation of magmatic variables such as pressure and temperature. For this reason, most of the interpretations were based on crystal chemistry alone and, where melt composition was needed for example for thermobarometry modelling (Chapter 3 and Chapter 4), an effort was made to find a representative bulk composition as close to equilibrium as possible with the modelled cargo. This was done by using mineral-melt partition coefficient relationships, identifying possible equilibrium bulk compositions from the published literature (Chapter 3 and Chapter 4), and testing the chosen bulk compositions using the built-in crystal-melt equilibrium models provided by the thermobarometers (Ford et al. 1983; Putirka et al. 2003; Putirka 2005; Putirka 2008; Ridolfi & Renzulli 2012; Neave & Putirka 2017). In the numerical model CrystalMath, this issue was partially avoided by using a pressure-independent melt thermometer (Ford et al 1983), and by having pressure as a user-defined parameter, input at the start of the model run.

6.2.1 Constraints on partition coefficients

In this study partition coefficients have played a major role in interpreting crystal cargo chemistry and for modelling and quantifying magmatic processes. Nevertheless the use of partition coefficients can result in large errors.

Trace element concentration in magmas is controlled by their partition coefficient (*D*), that is the ease by which a trace element would substitute into the crystal lattice or it's affinity for a specific igneous phase (Blundy & Wood 1991; Blundy & Wood 2003; Ren et al. 2003; Tepley et al. 2010; Bédard 2014; Laubier et al. 2014; Sun et al. 2017; Wagner et al. 2017; Nielsen et al. 2017). *D* can be defined by equation 1 below (Nielsen 1985):

$$D_i = \frac{X_i^{mineral}}{X_i^{liquid}} \quad (1)$$

Where *i* stands for a specific element and *X* is its concentration in the mineral or liquid. The distribution coefficient of an element is therefore described as the ratio of the weight fraction of the trace element in the solid to that in the melt. The concentration of compatible trace elements in magma changes (decreasing) as fractional crystallisation takes place. Incompatible trace elements on the other hand are preferentially partitioned into the melt, therefore their concentration increases during fractional crystallisation.

Both can however be affected by open system processes and this can help us identify magma interactions. Small changes in partition coefficients values can result in large changes in the resulting melt and crystal concentrations, posing major issues in geochemical modelling of magmatic processes.

Significant work has been undertaken on the quantification of the partitioning behaviour of trace elements between mineral and melt. The value of the distribution coefficient for a specific element in a specific mineral is mainly controlled by the ionic radius and charge of the cation, however partitioning behaviour is also dependent on a series of external variables such as: temperature, pressure, concentration, oxygen fugacity and the composition of the solid and liquid phase (e.g. Blundy and Wood 1991, 2003; Ren et al. 2003; Tepley et al. 2010; Bédard 2014; Laubier et al. 2014; Nielsen et al. 2017; Sun et al. 2017; Wagner et al. 2017). Partition coefficients are mostly determined experimentally; however this presents difficulties in the sense that these need to be determined specifically to each magmatic process and it is not often possible to recreate the exact conditions. Nevertheless it has been found that by performing experiments over an extremely wide range of pressure, temperature and composition it is possible to obtain calibrations for models in order to cater for most scenarios (Blundy & Wood 2003).

In this project attempts to calculate K_D values from mineral compositions and glasses were made. Groundmass grains for Icelandic samples were picked from 1mm-500µm and 500-250µm crushed size fractions, taking particular care in excluding groundmass still attached to mineral grains. The picked groundmass was then sent to the University of Mainz to be fused on an iridium strip heater to produce homogenised glasses (method by Nehring et al. 2008). The glasses were mounted onto a glass slide and analysed by LA-ICP-MS as presented in the methods section (Chapter 2). The analyses however were unsuccessful, partly due to the fact that the glass was very thin and the laser ablated through the material quickly, as well as the fact that the samples' glass surface was not flat therefore resulting in different amounts of material being ablated. Due to the small size of the samples' glasses, polishing and repetition of analyses was not possible. Glassy rhyolitic groundmasses in thin sections were also analysed by LA-ICP-MS, where the thickness and sample's surface allowed for a complete ablation. These analyses yielded good results and were used for Concentration Variance Decay calculations (Perugini et al. 2015) (Chapter 3), nevertheless a similar method applied to coarser grained groundmass of, for example, basaltic samples and Salina's samples, would have not

resulted in reliable results due to the likelihood of ablation of microphenocrysts and groundmass crystals. Whilst other methods with better spatial resolutions could have been used, e.g. EPMA, this was not possible within the time and funding limits of this project.

The errors associated with modelling melts and crystal compositions using partition coefficients are shown in Chapter 5 (Figure 10 and figure 28). As previously mentioned, the models used (Putirka et al. 2003; Putirka 2005; Putirka 2008; Neave & Putirka 2017) provide mineral-melt equilibrium tests which were used to assess the suitability of the selected partition coefficients and calculated melt compositions.

In both Chapter 3 and Chapter 4 mineral-melt partitioning models (Blundy and Wood 1991, Bindeman et al 1998) are used to initially characterise the degree of chemical (dis)equilibrium of the crystal cargoes with their melt, and to initially present the physical and geochemical processes which could cause such variations (Chapter 3, figure 7, Chapter 4, figure 10). This was then taken into account for thermobarometry calculations, where an estimated bulk equilibrium composition was selected to model, for example, crystal cores (e.g. Chapter 4, figure 11). Partitioning models were also used during fractional crystallisation, mixing and diffusion modelling (Chapter 3) and for magma mixing and crustal assimilation models (Chapter 4). Due to the sensitivity of petrological modelling to this parameter, when equations were not available, values were carefully selected from a database of published data (GERM) to ensure they are the most appropriate possible values for the magma being modelled. Choice was mostly based on the major and, where possible, trace elements content and SiO_2 range of the lava and/or pressure and temperature conditions. For the Icelandic system, further tests on the suitability of the choice of partitioning models and initial bulk composition was tested using the numerical model CrystalMath. The model uses a range of equations (e.g. Blundy and Wood 1991; Bindeman 1998) and user input partition coefficients from the literature (Chapter 5, Appendix 2). Model results (Chapter 5, figure 9 and 19) show that the partition coefficient values and models used, and the selected initial composition, are able to replicate the trend of the natural samples up to approximately MgO 5 wt.%. For certain elements, such as Al_2O_3 and Sr, CrystalMath results had a better fit than the model results using Petrolog3 (Chapter 5, figure 9). Similarly, modelling plagioclase compositions, Mg results using CrystalMath had a better fit compared to the Petrolog3 models, whilst both models results had a good fit for Sr and a bad fit for Ba. The ability to carry out these test in CrystalMath allowed for the best matching models and bulk compositions to be

selected for modelling of, for example, diffusion. These tests unfortunately were not possible for Salina due to the model being optimised for an ol-cp-pl and relatively anhydrous crystalline assemblage (Chapter 5).

6.2.2 Numerical models – Rationale and limitations

Diffusivity and diffusion modelling

When working with crystals it is also important to assess whether a mineral phase is able to record with reliability the original conditions of crystallisation. Diffusivity plays a major role in preserving compositional zoning and often varies between different mineral phases, temperature, crystallographic directions (i.e. Morgan et al. 2004; Costa et al. 2008). The main advantage of using plagioclase for reconstructing magmatic histories is that coupled interdiffusion of NaSi-CaAl in plagioclase An_{70-90} is relatively slow ~$1*10^{-21}$ m^2/s at 1200°C (Grove et al. 1984), compared to that of other early occurring phases. Whilst this varies for lower anorthite, these compositional ranges were not considered for diffusion modelling and are less frequent in the hybrid samples. Olivine Fe-Mg interdiffusion, for example, is faster at ~$8.08*10^{-17}$ (Dohmen & Chakraborty 2007) and is therefore less likely to preserve the original compositional profile to the same extent as plagioclase over long timescales. Nevertheless compositional zoning in both olivine (i.e. Kahl et al. 2011; Kahl et al. 2013 and references therein) and clinopyroxene (i.e. Morgan et al. 2004; Petrone et al. 2016) has frequently been used to model residence times in magmatic systems on the scale of <1 year. Even though a comparison of magmatic histories reconstructed from different mineral phases would have been more robust, in this thesis interpretations mostly rely on plagioclase. This is mostly, and almost solely, due to the fact that plagioclase was the most abundant phase in all samples, was present across the whole compositional range as shown in Table 6. 1, and presented evident and clear zoning patterns under the microscope. Nevertheless the timescales calculated using plagioclase in Chapter 3 are too low (on the scale of a few days) to be reliable.

Using plagioclase also presents disadvantages which can be accompanied by large errors and uncertainty in the use of partition coefficients and diffusivity models, such as anorthite-melt relationships being strongly affected by water content and pressure (Sisson & Grove 1993; Panjasawatwong et al. 1995; Takagi et al. 2005; Couch et al. 2003; S Couch et al. 2003; Danyushevsky 2001), as well as melt composition and temperature (Bindeman et al. 1998; Blundy & Wood 1991; Couch et al. 2003). An attempt to mitigate, or rather to better understand the effects of these processes in the natural samples, has

been carried out by developing and using the CrystalMath model. As previously discussed, partitioning models and bulk compositions were tested with the model to find the best fit for natural samples. Similarly, water content and pressure are both parameters can be fed in the model by the user, they are easily modifiable both at the start of each model run and throughout the run itself, as they could be set to change at a specific model iteration time (Chapter 5) to simulate events such as, for example, ascent and decompression. Model test runs for the Icelandic data were carried out at different pressures and temperatures, to be able to best match and infer initial crystallisation conditions able to replicate the crystal cargo in natural samples.

Moreover different elements in plagioclase present diffusion rates which, at given conditions, can differ by up to seven orders of magnitude (Grove et al. 1984; LaTourette and Wasserburg 1995). This large variability requires adequate kinetic models which consider the following issues: the partitioning behaviours of elements such as Mg, Ba, Sr at different anorthite contents (Blundy and Wood 1991; Bindeman et al. 1998); the varying of diffusion rates with varying anorthite contents; the choice of boundary conditions as well the possible effect of two-dimensional diffusion effects in elongated prismatic grains (Costa et al. 2003). Particular care should be taken into consideration with Mg which is strongly coupled to major element concentration gradients. These issues and uncertainties are further addressed below:

1. Partition coefficients – these have been determined and are well constrained from recent studies. Mg partitioning was calculated using the equation by Bindeman et al (1998).
2. Diffusion coefficients – many determinations of trace element diffusion coefficients in plagioclase are dependent on plagioclase major element compositions. Mg was found to be among the fastest diffusing elements in plagioclase (LaTourette and Wasserburg 1998), being approximately seven orders of magnitude faster than NaSi-CaAl interdiffusion. Costa et al. (2003) suggested that therefore the basis for modelling Mg relative to a fixed anorthite content is justified.
3. Temperature – temperature (and pressure) can affect the two above parameters. Nevertheless, the limited variations in temperature over the modelled crystal growth interval can be neglected in the case of partition coefficients (Blundy and Wood 1991). Whilst a larger effect is present on diffusion coefficients, Costa et

al. (2003) state that calculations carried out at a constant characteristic temperature result in the same results.

4. Boundary conditions and coupling – the liquid composition is calculated assuming equilibrium with the plagioclase rim composition and the diffusion calculations assume that the rim remains in equilibrium with the liquid. An issue arises in the case of fast growth rates immediately prior to eruption may prevent the rim to attain such equilibrium and therefore these cases can be avoided by examining the crystal composition profiles. For any chosen rim composition, it is also important to note that not all anorthite compositions can be in equilibrium with the same liquid, and therefore Mg (and other trace elements) try to attain equilibrium with both the melt and the anorthite concentration (Costa et al 2003).
5. Two-dimensional diffusion – whilst Mg is found to be weakly anisotropic during diffusion in plagioclase, the effects of two-dimensional diffusion are found to only become significant in small prismatic crystals and in the case of substantial composition modification (Costa et al. 2003). The latter issue does not apply to the samples in this study, and the former was avoided by not sampling such populations.

Crystallisation kinetics – assumptions and limitations

As discussed in Chapter 5 and in the sections above, CrystalMath can be used as a test model to quantify crystallisation conditions and processes, with a strong focus on crystal cargo chemistry. This was initially developed for parameters such as melt composition, pressure and temperature, water content and mineral-melt partitioning models. In the later stages of the model development, it became clear that thermodynamics and crystallisation kinetics, nucleation rates in particular, would be necessary in order to fully be able to model the evolution of a cargo, especially in the case where crystals are being physically removed from the melt, and where textural zoning and crystal proportions are taken into consideration such as in CrystalMath.

Whilst new numerical and experimental models are being developed (e.g Zieg and Lonfgren 2006; Polacci et al. 2018), constraints on crystal nucleation rates in the literature (e.g. Cashman and Marsh 1988; Marsh 1988; Toramaru 1991, Pupier et al 2008) remain largely unknown and difficult to scale and quantify when magma solidification parameters are unknown. For this reason, these parameters were treated as unknowns in the model.

The crystal population of a magma, and its textural and chemical evolution through time, is related to growth and nucleation rates (Marsh 1988) and ultimately on the degree of undercooling (Kirkpatrick 1975). CrystalMath gives the option of testing a series of nucleation rates combination rates, comparing the resulting equilibrium assemblage to that of the natural sample, i.e. number of crystals and phase proportions, showing the best fit results in a parameter space plot (Chapter 5, figure 16). From this plot it is possible to obtain the best combination of nucleation rates for all three crystallising phases, which can be manually fed into the model as input parameters for standard model runs. In Chapter 5 it is highlighted that this feature of the model is not yet able to reproduce the same Crystal Size Distributions as those of natural sample, nevertheless it provides a starting point for investigating and testing a semi-quantitative evolution of crystallisation rates and their effects on the cargo.

6.3 Rifts and volcanic arcs - Cargoes, magma crustal storage and eruptability

Both the Torfajökull and, to a lesser extent, the Salina magmatic systems show evidence for the storage of crustal magma chambers in a mushy state, frequent to replenishment (recharge) and mush disaggregation. It is now a common concept that within the crust and plumbing systems, magma is predominantly stored as a slowly cooling crystal rich body or in a mushy state (e.g. Bachmann and Bergantz 2004; Gelman et al. 2013; Stelten et al. 2014). However mush hosted and derived crystals indicate complex crystallisation histories which suggest magma mixing processes leading to transitions from locked crystalline network to an eruptible body (e.g. Chapter 3 and 4). An eruptible magma is defined to be any parcel of magma with less than 50% volume of crystals (Marsh 1981), above which rheology inhibits eruption. At 50-70 vol.% of crystals the crystal network is nearly rigid and therefore chamber wide convection absent. This, alongside cooling conditions and reduced thermal gradients allows for silicic interstitial melt segregation is occurs (Dufek & Bachmann 2010). This mechanism is thought to allow for the rapid formation on large volumes of crystal poor highly eruptible rhyolitic melts (Bachmann and Bergantz 2004; Gelman et al. 2013; Stelten et al. 2014). A cryptodome (or laccolith)-like structure has been identified in the southern area of the Torfajökull caldera (Soosalu et al. 2006). These structures are commonly formed by pooling of mushroom shaped intrusions of felsic magmas (Mattsson et al. 2018) and laccolith inflation can be recognised through flow bands and aligned phenocryst phases (Mattsson et al. 2018), and such features are observed in the rhyolites of Torfajökull (Chapter 3). Cryptodomes can

cause collapse of volcanic edifices and explosive eruptions, and periods of inflation and deflation have been detected at Torfajökull in the area adjacent to the low frequency earthquake location associated with the presence of active magma (Soosalu et al. 2006; Soosalu & Einarsson 2004; Larsen et al. 2015; Lippitsch et al. 2005). A silicic mush reservoir has not been identified in the products of the 871AD and 1477 eruptions, it is therefore possible that silicic melts underneath Torfajökull were subject to frequent replenishment, where the newly injected melt resulted in convective currents keeping the crystals into suspension (Bachmann & Bergantz 2004). This process results in crystals homogeneisation which could also explains why plagioclase populations in the Torfajökull rhyolites and trachytes do not present distinct populations, but some grain display reverse and oscillatory zoning (Chapter 3, and Figure 6. 3). Recurrent injections allow of the accumulation of eruptive magma and have been associated with frequent but relatively small eruptions as opposed to large volume eruptions (Figure 6. 4) (Caricchi et al. 2014). At Torfajökull, the onset of rhyolite-basalt mixed eruptions is also associated with the decrease in erupted volume of rhyolite material (McGarvie et al. 1990). The last major eruption of ca. 80,000 BP resulted in the eruption of ~26km^3 of homogeneous rhyolite, whilst the rhyolite volume of the subsequent eruptions was <1km^3 (McGarvie et al. 1990) suggesting that associated basaltic activity resulted in more frequent and sustained rhyolite production (Gunnarsson et al. 1998; Martin & Sigmarsson 2007; Zellmer et al. 2008) and therefore more frequent but smaller eruptions fitting the model proposed by Caricchi et al. (2014). Moreover injection of basaltic melts into silicic chambers resulted in the eruption of rhyolites as part of hybrid products, therefore likely impeding the accumulation of large volumes of rhyolite in the crust (Chapter 3).

In contrast, the products of the 871AD eruption show evidence for basaltic mush entrainment (Chapter 3). In Mid Ocean Ridge settings, mixing of an evolved phenocryst poor magma and a more primitive crystal bearing magma is a common process (Costa et al. 2010). Mixing between a mush reservoir and an aphyric magma has been found to happen on timescales of years to days, suggesting that mush rejuvenation by magma recharge acts as an eruption trigger. This mechanism prevents the eruption of primitive melts which instead pond at shallower levels in the crust (Costa et al. 2010). This is consistent with the lack of primitive basalt at Torfajökull, where the most primitive erupted sample presents 6.88 wt.% MgO (McGarvie et al. 1990; Macdonald et al. 1990b; McGarvie 1984), and mush disaggregation to eruption timescales on the scale of days

(Chapter 3). The mush derived glomerocrysts found in the HRN samples suggest a tight network of crystals, with little interstitial melt, which would therefore be non-eruptible. The injection of a new magma supplies increased melt volume and potential gas phases, unlocking the crystal mush. Modelling using CrystalMath shows that high anorthite plagioclase crystals in sample HNR-1 could crystallise from a transitional basalt with an MgO of 6.8 wt.%, and initial evolution to anorthites around 70 mol.% could be obtained by fractionation alone (Chapter 5, figure 10). This also supports the idea that, as discussed in Chapter 3, the abrupt zoning to anorthite 60 mol% cannot be generated by fractional crystallisation but would require mixing with a more evolved, crystal poor, melt. Whilst the model is not able to replicate physical entrainment processes such as that of mush entrainment, mixing models support the idea of interaction with a more evolved melt (Chapter 5). Similar observations were made carrying out similar modelling using Petrolog3, nevertheless whilst the equilibrium plagioclase compositions resulting from fractional crystallisation are similar to those observed with CrystalMath (Chapter 3, figure 10; Chapter 5, figure 10). Similarly low anorthite crystals (50 mol.%) (Chapter 5, figure 11) could be obtained with 30:70 mixing of a rhyolite and transitional basalt (Chapter 5, figure 13)

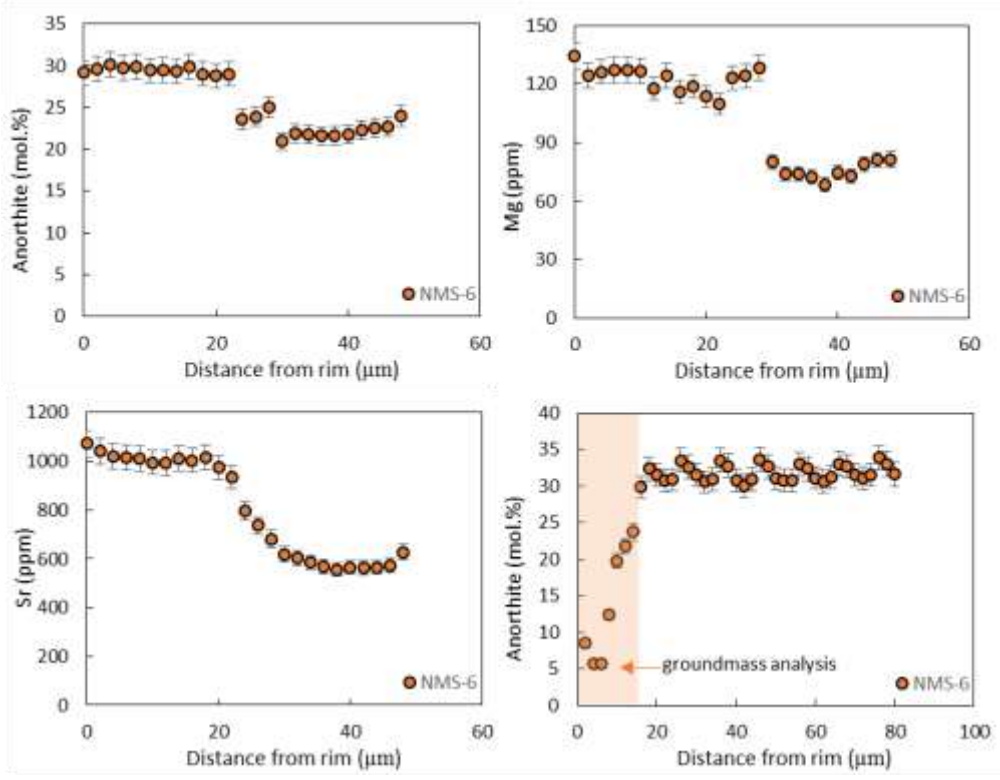

Figure 6. 3: SIMS data showing reverse (An_{20} to An_{30}) and oscillatory zoning (An_{30} to An_{35} over 60µm) in trachyte hosted plagioclase from the 1477 eruption of Torfajökull.

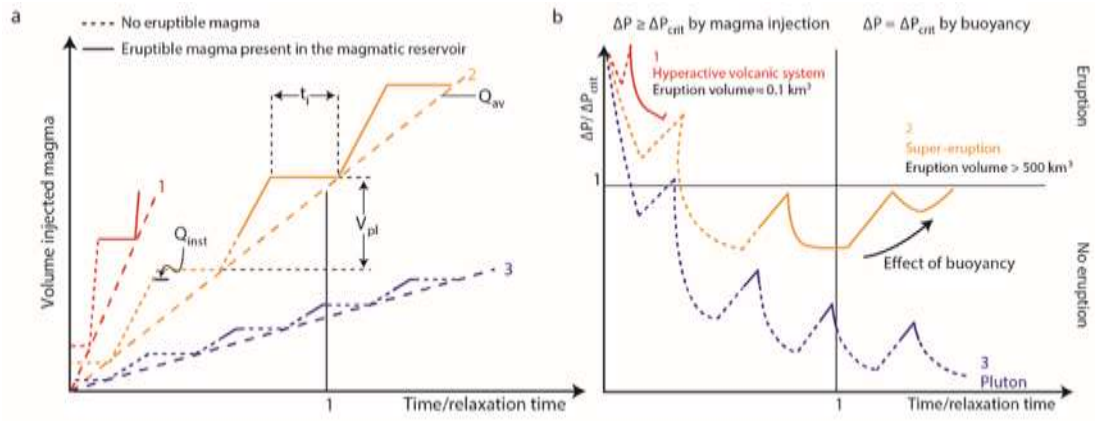

Figure 6. 4: possible scenarios of magma injection and associated overpressure (modified from Caricchi et al. (2014)). In the context of the Torfajökull volcanic system, recent activity involved frequent injections of basaltic magma into the system allowing for frequent replenishment and eruption of the silicic magma, therefore impeding the accumulation of large volumes of melt. (Gunnarsson et al. 1998; Martin & Sigmarsson 2007; Zellmer et al. 2008)

Having constrained the presence of a mushy reservoir, it is important to utilise magma storage and diffusion modelling with care. In fact, except for open systems, thermobarometry calculations only record the pressure and temperature conditions of crystallisation, not the conditions at which the magma was stored at (Cooper & Kent 2014). Similarly, Cooper & Kent (2014) argued that diffusion and growth timescales calculated using diffusion chronometry are only valid for the processes occurring at high magmatic temperatures and not for absolute crystal ages, making them unreliable for acquiring crystal total residence time in the crust. Nevertheless it is important to note that this study was based on cold storage in rhyolites, whereas storage processes and environments in basaltic melts and andesites would be different. Diffusion chronometry in this study was only carried out on basaltic samples and therefore this would have not been an issue in terms of constraining timescales of magma mixing and residence in the shallow crust post-entrainment.

Similarly to Torfajökull's basalts, the most primitive basalt erupted on Salina has an MgO content of 7.28 mol.%, (Lucchi et al. 2013) and is therefore far from being primitive. In subduction zone settings, the density of mafic magmas restricts their ascent through the thick crust to the surface (Cassidy et al. 2015). Prolonged shallow storage in crustal reservoirs enables extensive fractional crystallisation. Moreover, these magmas can be affected by a series of open system processes such as magma mixing and crustal assimilation. Recent models suggest that extensive differentiation also occurs in "deep crustal hot zones" (Annen et al. 2006; Solano et al. 2012), where the resulting hydrous

andesites proceed to ascend and pond in upper crustal storage regions subject to crystallisation and degassing (Annen et al. 2006), developing textural diversity. Deep basaltic melts, demonstrating textural evidence for having interacted with a possible magma mush (also inferred from previous studies (Lucchi et al. 2013)), are present on Salina. These basalts are relatively evolved ~5 wt.% MgO, and present both assimilated plutonic material and large and complexly zoned crystals. Whilst this does not undoubtedly suggest the presence of a magma mush, it suggests that these crystals were stored in an environment where they underwent repeated cycles of recharge, hybridisation and crystallisation. Fitting with deep rooted crustal magmatic system models, shallower crustal chambers are more evolved (andesitic and dacitic) and present chemically heterogeneous crystal populations as well as textural properties indicative of shallow storage, such as glomerophyric clusters and crystal microtextures (Chapter 4).

The crystal cargoes studied from the Torfajökull and Salina magmatic systems provide an insight into the different processes occurring in plumbing systems at rifts and arc magmatism settings. Both the Torfajökull and Salina samples provide evidence for magma recharge and mixing, nevertheless in Iceland this is often associated to eruption and therefore acts as an eruption trigger (Chapter 3). Moreover the large compositional differences between end members results in failed hybridisation processes. In contrast, Salina's cargoes and whole rock geochemistry variability suggests frequent magma mixing and recharge, followed by hybridisation and further fractional crystallisation, where recharge does not always act as an eruption trigger (Chapter 4). This could partly be due to the fact that, whilst relatively thick (Kaban et al. 2002), the Icelandic crust is subject to rifting and therefore provides paths for magmatic intrusions and ascent to the surface. In contrast, the crust underneath Salina, and volcanic arcs in general, is thick and prevents the ascent of magmas which stall to form reservoirs which can proceed to evolve in the shallow crust (Cassidy et al. 2015). Similarly, processes associated with ascent through the crust are more prominent in arc magmas, and Salina's samples give evidence for prolonged decompression, ascent and, occasionally, associated degassing also promoted by the high water content of the samples, associated with largely dissolved crystal cores and complex zoning patterns, including oscillatory zoning (Chapter 4). In contrast, Torfajökull's cargoes give little evidence for ascent and decompression, with the exception of coarse sieves in a minor amount of plagioclase crystals, and distinct storage levels of crystallisation for cores and rims of disaggregated mush crystals.

Compared to Salina's cargoes, the zoning patterns are simple and crystals cores are largely well preserved. Prolonged residence time in crustal reservoirs and ascent also promotes crustal assimilation processes. Salina's samples give evidence for crystal clots and gabbroic enclaves assimilated from the chamber's/conduit's walls where some present similar geochemistry signatures to that of basement rocks (Ventura 2013; Francalanci et al. 1993) (Chapter 4). An interesting point is that the Salina's samples, whilst each is more representative of a distinct decompression, mixing or crystallisation episode, they all share the same textural disequilibrium features to different extents (Chapter 4), whilst this is not observed in the Torfajökull samples. Moreover, it is interesting to note that the glomerocrysts observed in Salina's samples are varied, presenting more than one crystal phase such as plagioclase, oxides and clinopyroxenes. In contrast, Torfajökull's clots are highly plagioclase phyric. This could partly be due to the different degree of evolution of the melts, but also due to the difference in assimilation and entrainment process. Torfajökull's glomerocrysts are thought to be originating from a partly mushy reservoir where, due to buoyancy differences between phenocrysts in basaltic melts (Chapter 3), plagioclase could have separated from other phases such as olivine and clinopyroxene. In contrast, the clots in Salina's samples are associated with solid assimilation of cold wallrock material (Chapter 4).

In both Iceland and Salina, many studies had primarily focused on whole rock geochemistry (McGarvie et al. 1990; Macdonald et al. 1990b; McGarvie 1984; Zellmer et al. 2008; Lucchi et al. 2013; Gertisser & Keller 2000; Perugini et al. 2004; Calanchi et al. 1993; Zamboni et al. 2016). Mineral studies, if present, focussed primarily on major elements (e.g. Nicotra et al 2014) or compositional end members (Zellmer et al. 2008) and therefore the quantification and distinction of a series of superimposed magmatic processes, and associated crustal storage and plumbing system, had not been assessed in as much detail.

6.4 Conclusions: Towards an interdisciplinary approach for the quantification of magmatic processes

Throughout this project, it has been observed how petrological tools can be used alongside numerical models (and pre-existing geophysical observations, such as seismicity at Torfajökull (Chapter 3)), to reconstruct a more quantitative, holistic and interdisciplinary model of volcanic plumbing systems and processes. Taking the example of Torfajökull (Chapter 3), initial petrology and geochemistry showed evidence for mush

storage regions which were not previously observed at Torfajökull. Geochemical models such as thermobarometry supported this hypothesis by highlighting distinct storage levels for plagioclase cores and rims. Textural and kinetic models allowed for the reconstruction of crystallisation times and, combined with pressures, ascent rates towards the surface. Mineral-melt partitioning models allowed for an approximate reconstruction of original melt compositions, which are not erupted at the surface. All of these models and observations were tested using CrystalMath, in order to provide the best set of initial and crystallisation parameters, to allow for more accurate and quantifiable characterisation of processes such as magma mixing, as well as crystallisation histories, location and timing. Geophysical observation and studies in the literature further supported the presence of a mush chamber by seismically identifying a cooling crystalline body in the area of the caldera underlying the mush-rich eruptive products.

As previously discussed, in order to accurately reconstruct magmatic histories, models have been developed with the aim to provide information on mineral-melt relationships, storage conditions and textural interpretations. For crystal cargoes however these are often qualitative or semi-quantitative, and magmatic processes such as magma mixing are often invoked without quantification or identification of end member compositions, or only modelled using whole rock. This is mostly due to the large errors associated with the previously mentioned models and petrological tools, in particular the errors associated with partition coefficients. Whilst these issues in volcanology and petrology have long been present, and continue to be explored, CrystalMath provides a tool which combines these published models and forward models magmatic evolution, allowing the user to explore the different effects that crystallisation conditions, and other factors such as partitioning and crystallisation kinetics, have on the resulting melt and crystal cargo composition. Using natural samples as tie points, CrystalMath allows a fast and user-friendly method to model parameters and processes, allowing to test and better quantify the observations obtained from textural and chemical analyses. This is particularly useful when samples and geochemical analyses are widely available and obtainable, as the model provides a tool for, but not restricted to, volcanologists or geoscientists who may not have a specialised petrological background to be able to compare models to natural samples. The better quantification and understanding of the crystal cargo is a step further towards facilitating an interdisciplinary approach to volcanology, in order to provide a stronger basis for volcanic behaviour and hazard assessment.

6.5 Future research directions

- The Torfajökull volcanic system provides evidence for magma recharge, mixing and mingling processes between both alkali/transitional and tholeiitic basalts, rhyolites and basaltic crystal mushes. A key finding is that a crystal mush storage region has been identified from the eruptive products of the 871AD eruption. These are spatially associated with an area of high frequency earthquakes occurring on the western side of the Torfajökull caldera thought to be representing a cooling magma chamber. This chamber has been inferred at 8 km depth (Soosalu & Einarsson 2004), with mush crystals thermobarometry indicating depths between ~8-13 km. Basaltic mush crystals are also found in hybrid trachytes, suggesting that rhyolitic pockets are encountered upon ascent. In contrast, the 1477 eruption provides more evidence for physical mingling of tholeiitic and rhyolitic melts, proposing lateral tholeiite injection from Veiðivötn as a viable process for small volume rhyolite eruptions. Future research directions could better try and constrain the formation of rhyolites and their possible association with the magma mush zone, and to better try and identify the extent of this mush storage region by investigating older erupted products. No clear relationship has been identified between Torfajökull and Veiðivötn basalts, nevertheless distinct plagioclase trace element chemistry could provide a valuable tool for identification of, if any, basaltic hybrids. Overall this study led to the compilation of a comprehensive crystal chemistry database for the 871 AD and 1477 eruptions with a focus on the end members major and trace element chemistry as well as the hybrid products, which was not available before. Processes such magma mixing were previously known, but with this data their extent, location and timing were better constrained and quantified.
- The island of Salina provides evidence for complex superimposed open system processes. The study of crystal cargoes has enabled the separation and interpretation of distinct processes such as magma mixing, crustal assimilation and ascent related decompression. The role of amphibole in Salina's magmas petrogenesis has shown to be a particularly interesting subject, as amphiboles are found in basaltic products and give a distinct geochemical signature, but are not found in more evolved andesites and dacites. Nevertheless the latter present crystal clots interpreted to be the result of intense amphibole break down due to

sustained storage and shallow level, decompression and ascent. Salina's lavas give evidence for both magma mixing and decompression as viable eruption triggers. Whilst the process and magmatic history and evolution of this volcanic complex has been previously studied extensively, in particular using whole rock data, no crystal chemistry (major and trace elements) is available with the exception of the Rivi-Capo volcanic complex. Further work, including higher resolution core-rim profiles across crystals and the analyses of a higher number of samples across different volcanic epochs, could shed more light on the complex processes characterising volcanism on the Island of Salina and provide more information on the role of amphibole in Salina's, and in general, arc lavas. This study, due time constraints, only focused on 4 lava flows from two eruptive Epochs. As previously mentioned, the study of further samples could provide more information on the relationship between amphibole and more intermediate products, if any, and the effects of heating (provided by mixing) versus decompression could have on amphibole and its breakdown products.

- CrystalMath provides a strong basis for the further development of a forward model for the chemistry and textural relationship of crystal cargos hosted in an evolving magmatic system. The model is able to model fractional crystallisation in basalts including crystal geochemical and textural zoning. Whilst this model is currently optimised for a limited range of basaltic compositions, this can be improved in the future to allow for more evolved assemblages. Mixing models can be advanced by allowing the modelling of evolved compositions alongside that of basalts, allowing for the physical entrainment of grains and not just changes in melt chemistry. The modelling of nucleation rates and their effects on textural development and crystal size distributions, as well as the scaling of such processes to a limited melt volume, has proven the most challenging parameter so far. Whilst the addition of a temperature depended nucleation curve results in CSD trends similar to those found in natural samples, quantitative comparisons are not yet possible. Going forward it will be essential to better constrain and include the relevant thermodynamic constrains such as undercooling and cooling rates and their effect on crystal nucleation and growth. Other physical parameters such as crystal settlings and magma volume, shape and boundary conditions will also have to be better constrained and taken into consideration where necessary.

7. Bibliography

Andrew, R.E.B. & Gudmundsson, A., 2008. Volcanoes as elastic inclusions: Their effects on the propagation of dykes, volcanic fissures, and volcanic zones in Iceland. *Journal of Volcanology and Geothermal Research*, 177(4), pp.1045–1054. Available at: http://dx.doi.org/10.1016/j.jvolgeores.2008.07.025.

Annen, C., Blundy, J.D. & Sparks, R.S.J., 2006. The genesis of intermediate and silicic magmas in deep crustal hot zones. *Journal of Petrology*, 47(3), pp.505–539.

Arculus, R.J. & Wills, K.J.A., 1980. The petrology of plutonic blocks and inclusions from the lesser antilles Island arc. *Journal of Petrology*, 21(4), pp.743–799.

Ariskin, A.A. et al., 1993. Comagmat: a Fortran program to model magma differentiation processes. *Computers and Geosciences*, 19(8), pp.1155–1170.

Armienti, P. et al., 1994. Effects of magma storage and ascent on the kinetic of crystal growth. *Contirb. Mineral. Petrol.*, 115(March 1993), pp.402–414.

De Astis, G., Ventura, G. & Vilardo, G., 2003. Geodynamic significance of the Aeolian volcanism (Southern Tyrrhenian Sea, Italy) in light of structural, seismological, and geochemical data. *Tectonics*, 22(4), p.n/a-n/a. Available at: http://doi.wiley.com/10.1029/2003TC001506.

Bachmann, O. & Bergantz, G.W., 2004. On the origin of crystal-poor rhyolites: Extracted from batholithic crystal mushes. *Journal of Petrology*, 45(8), pp.1565–1582.

Bachmann, O. & Huber, C., 2016. Silicic magma reservoirs in the Earth ' s crust. *American Mineralogist*, 101(1), pp.2377–2404.

Beattie P, Ford C, Russell D., 1991. Partition coefficients for olivine-melt and 878 orthopyroxene-melt systems. Contrib to Mineral Petrol 109:212–224. doi: 879 10.1007/BF00306480

Beattie, P., 1994. Systematics and energetics of trace-element partitioning between olivine and silicate melts: Implications for the nature of mineral/melt partitioning. *Chemical Geology*, 117(1–4), pp.57–71.

Bédard, J.H., 2014. Parameterizations of calcic clinopyroxene - Melt trace element partition coefficients. *Geochemistry, Geophysics, Geosystems*, 15(2), pp.303–336.

Bégué, F. et al., 2014. Extraction, storage and eruption of multiple isolated magma batches in the paired Mamaku and Ohakuri eruption,Taupo volcanic zone, New Zealand. *Journal of Petrology*, 55(8), pp.1653–1684.

Bennett, E.N,, Lissenberg, C.J., Cashman, K.V., 2019. The significnce of plagioclase textures in mid-ocean ridge basalt (Gakkel Ridge, Arctic Ocean). *Contributions to Mineralogy and Petrology*, 179, pp. 49.

Bergantz, G.W., Schleicher, J.M. & Burgisser, A., 2015. Open-system dynamics and mixing in magma mushes. *Nature Geoscience*, 8(10), pp.793–796.

Bindeman, I. et al., 2012. Silicic magma petrogenesis in Iceland by remelting of hydrothermally altered crust based on oxygen isotope diversity and disequilibria between zircon and magma with implications for MORB. *Terra Nova*, 24, pp.227–

232.

Bindeman, I.N., Davis, A.M. & Drake, M.J., 1998. Ion microprobe study of plagioclase-basalt partition experiments at natural concentration levels of trace elements. *Geochimica et Cosmochimica Acta*, 62(7), pp.1175–1193.

Björnsson, A. et al., 1977. Current rifting episode in north Iceland. *Nature*, 266(5600), pp.318–323.

Blundy J, Cashman ., 2005. Rapid decompression-driven crystallization recorded by melt inclusions from Mount St. Helens volcano. *Geology*, 33, pp.793–796. https ://doi.org/10.1130/G2166 8.1

Blundy, J. & Cashman, K., 2008. Petrologic Reconstruction of Magmatic System Variables and Processes. *Reviews in Mineralogy and Geochemistry*, 69, pp.179–239.

Blundy, J. & Wood, B., 2003. Partitioning of trace elements between crystals and melts. *Earth and Planetary Science Letters*, 210(3–4), pp.383–397.

Blundy, J.D. & Wood, B.J., 1991. Crystal-chemical controls on the partitioning of Sr and Ba between plagioclase feldspar, silicate melts, and hydrothermal solutions. *Geochimica et Cosmochimica Acta*, 55, pp.193–209.

Bottinga Y, Kudo A, Weill D., 1966. Some observations on oscillatory zoning and crystallization of magmatic plagioclase. *American Mineralogist*, 51, pp 792

Brown, S.K., Auker, M.R. & Sparks, R.S.J.,2015. Populations around Holocene volcanoes and development of a Population Exposure Index. In: S.C. Loughlin, R.S.J. Sparks, S.K. Brown, S.F. Jenkins & C. Vye-Brown (eds) Global Volcanic Hazards and Risk, Cambridge: Cambridge University Press.

Browne, B.L. et al., 2006. Magma mingling as indicated by texture and Sr / Ba ratios of plagioclase phenocrysts from Unzen volcano, SW Japan. *Journal of Volcanology and Geothermal Research*, 154, pp.103–116.

Browne, B.L. & Gardner, J.E., 2006. The influence of magma ascent path on the texture, mineralogy, and formation of hornblende reaction rims. *Earth and Planetary Science Letters*, 246(3–4), pp.161–176.

Burchardt, S. & Galland, O., 2016. Studying Volcanic Plumbing Systems – Multidisciplinary Approaches to a Multifaceted Problem. In *Updates in Volcanology - From Volcano Modelling to Volcano Geology the*. InTech, pp. 23–53. Available at: http://dx.doi.org/10.5772/63959.

Burgisser, A. & Bergantz, G.W., 2011. A rapid mechanism to remobilize and homogenize highly crystalline magma bodies. *Nature*, 471(7337), pp.212–215. Available at: http://dx.doi.org/10.1038/nature09799.

Calanchi, N. et al., 1993. Silicic magma entering a basaltic magma chamber: eruptive dynamics and magma mixing - an example from Salina (Aeolian islands, Southern Tyrrhenian Sea). *Bulletin of Volcanology*, 55(7), pp.504–522.

Caricchi, L. et al., 2014. Frequency and magnitude of volcanic eruptions controlled by magma injection and buoyancy. *Nature Geoscience*, 7(2), pp.126–130. Available at: http://dx.doi.org/10.1038/ngeo2041.

Caricchi, L. & Blundy, J., 2015. The temporal evolution of chemical and physical properties of magmatic systems. *Geological Society, London, Special Publications*, 422(1), pp.1–15. Available at: http://sp.lyellcollection.org/lookup/doi/10.1144/SP422.11.

Cashman, K., Blundy, J., 2013. Petrological cannibalism: the chemical and textural consequences of incremental magma body growth. *Contributions to Mineralogy and Petrology*, 166, pp.703–729. https ://doi.org/10.1007/s0041 0-013-0895-0

Cashman, C. V & Marsh, B.D., 1988. Crystal size distribution (CSD) in rocks and the kinetics and dynamics of crystallisation II: Makaopuhi lava lake. *Contributions to Mineralogy and Petrology*, 99, pp.277–291. Available at: file:///C:/Users/Kirsty/Downloads/Marsh 1988 Contrib Min Pet small (1).pdf.

Cashman, K. V., Stephen, R. & Sparks, J., 2013. How volcanoes work: A 25 year perspective. *Bulletin of the Geological Society of America*, 125(5), pp.664–690.

Cassidy, M. et al., 2018. Controls on explosive-effusive volcanic eruption styles. *Nature Communications*, 9(1), p.2839. Available at: http://www.nature.com/articles/s41467-018-05293-3.

Cassidy, M. et al., 2015. Origin of basalts by hybridization in andesite-dominated arcs. *Journal of Petrology*, 56(2), pp.325–346.

Charlier, B.L.A. et al., 2006. Methods for the microsampling and high-precision analysis of strontium and rubidium isotopes at single crystal scale for petrological and geochronological applications. *Chemical Geology*, 232(3–4), pp.114–133.

Churikova, T.G. et al., 2013. Major and trace element zoning in plagioclase from Kizimen Volcano (Kamchatka): Insights into magma-chamber processes. *Journal of Volcanology and Seismology*, 7(2), pp.112–130. Available at: http://link.springer.com/10.1134/S0742046313020024.

Colucci, S., de' Michieli Vitturi, M. & Landi, P., 2017. CrystalMom: a new model for the evolution of crystal size distributions in magmas with the quadrature-based method of moments. *Contributions to Mineralogy and Petrology*, 172(11–12), pp.1–17.

Cooper, K.M, 2017. What does a magma reservoir look like? The "crystal-eye" view. *Elements*, 13, pp. 23-28.

Cooper, K.M. & Kent, A.J.R., 2014. Rapid remobilization of magmatic crystals kept in cold storage. *Nature*, 506(7489), pp.480–483. Available at: http://dx.doi.org/10.1038/nature12991.

Costa, F., Coogan, L.A. & Chakraborty, S., 2010. The time scales of magma mixing and mingling involving primitive melts and melt-mush interaction at mid-ocean ridges. *Contributions to Mineralogy and Petrology*, 159(3), pp.371–387.

Costa, F., Dohmen, R. & Chakraborty, S., 2008. Time Scales of Magmatic Processes from Modeling the Zoning Patterns of Crystals. *Reviews in Mineralogy and Geochemistry*, 69(1), pp.545–594. Available at: http://rimg.geoscienceworld.org/cgi/doi/10.2138/rmg.2008.69.14.

Couch, S. et al., 2003. Experimental constraints on the conditions of formation of highly calcic plagioclase microlites at the Soufrire Hills Volcano, Montserrat. *Journal of*

Petrology, 44(8), pp.1455–1475.

Couch, S., Sparks, R.J. & Carroll, M.R., 2003. The Kinetics of Degassing-Induced Crystallization at Soufriere Hills Volcano, Montserrat. *Journal of Petrology*, 44(8), pp.1477–1502. Available at: https://academic.oup.com/petrology/article-lookup/doi/10.1093/petrology/44.8.1477.

Cox, K.G., Bell, J.D. & Pankhurst, R.J., 1979. The Interpretation of Igneous Rocks. Allen and Unwin, London.

Cullen A, Vicenzi E, McBirney AR., 1989. Plagioclase-ultraphyric basalts of the Galapagos Archipelago. *Journal of Volcanology and Geothermal Research*, 37, pp.325–337. https ://doi.org/10.1016/0377-0273(89)90087 -5

Danyushevsky, L. V., 2001. The effect of small amounts of H2O on crystallisation of mid-ocean ridge and backarc basin magmas. *Journal of Volcanology and Geothermal Research*, 110(3–4), pp.265–280.

Danyushevsky, L. V. & Plechov, P., 2011. Petrolog3: Integrated software for modeling crystallization processes. *Geochemistry, Geophysics, Geosystems*, 12(7).

Davidson, J. et al., 2007. Amphibole "sponge" in arc crust? *Geology*, 35(9), pp.787–790.

Davidson, J. et al., 2001. Magma recharge, contamination and residence times revealed by in situ laser ablation isotopic analysis of feldspar in volcanic rocks. *Earth and Planetary Science Letters*, 184, pp.427–442.

Davidson, J.P., 1987. Crustal contamination versus subduction zone enrichment: Examples from the Lesser Antilles and implications for mantle source compositions of island arc volcanic rocks. *Geochimica et Cosmochimica Acta*, 51(8), pp.2185–2198.

Davidson, J.P. et al., 2007. Microsampling and isotopic analysis of igneous rocks: implications for the study of magmatic systems. Available at: http://oro.open.ac.uk/9162/.

Davidson, J.P., Morgan, D.J. & Charlier, B.L. a, 2007. Isotopic Microsampling of Magmatic Rocks. , pp.253–260.

DePaolo, D.J. 1981. Trace element and isotopic effects of combined wallrock assimilation and fractional crystallisation. *Earth and Planetary Science Letters*, 53, pp.189-202.

De Rosa, R., Donato, P. & Ventura, G., 2002. Fractal analysis of mingled/mixed magmas: An example from the Upper Pollara eruption (Salina Island, southern TyrrhenianSea, Italy). *Lithos*, 65(3–4), pp.299–311.

Dohmen, R. & Chakraborty, S., 2007. Fe-Mg diffusion in olivine II: Point defect chemistry, change of diffusion mechanisms and a model for calculation of diffusion coefficients in natural olivine. *Physics and Chemistry of Minerals*, 34(6), pp.409–430.

Drake MJ, Weill DF (1975) Partition of Sr, Ba, Ca, Y, Eu/2+/, EU/3+/, and other REE 919 between plagioclase feldspar and magmatic liquid - An experimental study. 39:689–920 712. doi: 10.1016/0016-7037(75)90011-3

Druitt, T.H. et al., 2012. Decadal to monthly timescales of magma transfer and reservoir growth at a caldera volcano. *Nature*, 482(7383), pp.77–80. Available at: http://www.ncbi.nlm.nih.gov/pubmed/22297973.

Dufek, J. & Bachmann, O., 2010. Quantum magmatism: Magmatic compositional gaps generated by melt-crystal dynamics. *Geology*, 38(8), pp.687–690.

Edmonds M, Cashman KV, Holness M, Jackson M. 2019 Architecture and dynamics of magma reservoirs. *Phil. Trans. R. Soc. A* 377: 20180298.

Ellam, R.M. & Harmon, R.S., 1990. Oxygen isotope constraints on the crustal contribution to the subduction-related magmatism of the Aeolian Islands, southern Italy. *Journal of Volcanology and Geothermal Research*, 44(1–2), pp.105–122.

Ford, C.E. et al., 1983. Olivine-Liquid Equilibria: Temperature, Pressure and Composition Dependence of the Crystal/Liquid Cation Partition Coefficients for Mg, Fe2+, Ca and Mn. *Journal of Petrology*, 24(3), pp.256–266. Available at: http://petrology.oxfordjournals.org/content/24/3/256.short.

Francalanci, L. et al., 1993. Geochemical and isotopic variations in the calc-alkaline rocks of Aeolian arc, southern Tyrrhenian Sea, Italy: constraints on magma genesis. *Contributions to Mineralogy and Petrology*, 113(3), pp.300–313.

Francalanci, L., Braschi, E., Di Salvo, S., Lucchi F., Petrone C.M., 2014. When magmas do not interact: paired Roman-age activity revealed by tephra studies at Stromboli volcano. *Bulletin of Volcanology*, 76, pp.884-903.

Gelman, S.E., Gutiérrez, F.J. & Bachmann, O., 2013. On the longevity of large upper crustal silicic magma reservoirs. *Geology*, 41(7), pp.759–762.

Gertisser, R. & Keller, J., 2000. From basalt to dacite: Origin and evolution of the calc-alkaline series of Salina, Aeolian arc, Italy. *Contributions to Mineralogy and Petrology*, 139(5), pp.607–626.

Ghiorso, M.S. & Sack, R.O., 1995. Chemical mass transfer in magmatic processes IV. A revised and internally consistent thermodynamic model for the interpolation and extrapolation of liquid-solid equilibria in magmatic systems at elevated temperatures and pressures. *Contributions to Mineralogy and Petrology*, 119(2–3), pp.197–212.

Ginibre, C., Wörner, G. & Kronz, A., 2002. Minor- and trace-element zoning in plagioclase: implications for mamga chamber processes at Parinacota volcano, northern Chile. *Contributions to Mineralogy and Petrology*, 143, pp 300-315.

Ginibre, C., Wörner, G. & Kronz, A., 2007. Crystal zoning as an archive for magma evolution. *Elements*, 3, pp.261–266.

Govindaraju, K., Potts, P.J., Webb, P.C. & Watson, J.S. 1994. 1994 report on Whin Sill dolerite WS-E from England and Pitscurrie Microgabbro PM-S from Scotland: Assessment by one hundred and four international laboratories. *Geostandards Newsletter*, 18, pp.211–300.

Gravley, D.M. et al., 2007. Double trouble: Paired ignimbrite eruptions and collateral subsidence in the Taupo Volcanic Zone, New Zealand. *Bulletin of the Geological Society of America*, 119(1), pp.18–30.

Green, T.H. et al., 2000. SIMS determination of trace element partition coefficients between garnet, clinopyroxene and hydrous basaltic liquids at 2-7.5 GPa and 1080-1200°C. *Lithos*, 53(3–4), pp.165–187.

Grove, T.L., Baker, M.B. & Kinzler, R.J., 1984. Coupled CaAl-NaSi diffusion in plagioclase feldspar: Experiments and applications to cooling rate speedometry. *Geochimica et Cosmochimica Acta*, 48(10), pp.2113–2121.

Grove, T.L. & Kinzler, R.J., 1986. Petrogenesis of Andesites. *Annual Review of Earth and Planetary Sciences*, 14(1), pp.417–454. Available at: http://www.annualreviews.org/doi/10.1146/annurev.ea.14.050186.002221.

Gudmundsson, A., 2000. Dynamics of volcanic systems in Iceland: example of tectonism and volcanism at juxtaposed hot spot and mid ocean ridge systems. *Annual review of Earth and Planetary Science*, 28, pp.107–140.

Gudmundsson, A., 1995. Infrastructure and mechanics of volcanic systems in Iceland. *Journal of Volcanology and Geothermal Research*, 64(94), pp.1–22.

Gudmundsson, A., Lecoeur, N. & Mohajeri, N., 2014. Dike emplacement at Bardarbunga , Iceland , induces unusual stress changes , caldera deformation , and earthquakes. , pp.1–7.

Gurenko, A.A. & Sobolev, A.V., 2006. Crust-primitive magma interaction beneath neovolcanic rift zone of Iceland recorded in gabbro xenoliths from Midfell, SW Iceland. *Contributions to Mineralogy and Petrology*, 151, pp.495–520.

Gunnarsson, B., Marsh, B.D. & Taylor, H.P., 1998. Generation of Icelandic rhyolites: silicic lavas from the Torfajokull central volcano. *Journal of Volcanology and Geothermal Research*, 83, pp.1–45.

Halldórsson, S.A., Óskarsson, N., Grönvold, K., Sigurðsson, G., Sverrisdóttir, G. & Steinthórsson, S. (2008). Isotopic-heterogeneity of the Thjorsa lava – Implications for mantle sources and crustal processes within the Eastern Rift Zone, Iceland. *Chemical Geology*, 255, pp.305–316.

Hansen, H. & Grönvold, K., 2000. Plagioclase ultraphyric basalts in Iceland: the mush of the rift. *Journal of Volcanology and Geothermal Research*, 98, pp.1–32.

Hardarson, B.S. et al., 1997. Rift relocation — A geochemical and geochronological investigation of a palaeo-rift in northwest Iceland. *Earth and Planetary Science Letters*, 153(97), pp.181–196.

Hartley, M.E. & Thordarson, T., 2013. The 1874-1876 volcano-tectonic episode at Askja, North Iceland: Lateral flow revisited. *Geochemistry, Geophysics, Geosystems*, 14(7), pp.2286–2309.

Harker, A. (1896). On certain Granophyres, modified by the Incorporation of Gabbro-Fragments, in Strath Skye. *Quarterly Journal of the Geological Society*, 52, pp.320–330.

Hawkesworth, C. et al., 2004. Time scales of magmatic processes. *Earth and Planetary Science Letters*, 218(1–2), pp.1–16.

Hawkesworth, C.J. et al., 1993. Mantle and slab contributions in arc magmas. *Annual review of Earth and Planetary Science*, 21, pp.175–204.

Hersum, T.G. & Marsh, B.D., 2007. Igneous textures: On the kinetics behind the words. *Elements*, 3(4), pp.247–252.

Higgins, M.D., 2002. Closure in crystal size distributions (CSD), verification of CSD calculations, and the significance of CSD fans. *American Mineralogist*, 87(8–9), pp.1242–1243.

Higgins, M.D., 1996. Magma dynamics beneath Kameni volcano, Thera, Greece, as revealed by crystal size and shape measurements. *Journal of Volcanology and Geothermal Research*, 70(1–2), pp.37–48.

Higgins, M.D., 2000. Measurement of crystal size distributions. *American Mineralogist*, 85, pp.1105–1116. Available at: http://www.intl-ammin.geoscienceworld.org/content/85/9/1105.full.

Hildreth, W., 2004. Volcanological perspectives on Long Valley, Mammoth Mountain, and Mono Craters: Several contiguous but discrete systems. *Journal of Volcanology and Geothermal Research*, 136(3–4), pp.169–198.

Hinton, R.W., 1990. Ion microprobe trace-element analysis of silicates: Measurement of multi-element glasses. *Chemical Geology*, 83(1–2), pp.11–25.

Holness, M.B., Martin, V.M. & Pyle, D.M., 2005. Information about open-system magma chambers derived from textures in magmatic enclaves: The Kameni Islands, Santorini, Greece. *Geological Magazine*, 142(6), pp.637–649.

Holness, M.B., Anderson, A.T., Martin, V.M., Maclennan, J., Passmore, E. & Schwindinger, K., 2007. Textures in Partially Solidified Crystalline Nodules: a Window into the Pore Structure of Slowly Cooled Mafic Intrusions. *Journal of Petrology*, 48, pp.1243–1264.

Horwitz, P.E., Chiarizia, R. & Dietz, M.L., 1992. A novel strontium selective extraction chromatographic resin. *Solvent Extraction and Ion Exchange*, 10(2), pp.313–336. Available at: http://www.tandfonline.com/doi/abs/10.1080/07366299208918107.

Humphreys, M.C.S., Blundy, J.D. & Sparks, R.S.J., 2006. Magma evolution and open-system processes at Shiveluch Volcano: Insights from phenocryst zoning. *Journal of Petrology*, 47(12), pp.2303–2334.

Humphreys, M.C.S., Blundy, J.D. & Sparks, R.S.J., 2008. Shallow-level decompression crystallisation and deep magma supply at Shiveluch Volcano. *Contributions to Mineralogy and Petrology*, 155, pp.45–61.

Iddings, J.P. (1899). On the crystallization of igneous rocks. Bulletin of the Philosophical Society of Washington, 11, 65–113.

Irving, A.J. & Frey, F.A., 1984. Trace element abundances in megacrysts and their host basalts: Constraints on partition coefficients and megacryst genesis. *Geochimica et Cosmochimica Acta*, 48(6), pp.1201–1221.

Jacoby, W. & Gudmundsson, M.T., 2007. Hotspot Iceland: An introduction. *Journal of Geodynamics*, 43, pp.1–5.

Jarosewich, E., 2002. Smithsonian Microbeam Standards. *Journal of Research of the National Institute of Standards and Technology*, 107(6), p.681. Available at: http://nvlpubs.nist.gov/nistpubs/jres/107/6/j76jar.pdf.

Jerram, D. A. & Martin, V., 2008. Understanding crystal populations and their significance through the magma plumbing system. Available at: http://dx.doi.org/10.1144/SP304.7.

Jerram, D.A., Dobson, K.J., Morgan, D.J., Pankjurst, M.J., 2018. The Petrogenesis of Magmatic Systems: Using Igneous Textures to Understand Magmatic Processes. In: Volcanic and Igneous Plumbing Systems, *Elsevier*, pp. 192-224.

Jochum, K.P. et al., 2005. GeoReM: A New Geochemical Database for Reference Materials and Isotopic Standards. *Geostandards and Geoanalytical Research*, 29, pp.333–338. Available at: http://doi.wiley.com/10.1111/j.1751-908X.2005.tb00904.x.

Jónasson, K., 2007. Silicic volcanism in Iceland: Composition and distribution within the active volcanic zones. *Journal of Geodynamics*, 43(1), pp.101–117.

Kaban, M.K., Flóvenz, Ó.G. & Pálmason, G., 2002. Nature of the crust-mantle transition zone and the thermal state of the upper mantle beneath Iceland from gravity modelling. *Geophysical Journal International*, 149, pp.281–299.

Kahl, M., Chakraborty, S., Costa, F. & Pompilio, M., 2011. Dynamic plumbing system beneath volcanoes revealed by kinetic modelling, and the connection to monitoring data: an example from Mt. Etna. *Earth and Planetary Science. Letters,* 308, pp. 11–22.

Kahl, M. et al., 2013. Compositionally zoned crystals and real-time degassing data reveal changes in magma transfer dynamics during the 2006 summit eruptive episodes of Mt. Etna. *Bulleting of Volcanology*, 75, pp. 692.

Kuo, L.C., and Kirkpatrick, R.J., 1982. Pre-eruptive history of phyric basalts from DSDP Legs 45 and 46: Evidence from morphology and zoning patterns in plagioclase. *Contributions to Mineralogy and Petrology*,79, 13-27

Lange AE, Nielsen RL, Tepley FJ, Kent AJR., 2013. The petrogenesis of plagioclase-phyric basalts at mid-ocean ridges. *Geochemistry Geophysics Geosystems*, 14, pp.3282–3296. https ://doi.org/10.1002/ggge.20207

Larsen, G. et al., 2015. The Torfajokull volcanic system. In *Ilyinskaya, Larsen and Gudmundsson (eds.): Catalogue of Icelandic Volcanoes. IMO, UI, CPD-NCIP.*

LaTourrette, T., Hervig, R.L. & Holloway, J.R., 1995. Trace element partitioning between amphibole, phlogopite, and basanite melt. *Earth and Planetary Science Letters*, 135(1–4), pp.13–30.

Laubier, M., Grove, T.L. & Langmuir, C.H., 2014. Trace element mineral/melt partitioning for basaltic and basaltic andesitic melts: An experimental and laser ICP-MS study with application to the oxidation state of mantle source regions. *Earth and Planetary Science Letters*, 392, pp.265–278. Available at: http://dx.doi.org/10.1016/j.epsl.2014.01.053.

Li C, Ripley EM., 2010. The relative effects of composition and temperature on olivine-981 liquid Ni partitioning: Statistical deconvolution and implications for petrologic 982 modeling. Chem Geol 275:99–104. doi: 10.1016/j.chemgeo.2010.05.001

Lippitsch, R., White, R.S. & Soosalu, H., 2005. Precise hypocentre relocation of microearthquakes in a high-temperature geothermal field: The Torfajokull central

volcano, Iceland. *Geophysical Journal International*, 160(1), pp.370–387.

Lofgren G., 1972. Temperature induced zoning in synthetic plagioclase feldspar. In: MacKenzie WS, Zussman J (eds) *The feldspars. Manchester University Press*, Manchester, England, pp 362–375

Lofgren G., 1974. An experimental study of plagioclase crystal morphology: isothermal crystallization. *American Journal of Science*, 274, pp.243–273

Lucchi, F. et al., 2013. Chapter 9 Eruptive history and magmatic evolution of the island of Salina (central Aeolian archipelago). *Geological Society, London, Memoirs*, 37(1), pp.155–211. Available at: http://mem.lyellcollection.org/cgi/doi/10.1144/M37.9.

Macdonald, R. et al., 1990a. Petrogenetic evolution of the torfajökull volcanic complex, Iceland I. Relationships between magma types. *Journal of Petrology*, 31(2), pp.461–481.

Macdonald, R. et al., 1990b. Petrogenetic Evolution of the Torfajokull Volcanic Complex , Iceland I. Relationship Between the Magma Types. *Journal of Petrology*, 31(2), pp.461–481.

Macdonald, R., Hawkesworth, C.J. & Heath, E., 2000. The Lesser Antilles volcanic chain: A study in arc magmatism. *Earth Science Reviews*, 49(1–4), pp.1–76.

Marsh, B.D., 1988. Crystal size distribution (CSD) in rocks and the kinetics and dynamics of crystallisation I: Theory. *Contributions to Mineralogy and Petrology*, 99, pp.277–291. Available at: file:///C:/Users/Kirsty/Downloads/Marsh 1988 Contrib Min Pet small (1).pdf.

Marsh, B.D., 1981. On the crystallinity, probability of occurrence, and rheology of lava and magma. *Contributions to Mineralogy and Petrology*, 78(1), pp.85–98.

Martin, E. & Sigmarsson, O., 2007. Crustal thermal state and origin of silicic magma in Iceland: The case of Torfajökull, Ljósufjöll and Snæfellsjökull volcanoes. *Contributions to Mineralogy and Petrology*, 153(5), pp.593–605.

Martin, E. & Sigmarsson, O., 2010. Thirteen million years of silicic magma production in Iceland: Links between petrogenesis and tectonic settings. *Lithos*, 116(1–2), pp.129–144. Available at: http://dx.doi.org/10.1016/j.lithos.2010.01.005.

Mattsson, T. et al., 2018. Syn-Emplacement Fracturing in the Sandfell Laccolith, Eastern Iceland—Implications for Rhyolite Intrusion Growth and Volcanic Hazards. *Frontiers in Earth Science*, 6(February). Available at: http://journal.frontiersin.org/article/10.3389/feart.2018.00005/full.

Matzen, A.K. et al., 2013. The temperature and pressure dependence of nickel partitioning between olivine and silicate melt. *Journal of Petrology*, 54(12), pp.2521–2545.

McGarvie, D.W. et al., 2006. Pleistocene rhyolitic volcanism at Torfajökull, Iceland: eruption ages, glaciovolcanism, and geochemical evolution. , 3(56), pp.57–75. Available at: http://oro.open.ac.uk/31472/.

McGarvie, D.W., 1984. Torfajökull : A volcano dominated by magma mixing. *Geology*, 12, pp.685–688.

McGarvie, D.W., Macdonald, R. & Pinkerton, H., 1990. Petrogenetic Evolution of the Torfajokull Volcanic Complex , Iceland II . The Role of Magma Mixing. *Journal of Petrology*, 31, pp.461–481.

Meyer, C.J., Anderson, D.H. & Bradley, J.G., 1974. Ion microprobe mass analysis of plagioclase from "non-mare" lunar samples. *Proceedings of the Fifth Lunar Conferece, (supplement 5, Geochemica et Cosmochimica Acta)*, 1, pp.685–706.

Mollo, S. & Hammer, J.E., 2017. Dynamic crystallization in magmas. *Mineral reaction kinetics: Microstructures, textures, chemical and isotopic signatures*, 16, pp.378–418. Available at: http://www.minersoc.org/emu-notes-16-12.html.

Morgan, D.J. et al., 2004. Time scales of crystal residence and magma chamber volume from modelling of diffusion profiles in phenocrysts: Vesuvius 1944. *Earth and Planetary Science Letters*, 222, pp.933–946.

Mørk, M.B.E., 1984. Magma mixing in the post-glacial veidivötn fissure eruption, southeast Iceland: a microprobe study of mineral and glass variations. *Lithos*, 17, pp.55–75.

Murphy, M.D. et al., 2000. Remobilization of Andesite Magma by Intrusion of Mafic Magma at the Soufriere Hills Volcano, Montserrat, West Indies. *Journal of Petrology*, 41(1), pp.21–42.

Neave, D.A., Buisman, I. & MacLennan, J., 2017. Continuous mush disaggregation during the long-lasting Laki fissure eruption, Iceland. *American Mineralogist*, 102(10), pp.2007–2021.

Neave, D.A. & Putirka, K.D., 2017. A new clinopyroxene-liquid barometer, and implications for magma storage pressures under Icelandic rift zones. *American Mineralogist*, 102(4), pp.777–794.

Neave, D. a et al., 2014. Crystal Storage and Transfer in Basaltic Systems : the Skuggafjoll Eruption , Iceland. , 55(12), pp.2311–2346.

Nehring, F. et al., 2008. Laser-ablation ICP-MS analysis of siliceous rock glasses fused on an iridium strip heater using MgO dilution. *Microchimica Acta*, 160(1–2), pp.153–163.

Nelson ST, Montana A., 1992. Sieve-textured plagioclase in volcanic rocks produced by rapid decompression. *American Mineralogist*, 77, PP.1242–1249

Ni, H. et al., 2014. In situ observation of crystal growth in a basalt melt and the development of crystal size distribution in igneous rocks. *Contributions to Mineralogy and Petrology*, 167(5), pp.1–13.

Nicotra, E. et al., 2014. Volcanological evolution of the Rivi-Capo Volcanic Complex at Salina, Aeolian Islands: Magma storage processes and ascent dynamics. *Bulletin of Volcanology*, 76(8), pp.1–24.

Nielsen, R.L., 1985. A method for the elimination of the compositional dependence of trace element distribution coefficients. *Geochimica et Cosmochimica Acta*, 49, pp.1775–1779.

Nielsen RL, Crum J, Bourgeois R., et al. 1994. Local diversity of MORB parent magmas: evidence from melt inclusions in high-an feldspar from the Gorda Ridge.

Mineralogical Magazine, 58A, pp.651–652. https ://doi.org/10.1180/minma g.1994.58A.2.75

Nielsen, R.L. et al., 2017. Trace element partitioning between plagioclase and melt: An investigation into the impact of experimental and analytical procedures. *Geochemistry, Geophysics, Geosystems*, 18(9), pp.3359–3384.

O'Hara, M.J., 1977. Geochemical evolution during fractional crystallisation of a periodically refilled magma chamber. *Nature*, 266(5602), pp.503–507.

Passmore, E., Maclennan, J., Fitton, J.G. & Thordarson, T., 2012. Mush Disaggregation in Basaltic Magma Chambers: Evidence from the AD 1783 Laki Eruption. *Journal of Petrology*, 35, pp.2593–2623.

Panjasawatwong, Y. et al., 1995. An experimental study of the effects of melt composition on plagioclase-melt equilibria at 5 and 10 kbar: implications for the origin of magmatic high-An plagioclase. *Contributions to Mineralogy and Petrology*, 118, pp.420–432.

Pankhurst, M.J. et al., 2018. Magmatic crystal records in time, space, and process, causatively linked with volcanic unrest. *Earth and Planetary Science Letters*, 493, pp.231–241. Available at: https://doi.org/10.1016/j.epsl.2018.04.025.

Pearce, J.A. & Peate, D.W., 1995. Tectonic Implications of the composition of Volcanic Arc Magmas. *Annual review of Earth and Planetary Science*, 23, pp.251–285.

Peccerillo, A. et al., 2013. Chapter 15 Compositional variations of magmas in the Aeolian arc: implications for petrogenesis and geodynamics. *Geological Society, London, Memoirs*, 37(1), pp.491–510. Available at: http://mem.lyellcollection.org/cgi/doi/10.1144/M37.15.

Peccerillo, A. et al., 2004. Sr-Nd-Pb-O isotopic evidence for decreasing crustal contamination with ongoing magma evolution at Alicudi volcano (Aeolian arc, Italy): Implications for style of magma-crust interaction and for mantle source compositions. *Lithos*, 78(1–2), pp.217–233.

Perugini, D. et al., 2015. Concentration variance decay during magma mixing: a volcanic chronometer. *Scientific reports*, 5, p.14225. Available at: http://www.scopus.com/inward/record.url?eid=2-s2.0-84942163079&partnerID=tZOtx3y1.

Perugini, D. et al., 2004. Kinematic significance of morphological structures generated by mixing of magmas: A case study from Salina Island (southern Italy). *Earth and Planetary Science Letters*, 222(3–4), pp.1051–1066.

Perugini, D., Poli, G. & Mazzuoli, R., 2003. Chaotic advection, fractals and diffusion during mixing of magmas: Evidence from lava flows. *Journal of Volcanology and Geothermal Research*, 124(3–4), pp.255–279.

Petrone, C.M. et al., 2016. Pre-eruptive magmatic processes re-timed using a non-isothermal approach to magma chamber dynamics. *Nature Communications*, 7, p.12946. Available at: http://www.nature.com/doifinder/10.1038/ncomms12946.

Plail, M. et al., 2018. Mafic enclaves record syn-eruptive basalt intrusion and mixing. *Earth and Planetary Science Letters*, 484, pp.30–40. Available at: https://doi.org/10.1016/j.epsl.2017.11.033.

Plank, T. & Langmuir, C.H., 1998. The chemical composition of subducting sediment and its consequences for the crust and mantle. *Chemical Geology*, 145(3–4), pp.325–394.

Pupier, E., Duchene, S. & Toplis, M.J., 2008. Experimental quantification of plagioclase crystal size distribution during cooling of a basaltic liquid. *Contributions to Mineralogy and Petrology*, 155, pp.555–570.

Putirka, K., 1999. Clinopyroxene + liquid equilibria to 100 kbar and 2450 K. *Contributions to Mineralogy and Petrology*, 135(November 1998), pp.151–163.

Putirka, K. et al., 1996. Thermobarometry of mafic igneous rocks based on clinopyroxene-liquid equilibria, 0-30 kbar. *Contributions to Mineralogy and Petrology*, 123(1), pp.92–108.

Putirka, K.D., 2005. Igneous thermometers and barometers based on plagioclase + liquid equilibria: Tests of some existing models and new calibrations. *American Mineralogist*, 90(2–3), pp.336–346.

Putirka, K.D. et al., 2003. New clinopyroxene-liquid thermobarometers for mafic, evolved, and volatile-bearing lava compositions, with applications to lavas from Tibet and the Snake River Plain, Idaho. *American Mineralogist*, 88(10), pp.1542–1554.

Putirka, K.D., 2008. Thermometers and Barometers for Volcanic Systems. *Reviews in Mineralogy and Geochemistry*, 69, pp.61–120.

Ren, M., Parker, D.F. & White, J.C., 2003. Partitionning of Sr, Rb, Y, and LREE between plagioclase and peraluminous silicic magma. *American Mineralogist*, 88, pp.1091–1103.

Renjith, M.L., 2014. Micro-textures in plagioclase from 1994-1995 eruption, Barren Island Volcano: Evidence of dynamic magma plumbing system in the Andaman subduction zone. *Geoscience Frontiers*, 5, pp.113–126. Available at: http://dx.doi.org/10.1016/j.gsf.2013.03.006.

Ridley, W.I., Perfit, M.R., Smith, M.C. & Fornari, D.J., 2006. Magmatic processes in developing oceanic crust revealed in a cumulate xenolith collected at the East Pacific Rise, 9°50'N. *Geochemistry Geophysics Geosystems*, 7, pp.Q12O04.

Ridolfi, F. & Renzulli, A., 2012. Calcic amphiboles in calc-alkaline and alkaline magmas: Thermobarometric and chemometric empirical equations valid up to 1,130°C and 2.2 GPa. *Contributions to Mineralogy and Petrology*, 163(5), pp.877–895.

Roeder PL, Emslie RF., 1970. Olivine-liquid equilibrium. Contrib to Mineral Petrol 1048 29:275–289. doi: 10.1007/BF00371276

Ruprecht, P. et al., 2012. The crustal magma storage system of volcán quizapu, chile, and the effects of magma mixing on magma diversity. *Journal of Petrology*, 53(4), pp.801–840.

Salaün, A., Villemant, B., Semet, M. & Staudacher, T., 2010. Cannibalism of olivine-rich cumulate xenoliths during the 1998 eruption of Piton de la Fournaise (La Réunion hotspot): Implications for the generation of magma diversity. *Journal of Volcanology and Geothermal Research*, 198, pp.187–204.

Schiavi, F. et al., 2010. A moissanite cell apparatus for optical in situ observation of crystallizing melts at high temperature. *American Mineralogist*, 95(7), pp.1069–1079.

Schindelin, J. et al., 2012. Fiji: An open source platform for biological image analysis. *Nature Methods*, 9(7), pp.676–682.

Shea, T. & Hammer, J.E., 2013. Kinetics of cooling- and decompression-induced crystallization in hydrous mafic-intermediate magmas. *Journal of Volcanology and Geothermal Research*, 260, pp.127–145. Available at: http://dx.doi.org/10.1016/j.jvolgeores.2013.04.018.

Shea, T., Lynn, K.J. & Garcia, M.O., 2015. Cracking the olivine zoning code: Distinguishing between crystal growth and diffusion. *Geology*, 43(10), pp.935–938.

Shorttle, O. & Maclennan, J., 2011. Compositional trends of Icelandic basalts: Implications for short-length scale lithological heterogeneity in mantle plumes. *Geochemistry, Geophysics, Geosystems*, 12(11).

Shorttle, O., Maclennan, J. & Piotrowski, A.M., 2013. Geochemical provincialism in the Iceland plume. *Geochimica et Cosmochimica Acta*, 122, pp.363–397. Available at: http://dx.doi.org/10.1016/j.gca.2013.08.032.

Sigurdsson, H. & Sparks, R.S.J., 1978. Rifting episode in north iceland in 1874-1875 and the eruptions of askja and sveinagja. *Bulletin Volcanologique*, 41(3), pp.149–167.

Sisson, T.W. & Grove, T.L., 1993. Experimental investigations of the role of H2O in calc-alkaline differentiation and subduction zone magmatism. *Contributions to Mineralogy and Petrology*, 113(2), pp.143–166.

Smith RK, Lofgren FE., 1979. The physio-chemical and crystal growth kinetics necessary for zonal development in plagioclase. *Geological Society of America Abstracts Program*, 7, pp.520

Smith, P.M. & Asimow, P.D., 2005. Adiabat-1ph: A new public front-end to the MELTS, pMELTS, and pHMELTS models. *Geochemistry, Geophysics, Geosystems*, 6(2), pp.1–8.

Smith, V.C., Blundy, J.D. & Arce, J.L., 2009. A temporal record of magma accumulation and evolution beneath Nevado de Toluca, Mexico, preserved in plagioclase phenocrysts. *Journal of Petrology*, 50(3), pp.405–426.

Solano, J.M.S. et al., 2012. Melt segregation in deep crustal hot zones: A mechanism for chemical differentiation, crustal assimilation and the formation of evolved magmas. *Journal of Petrology*, 53(10), pp.1999–2026.

Soosalu, H. & Einarsson, P., 2004. Seismic constraints on magma chambers at Hekla and Torfajökull volcanoes, Iceland. *Bulletin of Volcanology*, 66(3), pp.276–286.

Soosalu, H., Lippitsch, R. & Einarsson, P., 2006. Low-frequency earthquakes at the Torfajökull volcano, south Iceland. *Journal of Volcanology and Geothermal Research*, 153(3–4), pp.187–199.

Sparks, R.S.J. & Cashman, K. V., 2017. Dynamic magma systems: Implications for

forecasting volcanic activity. *Elements*, 13(1), pp.35–40.

Sparks, S.R.J., Sigurdsson, H. & Wilson, L., 1977. Magma mixing: A mechanism for triggering acid explosive eruptions. *Nature*, 267(5609), pp.315–318.

Špillar, V. & Dolejš, D., 2015. Heterogeneous nucleation as the predominant mode of crystallization in natural magmas: numerical model and implications for crystal–melt interaction. *Contributions to Mineralogy and Petrology*, 169(1).

Špillar, V. & Dolejš, D., 2014. Kinetic model of nucleation and growth in silicate melts: Implications for igneous textures and their quantitative description. *Geochimica et Cosmochimica Acta*, 131, pp.164–183.

Stelten, M.E. et al., 2014. Mechanisms and timescales of generating eruptible rhyolitic magmas at Yellowstone Caldera from Zircon and sanidine geochronology and geochemistry. *Journal of Petrology*, 56(8), pp.1607–1642.

Streck, M.J., 2008. Mineral Textures and Zoning as Evidence for Open System Processes. *Reviews in Mineralogy and Geochemistry*, 69(1), pp.595–622.

Sun, C., Graff, M. & Liang, Y., 2017. Trace element partitioning between plagioclase and silicate melt: The importance of temperature and plagioclase composition, with implications for terrestrial and lunar magmatism. *Geochimica et Cosmochimica Acta*, 206, pp.273–295. Available at: http://dx.doi.org/10.1016/j.gca.2017.03.003.

Tait, S.R., Jaupart, C. & Vergniolle, S., 1989. Pressure, gas content and eruption periodicity of a shallow crystallizing magma chamber [abs.]. *Eos, Transactions, American Geophysical Union*, v. 69(44), p.1465.

Takagi, D., Sato, H. & Nakagawa, M., 2005. Experimental study of a low-alkali tholeiite at 1-5 kbar: Optimal condition for the crystallization of high-An plagioclase in hydrous arc tholeiite. *Contributions to Mineralogy and Petrology*, 149, pp.527–540.

Tatsumi, Y. et al., 1989. Opening of the Sea of Japan back-arc basin by asthenopheric injection. *Tectonophysics*, 166, pp.317–329.

Tepley, F.J. et al., 2010. Trace element partitioning between high-An plagioclase and basaltic to basaltic andesite melt at 1 atmosphere pressure. *Lithos*, 118(1–2), pp.82–94. Available at: http://dx.doi.org/10.1016/j.lithos.2010.04.001.

Tepley, F.J., Davidson, J.P. & Clynne, M. a, 1999. Magmatic interactions as recorded in plagioclase phenocrysts of Chaos Crags, Lassen Volcanic Center, California. *Journal of Petrology*, 40(5), pp.787–806.

Thirlwall, M.., Singer, B.. & Marriner, G.., 2000. 39Ar–40Ar ages and geochemistry of the basaltic shield stage of Tenerife, Canary Islands, Spain. *Journal of Volcanology and Geothermal Research*, 103, pp.247–297.

Thirlwall, M.F. et al., 1994. High field strength element anomalies in arc lavas: Source or process? *Journal of Petrology*, 35(3), pp.819–838.

Thirlwall, M.F., Upton, B.G.J. & Jenkins, C., 1994. Interaction between Continental Lithosphere and the Iceland Plume — Sr-Nd-Pb Isotope Geochemistry of Tertiary Basalts, NE Greenland. *Journal of Petrology*, 35, pp.839–879.

Thordarson, T. & Larsen, G., 2007. Volcanism in Iceland in historical time: Volcano types, eruption styles and eruptive history. *Journal of Geodynamics*, 43, pp.118–152.

Tsune, A. & Toramaru, A., 2008. Quantitative description of oscillatory zoning in basaltic to dacitic plagioclases from the Shirahama Group, Japan. *Earth, Planets and Space*, 60(6), pp.653–660.

Turner, S.J., Izbekov, P. & Langmuir, C., 2013. The magma plumbing system of Bezymianny Volcano: Insights from a 54year time series of trace element whole-rock geochemistry and amphibole compositions. *Journal of Volcanology and Geothermal Research*, 263, pp.108–121. Available at: http://dx.doi.org/10.1016/j.jvolgeores.2012.12.014.

Ubide, T. et al., 2014. The relevance of crystal transfer to magma mixing: A case study in composite dykes from the central pyrenees. *Journal of Petrology*, 55(8), pp.1535–1559.

Ubide, T. & Kamber, B.S., 2018. Volcanic crystals as time capsules of eruption history. *Nature Communications*, 9, pp.326-337.

Vance JA, 1965. Zoning in igneous plagioclase: patchy zoning. *The Journal of Geology*, 73, pp.637–651

Ventura, G., 2013. Chapter 2 Kinematics of the Aeolian volcanism (Southern Tyrrhenian Sea) from geophysical and geological data. *Geological Society, London, Memoirs*, 37(1), pp.3–11. Available at: http://mem.lyellcollection.org/cgi/doi/10.1144/M37.2.

Vermeesch, P., 2004. How many grains are needed for a provenance study? *Earth and Planetary Science Letters*, 224(3–4), pp.441–451.

Viccaro, M. et al., 2016. Crystal residence times from trace element zoning in plagioclase reveal changes in magma transfer dynamics at Mt. Etna during the last 400 years. *Lithos*, 248–251, pp.309–323. Available at: http://dx.doi.org/10.1016/j.lithos.2016.02.004.

Viccaro, M. et al., 2010. Dynamics of magma supply at Mt. Etna volcano (Southern Italy) as revealed by textural and compositional features of plagioclase phenocrysts. *Lithos*, 116(1–2), pp.77–91. Available at: http://dx.doi.org/10.1016/j.lithos.2009.12.012.

Wagner, J. et al., 2017. Trace element partitioning between silicate melts – A molecular dynamics approach. *Geochimica et Cosmochimica Acta*, 205, pp.245–255.

Walter, T.R. et al., 2014. Possible coupling of Campi Flegrei and Vesuvius as revealed by InSAR time series, correlation analysis and time dependent modeling. *Journal of Volcanology and Geothermal Research*, 280, pp.104–110. Available at: http://dx.doi.org/10.1016/j.jvolgeores.2014.05.006.

Wood, B.J. & Blundy, J.D., 1997. A predictive model for rare earth element partitioning between clinopyroxene and anhydrous silicate melt. *Contributions to Mineralogy and Petrology*, 129(2–3), pp.166–181.

Zamboni, D. et al., 2016. Contrasting sedimentmelt and fluid signatures for magma components in the Aeolian Arc: Implications for numerical modeling of

subduction systems. *Geochemistry Geophysics Geosystems*, 17, pp.2034–2053.

Zellmer, G.F. et al., 2008. On the recent bimodal magmatic processes and their rates in the Torfajokull-Veidivotn area, Iceland. *Earth and Planetary Science Letters*, 269(3–4), pp.387–397.

Zieg, M.J. & Lofgren, G.E., 2006. An experimental investigation of texture evolution during continuous cooling. *Journal of Volcanology and Geothermal Research*, 154, pp.74–88.